

Ultra thin ZnO on metal substrates

An ab initio study

vorgelegt von
Dipl.-Phys.
Björn Bieniek
Köthen/Anhalt

Von der Fakultät II – Mathematik und Naturwissenschaften
der Technischen Universität Berlin
zur Erlangung des akademischen Grades

Doktor der Naturwissenschaften
Dr. rer. nat

genehmigte Dissertation

Promotionsausschuss:

Vorsitzender: Prof. Dr. rer. nat. Mario Dähne
1. Gutachter: Prof. Dr. rer. nat. Andreas Knorr
2. Gutachter: Prof. Dr. rer. nat. Patrick Rinke

Tag der wissenschaftlichen Aussprache: 12. Januar 2016

Berlin– 2016

ABSTRACT

In the context of catalysis and hybrid inorganic/organic systems, metal supported ultra-thin ZnO can be used as model systems within the surface science approach. However, it is not clear to what degree the ZnO films resemble the surfaces of ZnO or whether they exhibit significantly different properties.

To this purpose we investigate the structure of ultra-thin ZnO films (1 to 4 layers) on the (111) surfaces of Ag, Cu, Ni, Rh, Pd, and Pt by means of density-functional theory. The free-standing ZnO mono-layer adopts an α -BN structure. This structure prevails on the metal substrates, and we obtain coincidence structures in good agreement with experiment. Thicker ZnO layers, preferentially grow in the c-direction and adopt a wurtzite structure. The films exhibit a large random corrugation. The electronic structure is modified by the intrinsic polar nature of ZnO. The induced field leads to an upwards shift of the surface electronic states relative to the Fermi level with increasing film thickness. The states are eventually pinned at the Fermi level provided by the metal substrate, leading to an effective p-type doping of the thin film surface. Metal supported ultra-thin films might thus be a way to achieve the much coveted p-type doping of ZnO.

To investigate the thermodynamic stability of ZnO on the metal substrates we take the chemical potentials of Zn, O₂, H₂, and H₂O environments into consideration by means of *ab initio* thermodynamics. Up to three layers of unreconstructed ZnO are predicted to be stable on the metal substrates at experimentally accessible pressure ranges. A hydrogen over-layer with 50% coverage is formed at chemical potentials that range from low vacuum to ultra-high vacuum H₂ pressures. The surface structure and the density of states of these hydrogen passivated ZnO thin films agree well with those of the ZnO (000 $\bar{1}$)-(2 \times 1)-H surface.

ZnO ultra-thin films without hydrogen exhibit interesting and unique properties, whereas, the (2 \times 1)-H reconstructed films can be regarded as good ZnO surface models. The hydrogen chemical potential provides a handle to select and potentially switch between those two surface terminations.

We also include OH-reconstructions, Zn/O defects and sparse ring structures in our approach to draw up an extensive surface phase diagram that will guide future work on ultra-thin ZnO on metal substrates. For example, our calculations allow us to identify the ultra-thin films grown by Shiotari *et al.* on Ag as hydrogen-free ZnO double-layers.

In a joined effort with the group of A. Knorr at TU Berlin, "hybrid Bloch equations" based on a density-matrix formalism are parametrized by *ab initio* results. The parameterizations are based on dipole matrix elements and partial charges fitted to the electrostatic potential. Both methods were implemented as part of this Phd into the *FHI-aims* code to investigate excitonic process at ZnO/organic interfaces. The interaction of substrate and molecule was found to be strongest at low coverages and for a parallel alignment between the molecule and the surface dipole.

ZUSAMMENFASSUNG

In der heterogenen Katalyse und für hybride in-organische/organische Systeme können ultra-dünne ZnO Filme auf Metallen als Modell-System genutzt werden. Allerdings ist nicht geklärt ob diese Filme ZnO Oberflächen repräsentieren oder ob sie abweichende und damit für sie einzigartige Eigenschaften aufweisen.

Um diesen Sachverhalt zu klären untersuchen wir ultra-dünne ZnO Filme (1 bis 4 Lagen) auf den (111) Oberflächen von Ag, Cu, Ni, Rh, Pd, und Pt mit Hilfe von Dichtefunktionaltheorie. Der freistehende, einlagige ZnO Film weist eine α -BN Struktur auf. Diese Struktur bleibt auf den Metallsubstraten zunächst erhalten und wir können Koinzidenz-Strukturen in guter Übereinstimmung mit experimentellen Resultaten bestimmen. Dickere Filme nehmen eine Wurtzit-Struktur an. Die Filme weisen eine mit der Dicke zunehmende Korrugation auf. Die elektronische Struktur wird durch die intrinsische, polare Natur von ZnO modifiziert. Das induzierte elektrische Feld verschiebt die elektronischen Zustände an der Oberfläche mit zunehmender Filmdicke zu höheren Energien. Die Zustände werden schließlich am Fermi-Niveau des Metalls verankert. Dies führt zu einer effektiven p-Dotierung der Oberfläche des Dünnsfilms.

Während ultra-dünne ZnO-Filme ohne Wasserstoff interessante und einzigartige Eigenschaften aufweisen, können (2×1) -H rekonstruierte Filme zur Oberflächenmodellierung genutzt werden. Das chemische Potential des Wasserstoffes fungiert hierbei als Schalter zwischen beiden Oberflächenterminierungen.

Die Stabilität der ZnO-Filme auf Metallsubstraten wurde unter Berücksichtigung des chemischen Potentials von Zn, O₂, H₂ und H₂O mit Hilfe von *ab initio* Thermodynamik analysiert. Bis zu drei Lagen ZnO können auf den Metallsubstraten stabilisiert werden, bei experimentell realisierbaren Umgebungsbedingungen. Eine zusätzliche Absättigung der ZnO Oberfläche mit einer 50%igen Wasserstoffbedeckung ist bei chemischen Potentialen stabil die sich von niedrigen bis zu ultra-hoch-Vakuumbedingungen erstrecken. Die Oberflächenstruktur und die Zustandsdichte der passivierten ZnO Filme zeigen eine große Übereinstimmung mit der ZnO $(000\bar{1})$ - (2×1) -H Oberfläche.

Die Hinzunahme von OH-Rekonstruktionen, Zn/O Defekten und Ringstrukturen führt zu einem umfangreichen Phasendiagramm, dass zukünftige Untersuchungen von ZnO auf Metalloberflächen erleichtern wird. Zum Beispiel erlauben es unsere Resultate die von Shiotari *et al.* gewachsenen Dünnsfilme auf Ag als H-freie ZnO Doppellagen zu identifizieren.

In enger Kooperation mit der AG Knorr an der TU Berlin konnten die „Hybrid Bloch Gleichungen“ mit Hilfe von *ab initio* Rechnungen parametrisiert werden. Die Parametrisierung basiert auf Dipolmatrixelementen und Partialladungen, die an das elektrostatische Potential angepasst werden. Beide Methoden wurden im Rahmen dieser Arbeit in *FHI-aims* implementiert um excitonische Prozesse zwischen ZnO und organischen Molekülen zu untersuchen. Die Wechselwirkung zwischen Substrat und Molekül ist stärker bei geringen Bedeckungen und für parallel ausgerichtete Molekül- und Oberflächendipole.

CONTENTS

i	INTRODUCTION	1
ii	THEORETICAL CONCEPTS TO CHARACTERIZE SURFACES AND DEFECTS	7
1	THEORETICAL FRAMEWORK	9
1.1	The many-body problem	9
1.2	The Born-Oppenheimer approximation	10
1.3	Density Functional Theory	12
1.4	Approximate xc-functionals	14
1.4.1	Local density approximation (LDA)	14
1.4.2	Semi-Local density approximation	16
1.4.3	Hybrid functionals	17
1.5	Long range dispersion	18
1.6	Ab initio thermodynamics	20
1.7	DFT as implemented in FHI-aims	26
1.8	Calculating surface vibrations	28
1.9	Simulating STM apparent height maps	30
iii	ZNO ON METAL SUBSTRATES	33
2	INTRODUCTION	35
3	BULK ZNO	37
4	SURFACES OF ZNO	41
5	FREESTANDING ZNO THIN FILMS	47
5.1	Mechanical stability	48
5.2	Transition mono-layer to bulk	48
5.2.1	α -BN bulk ZnO	50
6	METAL SUPPORTED MONO-LAYER FILMS	53
6.1	Coincidence structures	54
6.2	Position in the 1x1 surface unit cell	59
6.3	Corrugation	59
7	METAL SUPPORTED MULTI-LAYER ZNO FILMS	63
7.1	Atomic structure of multiple layers of ZnO	63
7.2	Electronic structure of multiple layers of ZnO	65
8	THERMODYNAMIC STABILITY OF ZNO ON METAL SUBSTRATES	73
8.1	Hydrogen adsorption	73
8.1.1	Electronic structure of the (2x1)-H reconstruction.	78
8.2	Vacancies and ad-atoms	82
8.2.1	O vacancies and ad-atoms	83
8.2.2	Zinc defects and ad-atoms	85
8.2.3	Oxygen and zinc defects	87
8.3	Ring structures	89
8.4	Hydroxyl absorption	91

9	ZNO ON AG IN EXPERIMENT AND THEORY	103
9.1	Apparent heights in experiment	104
9.2	Results from DFT simulations	105
9.3	Conclusion	108
10	SPECIAL SURFACES	109
10.1	ZnO (0001)-(5×5)/Ag (111)-($3\sqrt{3} \times 3\sqrt{3}$)R30°	109
10.2	Rh (100)	114
11	PARAMETERIZATION OF DENSITY MATRIX FORMALISM BY DFT	119
11.1	Linking to Density-Matrix Theory	120
11.1.1	Dipole Approximation	123
11.1.2	Partial charge approximation	124
11.2	Results	129
iv	CONCLUSION	137
v	APPENDIX	143
A	CONSTANTS	145
B	REFERENCE ENERGIES	147
C	CONVERGENCE TESTS	149
D	COINCIDENCE STRUCTURES	153
E	CONVERGENCE WITH NUMBER OF METAL LAYERS	157
F	CORRUGATION MAPS	159
G	STRUCTURE OF MULTIPLE ZNO LAYERS	161
H	LAYER RESOLVED CORRUGATION MAPS	163
I	ELECTRONIC STRUCTURE OF MULTI-LAYER SYSTEMS	169
J	ELECTRONIC STRUCTURE OF (2x1)-H SYSTEMS	171
K	LAYER HEIGHTS FOR ZNO ON AG (111)	175
L	CURRENT DEPENDENCY OF APPARENT HEIGHTS	177
M	DEFECTS IN IDEAL α -BN ZNO MONO LAYER	179
N	CHARGE DENSITY DIFFERENCES	183
	PUBLICATIONS	i
	COLOPHON	iii
	BIBLIOGRAPHY	v

Part I

INTRODUCTION

The advances of semi conductor physics and surface science have changed the world in the last 100 years and lead to many technological applications that are integral part of our daily lives e. g. computers, flat and touch screens. One material, that is present in these developments since the beginning is ZnO [125]. It is not as prominent as Si or Ge, but as widely abundant, transparent, wide band gap semi-conductor has many applications e. g. in photo-voltaics [287, 103, 141, 289] or for laser diodes [264]. In this work it is of particular interest in the context of hybrid inorganic/organic systems (HIOS) for optoelectronic devices [137, 281, 233, 139]. Organic molecules and related compounds have already shown their potential e. g. for the application as OLEDs (organic light emitting diodes) [236, 43, 235, 90, 212], that even found their way into consumer electronics. Because of the low charge carrier mobilities in organic semi conductors [135, 80, 38, 256], these applications are mostly in areas that only require low device performances. A second issue are chemical reactions with metal electrodes [107, 37] and the general stability under realistic environmental conditions [115]. To realize devices, within the concepts established for inorganic semiconductors, the injection of electrons from one side and holes from the other side, transport of the charges and capture on the same molecule (as recombination center for radiative decay) are required [205]. Hybrid devices offer these features by combining the stability and the high charge carrier mobility of the inorganic, semi-conducting component with the chemical flexibility and strong light-matter coupling of the organic component. Especially resonant interactions such as effective non-radiative Förster energy transfer [82, 46, 34, 3] between both components are of interest. We can combine the best of two worlds: organic compounds and inorganic semi conductors.

Another important application of ZnO lies in the field of heterogeneous catalysis [184]. ZnO is required for the conversion of syn-gas in methanol production as catalyst [19]. This process captures CO₂ and produces methanol as a sustainable, environmentally friendly energy source. Here, ZnO supported metal nanoparticles are used in industry as high performance catalysts [25], but the reaction mechanism on the atomic scale is still under debate [95, 283].

For hybrid inorganic/organic systems and heterogeneous catalysis alike, metal supported ultra-thin oxide films have been proposed as model systems to understand the interface structure and its chemistry, because they facilitate the application of the standard tool set of surface science, such as photo-electron spectroscopy, and scanning tunneling microscopy, and prevent charging effects [87, 86]. However, some ultra-thin films exhibit their own interesting properties [88, 189, 234, 181], that differ from bulk materials. For example, the formation of a graphitic ZnO_x species was suggested and experimentally observed in the vicinity of metal nano-particles [175, 283]. It is thus not clear to what degree ultra-thin metal-supported ZnO films resemble the surfaces of ZnO or whether they exhibit significantly different properties. For ZnO ultra thin films a multitude of different polymorphs has been theoretically predicted and some even experimentally observed [83, 169, 170, 65].

Under ambient conditions ZnO adopts a wurtzite structure [1]. Other bulk polymorphs show equally interesting properties [228, 118]. In this work we will focus on the surfaces of wurtzite ZnO. The most common low index surfaces are the

(10 $\bar{1}$ 0), (1120), (0001) and (000 $\bar{1}$) surfaces. The discussion will mostly be restricted to the polar (0001) and (000 $\bar{1}$) surfaces. Only in the final chapter the (10 $\bar{1}$ 0) surface is used. The advances in epitaxial thin film growth [188] and surface preparation [93] make it possible to produce ZnO surfaces under highly controlled conditions [276]. However, the structure of the polar (000 $\bar{1}$) and (0001) surfaces, that are often used in hybrid systems [40, 5], is not fully understood [132, 161, 276, 262, 136, 267] hampering further quantitative interface studies.

To answer these questions and to characterize ultra-thin metal supported ZnO films as model systems for HIOS and heterogeneous catalysis, we performed density-functional theory (DFT) calculations for 1 to 4 layers ZnO films on various transition metal substrates. The theoretical insight gained in this work leads to predictions concerning the structure, thermodynamical stability and electronic structure of ZnO thin films on metal substrates. These predictions can guide experimentalists in preparing and understanding their samples to accurately model surfaces, interfaces and catalysts. The results of this work may help to create better devices in opto-electronics and to optimize chemical process on an industrial scale. We will focus on geometrical properties, e. g. the corrugation of the surface, and electronic properties, e. g. the density of states. Similarities and differences between ZnO thin films and bulk surfaces will be pointed out. Furthermore, the differences in the atomic structure and thermodynamic stability of pristine and reconstructed ultra-thin ZnO films on the transition metals: Ag, Cu, Pd, Pt, Ni, and Rh are investigated. The choice of the metal offers an additional degree of freedom in the selection of the model system.

In Chap 1 of this thesis we introduce the theoretical concepts and techniques required to achieve the broad spectrum of goals we have set out to achieve. We will shortly lay out the fundamentals of density-functional theory (DFT). For the practical application we used the Fritz Haber Institute ab initio simulation package (FHI-aims) [33]. The basics of the code are explained in Sec. 1.7, while the implementations for the code we performed for the description of Förster processes in HIOS (collaboration with the group of A. Knorr, TU Berlin) are deferred to Chap. 11. Based on DFT total energy calculations, we explain the construction of reliable surface phase diagrams in Sec. 1.6 and 1.8. The theoretical methods part concludes with the description of simulating STM graphs, to directly compare theory and experiment (Sec. 1.9).

To understand ultra-thin ZnO on metal substrates, the properties of bulk ZnO and its most prominent surfaces known from literature are discussed at the beginning of part II in Sec. 3 and 4. We first investigate freestanding ZnO films without a metal substrate in Sec. 5. Previous results [51, 83, 258] and calculations in this work demonstrate that it adopts an α -BN structure in analogy to graphene. Thicker films change to the wurtzite structure after 3-4 layers [255] (see Sec. 5.2). To obtain a stable combination of metal and ZnO mono-layer we address the lattice mismatch between the two constituents in Sec. 6 and obtain stable coincidence structures in good agreement with experimental results.

The observed differences in the atomic structure cannot only be explained by the strain that is introduced when ZnO is brought into contact with transition metals of different lattice constant. The role of the electron reservoir provided by the metal is therefore investigated in Sec. 7.2. We show that the potential difference

between the top and the bottom layer of the film, resulting from the intrinsic dipole of ZnO (000 $\bar{1}$), shifts the electronic states of ZnO upwards in energy until they are pinned at the Fermi level of the metal. This can be understood as effective p-type doping of the ultra-thin films.

In the context of previous results on the stability of the polar ZnO bulk surfaces [132, 267] the stability of the mono- and multi-layer ZnO films is addressed in Chap. 8. The films can be stabilized by the mechanisms valid for both the Zn and O-terminated bulk surface. The exact environmental conditions determine if the films are O- or Zn-terminated. For increased H₂ partial pressures the surface bonds are saturated by hydrogen, and the geometric and electronic structure resembles that of bulk terminated ZnO (000 $\bar{1}$) with a (2 × 1) hydrogen over layer (ZnO (000 $\bar{1}$)-(2 × 1)-H). At low H₂ partial pressures the clean ultra-thin film, exhibiting a graphitic (α -BN) character, is retained. The choice of metal and the partial pressures of H₂ and H₂O are additional degrees of freedom to switch between ultra-thin ZnO films, that differ from bulk ZnO, and films that resemble wurtzite ZnO and could serve as important models for the study of the ZnO (000 $\bar{1}$)-(2 × 1)-H surface. In Sec. 8.2.1 to Sec. 8.4 we successively develop and discuss an extensive surface phase diagram, considering the reconstruction mechanisms proposed for both polar ZnO surfaces. Furthermore, we discuss the accuracy, the influence of including vdW-corrections and the reliability of the PBE xc-functional.

In Chap. 9 the experimental results from the Department of Physical Chemistry (PC) of the FHI [237] are discussed and analyzed with the help of ab initio calculations. Special emphasis is put on the apparent heights measurements of ZnO on Ag [237]. The experimentally observed 5×5 reconstruction is discussed in Sec. 10.1 and included in the full surface phase diagram. In Sec. 10.2 we analyze the stability of ZnO on Rh (0001) [120] and compare it to the (111) surfaces, which offers the same three-fold symmetry as the ZnO thin films.

Finally we address non-radiative Föester process in the HIOsystem obtained by putting the ladder type quarter-phenyl molecule L4P [127] on ZnO (10 $\bar{1}$ 0) in Sec. 11 (in collaboration with AG Knorr, TU Berlin). The "hybrid bloch equations" derived by Verdanhoven, Richter, and Knorr are presented (see Ref. [265]). This density matrix formalism is parametrized by the atomic and electronic structure we obtain from DFT calculations. To model Förster processes we implemented the calculation and the output of dipole/momentum matrix elements and electrostatic potential partial charges in the FHI-aims code, that make it possible to approximate the coupling arising from the Coulomb matrix element between the organic and inorganic component.

The dissertation is summarized with a comprehensive discussion and an outlook on future work in Chap. iv.

Part II

THEORETICAL CONCEPTS TO CHARACTERIZE SURFACES AND DEFECTS

THEORETICAL FRAMEWORK

The theoretical results and predictions obtained in this thesis are based on the developments in quantum physics in the last century. The research in solid state physics has ultimately lead to the development of high performance computers, that are one key tool for achieving the goals outlined in the previous section. In the following sections the fundamental theoretical concepts used in this dissertation will be presented. They are themselves based on the axioms and theorems postulated and proven by many authors. For a rigorous derivation of the theory the reader is referred to standard textbooks of quantum and solid state physics. A short selection, that is entirely based on the preferences of the author are references [11, 247, 223, 124, 231, 182, 81, 76, 180, 42].

1.1 THE MANY-BODY PROBLEM

At the heart of all our efforts to understand molecular systems, solids and combinations of the former is the Many-body problem. For a system of electrons and nuclei the non-relativistic time-independent Schödinger equation [230] is:

$$H\Psi = E\Psi \quad (1)$$

with the Hamiltonian:

$$H = \underbrace{-\sum_{i=1}^N \frac{1}{2} \nabla_i^2 + \sum_{i=1}^N \sum_{j>i}^M \frac{1}{|\mathbf{r}_i - \mathbf{r}_j|} - \sum_{i=1}^N \sum_{a=1}^M \frac{Z_a}{|\mathbf{r}_i - \mathbf{R}_a|}}_{H_{elec}} \quad (2)$$

$$- \sum_{a=1}^M \frac{1}{2M_a} \nabla_a^2 + \sum_{a=1}^M \sum_{b>a}^M \frac{Z_a Z_b}{|\mathbf{R}_a - \mathbf{R}_b|} \quad (3)$$

\mathbf{r}_i : position of the electrons

\mathbf{R}_a : position of the nuclei

Z_a : charge of the nuclei

Throughout we are using atomic units:

$$m_e = e = \hbar = \frac{1}{4\pi\epsilon_0} = 1 \quad (4)$$

The energy is given in Hartree:

$$[Ha] = \frac{\hbar^2}{m_e a_0} = 27.21138505(60) \text{ eV}. \quad (5)$$

The unit of length is the Bohr radius:

$$a_0 = \frac{4\pi\epsilon_0 \hbar^2}{m_e e^2} = 0.529177208592(17) \text{ Å}. \quad (6)$$

The other relevant elementary constants are: m_e - electron mass, e - electron charge, $\hbar = h/2\pi$ - Planck constant, ϵ_0 - permittivity. Their values can be found in appendix A. The Schrödinger equation contains the mutual interaction of all electrons in the system, whose number can be exceedingly large ($\approx 10^{23}$ in solids). To demonstrate the futility of attempting an exact solution of eq. 2 let us consider a Silicon atom. Simply wanting to store the wave function on a grid with only 10 points in each dimensions produces a grid with $10^{3N}=10^{42}$ points. Assuming 128-bit double precision complex numbers, each sample point requires 16 bytes of storage, which gives approx 10^{43} bytes of data. A regular blue-ray disc holds about 50 GB and we would therefore need $\sim 10^{32}$ disks. This example illustrates that we have to use approximations to tackle the many-body problem in solid state physics.

1.2 THE BORN-OPPENHEIMER APPROXIMATION

For each configuration of the nuclei $\{\mathbf{R}_a\}$ the electrons are in an eigenstate of the electronic hamiltonian H_{elec} (eq. 2). If we consider their response to nuclear motion as instantaneous, no transitions between the eigenstates of H_{elec} are induced by the nuclei. Nuclear and electronic degrees of freedom decouple. This is known as the adiabatic or Born-Oppenheimer [36] approximation.

$$H = H_{elec} + H_{nucl} \quad (7)$$

$$\Psi(\{\mathbf{r}_i\}, \{\mathbf{R}_a\}) = \Psi_{elec}(\{\mathbf{r}_i\}, \{\mathbf{R}_a\}) \Psi_{nucl}(\{\mathbf{R}_a\}) \quad (8)$$

The electronic Hamiltonian can be solved by:

$$H_{elec}\Psi_{elec} = E_{elec}\Psi_{elec} \quad (9)$$

with the electronic wave function:

$$\Psi_{elec} = \Psi_{elec}(\{\mathbf{r}_i\}, \{\mathbf{R}_a\}) \quad (10)$$

which depends on:

$$\begin{array}{ll} \{\mathbf{r}_i\} & \text{explicitly} \\ \{\mathbf{R}_a\} & \text{parametrically} \end{array}$$

Also the total energy depends parametrically on the positions of the nuclei.

$$E_{elec} = E_{elec}(\{\mathbf{R}_a\}) \quad (11)$$

$\Psi_{nucl}(\{\mathbf{R}_a\})$ describes the vibrations, rotations and translations of a system. We can assess the validity of this approximation with the help of first order perturbation theory, where the first order coupling between different electronic eigenstates of the system is zero. The second order scales with the ratio of electron and nuclear mass. The nuclei are orders of magnitude heavier. Therefore, the second order term is considered small and can be safely neglected together with higher order terms. The potential felt by the electrons, caused by the nuclei, can

be approximated by a field of fixed nuclei. The kinetic energy of the nuclei is neglected and the repulsion between nuclei becomes a constant. The remaining Hamiltonian is H_{elec} (eq. 2), which describes the motion of N electrons in the field of M point charges.

Now we can reverse the argument and solve the problem for nuclei moving in an effective potential of the electrons. Since the electrons move much faster we can replace the electronic coordinates by values, which are averaged over electronic wave-functions.

$$\begin{aligned}
 H &= - \sum_{a=1}^M \frac{1}{2M_a} \nabla_a^2 + \sum_{a=1}^M \sum_{b>a}^M \frac{Z_a Z_b}{|\mathbf{R}_a - \mathbf{R}_b|} \\
 &\quad + \left\langle - \sum_{i=1}^N \frac{1}{2} \nabla_i^2 + \sum_{i=1}^N \sum_{j>i}^M \frac{1}{|\mathbf{r}_i - \mathbf{r}_j|} - \sum_{i=1}^N \sum_{a=1}^M \frac{Z_a}{|\mathbf{r}_i - \mathbf{R}_a|} \right\rangle \\
 H &= - \sum_{a=1}^M \frac{1}{2M_a} \nabla_a^2 + \sum_{a=1}^M \sum_{b>a}^M \frac{Z_a Z_b}{|\mathbf{R}_a - \mathbf{R}_b|} + E_{elec}(\{\mathbf{R}_a\})
 \end{aligned} \tag{12}$$

By using the Born-Oppenheimer wave function (eq. 8) and neglecting diagonal terms we obtain the total energy for a set of nuclear coordinates:

$$\begin{aligned}
 E_{tot}(\{\mathbf{R}_a\}) &= \langle \Psi(\{\mathbf{r}_i\}, \{\mathbf{R}_a\}) | H | \Psi(\{\mathbf{r}_i\}, \{\mathbf{R}_a\}) \rangle = E_{elec}(\{\mathbf{R}_a\}) + \\
 &\quad \left\langle \Psi_{nuc1} \left| - \sum_{a=1}^M \frac{1}{2M_a} \nabla_a^2 + \sum_{a=1}^M \sum_{b>a}^M \frac{Z_a Z_b}{|\mathbf{R}_a - \mathbf{R}_b|} \right| \Psi_{nuc1} \right\rangle
 \end{aligned} \tag{13}$$

In general, the nuclear wave function is peaked around the equilibrium position of the nuclei and can be approximated by point charges:

$$\begin{aligned}
 E_{tot}(\{\mathbf{R}_a\}) &= E_{elec}(\{\mathbf{R}_a\}) + \underbrace{\sum_{a=1}^M \sum_{b>a}^M \frac{Z_a Z_b}{|\mathbf{R}_a - \mathbf{R}_b|}}_{\text{classical electrostatic energy}} \\
 &\quad + \underbrace{\left\langle \Psi_{nuc1} \left| - \sum_{a=1}^M \frac{1}{2M_a} \nabla_a^2 \right| \Psi_{nuc1} \right\rangle}_{\text{quantum corrections}}
 \end{aligned} \tag{14}$$

The total energy of the electrons presents a potential energy surface for the motion of the nuclei. Forces can be calculated by the derivative of the total energy with respect to the coordinates of the nuclei.

$$\mathbf{F} = - \frac{dE_{tot}}{d\mathbf{R}_i} \tag{15}$$

The adiabatic approximation fails for systems where non-adiabatic effects, e. g. electron-phonon or electron-lattice interactions, are import. A variety of interesting phenomena can not be described, e. g. Jahn-Teller and Peiers distortions, superconductivity or thermal conductivity. The Born-Oppenheimer approximation also fails in cases where more than one energy landscape is present (e. g., when a molecule approaches a surface).

1.3 DENSITY FUNCTIONAL THEORY

Density functional theory is based on the relation between the particle density $n(\mathbf{r})$ and the many-body wave function of the ground state $\Psi(\mathbf{r}_1 \dots \mathbf{r}_N)$. The advantage is apparent. The many body wave function depends on the coordinates of all N electrons (spin is omitted), while the particle density is a scalar object that depends only on \mathbf{r} . In DFT we try to find the system energy $E([n])$ as a functional expression of the density $n(\mathbf{r})$ by a variational principle. The first and simplest theory in this spirit is the Thomas-Fermi-Theory [252, 79]. It is still of conceptual importance, but will not be discussed.

The goal is to recast the Schrödinger equation for the many body wave-function (eq. 3) in terms of the density with the electronic Hamiltonian

$$H_{\text{elec}} = - \underbrace{\sum_i^N \frac{\nabla_i^2}{2}}_T + \underbrace{\sum_i^N v_{\text{ext}}(\mathbf{r}_i)}_{V_{\text{ext}}} + \underbrace{\frac{1}{2} \sum_{i \neq j}^N \frac{1}{|\mathbf{r}_i - \mathbf{r}_j|}}_{V_{ee}} \quad (16)$$

$$= T + V_{\text{ext}} + V_{ee}. \quad (17)$$

T is the kinetic energy operator of the N -electron system, V_{ext} - the external potential operator and V_{ee} the electron-electron interaction (Coulomb operator). The foundation of DFT is formed by the Hohenberg-Kohn Theorems [102, 140]:

Hohenberg-Kohn Theorem I

The ground-state density $n(\mathbf{r})$ uniquely determines the potential (v_{ext}) up to an arbitrary constant.

$$v_{\text{ext}}(\mathbf{r}) \Longleftrightarrow n(\mathbf{r}) \quad (18)$$

Hohenberg-Kohn Theorem II

A universal functional for the energy $E[n]$ in terms of the density $n(\mathbf{r})$ can be defined, valid for any external potential $v_{\text{ext}}(\mathbf{r})$. For any given $v_{\text{ext}}(\mathbf{r})$, the exact ground state energy of the system is the global minimum of this functional, and the density that minimizes the functional is the exact ground state density.

$$\begin{aligned} E_{\text{HK}}[n] &= \underbrace{T[n] + V_{ee}[n]}_{F[n]} + \int d\mathbf{r} v_{\text{ext}}(\mathbf{r}) n(\mathbf{r}) \\ &= F[n] + \int d\mathbf{r} v_{\text{ext}}(\mathbf{r}) n(\mathbf{r}) \end{aligned}$$

By definition the Hohenberg-Kohn functional gives the minimum energy of the system for the ground state density and if the the functional is known the ground state density can be obtained from the variational principle. We can only obtain the ground state density and therefore only ground state properties. A fundamental problem is the missing prescription to construct the kinetic energy as a functional of the density. This was solved by a trick by Kohn and Sham [129], which lead to a breakthrough in modern DFT. Their solution was to consider an auxiliary system of N non-interacting electrons that has the same ground state density as the fully interacting system.

$$h_{\text{aux}} = -\frac{\nabla^2}{2} + V(\mathbf{r}) \quad (19)$$

The non-interacting electrons move in an effective potential. The full Hamiltonian is a sum over the auxiliary single particle Hamiltonians.

$$H(\{\mathbf{x}_i\}) = \sum_i h_{aux}(\mathbf{x}_i) = H_{aux}(\{\mathbf{x}_i\}). \quad (20)$$

This gives a set of single particle orbitals.

$$h_{aux}\varphi_i = \epsilon_i\varphi_i \quad (21)$$

This leads to the density

$$n(\mathbf{r}) = \sum_i^{N/2} \int d\mathbf{r} |\varphi_i(\mathbf{r}, \sigma)|^2, \quad (22)$$

Hartree energy

$$E_H[n] = \frac{1}{2} \sum_{ij} \int d\mathbf{r} d\mathbf{r}' \frac{|\varphi_i(\mathbf{r})|^2 |\varphi_j(\mathbf{r}')|^2}{|\mathbf{r} - \mathbf{r}'|} = \frac{1}{2} \int d\mathbf{r} d\mathbf{r}' \frac{n(\mathbf{r}) n(\mathbf{r}')}{|\mathbf{r} - \mathbf{r}'|} \quad (23)$$

and kinetic energy:

$$T_S[n] = -\frac{1}{2} \sum_i^{N/2} \int d\mathbf{r} \langle \varphi_i | \nabla^2 | \varphi_i \rangle = \frac{1}{2} \sum_i^{N/2} \int d\mathbf{r} |\nabla \varphi_i|^2. \quad (24)$$

This leads finally to the Kohn-Sham energy functional:

$$E_{KS}[n] = T_S[n] + \underbrace{\int d\mathbf{r} V_{ext}(\mathbf{r}) n(\mathbf{r})}_{=E_{ext}} + E_H[n] + E_{XC}[n] \quad (25)$$

With this energy functional we can define a Lagrange functional:

$$L[n] := E_{KS}[n] - \sum_i \epsilon_i \int d\mathbf{x} \varphi_i^*(\mathbf{x}) \varphi_i(\mathbf{x})$$

and minimize it with respect to the single electron orbitals

$$\frac{\delta L}{\delta \varphi_i^*} = 0 \quad \forall i \quad (26)$$

This leads to the key result in our derivation:

$$\left[-\frac{1}{2} \nabla^2 + V_{KS}(\mathbf{r}) \right] \varphi_i(\mathbf{r}) = \epsilon_i \varphi_i(\mathbf{r}) \quad (27)$$

The Kohn-Sham equations [129]

with the (effective) Kohn-Sham potential:

$$V_{KS}(\mathbf{r}) = V_{eff}(\mathbf{r}) = v_{ext}(\mathbf{r}) + v_H(\mathbf{r}) + v_{XC}(\mathbf{r}) \quad (28)$$

$$v_{XC}(\mathbf{r}) := \frac{\delta E_{XC}[n]}{\delta n(\mathbf{r})} \quad (29)$$

The Kohn-Sham equation has to be solved self-consistently because v_{KS} depends on the solution of the system of differential equations. Now we have to find good approximations for $E_{xc}[n]$. It is the only missing ingredient to solve the many-body problem. We have introduced $E_{xc}[n]$ in order to map our fully interacting system on a system of non-interacting electrons. $E_{xc}[n]$ is in general small, because T_S and E_H capture a large part of T and V_{ee} .

1.4 APPROXIMATE XC-FUNCTIONALS

As we have seen at the end of the last chapter, by introducing the effective non-interacting system we have obtained a well defined set of equations. The Kohn-Sham equations can be transformed into an eigenvalue problem, which can be solved with high (computational) efficiency [92, 30, 277, 31, 156]. The cost for this transformation is the loss of the knowledge about the exact form of the energy functional and the quantities derived from it. The non-interacting (model) system can be modified to continuously switch back to the fully interacting (physical) system by "adiabatic continuation" [225]. The solution would be exact, but the computational effort to solve the problem is unfeasible. To take advantage of the Kohn-Sham equations many different approximations for the notorious xc-energy functional have been proposed. The development of new functionals, adopted to special classes of systems or problem sets as well as the generalization of functionals based on basic quantum mechanical principles is an active field of scientific research. In this chapter only the functionals used for obtaining the results in this work will be presented. The reader is referred to the literature for other functionals and their applications [85, 114].

1.4.1 Local density approximation (LDA)

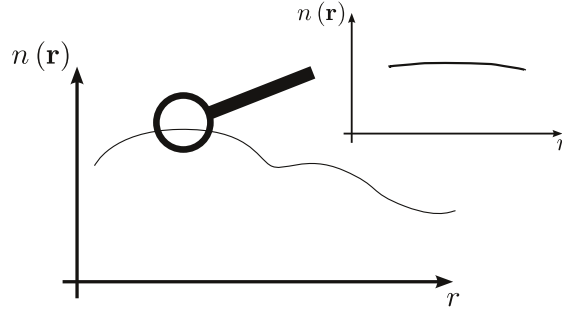


Figure 1: Schematic illustration of the local behavior of the density.

Inhomogeneous systems with a slowly varying density look locally like the homogeneous electron gas (see Fig. 1). Making a local approximation, the xc-energy $E_{xc}[n]$ can be expressed as an integral over the density and the xc-energy density $\epsilon_{xc}^{HEG}([n], \mathbf{r})$ at \mathbf{r} of the homogeneous electron gas. It only depends on

the density at \mathbf{r} .

$$\implies E_{xc}[n] = \int d\mathbf{r} n(\mathbf{r}) \epsilon_{xc}^{\text{HEG}}([n], \mathbf{r}) \quad (30)$$

The exchange-correlation potential v_{xc} is obtained by a functional derivative:

$$v_{xc}(\mathbf{r}) = \frac{\delta E_{xc}[n]}{\delta n(\mathbf{r})} = \epsilon([n], \mathbf{r}) + n(\mathbf{r}) \frac{\delta \epsilon([n], \mathbf{r})}{\delta n(\mathbf{r})} \quad (31)$$

The exchange part of the exchange-correlation energy for the homogeneous electron gas is known exactly [260]:

$$\epsilon_x^{\text{HEG}}[n] = \frac{3k_F}{4\pi}, \quad (32)$$

with the Fermi momentum $k_F = (3\pi^2 n)^{1/3}$. By inserting eq. 32 in eq. 30 we obtain

$$E_x[n] = \int d\mathbf{r} n(\mathbf{r}) \epsilon_x([n], \mathbf{r}) = \frac{3}{4} \left(\frac{3}{\pi} \right)^{1/3} \int d\mathbf{r} n(\mathbf{r})^{4/3} \quad (33)$$

for the exchange energy and

$$v_x[n] = \left(\frac{3}{\pi} \right)^{1/3} n^{1/3} \quad (34)$$

for the exchange potential by inserting eq. 32 into eq. 31.

The correlation energy density for the homogeneous electron gas is not known analytically. An approximate analytic expression was first given by Wigner in 1938 [273] (see Fig. 2):

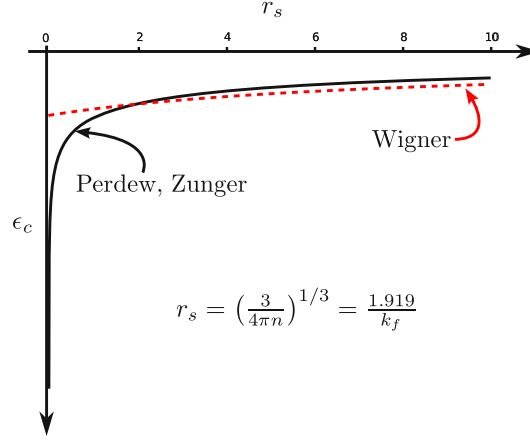
$$\epsilon_c[n] = -\frac{0.44}{r_s + 7.8}, \quad (35)$$

with $r_s = \left(\frac{3}{4\pi n} \right)^{1/3} = \frac{1.919}{k_F}$. A better parameterization was computed with high precision Quantum Monte Carlo techniques by Perdew and Zunger [195]:

$$\epsilon_c[n] = \begin{cases} \overbrace{A \ln r_s + B + C r_s \ln r_s + D r_s}^{\text{Gell-Mann/Brückner}} & r_s \leq 1 \\ \frac{\gamma}{1 + \beta_1 \sqrt{r_s} + \beta_2 r_s} & r_s > 1 \end{cases} \quad (36)$$

The numerical values of $A, B, C, D, \gamma, \beta_1$ and β_2 are given in Ref. [195].

The local density approximation is exact for the homogeneous electron gas. It is expected to perform well for systems with slowly-varying densities such as simple metals. Typical dissociation energies and cohesive properties are with 10% to 20% experimental values [57]. Bond lengths and lattice parameters are typically underestimated by 1% to 2% [241, 55]. LDA does not perform well for systems with a rapidly changing density e. g. atoms.

Figure 2: $\epsilon_c[n]$ as parameterized by Wigner and Perdew/Zunger.

1.4.2 Semi-Local density approximation

To improve on the approximation of a homogeneous density, gradients were introduced into E_{xc} [24]

$$\begin{aligned} E_{xc}^{GGA}[n] &= \int d\mathbf{r} n(\mathbf{r}) \epsilon_{xc}(n, |\nabla n|, \dots) \\ &= \int d\mathbf{r} n(\mathbf{r}) \epsilon_x^{\text{HEG}} F_{xc}(n, |\nabla n|, \dots). \end{aligned} \quad (37)$$

We can define a scaled gradient, that measures on the scale of the density itself:

$$S(\mathbf{r}) = \frac{|\nabla n(\mathbf{r})|}{2k_F n(\mathbf{r})} \quad (38)$$

leading to the generalized gradient expansion (GGA) [196].

$$E_{xc}^{GGA}[n] = \int d\mathbf{r} n(\mathbf{r}) \epsilon_x^{\text{HEG}}[n] F_{xc}(n, S). \quad (39)$$

There is no unique form of F_{xc} . Many different parameterizations exist in literature, that are often named by the initials of their creators: Perdew-Burke-Ernzerhof (PBE) functional [196], Perdew-Burke-Ernzerhof functional for solids (PBEsol) [200], Perdew-Burke-Ernzerhof functional for interfaces (PBEint) [78], revised Perdew-Burke-Ernzerhof functional (revPBE) [94], Armiento-Mattsson functional from 2005 (AM05) [9], Becke-Lee-Yang-Parr functional (BLYP) [23, 138]. They are usually designed to describe a predefined class of materials (e.g. organic molecules, surfaces). There are two major strategies to construct F_{xc} :

- Construct F_{xc} to fulfill certain exact conditions, e. g. asymptotic behavior of the homogeneous electron gas.
- Fit the parameters in F_{xc} to reproduce certain properties of test sets, that have been obtained from very accurate high level methods.

Functionals based on the general gradient approximation improve in many aspects the accuracy of the local density approximation [197], e. g. the errors in

total energies and the over-binding of LDA are reduced. In general GGAs perform best in the regime for which they were designed. The next logical step to further improve our approximations are meta-GGA functionals, that include the second and higher order derivatives in the exchange correlation functional [201]. We will not further discuss meta-GGAs and directly progress to functionals with the exchange part expressed by the Kohn-Sham orbitals.

1.4.3 Hybrid functionals

The energy expression obtained from DFT is eq. 25 with the Hartree energy in eq. 23. For $i = j$ the electron interacts with itself. This is the so called self interaction. In Hartree-Fock theory this term is canceled exactly by the exchange energy:

$$E_x = -\frac{1}{2} \sum_{ij} \int d\mathbf{r} d\mathbf{r}' \frac{\psi_i^*(\mathbf{r}) \psi_j(\mathbf{r}) \psi_j^*(\mathbf{r}') \psi_i(\mathbf{r}')}{|\mathbf{r} - \mathbf{r}'|}$$

for $i = j$, $E_H + E_x$ is 0. For the local and semi-local functionals in DFT, this cancellation does not occur. E_x is part of E_{xc} in eq. 39. The self interaction error in such a functional was defined by Perdew and Zunger [195] as:

$$\delta_i = \frac{1}{2} \int d\mathbf{r} d\mathbf{r}' \frac{|\psi_i(\mathbf{r})|^2 |\psi_i(\mathbf{r}')|^2}{|\mathbf{r} - \mathbf{r}'|} + E_{xc} [|\psi_i(\mathbf{r})|^2] \quad (40)$$

For local and semi-local functionals this value is in general not zero. The self interaction error can lead to a over-delocalization of states. To improve the thermochemical accuracy of LDA and GGA based functionals for molecular systems the inclusion of exact exchange (Hartree-Fock exchange) information was proposed by Becke [24]. An additional advantage is the remediation of the self-interaction error.

$$E_{xc}^{hyb} = E_{xc}^{DFT} + \alpha (E_x^{HF} - E_x^{DFT}). \quad (41)$$

In this simple form a portion of the exchange contribution of DFT is replaced with exact exchange (Hartree-Fock). The correlation contribution is purely DFT. Other hybrid functionals with more complex parameterizations exist (e. g. B3LYP [24, 138, 266, 244, 232]). A separation of long (LR) and short range (SR) contributions in E_x and E_c can be introduced

$$E_{xc}^{PBEh} = a E_x^{HF,SR}(\omega) + (1 - a) E_x^{PBE,SR}(\omega) + E_x^{PBE,L R}(\omega) + E_c^{PBE}, \quad (42)$$

where a is the mixing parameter and ω is an adjustable parameter controlling the short-ranginess of the interaction. The range separation is typically achieved by an error function. With $a = \frac{1}{4}$ and $\omega = 0.2$ the HSE06 [99, 134, 100] xc-functional is obtained. Setting $\alpha = 0.25$ in eq. 41 and using exchange from the GGA xc-functional PBE [196], yields the functional known as PBE0 [2]. The exchange correlation potential is calculated as in Hartree-Fock (functional derivative with respect to orbitals, $\frac{\delta E_{xc}}{\delta \phi_i^*}$, not the density). This leads to a non-local potential:

$$v_{xc}^{hyb}(\mathbf{r}, \mathbf{r}') = [v_{xc}^{DFT}(\mathbf{r}) - \alpha v_x^{DFT}(\mathbf{r})] \delta(\mathbf{r} - \mathbf{r}') + \alpha \Sigma_x^{HF}(\mathbf{r}, \mathbf{r}') \quad (43)$$

with

$$\Sigma_X^{\text{HF}}(\mathbf{r}, \mathbf{r}') = \sum_i^N \frac{\psi_i(\mathbf{r})\psi_i^*(\mathbf{r}')}{|\mathbf{r} - \mathbf{r}'|}. \quad (44)$$

The formalism introduces new parameters, that can be chosen on the basis of the satisfaction of exact conditions, a best fit to test set properties obtained with higher level methods or a best match for the system dependent properties under investigations [14, 158, 4, 243, 213].

1.5 LONG RANGE DISPERSION

In this work we follow the convention of Ref. [245] and refer to the van-der-Waals (vdW) energy as the attractive interaction between fluctuating multi-poles. This description is based on concepts first introduced by London [75, 145, 146]. The basic idea is to add the long range dispersion contributions, which are missing in DFT calculations employing LDA, GGA and hybrid xc-functionals. Many methods have been developed to calculate the vdW-energy and coupling them to the underlying functional e.g. DFT-vdW[254], vdW-DF[70]. The reader is deferred to recent reviews for discussion and developments [84, 253, 71, 116]

In this work we apply the method developed by Tkatchenko and Scheffler [254] with additional parameterizations from Ruiz *et al.* [220] and Zhang *et al.* [286]. The vdW energy is expressed as:

$$E_{\text{vdW}} = -\frac{1}{2} \sum_A \sum_B f_{\text{damp}}(R_{AB}, R_{AB}^0) \frac{C_6^{AB}}{R_{AB}^6}, \quad (45)$$

with R_{AB} the inter atomic distance between atoms A and B, $R_{AB}^0 = R_A^0 + R_B^0$ the vdW radius, C_6^{AB} the corresponding vdW coefficients and f_{damp} a damping function. The Tkatchenko and Scheffler method (TS) [254] obtains R_{AB}^0 and C_6^{AB} from the electronic ground-state density by Hirshfeld-volume partitioning [101]. Empirical parameters are only introduced in the damping function f (eq. 52). The starting point of the formalism is a set of accurate vdW parameters (C_6^i , R_6^i and α^i) for the free atoms that are determined from the ground state mean field density [254] or from high level time dependent density functional theory (TD-DFT) [157, 191] calculations in improved/specialized versions [286, 220]. The change in the chemical environment of the free atoms and the system in a molecule or a solid is captured by calculating the volume of these atoms [101].

$$V_i^{\text{free}} = \int d\mathbf{r} n_i^{\text{free}}(\mathbf{r}) |\mathbf{r} - \mathbf{R}_i|^3 \quad (46)$$

$$V_i^{\text{eff}} = \int d\mathbf{r} n_i^{\text{H}}(\mathbf{r}) |\mathbf{r} - \mathbf{R}_i|^3 \quad (47)$$

with \mathbf{R}_i the position of atom i and the density of the free atom $n_i^{\text{free}}(\mathbf{r})$ or the Hirshfeld-volume partitioned density $n_i^{\text{H}}(\mathbf{r})$:

$$n_i^{\text{H}}(\mathbf{r}) = n(\mathbf{r}) \frac{n_i(\mathbf{r})^{\text{free}}}{\sum_j n_j(\mathbf{r})^{\text{free}}} \quad (48)$$

Species	C_6	α	R_6
Ag[220]	122	15.4	2.57
Cu[220]	59	10.9	2.40
Pd[220]	110.6	14.4	3.10
Pt[220]	129.5	15.0	2.83
Zn[286]	46.02	13.774	2.818
O [286]	4.45	4.285	2.953

Table 1: Free atom parameters from references [286, 220] used as input for the TS-method [254].

The free atom values for $C_{6,free}^i$, $R_{6,free}^i$ and α_{free}^i are rescaled by the volume ratio to represent the chemical environment in a molecule or solid.

$$\alpha^i = \alpha_{free}^i \times \frac{V_i^{eff}}{V_i^{free}} \quad (49)$$

$$C_6^i = C_{6,free}^i \times \left(\frac{V_i^{eff}}{V_i^{free}} \right)^2 \quad (50)$$

$$R_6^i = R_{6,free}^i \times \left(\frac{V_i^{eff}}{V_i^{free}} \right)^{1/3} \quad (51)$$

Only the damping function in eq. 45, which is required to remove the R_{AB}^{-6} singularity at short distances, has to be chosen. A Fermi-type function is used in the TS-method [254].

$$f_{damp}(R_{AB}, R_A^0, R_B^0) = \frac{1}{1 + \exp \left[-d \left(\frac{R_{AB}}{s_R R_{AB}^0} - 1 \right) \right]} \quad (52)$$

Only d and s_R are free parameters. d determines the steepness of the function. $d = 20$ has been chosen. s_R reflects the damping behavior of the xc-functional. It determines the electron correlation covered by a given functional. s_R was obtained by fitting to the S22 [117] test set [254] for different xc-functionals.

The free atom parameters $C_{6,free}^i$, $R_{6,free}^i$ work well for molecular systems. To include vdW effects for ionic solids such as ZnO and polarisable surfaces these parameters have to be adjusted. For ionic and semi-conducting crystals a combination of again TD-DFT and the Clausius-Mossotti equation [172, 53, 221]

$$\alpha(\omega) = V \frac{\epsilon(\omega) - 1}{\frac{4\pi}{3}\epsilon(\omega) - \frac{4\pi}{3} + 4\pi} \quad (53)$$

is used for calculating accurate free atom parameters [220]. From TD-DFT cluster calculations the total static polarizabilities are obtained from the microscopic dielectric function $\epsilon(\omega)$. C_6 , R_6 and α are calculated from those results in the same manner as in the original TS-method [254].

For an inorganic (metallic) surface the many-body collective response of the bulk

Species	V_{eff}	$C_{6,\text{eff}}$	α_{eff}	$R_{6,\text{eff}}$
Ag	1.054	109.963	14.614	2.526
Cu	1.084	50.214	10.056	2.336
Pd	1.044	101.538	13.797	3.056
Pt	0.990	132.367	15.165	2.840
Zn	0.915	54.975	15.055	2.903
O	0.978	4.651	4.381	2.975

Table 2: Effective vdW-parameters.

electrons inside the surface has to be included in the description of the vdW-interaction to calculate accurate C_6 , R_6 and α parameters. This was achieved by applying Lifshitz-Zaremba-Kohn theory for the nonlocal Coulomb screening within the bulk [285]. The C_6^{ab} for atom sort a and b can be obtained from C_3^{aB} for atom a at a solid surface B .

$$C_3^{aB} = n_s \left(\frac{\pi}{6} \right) C_6^{ab} \quad (54)$$

C_3^{aB} is calculated from:

$$C_3^{aB} = \frac{\hbar}{4\pi} \int_0^\infty d\omega \alpha(i\omega) \frac{\epsilon_B(i\omega) - 1}{\epsilon_B(i\omega) + 1} \quad (55)$$

with $\alpha(i\omega)$ the polarizability of atom a and $\epsilon_B(i\omega)$ the dielectric function of solid B . $\epsilon_B(i\omega)$ is calculated from its imaginary part obtained from experimental data by the Kramers-Kronig relation [60, 130]. By combination with the same scheme as in the TS-method (Pade-approximant model) [254, 16] $C_{6,\text{eff}}$, $R_{6,\text{eff}}$ and α_{eff} are calculated.

The values acquired with the methods described above are listed in tab. 1. The effective volume is taken from FHI-aims [33] calculations for each system employing the PBE xc-functional [196] with the tight basis set provided by the software package [33]. The effective vdW parameters are listed in tab. 2 for the systems considered in this work.

1.6 AB INITIO THERMODYNAMICS

Density-functional theory provides a versatile and flexible framework to accurately describe microscopic properties of many different systems. The electronic structure is provided by the calculated density. The atomic structure can be determined by minimizing the forces on the nuclei of the constituents. Many other properties can directly be calculated or estimated from these quantities. By applying methods known from thermodynamics (and statistical mechanics) the microscopic information obtained from DFT can be extended to the meso- and macroscopic regime.

In practice many structures of different size and atomic composition lie in a very narrow energy range. The combination of DFT and concepts from thermodynamics facilitates a comparison of these systems to access their relative stability. DFT

is in this context referred to as *ab initio* or *from first principles* because it is fully derived from quantum mechanics without introducing parameters, that have to be fitted to empirical data. In this section the concepts of *ab initio* thermodynamics [226, 214] will be presented for the example of the ZnO (000 $\bar{1}$) surface.

The solution of the KS-equation in DFT is the ground state of the system and is only valid for $T = 0$ K and $p = 0$ mbar, but we can extend DFT to finite temperatures and pressures with the help of well established concepts from thermodynamics [214]. The key quantity for all further considerations is the Gibbs free energy G for the (T, p) -ensemble:

$$G(T, p) = E^{\text{internal}} + F^{\text{vib}} - TS^{\text{conf}} + pV = N\mu(T, p) \quad (56)$$

The leading term is the internal energy E^{internal} , which can be obtained directly from DFT calculations. The contributions from the other three terms are highly system dependent and have to be accessed for every problem. The second term is the vibrational free energy $F^{\text{vib}} = E^{\text{ZPE}} - TS^{\text{vib}}$ with the zero point energy E^{ZPE} and the vibrational entropy S^{vib} . It accounts for contributions from the vibrational degrees of freedom of the system. The third term in G accounts for the configurational entropy S^{conf} . The last term includes the volume V and the external pressure p . It is import to note that this approach is only applicable for systems that are in thermodynamic equilibrium. Such systems can be divided into smaller subsystems, which are again in thermodynamic equilibrium with each other. These smaller, computational more feasible systems can be treated more easily with DFT (e. g. a semi-infinite bulk surface in a gas atmosphere, that both act as reservoirs). Dynamical or kinetically enabled processes cannot be described with eq. 56.

The internal energy of a one component system (e. g. a bulk metal) fully describes that system in equilibrium.

$$E^{\text{internal}} = TS - pV + N\mu. \quad (57)$$

It is the sum of the products of entropy and temperature minus the pressure times volume and the number of particles in the system times the chemical potential. By cleaving the bulk crystal and creating a surface we have to pay a penalty proportional to the created surface area. This energy per surface area is defined as the surface energy γ [284]. The internal energy for a surface is

$$E_{\text{surf}}^{\text{internal}} = TS - pV + N\mu + \gamma A. \quad (58)$$

With the help of the Gibbs free energy (eq. 56) we can rewrite eq. 57 for the surface energy.

$$\gamma(T, p_i) = \frac{1}{A} \left[G^{\text{surf}} - \sum_i N_i \mu_i(T, p_i) \right] \quad (59)$$

G^{surf} is the Gibbs free energy of surface and solid and $\mu_i(T, p_i)$ are the chemical potentials of the different species (i) in the system. For a ZnO surface eq. 59 includes the three species in the system: Zn, O and H. The ZnO surface is in equilibrium with the bulk ZnO, which acts as a reservoir. The chemical potentials

of O and Zn are not independent. They are connected by the Gibbs free energy g (per formula unit).

$$g_{\text{ZnO}}^{\text{bulk}}(T, p) = \mu_{\text{Zn}} + \mu_{\text{O}} \quad (60)$$

By putting μ_{Zn} , μ_{O} and μ_{H} into eq. 59 and using eq. 60 we obtain:

$$\gamma_{\text{ZnO}}(T, p_{\text{O}}, p_{\text{H}}) = \frac{1}{A} [G^{\text{surf}}(T, p_{\text{O}}, N_{\text{Zn}}, N_{\text{O}}) - N_{\text{Zn}} g_{\text{ZnO}}^{\text{bulk}} - (N_{\text{O}} - N_{\text{Zn}}) \mu_{\text{O}}(T, p_{\text{O}}) - N_{\text{H}} \mu_{\text{H}}(T, p_{\text{H}})] \quad (61)$$

The limits of the chemical potential can be derived from thermodynamical considerations. The upper limit for the gas phase components, H and O, is determined by the point when they are so highly concentrated, that condensation at the oxide surface starts. For a ZnO surface in equilibrium with a oxygen and hydrogen atmosphere this is determined by:

$$\mu_{\text{O}} \leq \frac{1}{2} E_{\text{O}_2}^{\text{tot}}, \quad \mu_{\text{H}} \leq \frac{1}{2} E_{\text{H}_2}^{\text{tot}} \quad (62)$$

The oxide starts to decompose at low oxygen chemical potentials when the chemical potential of Zn becomes greater than its bulk Gibbs free energy.

$$\mu_{\text{Zn}} \leq g_{\text{Zn}}^{\text{bulk}} \quad (63)$$

With eq. 62 and eq. 63 the limits for the oxygen chemical potential are:

$$g_{\text{ZnO}}^{\text{bulk}}(T, p) - g_{\text{Zn}}^{\text{bulk}} - \frac{1}{2} E_{\text{O}_2}^{\text{tot}} \leq \Delta\mu_{\text{O}}(T, p) - \frac{1}{2} E_{\text{O}_2}^{\text{tot}} \leq 0 \quad (64)$$

The upper boundary for μ_{O} is set to zero by defining $\Delta\mu_{\text{O}}(T, p) = \mu_{\text{O}}(T, p) - \frac{1}{2} E_{\text{O}_2}^{\text{tot}}$ and $\Delta\mu_{\text{H}}(T, p) = \mu_{\text{H}}(T, p) - \frac{1}{2} E_{\text{H}_2}^{\text{tot}}$ for μ_{H} . The lower limit for μ_{H} cannot be derived from the equilibrium conditions. In practice the limit is chosen to give a physically reasonable pressure limit at a given temperature. The relationship between the chemical potential of a gas phase component and the pressure and temperature is calculated using statistical thermodynamics [214] or from the ideal gas law [133, 52] and tabulated values for entropy and Helmholtz energy terms [178].

$$\mu_{\text{O}}(T, p) = \mu_{\text{O}}(T, p^0) + \frac{1}{2} k_{\text{B}} T \ln \left(\frac{p}{p^0} \right). \quad (65)$$

The temperature and pressure dependence can be determined if $\mu(T, p^0)$ is known at one pressure. The reference value of the chemical potential of the gas phase component at $T=0$ K is set to the total energy of an isolated molecule.

$$\mu(0\text{K}, p^0) = \frac{1}{2} E_{\text{O}_2}^{\text{tot}} = 0 \quad (66)$$

With respect to this reference and using the relation between Gibbs free energy G and enthalpy H , $G = H - TS$, the chemical potential at p^0 is given by

$$\mu_{\text{O}}(T, p^0) = \frac{1}{2} (H(T, p^0) - H(0\text{K}, p^0)) - \frac{1}{2} TS(T, p^0) \quad (67)$$

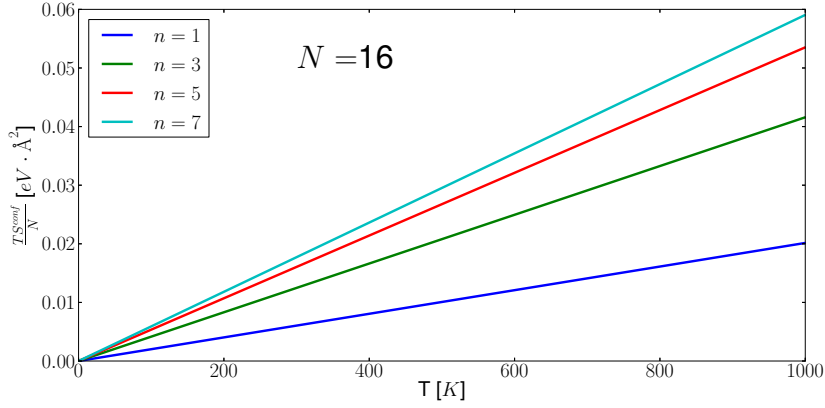


Figure 3: Confrontational entropy $\text{fracTS}^{\text{conf}} \text{NA}_{\text{site}}$ as a function of temperature T .

For the standard pressure $p=0.1$ MPa, $H(T, p^0) - H(0K, p^0)$ and $S(T, p^0)$ are tabulated and can be obtained from the NIST data base [178] for many substances.

To obtain the surface energy for a given system we have to evaluate the three missing terms in the Gibbs free energy (eq. 56). The pV term is discussed by a dimension analysis. The unit of $[pV/A]$ is $[\text{atm } \text{\AA}^3/\text{\AA}]$, $1 \text{ atm times } 1 \text{ \AA}^3$ is 10^{-3} meV . For a pressure of 100 atm it is then of the order $pV/A \sim 0.1 \text{ meV}/\text{\AA}^2$ and can be safely neglected for the surfaces in this work.

The configurational entropy is strongly system dependent. It can be calculated very accurately with Monte Carlo techniques from statistical mechanics [29, 202, 203, 217]. This approach is out of scope for the present work. An estimation of the contribution can be achieved for the relation for non-interacting particles from statistical mechanics.

$$S^{\text{conf}} = k_B \ln \frac{N!}{N!(N-n)!} \quad (68)$$

This relation can be derived from combinatorics for calculating the possible configurations by selecting N times from a set of n samples and putting them back. Here we are considering a surface with N surface sites and n defects or adsorbate atoms to adsorb on the N sites. Eq. 68 can be approximated with the Sterling formula for $n, N \gg 1$.

$$\ln(n!) \approx n \ln(n) - n \quad (69)$$

For the contribution to the Gibbs free energy of the configurational entropy per surface Area, $A = \text{NA}_{\text{site}}$, this yields.

$$\frac{\text{TS}^{\text{conf}}}{\text{NA}_{\text{site}}} = \frac{k_B T}{A_{\text{site}}} \left[\ln \left(\frac{N}{N-n} \right) + \frac{n}{N} \ln \left(\frac{N}{n} - 1 \right) \right] \quad (70)$$

To further estimate the configurational entropy we consider a 4×4 ZnO (000 $\bar{1}$) surface. A total number of $N = 16$ adsorption/defect sites are available. In Fig. 3 $\frac{\text{TS}^{\text{conf}}}{N}$ (eq. 70) is plotted as a function of the temperature T for $N = 16$ and different numbers n of adsorbates/defects. The maximum number n is $n = N/2$,

here the interaction between the adsorbates would reduce the configurational entropy. These interactions were neglected in the previous considerations. They can reduce the configurational entropy even at lower, highly symmetric coverages, as shown by Monte Carlo calculations [217]. The line for $n = N/2$ in Fig. 3 represents an upper limit for the contribution to the Gibbs free energy. The area of a ZnO (000 $\bar{1}$) surface unit cell is $A_{\text{ZnO}} = 7.5 \text{ \AA}^2$. The upper limit for the contribution to the Gibbs free energy (n is $n = N/2$) is:

$$\frac{TS^{\text{conf}}}{(n/2)A_{\text{ZnO}}^{\text{site}}} \leq 8 \text{ meV}. \quad (71)$$

The contribution is small, but should be discussed or accounted for, for all considered systems.

The final contribution to the Gibbs free energy of our surface is the free energy of vibration F^{vib} . From statistical mechanics and thermodynamics we know that

$$F^{\text{vib}}(T, V) = E^{\text{vib}} - TS^{\text{vib}} = -k_B T \ln Z^{\text{vib}} \quad (72)$$

with Z^{vib} the partition function of the vibrational degrees of freedom of a N -atomic system. It is defined as

$$Z^{\text{vib}} = \sum_i \int \frac{d\mathbf{k}}{(\pi)^3} \frac{\exp\left(\frac{-1}{2\beta\hbar\omega_i(\mathbf{k})}\right)}{[1 - \exp(\beta\hbar\omega_i(\mathbf{k}))]} \quad (73)$$

with $\beta = 1/k_B T$ and $\omega_i(\mathbf{k})$ the $3N$ vibrational modes of the N atom system. By introducing the phonon density of states $\sigma(\omega)$ (DOS) and inserting eq. 73 into eq. 72 we get

$$F^{\text{vib}}(T, V) = \int d\omega \left[\frac{1}{2}\hbar\omega + k_B T \ln(1 - e^{-\beta\hbar\omega}) \right] \sigma(\omega). \quad (74)$$

F^{vib} can thus be calculated from the phonon density of states $\sigma(\omega)$ for all bulk and surface phases in the system. F^{vib} enters the surface free energy $\gamma(T, p)$ (eq. 59) as a difference between these bulk and surface phases (G^{surf} and g^{bulk}). Calculating the phonons for the surfaces considered in this work is not feasible. To approximate the contributions from vibrating surface adsorbates we can select one characteristic frequency in eq. 74 by using the Einstein model [74]. The phonon density of states $\sigma(\omega)$ is replaced by a delta distribution at the characteristic frequency $\hat{\omega}$.

$$F^{\text{vib}}(T, V) = \frac{1}{2}\hbar\hat{\omega} + k_B T \ln(1 - e^{-\beta\hbar\hat{\omega}}) \quad (75)$$

As a first approximation for F^{vib} at moderate temperatures ($T < 1000$) only the first term in eq. 75 is evaluated (zero point energy). The vibrational energy contribution of a hydrogen atom adsorbed at an oxygen surface site can be approximated by the difference between the experimental H_2 gas phase stretching mode at $\omega_{\text{H}_2} = 4138 \text{ cm}^{-1}$ [207] and the the frequency obtained by a finite difference

DFT calculation $\omega_{\text{O-H}}^{\text{surf}} = 3657 \text{cm}^{-1}$. The vibrational contribution to the surface free energy for n hydrogen on N possible sites is:

$$\gamma_{\text{vib}} = \frac{1}{A} \left[\frac{1}{2} \hbar \omega_{\text{O-H}}^{\text{surf}} - \frac{1}{2} \hbar \omega_{\text{H}_2} \right] = \frac{n}{NA_{\text{site}}} 0.03 \text{eV} \quad (76)$$

The contribution is small, but has to be discussed for the system under investigation. For high coverages the contribution could be non-negligible.

To calculate the surface free energies and to determine the energetically most stable surface phases at a given pressure and temperature, the vibrational energy and configurational entropy have to be considered for the systems of interest. The total energy obtained from DFT is indeed the leading term, but disorder and vibrations could stabilize otherwise unstable surface phases.

For the systems of ZnO on metal substrates eq. 61 has to be extended to include a water atmosphere as reservoir. Under typical UHV conditions the partial pressures of H_2 , O_2 , and H_2O are of the same order of magnitude. Previously only H_2 and O_2 were considered. The chemical potential $\mu_{\text{H}_2\text{O}}$ of water can only be included in eq. 61 together with μ_{H_2} or μ_{O_2} to satisfy element conservation for the surfaces considered. In this approach one of the surface species is always neglected. The resulting surface phase diagrams can differ significantly as this method assumes unrealistic partial pressures in equilibrium for the missing species. Under experimental conditions these three species are not in thermodynamic equilibrium because of the negligible rate of spontaneous gas-phase reactions. The most common approach is to only use H_2 and O_2 as gaseous reservoirs and constrain them by the chemical potential of water:

$$\mu_{\text{H}_2} + \frac{1}{2} \mu_{\text{O}_2} > \mu_{\text{H}_2\text{O}}. \quad (77)$$

As water is not explicitly included in the calculation, its partial pressure is ill-defined. The chemical potential of water is therefore approximated by the DFT total energy in the gas phase $E_{\text{H}_2\text{O}}$. The argument here is that outside the proposed boundary in eq. 77 water would macroscopically condense on the surface [73, 132, 161, 261, 267]. This portion of the phase diagram is considered unreliable because no prediction about the structure can be made. Unfortunately, the pressure range of experiments often lies in this area.

Herrmann and Heimeel recently [98] proposed a solution to this problem of the thermodynamic theory by explicitly including the chemical potentials of all three species μ_{H_2} , μ_{O_2} , and $\mu_{\text{H}_2\text{O}}$. Eq. 61 now reads:

$$\gamma_{\text{ZnO}} = \frac{1}{A} \left[G^{\text{surf}} - N_{\text{Zn}} g_{\text{ZnO}}^{\text{bulk}} - N_{\text{O}} \mu_{\text{O}} - N_{\text{H}} \mu_{\text{H}} - N_{\text{H}_2\text{O}} \mu_{\text{H}_2\text{O}} \right]. \quad (78)$$

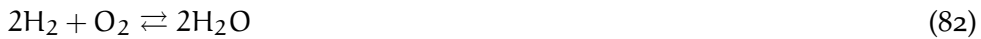
Element conservation requires

$$Z_{\text{Zn}} = N_{\text{ZnO}} \quad (79)$$

$$Z_{\text{H}} = 2N_{\text{H}_2} + 2N_{\text{H}_2\text{O}} \quad (80)$$

$$Z_{\text{O}} = 2N_{\text{O}_2} + N_{\text{H}_2\text{O}} + N_{\text{ZnO}} \quad (81)$$

This is a set of three equations with four unknowns and thus under-determined. An additional condition has to be introduced. Only energy contributions which are a multiple of the water gas-phase reaction



are permitted or in the terminology of the set of linear equations, to the solution vector $\mathbf{N}=(N_{\text{ZnO}}, N_{\text{H}_2}, N_{\text{O}_2}, N_{\text{H}_2\text{O}})$ a multiple of the vector $\mathbf{v}=(0,-2,-1,2)$ can be added. These are the stoichiometric coefficients of the water gas-phase reaction. Herrmann and Heimele eliminate this under-determination by demanding, that the virtual reaction of putting all species back into their reservoirs is orthogonal to the water gas-phase reaction

$$\mathbf{v} \cdot \mathbf{N} = 0. \quad (83)$$

The surface energy now depends on three variables and has to be analyzed in three dimensions. No constraints for μ_{H_2} , μ_{O_2} , and $\mu_{\text{H}_2\text{O}}$ are required and there is no condensation of water on the surface until the vapor pressure of water is reached.

1.7 DFT AS IMPLEMENTED IN FHI-AIMS

In this section the practical aspects of carrying out the DFT calculations in this work are presented. As the mayor tool, we will focus on the implementation in the all-electron code FHI-aims [33], developed at the Fritz Haber Institute. All electron here refers to the fact, that the wave functions of all electrons with the full potential are treated explicitly. Valence and core electrons are treated on equal footing. We will introduce the basis set employed and give an overview over the algorithm(s) for constructing and solving the Kohn-Sham equations.

The particular choice in FHI-aims for the basis set are numeric atom-centered orbitals (NAO):

$$\varphi_i(\mathbf{r}) = \frac{u_i(r)}{r} Y_{lm}(\theta) \quad (84)$$

The $Y_{lm}(\theta)$ in eq. 84 are the complex spherical harmonics and $u_i(r)$ are the numerically tabulated radial functions. They are chosen to solve the radial Schrödinger equation [230] for the potential $v_i^{\text{tot}}(r) = v_i(r) + v_{\text{cut}}(r)$. $v_i(r)$ defines the main behavior of $u_i(r)$ and is chosen as the self-consistent free atom potential (hydrogen-like, cation-like or atom-like). $v_{\text{cut}}(r)$ is a steeply increasing (exponential) confining potential, to cut off any slowly decaying tails. The radial Schrödinger equation is solved on a dense logarithmic grid [91] and the resulting radial functions are orthonormalized by a Gram Schmitt process [8]. These procedure provides a pool of basis functions that was optimized to yield a basis set that can be gradually increased in accuracy and computational cost.

They are well tested with local (e.g. [129]), semi-local (e.g. [128]) functionals as well as Hartree-Fock based functionals (e.g. [248]). The first advantage of these NAOs is the seamless descriptions of all electrons and an accurate description of the orbitals near the nuclei. The second advantage is the localized nature of the orbitals. After a certain distance the radial functions can be cut off and set to zero for larger distances. This is especially advantageous for large systems. Here the overlap of orbitals localized on spatially separated atoms is zero, increasing the sparsity of important quantities such as the Hamiltonian matrix.

The evaluation of the KS equations (eq. 27) requires a numerical integration on a

real-space grid [63, 17, 246, 23] for the setup of the overlap and the Hamiltonian matrices. These extended integrands are divided into atom-centered pieces

$$\int d^3r \varphi_i(\mathbf{r}) \hat{H}_{KS} \varphi_j(\mathbf{r}) = \sum_{\text{at}, s, t} w(\mathbf{r}) \varphi_i(\mathbf{r}) [\hat{H}_{KS} \varphi_j(\mathbf{r})] \quad (85)$$

with $\mathbf{r} = \mathbf{r}(\text{at}, s, t)$, \hat{H}_{KS} the Kohn-Sham-Hamilton operator and $w(\mathbf{r}) = p_{\text{at}}(\mathbf{r}) \cdot w_{\text{rad}}(s) \cdot w_{\text{ang}}(t)$, the total partition function p_{at} as product of the atom centered partition functions $p_{\text{at}}(\mathbf{r})$ [63], the radial $w_{\text{rad}}(s)$ and angular $w_{\text{ang}}(t)$ partition function [17]. In practice the integration grid is divided into batches recursively [96]. Taking advantage of sparsity, the non-zero basis functions in each batch are tabulated. For those basis functions $\varphi_i(\mathbf{r})$ and $\hat{H}_{KS} \varphi_j(\mathbf{r})$ are evaluated and summed up by matrix multiplication.

For periodic boundary conditions Bloch-like generalized basis functions are defined from the real-space basis functions $\varphi_i(\mathbf{r})$, that are centered in unit cells. The integration is formally carried out by the previously described integration over one unit cell and the sums over the basis function $\varphi_i(\mathbf{r})$ that are shifted by $\mathbf{T}(\mathbf{N})$ [$\mathbf{N} = (N_1, N_2, N_3)$] and have a contribution in the first unit cell

$$h_{ij}(\mathbf{k}) = \sum_{\mathbf{M}, \mathbf{N}} \exp(i\mathbf{k}[\mathbf{T}(\mathbf{N}) - \mathbf{T}(\mathbf{M})]) \int_{\text{unit cell}} d^3r \varphi_{i, \mathbf{M}}(\mathbf{r}) \hat{H}_{KS} \varphi_{j, \mathbf{N}}(\mathbf{r}), \quad (86)$$

with the \mathbf{k} -point vectors \mathbf{k} .

Now, the single particle eigenvalue problem can be solved. For this task highly efficient linear algebra libraries are employed. For large numbers of \mathbf{k} -points (more or equal number of \mathbf{k} -points as computing tasks) the Lapack library [7] is used. For larger and cluster systems, ScaLapack [30] and the ELPA [156] libraries are employed to make use of the highly parallelized structure of modern super computers.

From the eigenstates c_{ij} , that are the solution to the KS-eigenvalue problem, a new density is calculated. First the density matrix is set up

$$n_{ij} = \sum_l^{N_{\text{occ}}} f_l c_{il} c_{jl} \quad (87)$$

by summing the outer product between eigenstate pairs and multiplying with the occupation number f_l of state l . The density on the grid is obtained by a matrix operation

$$n(\mathbf{r}) = \sum_{ij} \varphi_i(\mathbf{r}) n_{ij} \varphi_j(\mathbf{r}). \quad (88)$$

From this density the potential can be calculated and the KS-eigenstate problem re-evaluated. This is the self-consistent field (s.c.f.) cycle (see Fig. 4). The procedure is repeated until the change (as compared to the previous step) of the integrated density, energy or sum of eigenvalues falls below a certain threshold. In practice only a fraction of the new density is mixed with the original density. This results in a more stable convergence behavior. A well established mixing scheme is Pulay's direct inversion of the iterative subspace or Pulay mixing [209, 131]. It is based on the idea to find the best linear combination of the

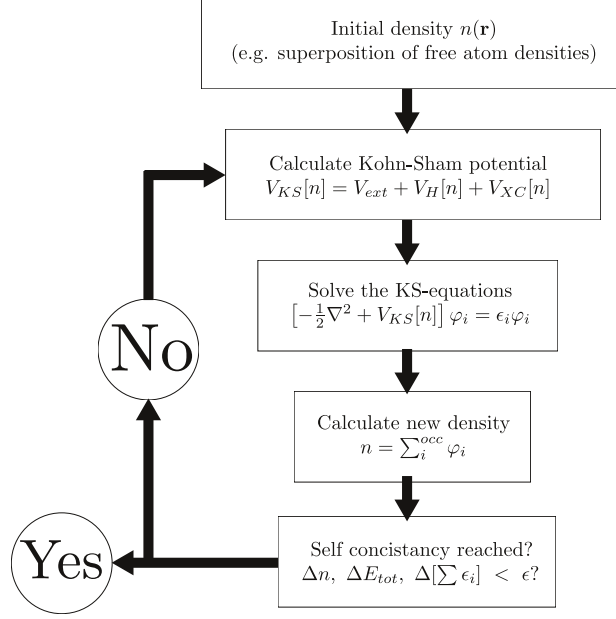


Figure 4: Self consistent field cycle.

residuals (difference between two consecutive densities) of all previous densities. Another useful technique is the preconditioning of the density to improve convergence and reduce long-range oscillations in the residual of the densities. This problem is especially notorious in slab calculations. Charge-density can be transferred over the vacuum region in one s.c.f. step and back in the next. This leads to an oscillation of the density, ultimately preventing convergence. This problem can be tackled by applying a pre-conditioner. A robust and well tested choice is the Kerker pre-conditioner [121, 177, 154].

After convergence of the s.c.f. cycle the force on each atom can be calculated by

$$\mathbf{F}_{\text{at}} = -\frac{\partial}{\partial \mathbf{R}_{\text{at}}} E_{\text{tot}}. \quad (89)$$

By minimizing the forces on the atoms the (local) minimum on the Born-Oppenheimer-energy surface can be obtained. To optimize the atomic positions the trust-radius method [179] or the standard Broyden-Fletcher-Shanno-Goldfarb (BFGS) algorithm [206, 33] are used, which try to minimize the Born-Oppenheimer-energy surface in the direction of the steepest decent. After an optimization step a new s.c.f. cycle is started with the new atom coordinates. This procedure is repeated until the residual force on the atoms is below a certain threshold. From the density and eigenvalues of such an optimized structure many important properties can be obtained/calculated, e.g. cohesive energy, surface energy, the band structure $E_n(\mathbf{k})$, density of states or transition matrix elements.

1.8 CALCULATING SURFACE VIBRATIONS

After calculating and minimizing the energy on the Born-Oppenheimer potential energy surface we want to calculate molecular vibrations and phonons. They are essential to accurately account for the surface free energy of vibration (eq. 72).

This contribution to the total surface free energy, although typically small, can determine the stability of surface reconstructions that are close in energy. We require the phonon density of states (eq. 74) for the surface free energy of vibration. Its full calculation, although possible, is not feasible for the system investigated in this work. We will restrict the discussion to the description of vibrations of surface adsorbates within the harmonic approximation. The change in vibrational modes between surface adsorbate and free molecule is expected to be the leading term in the calculation of the surface free energy. We will omit changes in pure surface and pure bulk modes. A comprehensive description of the phonons and molecular vibrations can be found in standard text books [124, 11, 85].

The nuclei of the system move in the effective potential of the electrons (eq. 12 and 15). The forces are the derivatives of this potential with respect to the coordinates of the nuclei:

$$m_a \ddot{\mathbf{R}}_a = \mathbf{F}_a = -\frac{\partial E_{\text{tot}}}{\partial \mathbf{R}_a} = -\frac{\partial}{\partial \mathbf{R}_a} \left[\sum_{a=1} \sum_{b>a} \frac{Z_a Z_b}{|\mathbf{R}_a - \mathbf{R}_b|} + E_{\text{elec}}(\{\mathbf{R}_a\}) \right] \quad (90)$$

If we define \mathbf{R}_i^0 as the equilibrium positions of the atoms in the system we can Taylor expand the potential in eq. 90 around the minimum of the Born-Oppenheimer potential energy surface:

$$E_{\text{tot}}(\{\mathbf{R} - \mathbf{R}^0\}) = E_{\text{tot}}(\{\mathbf{R}^0\}) + \sum_{a=1} \left(\frac{\partial E_{\text{tot}}}{\partial \mathbf{R}_a} \right)_{\mathbf{R}_a^0} + \sum_{a=1} \sum_{b=1} \left(\frac{\partial^2 E_{\text{tot}}}{\partial \mathbf{R}_a \partial \mathbf{R}_b} \right)_{\mathbf{R}_a^0, \mathbf{R}_b^0} (\mathbf{R}_a - \mathbf{R}_a^0)(\mathbf{R}_b - \mathbf{R}_b^0) + \dots \quad (91)$$

The first order term is zero for a minimum. Only the second order has to be considered. The matrix of second derivatives is called Hessian matrix and is in practice calculated by displacing the atoms by $\pm\delta$ in x, y and z direction (finite differences):

$$\frac{\partial^2 E_{\text{tot}}}{\partial x_i \partial x_j} = \frac{\mathbf{F}_i(x_j + \delta) - \mathbf{F}_i(x_j - \delta)}{2\delta}. \quad (92)$$

By omitting higher order terms in the potential and with the Ansatz for the harmonic oscillator $\mathbf{v}_a = \mathbf{A} \exp(i\omega t + \phi)$ the dynamical matrix is constructed

$$D_{ab}(\mathbf{q}) = \sum_{b'} \frac{e^{i(\mathbf{q} \cdot \mathbf{R}_{bb'})}}{\sqrt{m_a m_b}} \left. \frac{\partial E}{\partial x_a \partial x_b} \right|_{\mathbf{R}_{bb'}} \quad (93)$$

with the atomic masses m_a and the connecting vector between atoms b and b', $\mathbf{R}_{bb'}$. This dynamical matrix determines the equation of motion for a periodic array of harmonic atoms for each reciprocal vector \mathbf{q}

$$\mathbf{D}(\mathbf{q}) [\mathbf{v}(\mathbf{q})] = \omega^2(\mathbf{q}) [\mathbf{v}(\mathbf{q})]. \quad (94)$$

The eigenvalues ω^2 of the dynamical matrix $\mathbf{D}(\mathbf{q})$ completely describe the dynamics of the system (in the harmonic approximation).

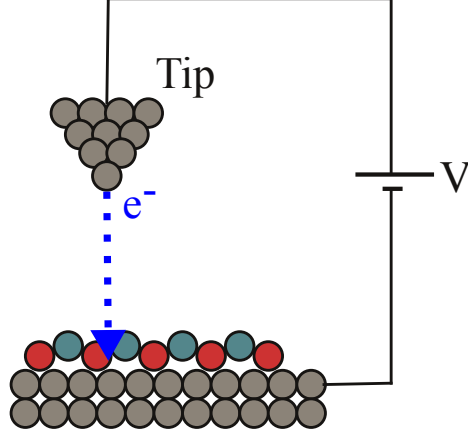


Figure 5: Schematic illustration of a Scanning tunneling microscope.

1.9 SIMULATING STM APPARENT HEIGHT MAPS

One of the best established experimental techniques to image surfaces is scanning tunneling microscopy (STM). It is capable of locally imaging the electron density of a conducting surface. The basic principle is shown in Fig. 5. A conducting tip (e.g. tungsten) is brought in the vicinity of the surface and a voltage (bias voltage) is applied between tip and surface. If the distance (d) between tip and surface is small enough electrons can tunnel between tip and sample depending on the applied voltage. This tunneling current is measured at different lateral positions, resulting in a spatially resolved map of the density of states. The position above the surface is kept fixed. This is the constant height operation mode. Another operating mode is the constant current mode. The tunneling current between sample and tip is kept constant by a feedback loop that automatically adjusts the sample tip distance. The actuation is typically achieved by very precise piezo-crystals.

The theoretical description of STM measurements was given by Tersoff and Hamman [250]. The quantity we want to calculate from theoretical considerations is the tunneling current $J(\mathbf{r}, V_B)$. It is a function of the tip position and the applied bias or potential. To describe the tunneling between surface and tip the interaction between tip and surface is assumed to be weak. This assumption is valid for typical experimental tunneling conditions. It can be treated in first order perturbation theory (Fermi's Golden Rule)

$$J = \frac{2\pi e}{\hbar} \sum_{i,j} (f(E_i) [1 - f(E_j)] - f(E_j) [1 - f(E_i)]) |M_{ij}|^2 \delta(E_i + V - E_j) \quad (95)$$

with the Fermi function [11] $f(E)$, V the bias voltage and M_{ij} the tunneling matrix element between the states φ_i and φ_j of the electrodes (sample and tip). E_i is the energy of the state φ_i . By taking the limit $T \rightarrow 0$ the Fermi functions become step functions and eq. 95 simplifies to

$$J = \frac{2\pi}{\hbar} e^2 V \sum_{i,j} |M_{ij}|^2 \delta(E_i - E_F) \delta(E_j - E_F). \quad (96)$$

The task is to calculate the tunneling matrix element in eq. 96. Bardeen showed that it can be expressed as [20]

$$M_{ij} = \frac{\hbar^2}{2m} \int d\mathbf{S} (\varphi_i^* \nabla \varphi_j - \varphi_j \nabla \varphi_i^*). \quad (97)$$

The integral is over any surface lying in the barrier region. This expression is valid for a free-electron approximation for the normal state (Wentzel, Kramers, Brillouin (WKB) -approximation). To further simplify, a model for the tip is usually considered. The simplest approximation was put forward by Tersoff and Hamann [250]. They idealized the STM tip as a mathematical point source of current, that has maximum resolution and no interaction between surface and tip. Eq. 96 is reduced to

$$J \sim V \sum_i |\varphi_i(\mathbf{r}_t)|^2 \delta(E_i + V - E_F). \quad (98)$$

The authors also showed, that this approximation is even valid for more realistic models. The tip can be considered as an s-wave function and \mathbf{r}_t is the center of the wave function. The model breaks down for considerable tunneling to several tip atoms and if the tip and sample wave function start to overlap for small distances.

We can use eq. 98 to simulate experimental results from the density obtained by our DFT calculations. We integrate the local density $\rho(\mathbf{r}, \epsilon)$ from the Fermi energy E_F to $E_F + V$. The result is a map of the current (local density of states) at a constant distance \mathbf{r}_t above the surface. To compare to experimental results obtained in the constant current mode, the current has to be calculated for different \mathbf{r}_t and be rearranged to represent the height for a constant current. Absolute values can not be compared between theory and experiment, because electronic and geometric properties of the tip, that are difficult to determine experimentally, enter into the matrix elements in eq. 96. Another general issue is the necessity to calibrate height measurements for the STM. For this task accurately known step edge heights are measured. For systems composed of substrate and ad-layer the STM is typically calibrated on the step edges of the substrate. This introduces systematic errors if the interaction between tip and substrate differs from the interaction between tip and ad-layer. Here only height differences between ad-layers or substrate step edges can be compared to theoretical results calculated by the above method. Another approach is to calculate heights by subtracting the height obtained from simulating the bare substrate from the ad-layer system. This theoretical calibration is in analogy to experiment and allows to qualitatively and quantitatively compare theoretical and experimental results.

Part III

ZNO ON METAL SUBSTRATES

INTRODUCTION

Zinc oxide (ZnO) is a group II-VI semiconductor with a 3.4 eV large, direct band gap [1]. In nature it is found as the mineral zincite. Its color is yellow to red because of the naturally occurring manganese content [125]. The ZnO used in industry and science is a clear and colorless synthetic material [208]. It is not poisonous and Zn as its main production source is easily available [185]. Zn forms 0.0076 % of the earth's crust [160] and is therefore one of the more abundant materials.

ZnO has many applications in industry and science. It is produced on industrial scales in the order of 10^5 tons per year [125, 165]. It is used as an additive for the production of ceramics. By adding ZnO to ceramics the thermal conductivity is increased and the elasticity improved [165]. Another major application lies in tire production. The admixture of ZnO to rubber helps to dissipate the heat during vulcanization [125, 165]. Other fields of application include medicine [190] and cosmetics [105]. Here ZnO is used as UV-blocker in suntan solutions [164]. In photo-voltaics it is used as front contact for solar cells or liquid crystal displays [126, 18].

A first period of strong interest in ZnO peaked in the middle of the 20th century. The focus was on possible application in opto-electronics [125]. These efforts subsided because it was deemed impossible to p-type or n-type dope ZnO. A second period of intensified ZnO research started in the middle of the 1990 when the advances in thin-film technology made it possible to grow epitaxial films, quantum dots and other nano structures [187]. The goal is to replace GaN as material for light emitting diodes in opto-electronics (Ga is expensive and poisonous) by ZnO [18, 148]. Other applications might include spin-tronics for ZnO doped with atoms of high magnetic moment [204]. A large effort goes into replacing tin oxide by ZnO doped with Al, Ga, etc. to achieve high conductivity while sustaining opaqueness [126].

Another major field of research is heterogeneous catalysis. ZnO is used as catalyst in industrial scale synthesis of methyl [25]. The active components are ZnO supported metal nano particles. However, the actual catalytic mechanism as well as the atomic structure of the catalytically active ZnO are still under investigation [136].

We will start with a short description of the bulk phases of ZnO and their stability [1]. Then we will shortly discuss the low index surfaces of ZnO. From the polar surfaces ZnO (0001) and (000 $\bar{1}$) ultra-thin films will be derived and sub-sequentially fitted to metal substrates. We will investigate the atomic and electronic structure of these ultra-thin ZnO films on metal substrates and access their stability by means of *ab initio* thermodynamics (see Sec. 1.6) with respect to their chemical environment.

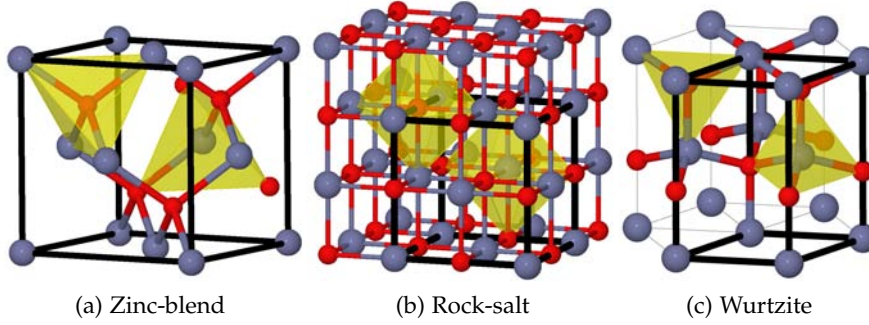


Figure 6: Crystal structures of ZnO. The unitcell is marked in black. Zn - purple, O - red

The most stable bulk phase of ZnO under ambient conditions is the wurtzite structure which is shown in Fig. 6 c. The c-axis of the crystal is chosen parallel to the z-direction. Wurtzite exhibits a hexagonal symmetry along the c-axis as well as strong polarity along this axis. Zn atoms are 4-fold coordinated with O and vice versa. The tetrahedra created by this coordinations are indicated in Fig. 6 c for one Zn and O atom. The ideal value for the c/a ratio is $c/a = \sqrt{8/3} = 1.633$ [1]. Another ZnO polymorph is zinc-blend. Zinc-blend can be stabilized by epitaxial growth on suitable cubic substrates [12]. The zinc-blend structure is shown in Fig. 6 a. The four-fold coordination between Zn and O are indicated by yellow tetrahedra. By application of high pressures ZnO can be stabilized in the rock-salt structure [68]. This structure is shown in fig. 6 b. ZnO in rock-salt structure has a much closer packing and a 6-fold co-ordination which is indicated by the yellow polyhedra in fig. 6 b. Other structures have been proposed to grow at even higher pressures [109, 282].

To determine the lattice parameters a fit to the Birch-Murnighan equation of state (eq. 99) [174]

$$E(V) = E_0 + \frac{B_0 V}{B'_0} \left(\frac{(V_0/V)^{B'_0}}{B'_0 - 1} + 1 \right) - \frac{B_0 V_0}{B'_0 - 1} \quad (99)$$

was performed for the three most common crystal structures of ZnO: wurtzite, rock-salt and zinc-blend. These structures represent only a small portion of a much larger phase space [109, 282]. The theoretical investigation of all these phases is not in the scope of this work and the reader is referred to the literature.

The Energy per atom $E(V)$ curves for the three crystal structures is shown in Fig. 7 for the local PW-LDA [199], semi-local PBE [196] and the hybrid xc-functional HSE06 [100]. By fitting to eq. 99 the equilibrium cohesive energy E_0 , the bulk modulus B_0 , its derivative B'_0 and the equilibrium volume V_0 are determined.

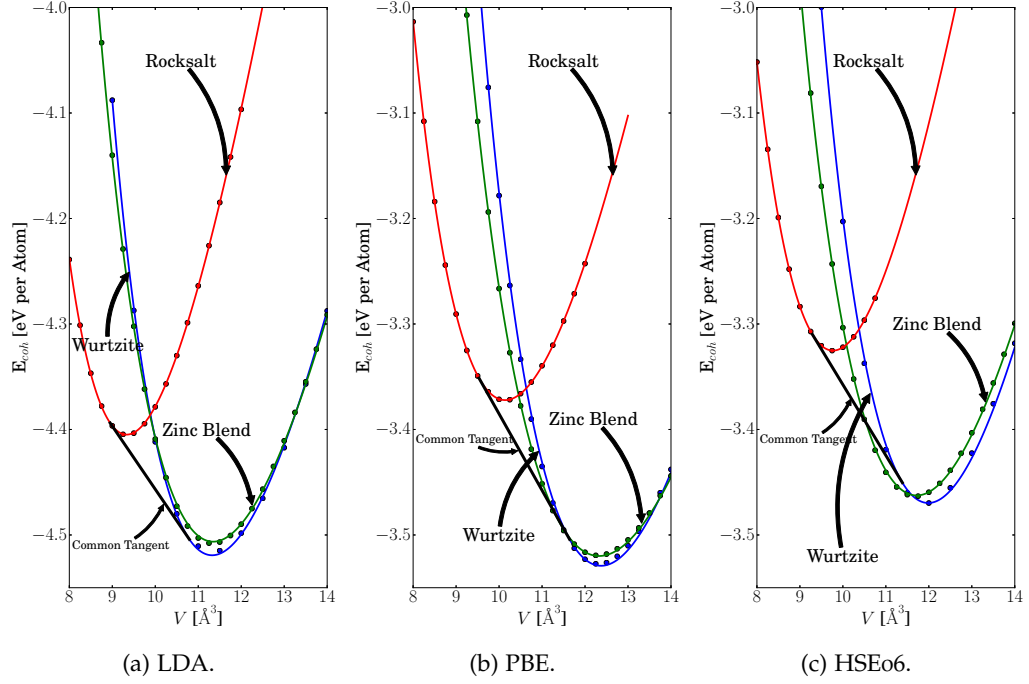


Figure 7: Cohesive energy versus crystal volume for different bulk phases of ZnO for different xc-functionals.

The fitted values for the three xc-functionals of Fig. 7 are presented in Tab. 3 together with experimental reference data. From the values for the cohesive properties, the general remarks from sections 1.4.1, 1.4.2 and 1.4.3 are confirmed. PBE improves the over-binding of LDA, leading to lattice parameters in good agreement with experimental values in Tab. 3. By using HSE06, the overall agreement between theory and experimental values is slightly increased for wurtzite and rock salt. For the wurtzite structure the lattice parameter in c-direction is larger than observed in experiment, while the lattice parameter in the a/b-plane is now below the experimental value. However, the comparability of experiment is limited, because experimental values were measured at room temperature and no finite temperature effects were included in the calculations ($T=0$ K). By means of the Maxwell construction [54] a common tangent is fitted to the $E(V)$ curves in Fig. 7 for wurtzite and rock salt. The slope of the tangent determines the transition pressure between both structures. The slope of the common tangent in Fig. 7 a is 9.58 GPa, Fig. 7 b is 11.6 GPa and Fig. 7 c is 10.8 GPa.

In Fig. 8 the electronic band structures and (projected) density of state (DOS) for rock-salt (a and b), zinc-blend (c and d), and wurtzite (e and f) are shown for the PBE [196] and HSE06 xc-functional. Calculating the electronic structure with local or semi-local DFT leads to an underestimation of the band gap and inter-band transition energies. The effect of the notorious self interaction error is greatly reduced by applying the hybrid xc-functional HSE06 [100]. The band gaps calculated with the PBE (HSE06) xc-functional are 0.73 eV (2.57 eV) for wurtzite, 0.64 eV (2.51 eV) for zinc-blend and 1.97 eV (3.71 eV) for rock-salt at the Γ -point. For wurtzite and zinc blend this is the direct band gap. For rock-salt a indirect band gap between the Γ - and L-point of 0.75 eV (2.69 eV) is observed. The large

	PW-LDA	PBE	HSEo6	Exp.
Wurtzite				
V_0 [\AA^3]	22.700	24.619	23.96	23.99 [61]
E_0 [eV]	9.13	7.425	6.77	7.52[61]
B_0 [GPa]	177	125	140	181[61]
B'_0	5.09	4.13	3.9	4.0[61]
c [\AA]	5.150	5.291	5.239	5.220[61]
a [\AA]	3.190	3.279	3.250	3.258[61]
u	0.379	0.379	0.379	0.382[61]
Zinc-blend				
V_0 [\AA^3]	22.694	24.656	23.434	
E_0 [eV]	11.316	7.040	3.463	
B_0 [GPa]	158.76	129.655	155.460	
B'_0	4.244	3.950	4.005	
a [\AA]	4.083	4.620	4.543	4.463[13]
Rock-salt				
V_0 [\AA^3]	18.669	20.283	19.540	19.484[119]
E_0 [eV]	11.114	6.744	6.650	
B_0 [GPa]	205.549	163.469	190.659	228[119]
B'_0	4.781	4.343	4.185	
a [\AA]	4.211	4.329	4.276	4.271[119]

Table 3: Lattice parameters for zinc blend, rock salt and wurtzite bulk ZnO. Experimental data was measured at room temperature.

peaks in the DOS in the valence band originate from Zn 3d states. The valence band highest in energy is dominated by states of O 2p character. The conduction band lowest in energy around the Γ -point is dominated by Zn 4s-like states. Qimin *et al.* showed, that by a quasi particle correction within the GW approximation [280] the agreement of theoretical and experimental electronic structure can be further increased.

The semi-local PBE xc-functional will be the basis for the surface calculations in the following sections. The obtained cohesive parameters are in good agreement with experimental data and calculations with the HSEo6 hybrid xc-functional. The band gap is significantly underestimated, but the electronic structure is otherwise in good agreement with HSEo6 results. If feasible the accuracy of the results will be tested with HSEo6.

In the following sections, due to its prevalence, the wurtzite structure is the major structure for our investigation.

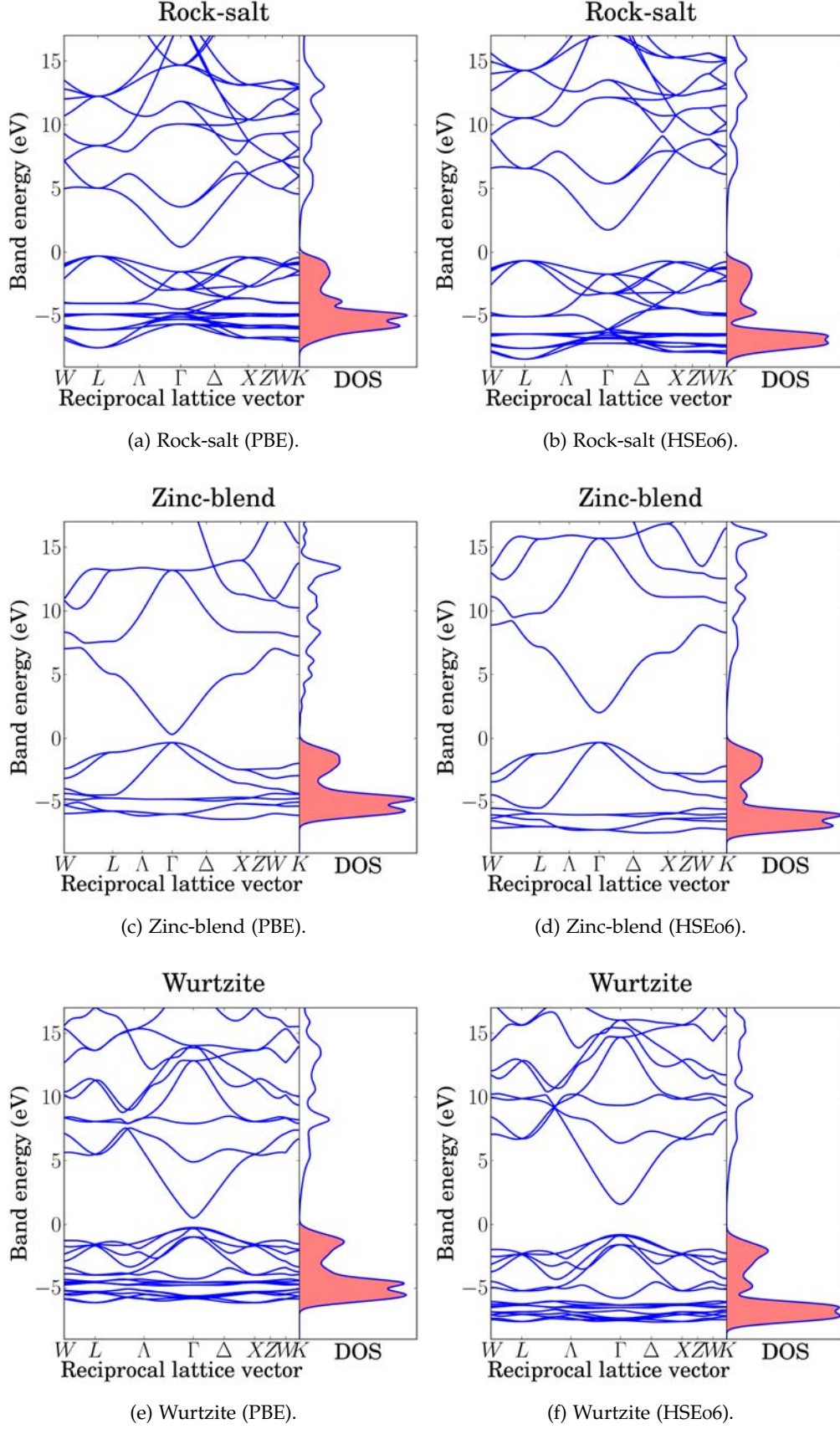


Figure 8: Electronic band structure and density of states (DOS) for the three prevalent bulk crystal structures of ZnO calculated with the PBE [196] (a, c, e) and HSE06 [100] (b, d, f) xc-functional. The occupied states in the DOS are colored in light red. The Fermi energy is set as zero for all graphs.

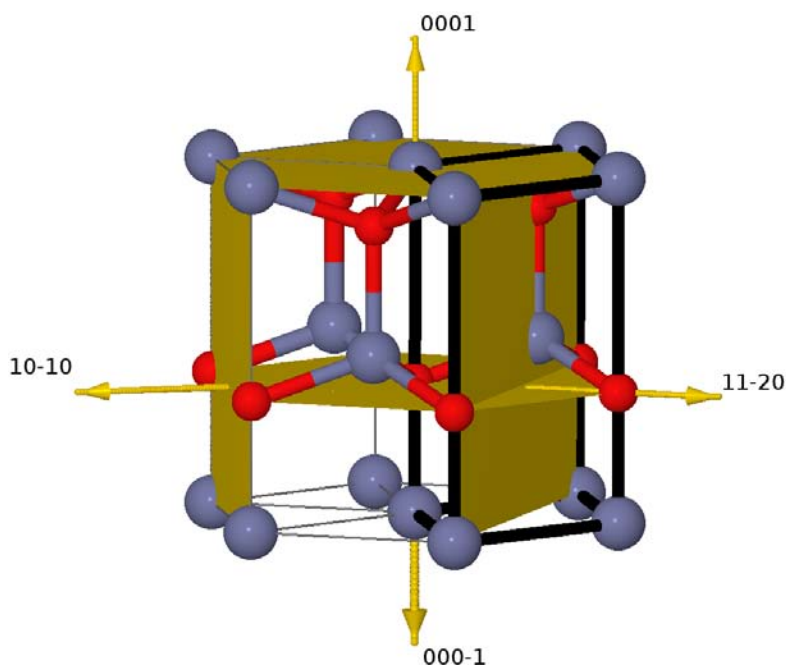


Figure 9: ZnO planes

ZnO has a wide range of applications, especially in opto-electronics and heterogeneous catalysis. Surfaces and interfaces are of crucial importance for these fields. Most chemical processes occur at surfaces and devices can have interfaces (e. g. hetero junctions). The experimental techniques available are manifold. The standard technique for the experimental investigation of ZnO surfaces is low energy electron diffraction (LEED) [284]. It is very sensitive to periodically ordered structures on the surfaces. The LEED diffraction patterns of all low index surfaces have been reported [72]. Another method is the scattering of helium atoms [284]. Its particular advantage is its sensitivity for hydrogen. Hydrogen over-layers on ZnO could be detected with this techniques [72, 275]. Other methods for obtaining information about the chemical composition of ZnO surfaces are: X-ray photo electron spectroscopy (XPS) [284], photo electron spectroscopy (UPS) [284], X-ray emissions spectroscopy (XES) and near edge X-ray absorption fine structure spectroscopy (NEXAFS) [284]. For measuring binding energies thermal desorption spectroscopy (TDS) can be used. To investigate and identify adsorbates at surfaces, vibrational spectroscopy is used. Infrared spectroscopy (IR) [284] is a widely applied technique for this purpose. For direct structural characterization and local spectroscopy scanning tunneling microscopy and spectroscopy are important methods (see Sec. 1.9). The four scientifically most important low index surfaces are indicated in Fig. 9. A general problem is the requirement of a conducting sample for many experimental techniques.

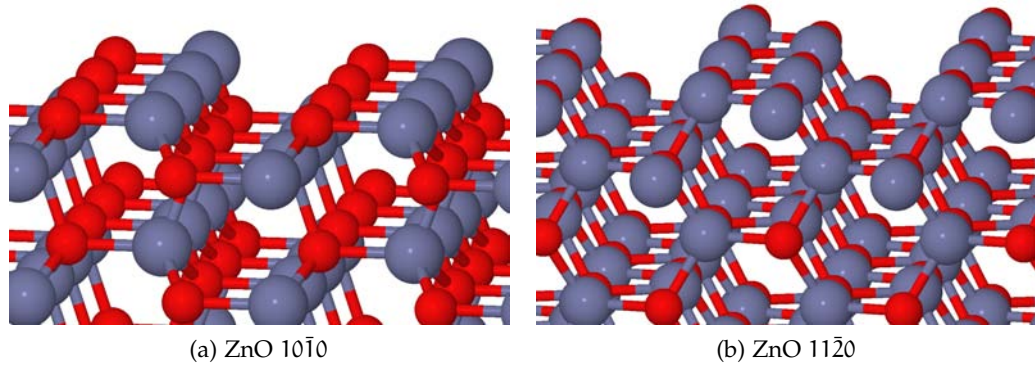


Figure 10: ZnO non-polar surfaces

Low conductance can lead to charging effects and ultimately the destruction of the sample. Methods capable of atomic resolution e. g. scanning tunneling microscopy are therefore difficult to apply. A comprehensive presentation of the results obtained with the experimental methods mentioned previously can be found in the review by Wöll [276].

The scientifically interesting surfaces of ZnO are divided into two categories: the non-polar surfaces ZnO ($10\bar{1}0$) and ZnO ($11\bar{2}0$) (Fig. 10) and the polar surfaces ZnO-Zn (0001) and ZnO-O ($000\bar{1}$) (Fig. 11). For ionic crystals, such as ZnO, without a mirror plane in the z -direction and no inversion symmetry, both types of surfaces exist. They can be defined by the projection of the bulk unit cell dipole moment on the surface normal. A polar surface is observed if this projection is non-zero. For ZnO this is the case for the $\{0001\}$ surfaces, because the bulk dipole moment is directed along the $\{0001\}$ direction. The non-vanishing dipole moment in this direction creates an electric field. Within a simple ionic model $1/4$ of the Zn^{+2} -ions on the Zn-terminated and $3/4$ of the Zn- and O-ions at the O-terminated surfaces are missing in every building block of a slab (see Fig. 11). This results in an excess charge of $+1/2$ electrons and $-1/2$ electrons at the (0001) and ($000\bar{1}$) surface, respectively. This ultimately leads to a polarization catastrophe for the ZnO (0001) surfaces. These stability problems were first addressed by Tasker [249] (Tasker-Type-II surfaces). The infinite potential difference

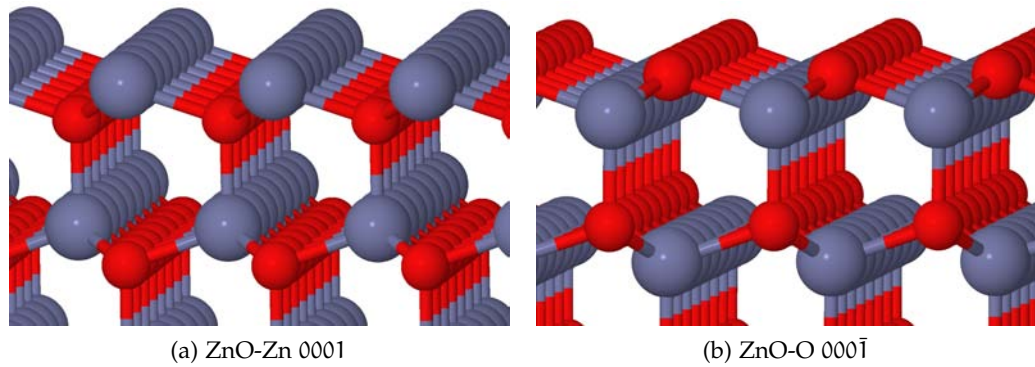


Figure 11: ZnO polar surfaces

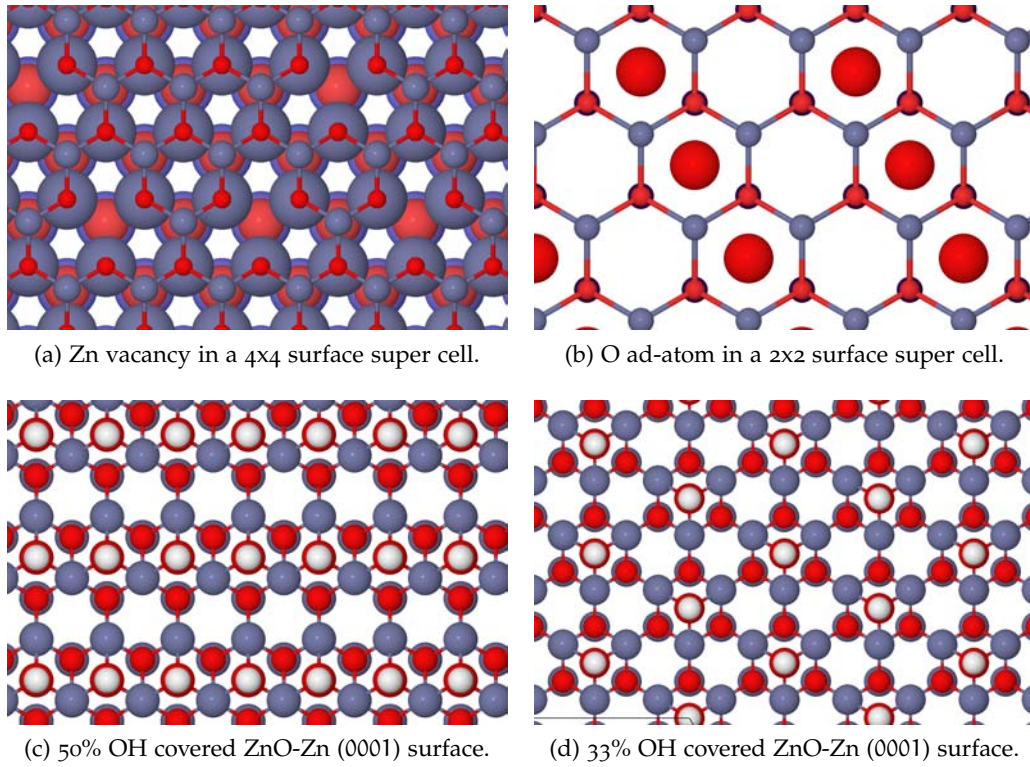


Figure 12: ZnO-Zn (0001) stabilization mechanisms.

is unphysical and basically a consequence of the simple ionic model. There are three dominant mechanisms to stabilize these polar ZnO (0001) surfaces. Charge redistribution of $1/2$ electron from the Zn to the O terminated surface or a geometry reconstruction would quench the dipole moment. The third possibility is the adsorption of atoms or molecules, that provide a compensating charge. For the non-polar $(10\bar{1}0)$ and $(11\bar{2}0)$ surfaces a structure close to a bulk truncation is expected [162, 242].

The main topics of this work are the atomic and electronic structure of ZnO thin films on metal substrates. Before we start investigating thin films, previous results on reconstruction mechanisms and stability for the ZnO (0001) and $(000\bar{1})$ surface will be presented. These results are a valuable guideline for our discussions of ultra-thin ZnO on metal substrates.

The Zn terminated ZnO (0001) surface is experimentally and theoretically better understood than the O terminated surface ZnO $(000\bar{1})$. In joined experimentally and theoretically effort different stabilizing mechanisms for the ZnO (0001) surface were investigated [132, 261]. Both works applied DFT based on the PW91 xc-functional [199] and the projector augmented wave method [32]. The reconstructions investigated by Kresse *et al.* and Valtiner *et al.* for the Zn terminated ZnO (0001) surface are:

- Zn vacancies or O ad-atoms (Fig. 12 a and b)
- Adsorption of hydrogen or OH groups (Fig. 12 c and d)
- Triangular pits (see Fig. 13 a to c), experimentally observed by Dulub *et al.* [72]

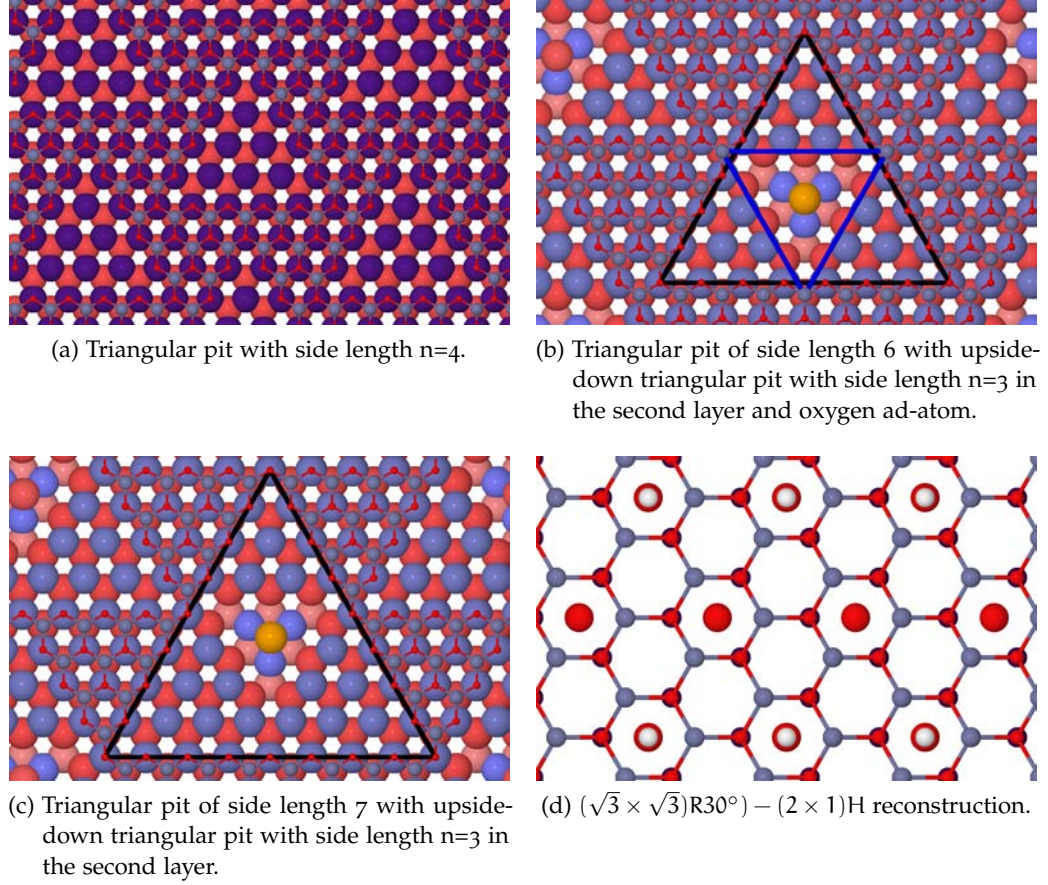


Figure 13: ZnO-Zn (0001) stabilization mechanisms.

- A $(\sqrt{3} \times \sqrt{3})R30^\circ$ reconstruction with hydrogen arranged in a (2×1) structure [261] (see Fig. 13 d)

By taking into account these structures the authors constructed surface phase diagrams. Valtiner et. al introduced the explicit temperature dependence in the phase diagram by including the vibrational free energy (see. chapter 1.6). The authors found that at low hydrogen and oxygen chemical potentials the triangular pits are favored. At high hydrogen chemical potential OH-reconstructed surfaces are stable. The structure with 50% OH coverage is most stable for a wide range of chemical potentials. At intermediate oxygen and hydrogen potentials the $(\sqrt{3} \times \sqrt{3})R30^\circ - (2 \times 1)H$ and 2×2 O-ad atom reconstructions are most stable.

For the oxygen terminated surface ZnO-O (000 $\bar{1}$) an extensive theoretical investigation was conducted by Wahl *et al.* [267]. The PW91 xc-functional [199] was applied within the projector augmented wave method [32]. Vibrational free energy and configurational entropy were neglected. The considered structures were:

- O vacancies or Zn ad-atoms (Fig. 12 a and b)
- Adsorption of hydrogen (Fig. 14 a)
- Triangular pits (see Fig. 13 a to c)

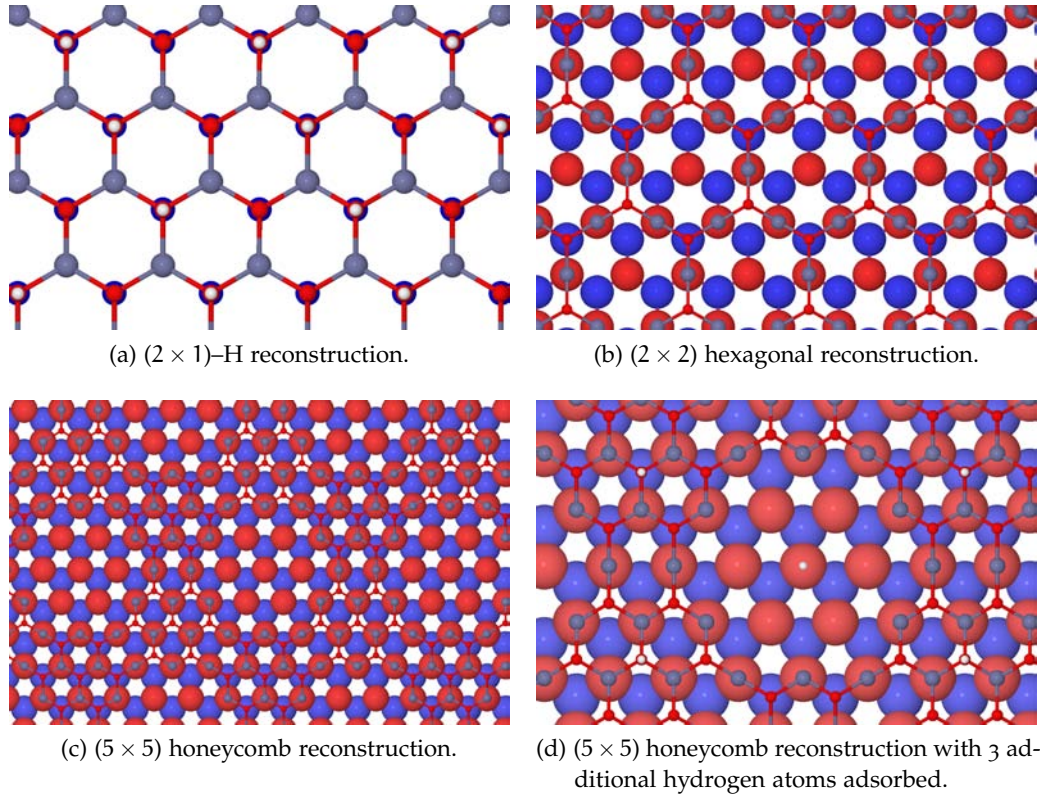


Figure 14: Reconstructions for ZnO-O $(000\bar{1})$, that are not observed for ZnO-Zn (0001) . For triangular pits see Fig. 13.

- A hexagonal honeycomb phase (see Fig. 14 c and d)
- A (2×2) reconstruction by removing two oxygen and one zinc atom from the surface (see Fig. 14 b)

A full surface phase diagram was constructed by Wahl *et al.* [267] with these structures. The authors found, that the (2×2) reconstruction is preferred at intermediate to low oxygen chemical potentials. At very low oxygen chemical potentials the 25% oxygen vacancy reconstruction prevails. At high oxygen chemical potential and low hydrogen chemical potential the honeycomb structure is most stable. For intermediate hydrogen chemical potential honeycomb structures with additional hydrogen atoms adsorbed at the surface are stable for most oxygen chemical potentials. At higher hydrogen chemical potentials the 50% hydrogen covered surface is most stable.

Apart from the geometric structure, it is interesting to look at the electronic structure of ZnO surfaces and compare it to bulk ZnO. In Fig. 15 the band structure for ZnO $(000\bar{1})$ - (2×1) -H and $(10\bar{1}0)$ is projected on the bands of bulk ZnO. The band structure and DOS was calculated with the HSE xc-functional. We chose the fraction of exact exchange in the HSE xc-functional to be $\alpha=0.4$, yielding the calculated band width [211] and band gap within 0.1 eV of error (Moll *et al.* [167]: $\alpha=0.4$, Oba *et al.* [183]: $\alpha=0.375$). The bulk like bands are shaded in gray. For ZnO $(000\bar{1})$ the density of states of the surface is quite similar as compared to bulk. There are no pronounced surface bands emerging. The situation is very different

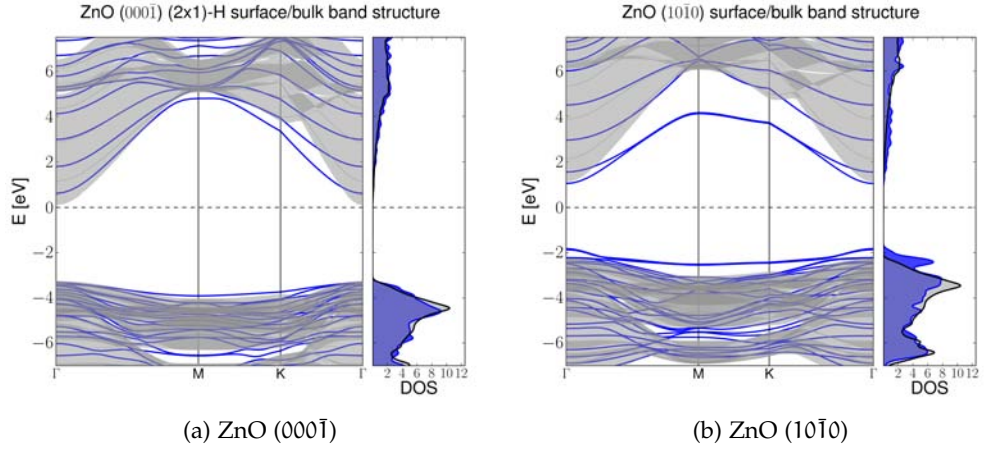


Figure 15: Projected band structures for two ZnO surfaces (HSE, $\alpha = 0.4$). The surface band structure is projected on the bulk bands. The bulk-like bands are shaded in gray, surface bands are blue. The DOS is plotted to the right of the band structure for bulk ZnO in gray and in blue for the surfaces.

for ZnO (10 $\bar{1}$ 0). Here two surface bands close to the conduction band and close to the valence band are observed. These bands are formed by the states that originated from the dumbbells at the surface, breaking the bulk symmetry (see Fig. 10 a) in analogy to the Si (0001) surface. These surface bands result in a reduction of the band gap and a pronounced increase of the density of states close to the Fermi level.

FREESTANDING ZNO THIN FILMS

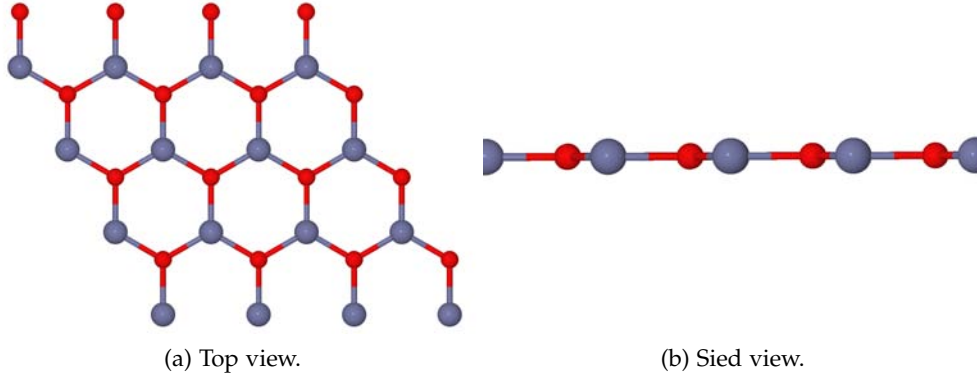


Figure 16: Atomic structure of an ideal ZnO mono-layer in α -BN structure.

Before we proceed to putting ZnO films on metal substrates, we will briefly investigate the structure and stability of a hypothetical free-standing ZnO mono-layer. Our calculations predict the ZnO mono-layer to be stable in the α -BN structure in agreement with previous results [258], see Fig. 16 a. The equilibrium corrugation for the mono-layer is zero. Therefore, only the in-plane lattice parameter has to be varied for the Murnaghan-EOS fit. The same values for the k-point grid (k_x -/ k_y -plane) and basis set settings as for bulk wurtzite ZnO were used (see Appendix C). In Tab. 4 the equilibrium lattice parameter of the freestanding ZnO mono-layer is listed for the local PW-LDA [199], the semi-local PBE [196] and the hybrid xc-functional HSE06 [100]. The general remarks of Sec. 1.4.1, 1.4.2 and 1.4.3 are confirmed by the comparison. The over-binding of LDA is reduced when using the PBE xc-functional. The lattice parameters obtained with PBE and HSE06 are similar, following the same trend as observed for bulk wurtzite

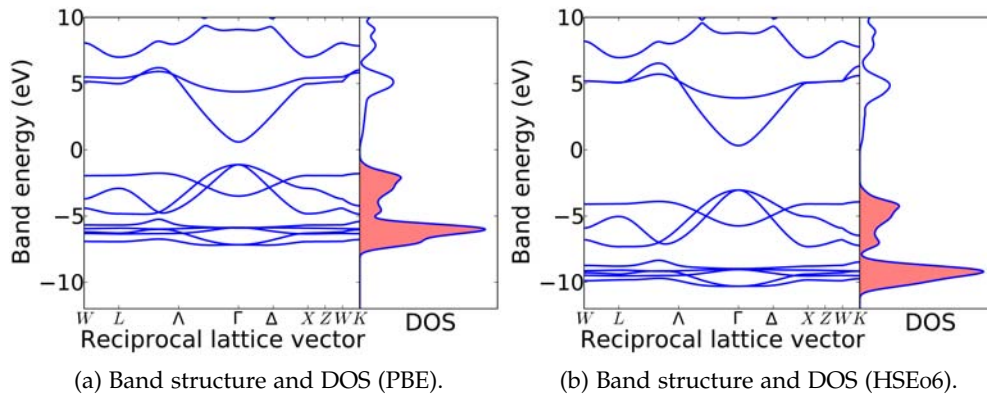


Figure 17: Electronic structure of an ideal ZnO mono-layer in α -BN structure.

xc	PW-LDA	PBE	HSEo6
a [Å]	3.198	3.277	3.252
Gap [eV]	1.78	1.77	3.49

Table 4: In-plane lattice parameter a of the ZnO mono-layer for different functionals.

ZnO (see Tab. 3). Topsakal *et al.* [255] confirmed the stability of the freestanding ZnO mono-layer by frozen phonon-calculations and *ab initio* molecular dynamics simulations. No negative phonon modes were observed, which would lead to a dissociation of the mono-layer. It is a direct band-gap semi-conductor, the band gaps for the LDA, PBE and HSEo6 xc-functional are listed in Tab. 4. The band structure and the DOS are shown in Fig. 17 a for PBE and in Fig. 16 b for HSEo6 [100]. The bonding is of sp^2 hybrid orbital nature. The upper part of the valence band is derived from O-2p orbitals, and the lower part of the conduction band from the Zn-3d orbitals.

5.1 MECHANICAL STABILITY

In agreement with the results of Peng *et al.* [194] we found that the freestanding ZnO mono-layer is much softer than graphene-like hexagonal boron nitride [269]. Smaller strains could be applied to the mono-layer before destruction. Peng *et al.* [194] performed a least square fit of the stress-strain responses and concluded that the ultimate strength of the hypothetical freestanding ZnO mono-layer is about half of graphene and hexagonal boron nitride. The elastic constants were obtained by straining the film in the direction of an Zn-O bond and perpendicular to this direction. The strain η was defined as the relative change of the lattice vector in the direction of straining.

5.2 TRANSITION MONO-LAYER TO BULK

The transition from the α -BN (graphene-like) ZnO structure is of particular interest in the context of layer by layer film growth e. g. by molecular beam epitaxy. This transition was reported to occur at 18 single layers ZnO [51]. The authors compared the cleavage energy of the ZnO film in α -BN structure with an inter-layer spacing of 2.4 Å to the binding energy of the ZnO thin films in wurtzite structure. The fixed inter-layer spacing between the ZnO layers has been pointed out as possible source for errors by other authors [258]. By considering the interlayer attraction coming from the spontaneous polarization of the layers, when switching to wurtzite, Tu *et. al.* [258] determined the critical layer number as 3 or greater. To confirm these previous results we calculated the cohesive energy of ZnO thin-film slabs of different thickness in wurtzite and α -BN. For both structures the lattice parameter c is kept at a constant value of 5.24 Å. This translates into an inter-layer spacing of 2.62 Å for the films in α -BN structure. The result is shown in Fig. 18 a for the PBE xc-functional. The transition is observed at 4 double layers of ZnO, 8 layers of planar ZnO. The effect of including contri-

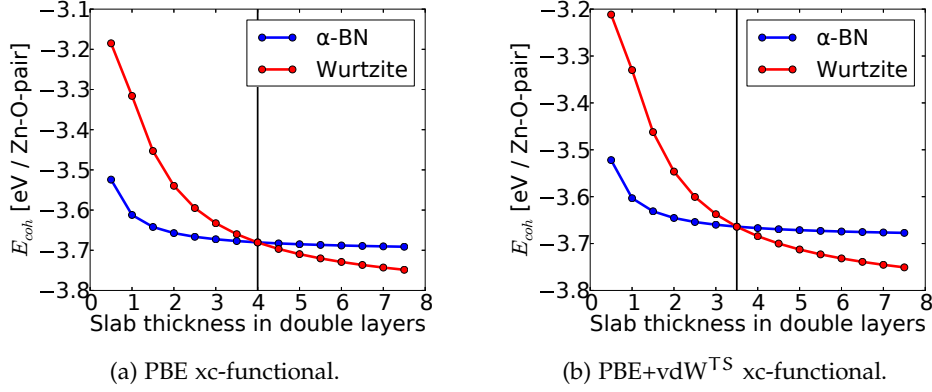


Figure 18: Cohesive energy per ZnO-pair for ZnO in α -BN and wurtzite structure against slab thickness for semi-local functionals.

contributions from van-der-Waals interactions is shown in Fig. 18 b). The TS-scheme [254] with parameters provided by Zhang *et al.* [286] was used (also see Sec. 1.5). The cohesive energy of both structures is lower. For wurtzite ZnO the effect is more pronounced. The transition from α -BN is observed one planar layer earlier as compared to the plain PBE xc-functional. If we use the hybrid functional HSE06 [100] including contributions from van-der-Waals interactions with the TS-scheme (Fig. 19 a) the transition occurs at 4 and a half double layers (Fig. 19 a). With the xc-functional HSE06* [167, 211] (HSE06 [100] with 40% exact exchange, $\alpha=0.4$) the transition is predicted above 5 double layers.

We can conclude, after taking into account van-der-Waals contributions and results obtained with the PBE and HSE06 xc-functional, that the α -BN to wurtzite transition will occur above 4 double layers or 8 planar mono-layers.

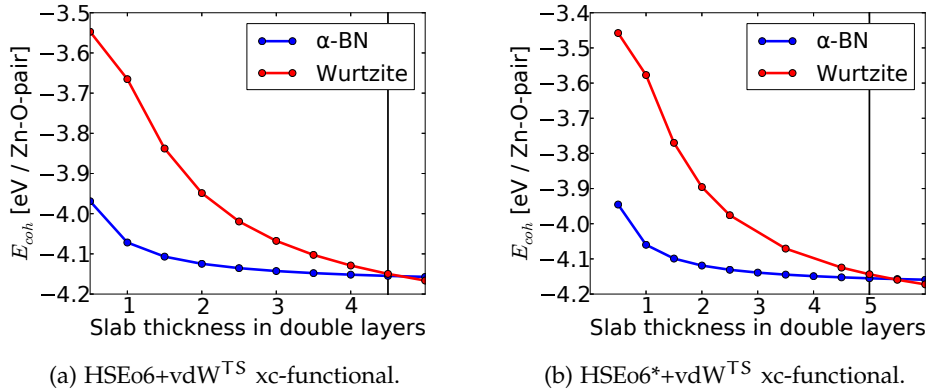
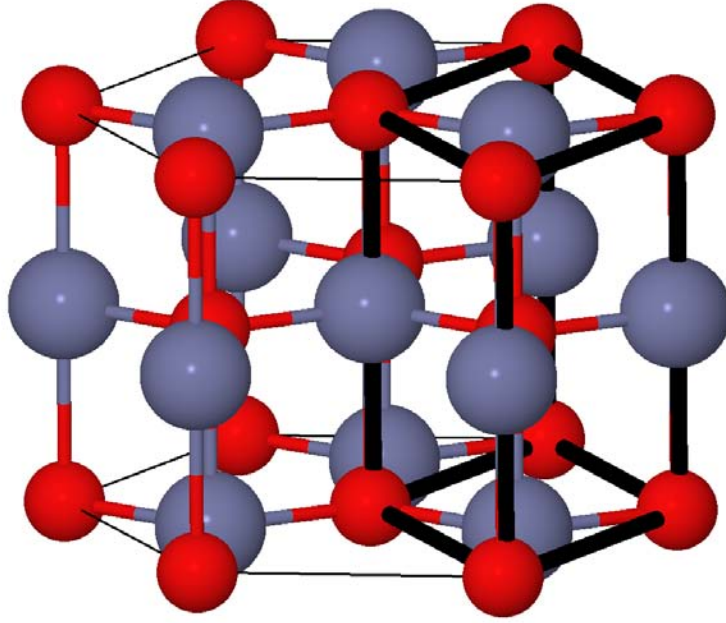


Figure 19: Cohesive energy per ZnO-pair for ZnO in α -BN and wurtzite structure against slab thickness for hybrid functionals.

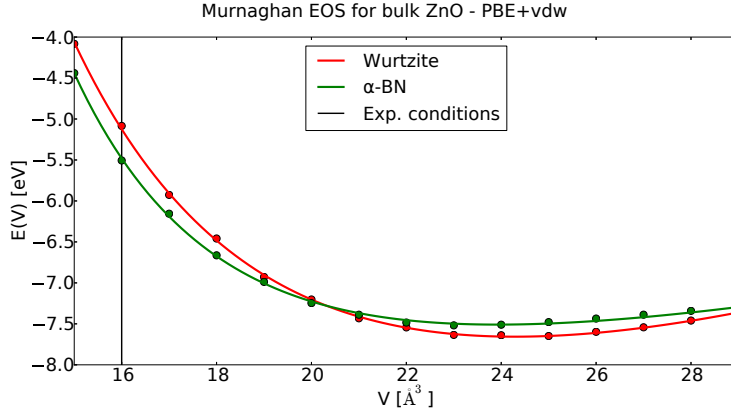
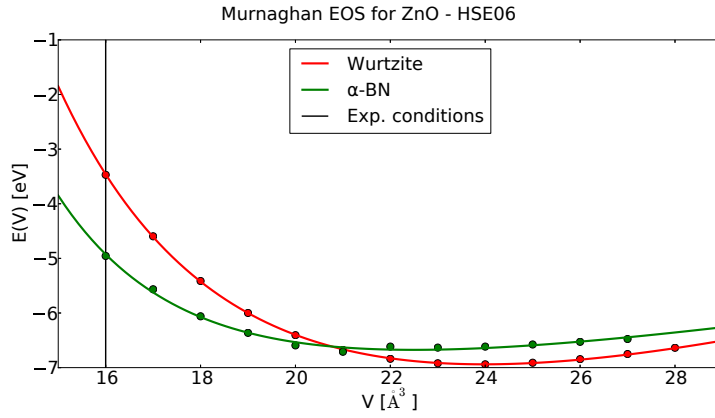
Figure 20: α -BN bulk ZnO.

5.2.1 α -BN bulk ZnO

Metastable α -BN bulk ZnO was synthesized experimentally through a molecular precursor route at low temperatures (2°C) [144]. The unit cell of the material is shown in Fig. 20 a. The major difference to wurtzite ZnO is that Zn and O form layers with Zn and O having the same position in the lateral direction for each layer. The experimental lattice parameters obtained by powder x-ray diffraction are $a=3.099\text{\AA}$ and $c=3.858\text{\AA}$ [144], resulting in a crystal volume of $V = (\sqrt{3}a^2)c/4 = 16.044\text{\AA}^3$. The material was found to be stable up to 200°C, when it transforms into the thermodynamically most stable wurtzite structure. We obtained the PBE and HSE06 lattice parameters from an fit to the Murnaghan equation of state [174]. They are shown in Tab. 5. The results are in agreement with previous results [210, 268]. The experimentally observed structure is meta-stable. By comparing the energy versus volume curves of ZnO in α -BN and wurtzite structure (see Fig. 21), we find the α -BN phase to be energetically

xc	PBE	HSE06
$V_0 [\text{\AA}^3]$	23.70	22.87
$E_0 [\text{eV}]$	6.89	6.63
$B_0 [\text{GPa}]$	238.24	296.40
B'_0	7.77	7.90
$a [\text{\AA}]$	3.45	3.40
$c [\text{\AA}]$	4.598	4.57

Table 5: Equilibrium lattice parameters for α -BN ZnO.

(a) PBE+vdW^{TS} xc-functional.

(b) HSE06 xc-functional.

Figure 21: Comparison of $E(V)$ for bulk wurtzite and α -BN ZnO.

ically most stable at the experimentally observed volume. The lattice parameters for the PBE (HSE06) xc-functional $a=3.08$ \AA (3.1 \AA) and $c=3.90$ \AA (3.84 \AA) are in good agreement with experimental results [144]. However, we find in agreement with Rakshit *et al.* [210] and Wang *et al.* [268], that the experimental structure has negative phonon modes for the PW-LDA and PBE xc-functional and is therefore unstable. This disagreement between experiment and theory, which works well for wurtzite ZnO, is not fully understood. Rakshit *et al.* [210] showed that by applying PBE+U the α -BN crystal can be stabilized and the negative phonons are removed. They attributed this effect to the wrong energetic position of the Zn-d orbitals, which is corrected by the +U formalism.

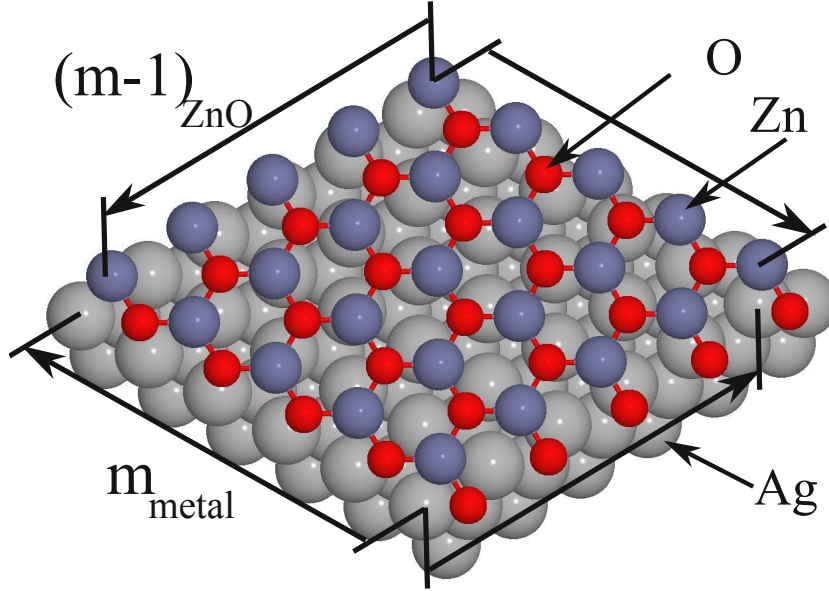


Figure 22: Exemplary coincidence structure of 6×6 surface unit cells of Ag (111) and 5×5 unit cells of mono-layer α -BN ZnO.

Ultra-thin ZnO films have been experimentally observed on the (111) surface of the metal substrates Ag [259, 237], Pd [270], Pt [159], Cu (brass) [229], Au [67], and also on Ru (0001) [120]. For Ag, Au, Pd, and Pt, coincidence structures have been deduced from the observation of Moiré patterns and crystallographic data. The observed coincidence structures are combinations of $m \times m$ many metal (111) surface unit cells and $m - 1 \times m - 1$ many mono- or multi-layers of ZnO (see Fig. 21). Sub-mono-layer coverages yield flat graphitic (α -BN) islands of ZnO. For ZnO on Ag, the transition to the wurtzite structure occurs between 3 and 4 layers [259], but already at 2 layers the onset of corrugation has been observed on Ag and Pd [259, 270]. Theoretical investigations of freestanding and supported ZnO films show that lateral strain influences the corrugation of the films [278, 66] and may decrease the number of ZnO layers necessary for the transition to wurtzite. Weirum *et al.* [270] found that oxygen promotes the growth of bilayer structures for low coverages, leading to the transformation of mono-layer islands to bilayer islands on Pd. The authors assigned the film thickness based on STM apparent height measurements. For the bulk ZnO surfaces, hydrogen has a significant effect on the surface structures [132, 261, 267]. However, at present it is unclear if hydroxyl groups form on the ultra-thin films and how they effect the atomic and electronic structure. The influence of the different metal substrates has also not yet been investigated systematically.

In this chapter we will investigate the lattice mismatch between an ideal mono-layer of ZnO and the metal substrates Ag, Cu, Pd, Ni and Rh. Furthermore we

will address the differences in the atomic structure and thermodynamic stability of pristine ultra-thin ZnO and ZnO on transition metals. The starting point for our investigation will be hypothetical freestanding ZnO films we introduced in Chap. 5.

6.1 COINCIDENCE STRUCTURES

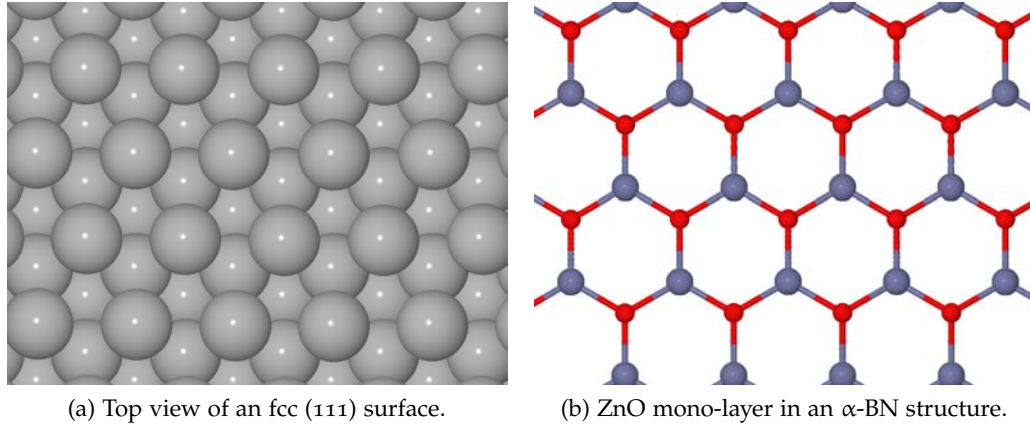


Figure 23: Hexagonal structure of fcc (111) and ZnO (0001/000 $\bar{1}$)

Fcc (111) surfaces as well as mono-layer ZnO in the α -BN structure have a hexagonal symmetry (see Fig. 23). Ideally the "honeycombs" of the ZnO sheet would fit on the "honeycombs" of the fcc (111) surface. The in-plane lattice parameter of these commensurable ZnO mono-layers is easily calculated by dividing the metal (fcc) lattice parameter by $\sqrt{2}$. In Fig. 24 the resulting ZnO lattice parameters are indicated by black vertical lines, labeled with the chemical symbol of the metal. Together with these values we show in Fig. 24 the cohesive energy of a freestanding ZnO mono-layer as a function of the in-plane lattice parameter in the α -BN structure ($dz=0$ Å, see Fig. 24 for definition), with wurtzite-like spacing between Zn and O along the surface normal ($dz=0.63$ Å) and with the atomic positions (z) along the surface normal relaxed. We find that commensurable structures would favor wurtzite-like corrugation because of the strong compression of the in-plane lattice parameter of ZnO for most transition metal (111) surfaces. The only exception is the (111) surface of Pb, which has a larger in-plane lattice parameter than ZnO (see Fig. 24). Too much strain will force the film out of its preferred planar structure towards a wurtzite-like structure [278]. According to the results shown in Fig. 24 the switch from planar to wurtzite occurs at a ZnO in-plane lattice parameter of 3 Å ($\sim 9\%$ strain), indicated by the dashed line. The strain in the films will be minimized when the in-plane lattice parameter of the metal-supported ultra-thin films matches the lattice parameter of freestanding mono-layer ZnO. The most likely coincidence structure can be estimated by min-

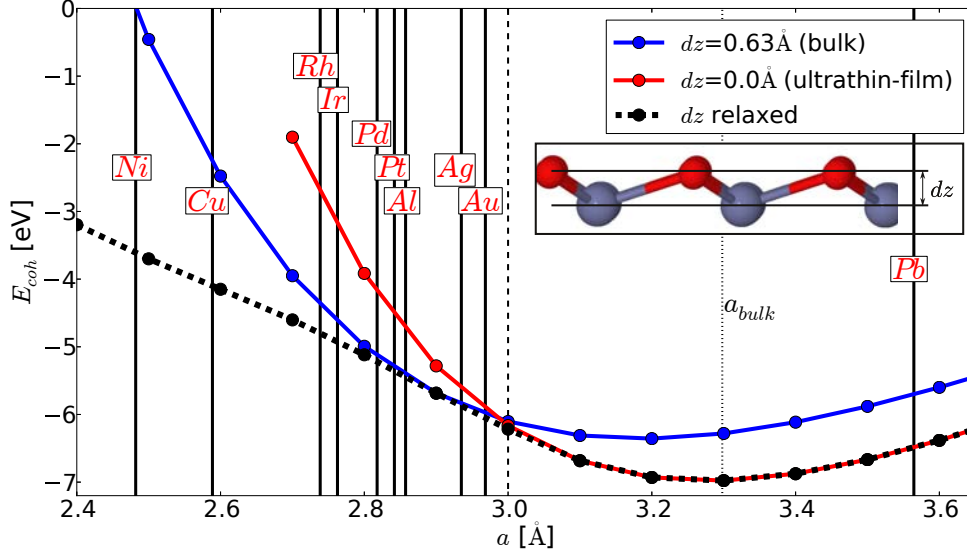


Figure 24: Cohesive energy E_{coh} of an ideal α -BN ($dz=0\text{\AA}$), a wurtzite/zincblende ($dz=0.63\text{\AA}$) and a relaxed ZnO mono-layer as a function of the in-plane lattice parameter a . The in-plane lattice parameters ($a/\sqrt{2}$) of the (111) surface of selected fcc transition metals are indicated by vertical lines.

imizing the strain on the in-plane lattice parameter a of the ZnO mono-layer as compared to the ideal freestanding film:

$$\min_m \left(a_{ZnO} - \frac{m}{m-1} \frac{a_M}{\sqrt{2}} \right). \quad (100)$$

In Tab. 6 the most likely coincidence structures for different transition metal fcc (111) surfaces are calculated from the equilibrium lattice parameters obtained with the PBE xc-functional. To confirm the predicted coincidence structure we consider the formation energy ΔH of the combined system (ZnO mono-layer on metal) as a function of the number of unit cells m along the in-plane lattice vectors of the metal

$$\Delta H = (E_{Tot} - m^2 E_M - (m-1)^2 E_{ZnO})/A. \quad (101)$$

Here E_{Tot} is the total energy of the coincidence slab, E_M is the energy of the 1×1 metal surface, E_{ZnO} is the energy of freestanding 1×1 ZnO mono-layer and A the surface area of the structure. Reference energies and lattice parameters for metals and ZnO are reported in Appendix B. For $m \times m$ metal unit cells with a fixed lattice parameter a_M this results in $(m-1) \times (m-1)$ unit cells of ZnO with a ZnO lattice parameter of $a_{ZnO} = \frac{m-1}{m} \frac{a_M}{\sqrt{2}}$. The formation energy (ΔH) curves for one layer of ZnO on different metals are shown in Fig. 25 and the coincidence structures with the lowest formation energy ΔH are listed in Tab. 7. The agreement with experimental values for sub-mono-layer ZnO islands is good (Ag [259, 237], Pd [270], Pt [159], Au [67], Cu (brass) [229], Ru (0001) [120]). The coincidence structures for which the ZnO in-plane lattice parameter is closest to that of the freestanding structure gives the lowest formation energy. These theoretically predicted coincidence structures depend on the relation between the metal

Table 6: Coincidence structures calculated from the lattice parameters obtained with the PBE xc-functional for fcc metals by eq. 100.

Metal	a_{Exp} [Å]	a [Å]	$\frac{a}{\sqrt{2}}$ [Å]	coincidence	Exp.
Ag	4.08	4.15	2.934	9 / 8	8 / 7 [259, 237]
Pt	3.92	3.97	2.807	7 / 6	6 / 5 [159]
Pd	3.89	3.942	2.787	7 / 6	6 / 5 [270]
Au	4.07	4.158	2.94	10 / 9	8 / 7 [67]
Pb	4.95	5.041	3.565	15 / 14	-
Al	4.04	4.041	2.857	8 / 7	-
Cu	3.62	3.632	2.568	5 / 4	-
Ni	3.52	3.51	2.482	4 / 3	-

and ZnO lattice parameters obtained with a specific xc-functional. For larger coincidence structures (Ag, Au) small changes in the lattice parameters can lead to different predicted coincidence structures, while systems with small coincidence structures (Pt, Pd, Ni, Cu) are less sensitive (see Appendix D for a list of predicted coincidence structures for different xc-functionals). For the metals with lattice parameters larger than 4 Å (Ag, Au) the predicted coincidence structures can differ by up to two digits for the BLYP xc-functional, which was optimized for soft matter. Overall, the differences between xc-functionals are small and we attribute them to small differences in the equilibrium lattice parameters. For metals with lattice parameters smaller than 4 Å (Pt, Pd, Cu, Ni) the predicted coincidences do not depend on the employed xc-functional. In the following sections we will use the PBE xc-functional because of its good agreement with experimental results

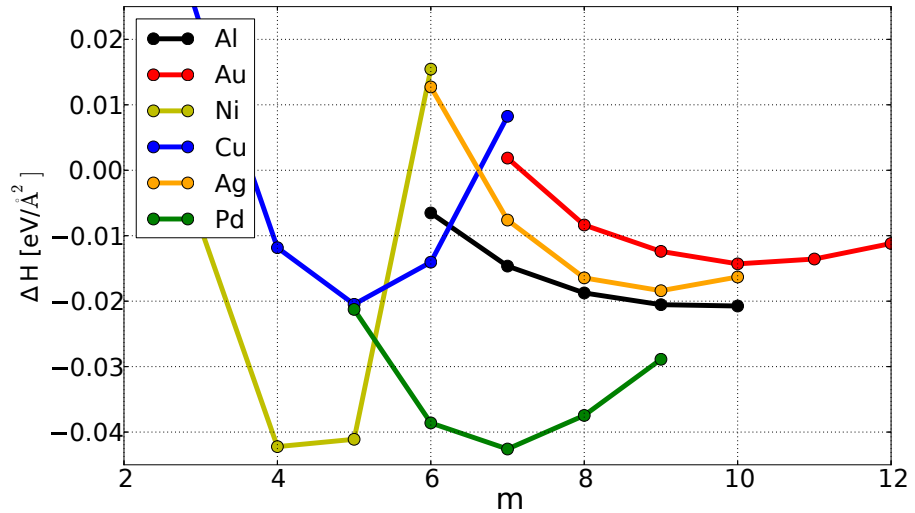


Figure 25: Formation energy of differently sized coincidence structures for selected transition metals.

Metal	strain	coincidence	experimental	$\Delta\Phi$ [eV]	dz [Å]
Ag	0.7%	9 / 8	8 / 7 [259, 237]	0.14	0.127
Pd	0.8%	7 / 6	6 / 5 [270]	0.06	0.237
Pt	0.2%	7 / 6	6 / 5 [159]	-0.04	0.246
Ni	1.0%	4 / 3	-	-0.05	0.266
Cu	-2.0%	5 / 4	-	0.43	0.292
Rh	0.8%	6 / 5	-	0.07	0.337

Table 7: Experimental and calculated (PBE) coincidence structures ($m \times m-1$) for ZnO mono-layers on the (111) surface of different transition metals. dz is the corrugation of the ZnO mono-layer and the strain is the lattice mismatch between adsorbate film and freestanding mono-layer. For ideal bulk wurtzite ZnO dz is 0.63 Å and 0 Å for an ideal freestanding ZnO α -BN mono-layer. $\Delta\Phi$ is the work function change between the bare metal surface and the ZnO mono-layer on the metal substrate.

and its generality [196].

Another aspect, that could influence the coincidence structure observed in experiment is the chemical environment. Different concentrations of Zn on the surface or the O_2 -partial pressure could lead to larger or smaller coincidence structures. We will use the framework of *ab initio* thermodynamics, which we introduced in

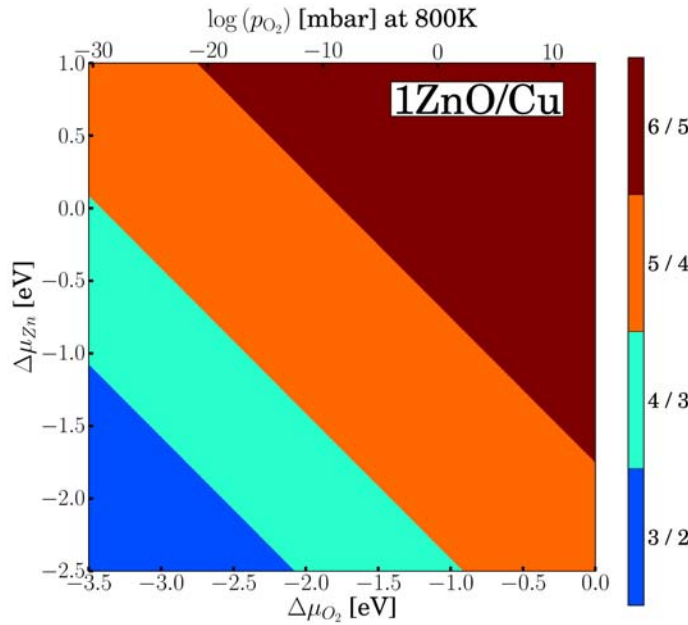


Figure 26: Surface phase diagram for differently sized coincidence structures of one layer of ZnO on Cu (1ZnO/Cu). The size of the coincidence structures is indicated by the color-bar (m/n). The dashed line represents the condition of bulk ZnO as reservoir for Zn/O atoms (eq. 60).

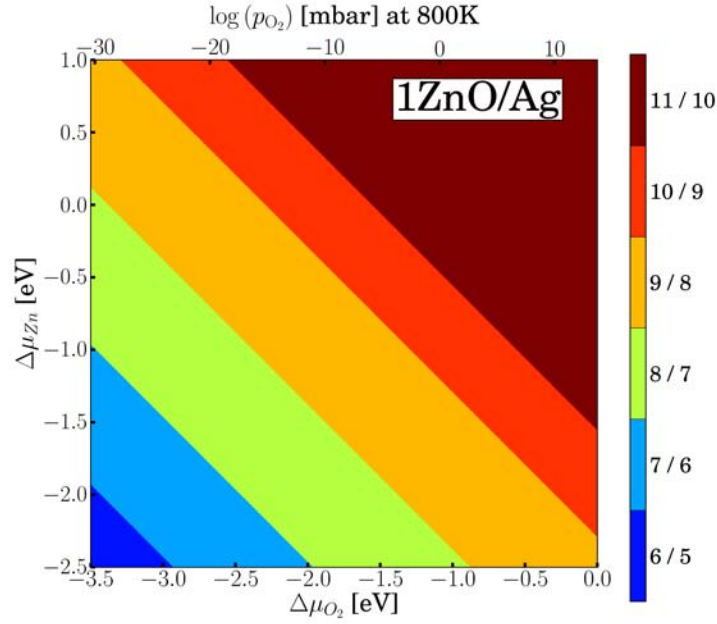
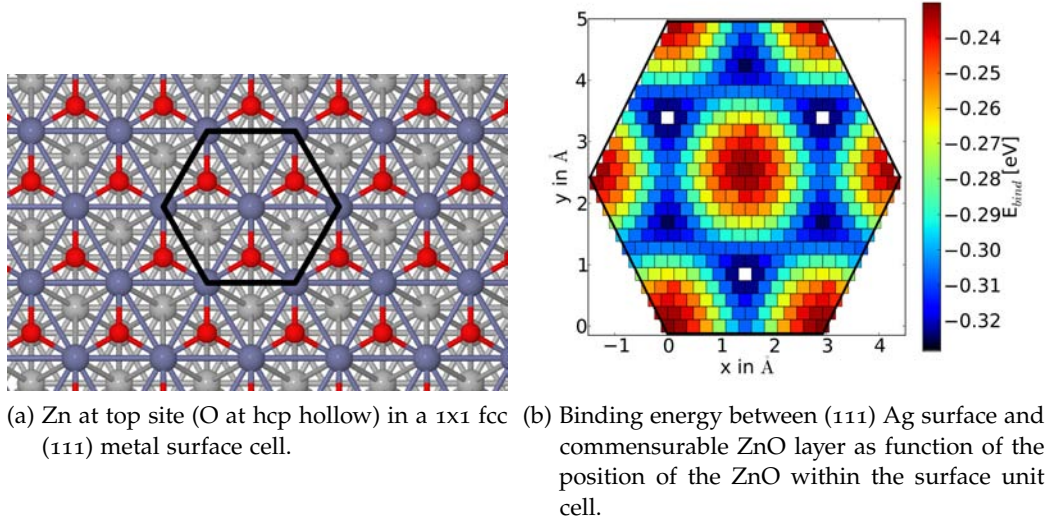


Figure 27: Surface phase diagram for differently sized coincidence structures of one layer of ZnO on Ag (1ZnO/Ag). The dashed line represents the condition of bulk ZnO as reservoir for Zn/O atoms (eq. 60).

Chap. 1.6, to analyze the stability of differently sized coincidence structures. In Fig. 26 a the surface free energy of differently sized coincidence structures for one layer of ZnO on Cu (1ZnO/Cu) is shown as a function of the oxygen and zinc chemical potentials. In Fig. 27 the same surface phase diagram is shown for one layer of ZnO on Ag (1ZnO/Ag). We lifted the condition of bulk ZnO as reservoir for Zn, that is imposed by eq. 60. $\Delta\mu_{Zn}$ and $\Delta\mu_O$ are therefore treated as independent variables. The oxygen chemical potential is translated to partial pressures with the help of thermodynamical tables [178]. As temperature for the partial pressure we chose 800 K, which lies in the vicinity of the temperature used in experiments during the growth of ZnO films by molecular beam epitaxy (MBE) [188, 270, 159, 237] (see Sec. 9 for a more detailed discussion of experimental results). If we would impose the condition of a Zn reservoir via bulk ZnO (eq. 60) we would only find one stable structure (see Tab. 7). The path through the surface phase diagram corresponding to eq. 60 is marked in Fig. 26 and Fig. 27 by dashed lines. Along this path only the coincidence structure found by minimizing the strain in the ZnO film is stable (Ag: 9/8, Cu: 5/4). This coincidence is also the most stable structure in the full phase diagrams of Fig. 26 and Fig. 27 for oxygen partial pressures typically encountered in experiment ($1 \cdot 10^{-10}$ mbar) and for a wide range of Zn chemical potentials (Zn surface concentration). This situation is encountered for all metals discussed previously and we will focus on the coincidence structures presented in Tab. 7 for the following discussions.

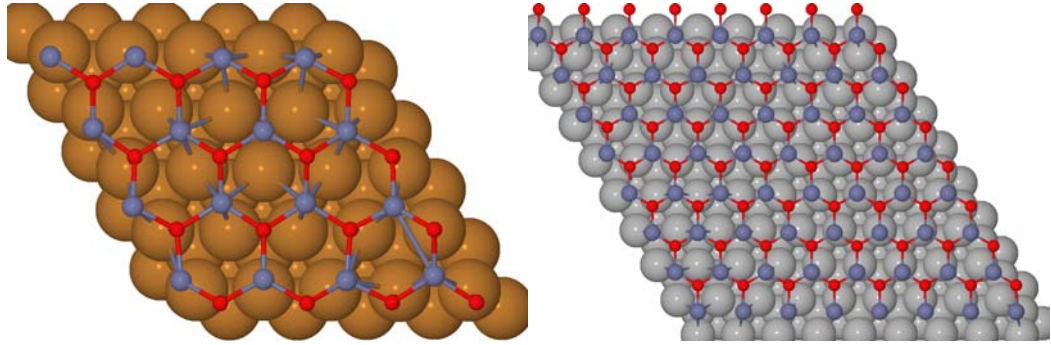
6.2 POSITION IN THE 1X1 SURFACE UNIT CELL

Figure 28: ZnO mono-layer on Ag in a 1×1 geometry.

In addition to the lattice match between ZnO and a given metal discussed in the previous section we must also consider the relative position of the Zn and O atoms with respect to the surface. The most favorable position of Zn and O is best investigated within a 1 by 1 coincidence structure in which ZnO has the same lattice constant as the in-plane lattice constant of the metal. An illustration is shown in Fig. 28 a. First Zn is positioned above the topmost metal atom and O above the metal atom in the third layer (hcp hollow site). Then ZnO is moved within the 1×1 surface unit cell of the metal and the binding energy between metal and ZnO is determined. In Fig. 28 b the binding energy between ZnO and the metal surface is plotted with respect to the positioning of Zn in the Ag 1×1 cell. The data is extended to the hexagonal cell for better assessment of the results. The most favorable geometry is Zn at the hcp hollow site and O at the top site. The fcc bridge site is unfavorable.

6.3 CORRUGATION

We will now return to the discussion of the full coincidence structures found in Sec. 6.1. The ZnO is placed relative to the metal substrate as discussed in the previous section. To distinguish between the α -BN and the wurtzite structure we define the corrugation dz as the mean distance of the O/Zn atoms from the plane spanned by its three surrounding Zn/O atoms. This definition has as limiting cases ideal α -BN, where dz would be 0 Å and wurtzite ZnO with $dz=0.63$ Å. The average dz values for each film are listed in Tab. 7 of the previous section. The corrugation dz does not correlate with the lattice mismatch between metal and film. The freestanding mono-layer would not exhibit any corrugation within the range of residual strains observed for ZnO on the metal substrates (see Fig. 24). We attribute the larger corrugation of ZnO on Cu, Rh, Pd and Pt



(a) Atomic structure of one layer of ZnO on Cu. (b) Atomic structure of one layer of ZnO on Ag.

Figure 29: Atomic structure of ZnO on Cu and Ag.

to chemical effects such as a larger affinity for oxygen and thus a prevalence for oxide formation and the different distances between surface metal atoms and ZnO due to the varying size of the coincidence structures. In Fig. 29, 30 and 31 the corrugation within the super-cell is visualized for Cu and Ag by assigning a color scale to the height of the Zn and O atoms. The corrugation maps for Ni, Rh, Pd, and Pt are shown in Appendix F. For smaller coincidence structures such as ZnO on Cu ($m=5$) (Fig. 29), the structure is rather disordered as compared to ZnO on Ag (Fig. 30 b). The overall corrugation follows the mismatch between the surface metal atoms and ZnO. If Zn is in registry with the metal fcc top site the ZnO-metal distance is smallest. If in registry with the hcp hollow site the ZnO-metal distance is largest. This results in the also experimentally observed Moiré pattern [237]. Closely connected to the corrugation is the mean distance between Zn and O atoms. In the case of ZnO on Cu, the lateral distance between Zn and O reaches the wurtzite limit of 0.63 \AA if the O is located at the fcc top site. For ZnO on Ag the lateral distance between O and the surrounding Zn atoms is about 0.1 \AA and basically follows the mismatch between ZnO and the Ag fcc

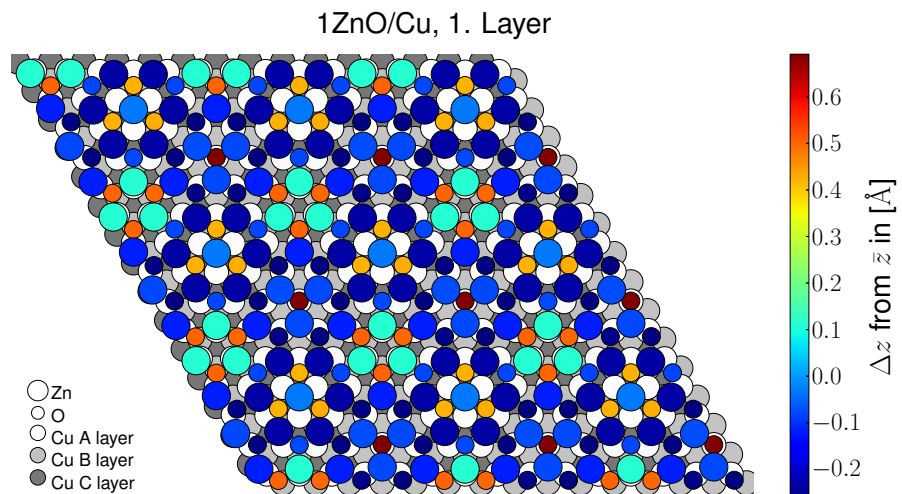


Figure 30: Corrugation map (unit cell tripled) of ZnO on Cu. Each Zn and O atom is assigned a color according to their lateral position.

(111) surface. The ZnO mono-layer on Pd and Pt behaves similar as on Ag, while the behavior on ZnO on Ni is comparable to the Cu case. For ZnO on Rh the corrugation is not as pronounced as for Cu and Ni, but the film is not as flat as in the case of Ag. For ZnO on Pd, Pt, and Au the same behavior is observed.

In summary we find, that the mono-layer ZnO films are characterized by a α -BN structure. For larger coincidence structure, such as ZnO/Ag, ZnO/Au, ZnO/Pd, ZnO/Pd and ZnO/Rh the α -BN structure is retained almost ideally. For smaller coincidences we find a strong corrugation. In both cases the corrugation follows the mismatch between metal surface atoms and ZnO atoms. Therefore, the films exhibit significantly different geometric properties in comparison to the polar ZnO surfaces ((0001)-Zn and (000 $\bar{1}$)-O). They may not be suited as model system for these surfaces. We will proceed to analyze the atomic structure of thicker films and the electronic structure to gain further insight.

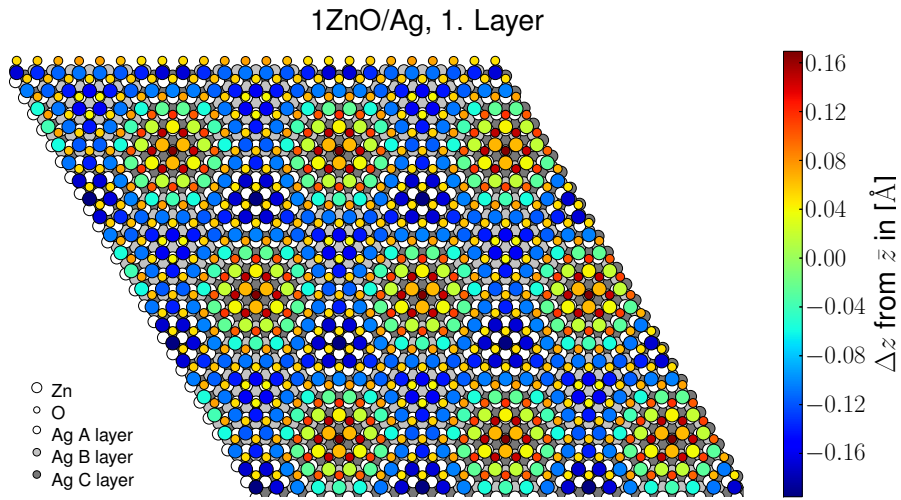


Figure 31: Corrugation map (unit cell tripled) of ZnO on Ag. Each Zn and O atom is assigned a color according to their lateral position.

METAL SUPPORTED MULTI-LAYER ZNO FILMS

After investigating mono-layer films of ZnO on metal substrates we will proceed to look at films with thicknesses of up to 4 layers. In this section we will focus on defect-free, bare ZnO films. The discussion regarding defects and ad-atoms is presented in Sec. 8.1. All calculations, unless stated otherwise, were carried out with the PBE+vdW^{TS} [196, 254] xc-functional with additional parameters by Zhang *et al.* and Ruiz *et al.*. All ZnO films were initialized in an ideal α -BN structure and the forces on all atoms in the films and the top most metal layers were relaxed below $5 \cdot 10^{-3}$ eV/Å. We will first discuss the atomic structure and then proceed to the electronic structure.

7.1 ATOMIC STRUCTURE OF MULTIPLE LAYERS OF ZNO

dz [Å] / Metal	Ag	Cu	Pd	Pt	Rh	Ni
1 Layer						
1. Layer	0.159	0.314	0.228	0.282	0.338	0.334
2 Layers						
1. Layer	0.267	0.471	0.335	0.430	0.430	0.426
2. Layer	0.219	0.348	0.278	0.269	0.305	0.276
3 Layers						
1. Layer	0.426	0.544	0.455	0.553	0.514	0.520
2. Layer	0.388	0.502	0.394	0.459	0.453	0.481
3. Layer	0.285	0.366	0.290	0.290	0.333	0.341
4 Layers						
1. Layer	0.436	0.631	0.589	0.654	0.549	0.577
2. Layer	0.415	0.551	0.493	0.559	0.509	0.425
3. Layer	0.387	0.513	0.451	0.509	0.487	0.444
4. Layer	0.226	0.340	0.292	0.312	0.324	0.267

Table 8: Layer resolved corrugation (see text for definition) for 1 to 4 layers of ZnO on Ag, Cu, Pd, Pt, Ni, and Rh. The corrugation dz for ideal α -BN ZnO would be 0 Å and 0.63 Å for wurtzite ZnO.

With growing number of ZnO layers on the metal substrates the corrugation of the ZnO ultra-thin films increases. The corrugation is defined, as in the previous section, as the mean distance of the O/Zn atoms from the plane spanned by its three surrounding Zn/O atoms. Strain in the ZnO films (Cu, Ni, Pd, Pt) facilitates the formation of a wurtzite-like structure. To illustrate the transition from the α -

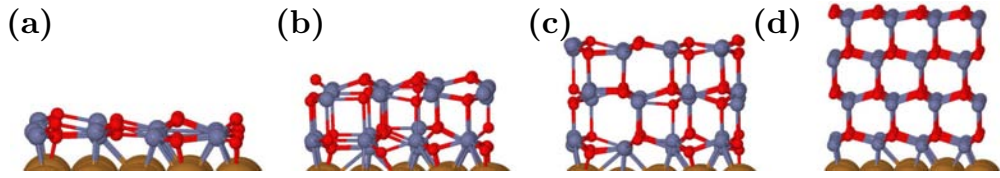


Figure 32: The relaxed structures for hydrogen free ZnO films on Cu (111); a) mono-layer, b) bilayer, c) 3 layers, d) 4 layers of ZnO.

BN structure to a more wurtzite-like structure, the relaxed geometries for ZnO on Cu are shown in Fig. 32, for Ni in Fig. 33, for Ag in Fig. 34, for Pd, Pt, and Rh in Appendix G. The films gradually progress from the α -BN to the wurtzite structure. O-terminated structures (ZnO (000 $\bar{1}$)) always emerge as the dominant surface termination once the ZnO films reach a thickness of 4 layers on any metal substrate we investigated. However, the full transformation to ZnO (000 $\bar{1}$) is not accomplished for all systems within this 4 layers limit.

To investigate the stability of the O-terminated ZnO films with respect to their Zn-terminated form we initialized four layers of ZnO on Cu in the Zn-terminated structure before relaxation. The Zn-termination prevails after the force relaxation. However, the O-terminated structure has a lower total energy. The difference amounts to ~ 20 meV per 1×1 Cu surface unit cell. In Sec. 8.1 we will return to the question of film termination in the context of surface defects and ad-atoms. For now we will focus on the defect-free, bare films.

The corrugation of the multi-layer ZnO films for all six investigated metal substrates is listed in Tab. 8. We calculated the corrugation for each layer of the 1 to 4 layer systems separately. The trend to form wurtzite ZnO is observed for all the investigated metal substrates. For Cu, Pd, and Pt the structure has already transformed to wurtzite at a film thickness of 4 layers. For Ni this is achieved at six layers. For Ag and Rh more than 5 layers are required for the transformation to wurtzite. In Tab. 8 we observe a decrease of the corrugation with increasing distance from the metal substrates. At the surface the O retracts into the surface, reducing the corrugation. This is a well known behavior from the investigation of the bulk ZnO-O (000 $\bar{1}$) surface [162].

While the thicker films (4 and more layers) nearly completely transform to wurtzite, the thinner films (less than 4 layers) exhibit patches of α -BN and simultaneously patches of wurtzite-structure. Morgan *et al.* [171, 169, 170] predicted a transition from the layered α -BN (h-MgO) to d-BCT (body-centered tetragonal) structure, to wurtzite (B₄) for free-standing ZnO films (no substrate). They predict the transition to d-BCT to occur at 8 ZnO layers. The transition to wurtzite

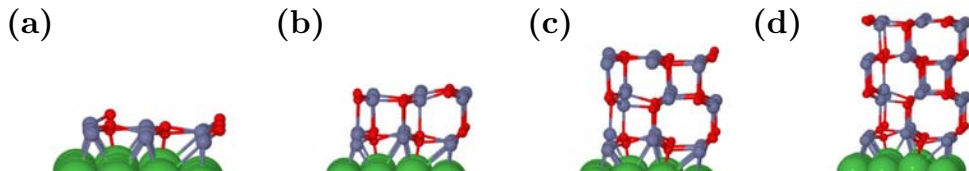


Figure 33: The relaxed structures for hydrogen free ZnO films on Ni (111); a) mono-layer, b) bilayer, c) 3 layers, d) 4 layers of ZnO.

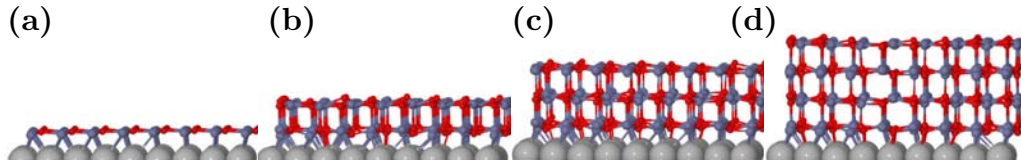


Figure 34: The relaxed structures for hydrogen free ZnO films on Ag (111); a) monolayer, b) bilayer, c) 3 layers, d) 4 layers of ZnO.

would only occur at rather thick films of 56 layers, although the wurtzite film was found to be meta-stable starting from 16 layers. Morgan *et al.* further report that for up to 6 layers of free-standing ZnO the α -BN and d-BCT structures are indistinguishable because the α -BN film slightly buckles during relaxation while the d-BCT film contracts. However, the lack of the trigonal basal plane symmetry in the d-BCT structure leads to an incompatibility with epitaxial growth on (111) metal surfaces.

By applying network theory Demiroglu *et al.* [65] suggest further stable structures, that are similar to the α -BN and d-BCT structure. We could not identify any of the structures proposed by Morgan *et al.* [171, 169, 170] or Demiroglu *et al.* [65] in our calculations. The transition to wurtzite (B₄) leads to a competition between O- and Zn-terminated patches at the interface, that are determined by the distance between Zn/O and metal atoms due to the differently sized coincidence structures. Only for Ni at 3 and 4 layers (Fig. 33) and Rh at 4 layers (Fig. 109) we find a d-BCT structure. For Ni with four layers of ZnO the structure is almost perfectly ordered. The observation of the d-BCT structure is in contrast to the results by Morgan *et al.* [171, 169, 170] for free-standing ultra-thin films where the films are stretched (positive strain) with respect to their free-standing equilibrium lattice parameter. They predict positive strain to facilitate the layered α -BN structure. In our calculations six layers of ZnO on Ni then relax to the wurtzite structure.

In summary the prevalence for oxide formation and the different distances between surface metal atoms and ZnO due to the varying size of the coincidence structures influence the final structure and the transition to wurtzite. The evolution of the electronic structure is of particular interest and will be investigated in the following section.

7.2 ELECTRONIC STRUCTURE OF MULTIPLE LAYERS OF ZNO

We have seen in the previous section that the combination of metal surfaces and ZnO yields interesting effects on the atomic structure of multi-layer films. The electronic structure is affected in a similarly interesting fashion. The overall alignment of the electronic structure of metals and ZnO thin-films has been investigated within the context of Schottky barrier heights in electronic devices with DFT [58]. The authors analyzed the interface electronic structure for metals adsorbed on ZnO in a 1×1 and $(\sqrt{3} \times 2)R30^\circ$ -geometry. The nature of the metal-semiconductor interface was found to be very sensitive to the chemical bonding. Ohmic contacts of Schottky barriers could be observed depending on the ZnO termination and the metal. The authors identified two types of interface states, metal

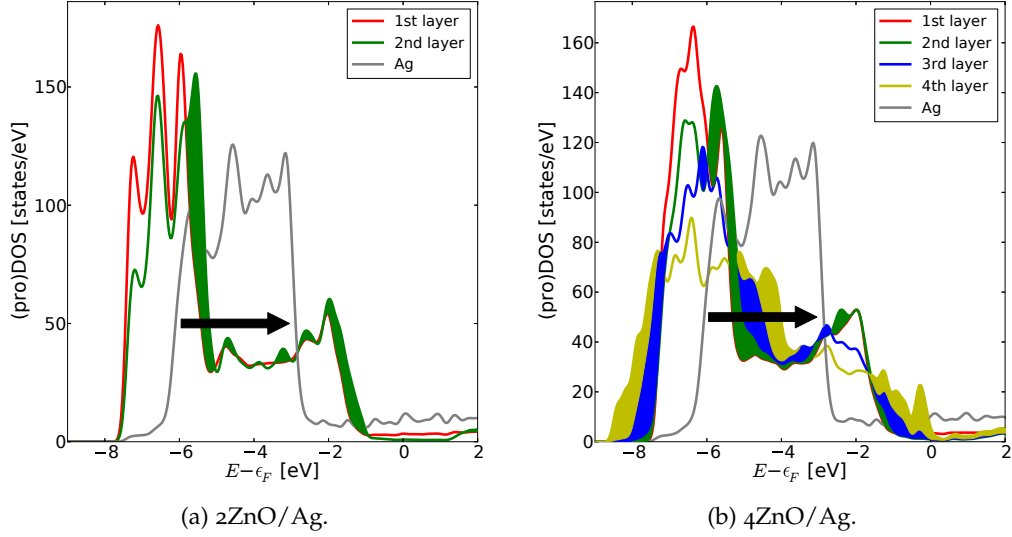


Figure 35: Layer resolved projected density of states for two and four layers of ZnO on Ag obtained with the PBE+vdW^{TS} [196, 254] xc-functional.

induced gap states and energetically well defined states due to chemical bonding. The overall behavior can be understood as an interplay of surface charge and image charge effects [26, 257]. The electric field due to the polar nature of the bulk truncated ZnO (0001) or (000 $\bar{1}$) surface is screened by the metal. An image charge of opposite sign forms in the metal, which results in the creation of an interface dipole. The electric field is mainly due to the negatively charged O ions at the O-terminated side and due to the positively charged Zn ions at the Zn terminated side. The interface dipole between metal and ZnO shifts the oxygen bands up or down with respect to the metal and the Fermi energy.

For our systems of mono and multi-layers of ZnO on fcc (111) transition metals the situation is different; the thickness of the ZnO films and their structure are additional degrees of freedom that have to be considered. We will focus on the influence of film thickness and the choice of the metal substrate. Possible surface reconstructions of the ZnO will be discussed later.

In the previous section we observed the emergence of the wurtzite structure in the ZnO films on different metal substrates for increasing film thickness. We can further investigate this behavior by looking at the density of states (DOS) of these systems. In Fig. 35, Fig. 36, and Fig. 37 the projected DOS obtained with the PBE+vdW^{TS} [196, 254] xc-functional for each layer of a slab with 2 and 3 (4) layers of ZnO on Ag and Cu is shown. The influence of exact-exchange admixture in the DFT-functional, which is quantitative rather than qualitative will be discussed throughout the chapter for the HSE06 xc-functional.

The electronic states of each successive layer are pushed further up in energy. In Fig. 35, 36 and 37 the increase in the projected DOS with respect to the previous layer is indicated by the colored areas. The arrows show the direction of the shift for the Zn 3d bands. The situation is shown schematically in Fig 38. Figure 38 a depicts the isolated system, and Fig. 38 b the combined system. The intrinsic dipole of ZnO leads to a potential difference across the ultra-thin film.

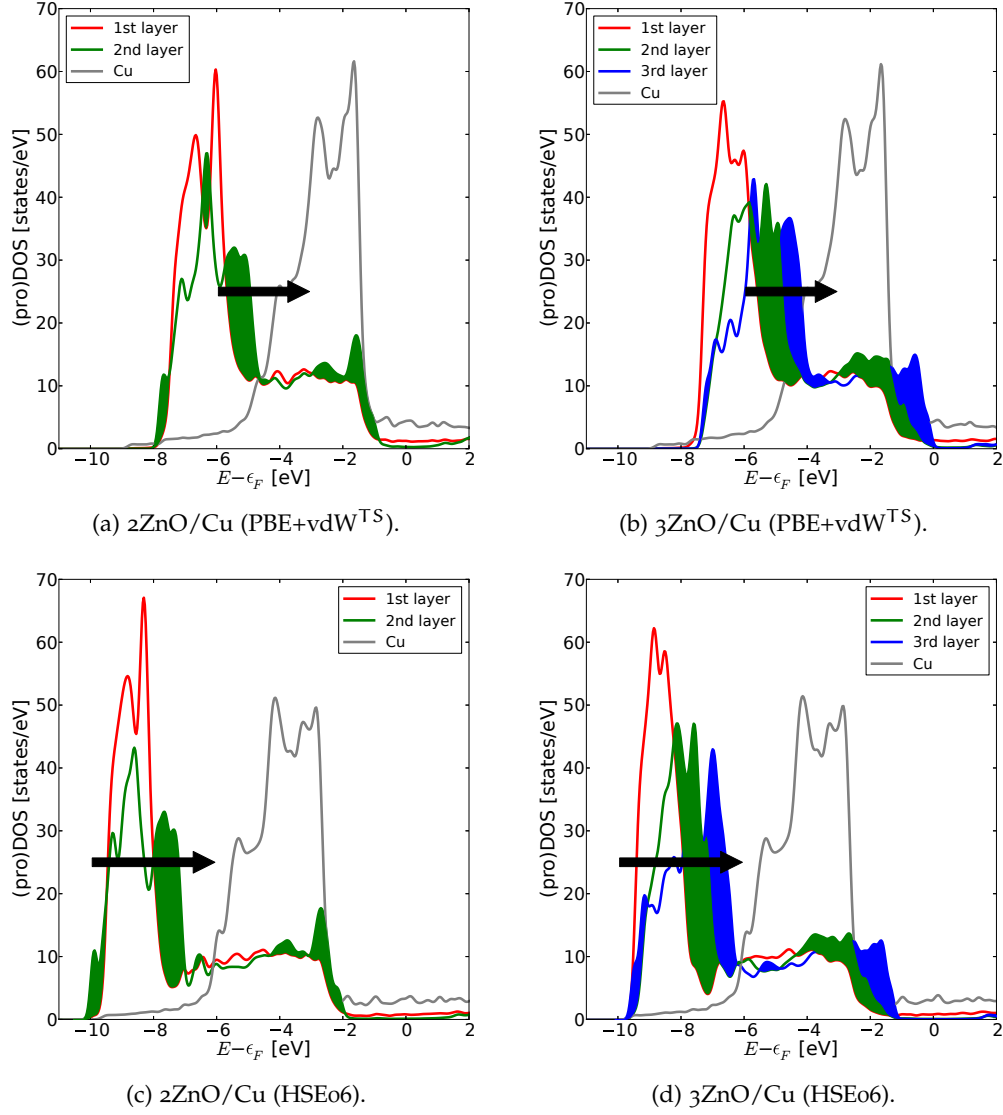


Figure 36: Layer resolved projected density of states for two layers and three layers of ZnO on Cu obtained with the PBE+vdW^{TS} [196, 254] and HSE06 [100] xc-functional.

This mechanism can be understood within the ionic picture of Tasker [249] for the ZnO part of the system. Tasker's model yields $1/2$ electrons (per unit cell) of excess charge at the oxygen side and $(-1/2)$ electrons at the Zn terminated side of a finite ZnO slab. This gives rise to a potential difference (in analogy to a capacitor) between the Zn and the O terminated site of the ZnO slab. The unrealistic divergence with increasing thickness can be removed from the model by transferring half an electron from the O- to the Zn-side. This means that for the ideal bulk-truncated ZnO on the O-terminated side the valence band is not entirely filled and electrons enter the conduction band. It was found by Kresse *et al.* [132] that this model still lacks some rather important details. The states arising from the Zn-surface atoms penetrate deep into the bulk, leading to a charge transfer to these states. The resulting counter-field shifts the O 2p and Zn 4s states to higher

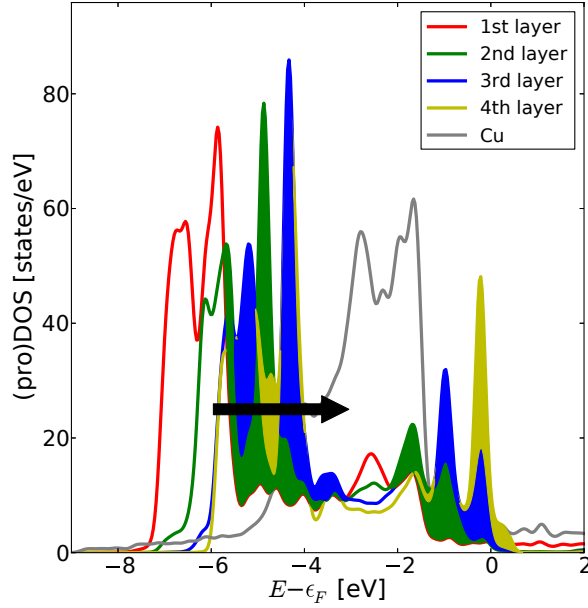


Figure 37: Layer resolved projected density of states for four layers of ZnO on Cu (4ZnO/Cu) obtained with the PBE+vdW^{TS} [196, 254] xc-functional.

energies. This effect is referred to as band bending. Due to the finite nature of the slab approach electrons are transferred (back) from the Zn-terminated site to holes at the O-terminated site. In calculations for the bulk truncated surfaces, this effect is considered an artifact of the finite model [132].

However, the situation for metal supported ZnO thin-films is different. The ZnO mono-layer does not have a wurtzite, but an α -BN structure on metal supports. The bonding is thus different from wurtzite and the ionic model cannot be applied. With increasing thickness the polar character of wurtzite ZnO emerges as the films structurally become more and more wurtzite-like. Charge is again transferred from the Zn-terminated interface to adjacent layers. The resulting field shifts the electronic states upwards until the Fermi energy, provided by the metal, is reached and the film becomes effectively p-type doped at its surface by pinning the electronic states of the top most layer(s) at the Fermi level. Here, p-type doping refers to a position of the Fermi level in the semi-conductor below the center of the band gap or close to the valence band maximum.

This mechanism can be observed e. g. in the layer-projected DOS of 2 to 4 layers of ZnO on Cu and Ag in Fig. 35, Fig. 36, and Fig. 37. For 4 layers of ZnO on Ag in Fig. 35 the electronic states of the 2nd to fourth layer are shifted upwards in energy, relative to the Fermi level and with respect to the electronic states of the previous layer. The portion of the DOS, that has higher density than the DOS of the previous layer, is filled with the color of the respective curve. The shift is observed best at the Zn d-band between -4 and -6 eV. The electronic states of the fourth and topmost layer have reached the Fermi energy, leading to an increased DOS at $E=\epsilon_F$. The states are pinned at the Fermi level, which is provided by the metal. For 4ZnO/Cu in Fig. 37 this effect is even more pronounced. The electronic states of the third layer are already pinned at the Fermi level and for the electronic states of the fourth layer no further upwards shift is observed,

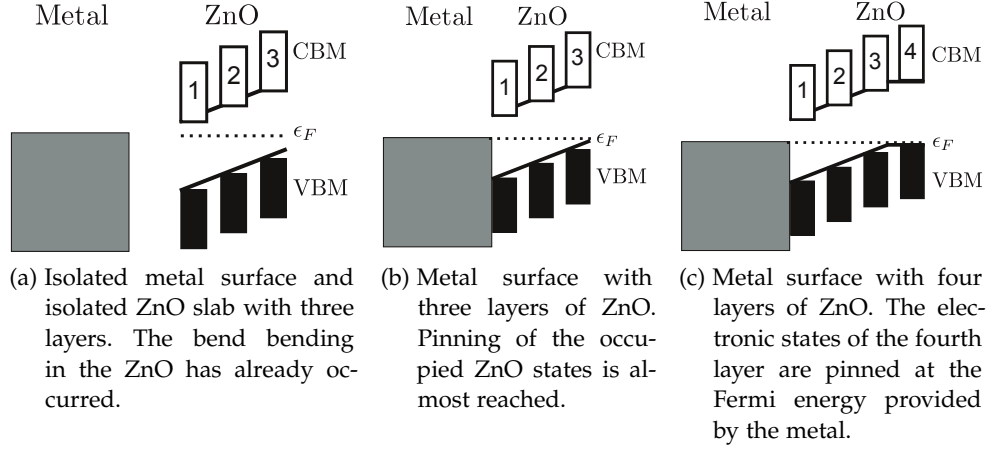


Figure 38: (a) Illustration of the level alignment for the isolated systems, (b) for the combined system, (c) for the combined system with a sufficient number of ZnO layers to achieve pinning.

thus making the surface of these films effectively p-type doped. The effect is qualitatively the same regardless if we apply the PBE+vdW^{TS} or the HSE06 hybrid xc-functional. In Fig. 36 the projected DOS for 2ZnO/Cu and 3ZnO/Cu are shown for both functionals. The band gap of the ZnO is increased by admixture of exact exchange and the onset of the electronic states of the ZnO is about 1 eV lower in energy. However, the upwards shift per layer is quantitatively the same (~ 0.5 eV).

P-type doping is notoriously difficult to achieve in bulk ZnO samples, which are usually intrinsically n-type doped [276]. The origin of both types of doping in bulk ZnO is still under debate [111, 215]. For p-type doping in ZnO only very few candidate shallow acceptors are available. Nitrogen is the most promising candidate for the formation of shallow acceptor levels. The other column V elements are deep acceptors [193]. On the other hand there are quite a few defects that can act as compensating centers for p-type doping [112, 110, 113]. Another fundamental reason for the difficulties to achieve p-type doping in ZnO is that the valence band edge lies too deep below the Fermi level. Attempts to p-type doping will be compensated by other defects before the Fermi energy is shifted far enough [215, 149].

In the mechanism for achieving p-type doping, we describe for the surface of a ZnO thin film, the Fermi level is fixed by the metal substrate. The valence band is moved upwards in energy, towards the Fermi level. This mechanism for achieving p-type doping at the surface of ZnO films could explain experimental reports of p-type doping for ZnO, that are difficult to reproduce [163, 222, 147, 122, 279, 49] or provide a novel way to achieve p-type doping in ZnO. The (thermodynamic) stability of the films under conditions realized by experiment will be investigate in the next section.

Preliminary experimental evidence for the behavior described above is the effect on the measured dI/dV spectra (STS measurement, see Sec. 1.9) as a function of bias voltage for ZnO films of different height reported by Shiotari *et al.* [237]. The authors observe the onset of the signal at lower bias voltages for the thick

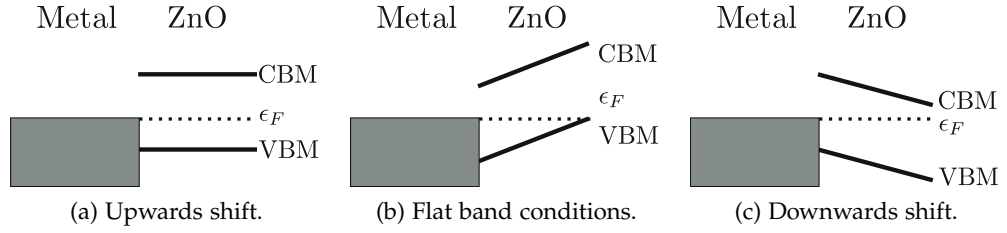


Figure 39: Possible effect of intrinsic dipolar field and surface reconstruction in ZnO thin films on metal substrates. See text for further explanations.

film ("high" ZnO) than for the thinner film ("low" ZnO). The dI/dV spectra can be considered approximately proportional to the (local) DOS of the sample [250]. This is an indication for a (downwards) shift of the unoccupied electronic states of the thicker ZnO film with respect to its thinner version. In our model, derived from our DFT calculations, we had, however, found an upwards shift of the occupied electronic states with increasing film thickness. For the results reported by Shiotari *et al.* [237] two scenarios are plausible, which are depicted in Fig 39. The first scenario is that the electronic states of the "low" ZnO are indeed shifted upwards in energy (Fig 39 a), but the "high" ZnO is (2×1) -H reconstructed (see Sec. 8.1) and no shift occurs (Fig 39 b). The electronic states of the "high" ZnO appear to be shifted downwards in energy with respect to the "low" ZnO. The second scenario is based on a different orientation of the ZnO film. If the ZnO in experiment is (0001) -Zn terminated and not $(000\bar{1})$ -O terminated, the intrinsic field would be of opposite sign. This would shift the electronic states downwards in energy with increasing film thickness. Both scenarios are possible, because a (2×1) -H reconstruction is difficult to determine experimentally and the difference in formation energies for a (0001) -Zn and $(000\bar{1})$ -O terminated films are small (see Sec. 7.1). However, it has to be noted that Shiotari *et al.* [237] mainly focused on other properties of the film, that we will discuss in Sec. 9 and further careful experimental and theoretical analysis is required. Especially the role of the substrate requires further consideration.

The number of layers necessary to reach pinning and effective p-type doping depends on the metallic substrate. More layers are required to reach pinning if the initial valence band maximum of the ZnO ultra-thin film is positioned further below the Fermi level of the metal. In the PBE+vdW^{TS} calculations for the Ag substrate 4 layers are required to reach pinning while for Cu the upwards shift of the ZnO states already stops after three layers (Fig. 35, Fig. 36 a and b, and Fig. 37). The electronic structure of ZnO on Pd shows a similar behavior as on Cu with pinning after three layers (Fig. 117). For Pt and Rh the onset of the pinning occurs already after 2 layers (Fig. 116 and Fig. 118). In the case of Ni five layers are required (Fig. 119).

The potential difference over the extent of the films eventually shifts the valence band minimum on the top layer into resonance with the conduction band minimum of the layer closest to the metal, thus closing the band gap of the ZnO film. For the higher level HSE06 hybrid xc-functional the band gap is larger and hence the band gap closes at a higher number of ZnO layers. This is shown for ZnO on Cu in Fig. 36 c and d (for a direct comparison of PBE and HSE06 see Fig. 40).

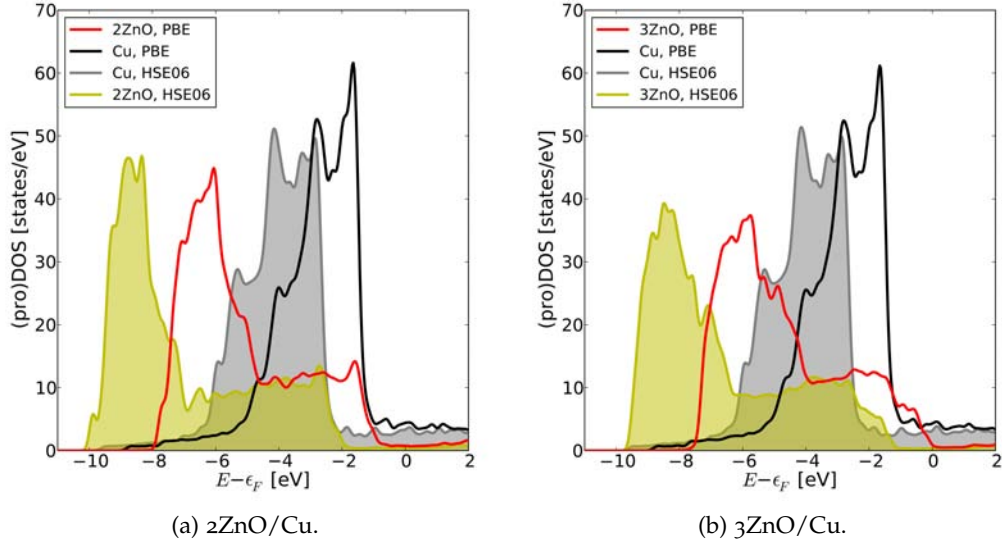


Figure 40: Layer resolved projected density of states for two layers and three layers of ZnO on Cu, direct comparison between the PBE+vdW^{TS} [196, 254] and HSE06 [100] xc-functionals. The Fermi energy is set to zero.

Analogously the pinning and effective p-type doping occurs at higher layer numbers because the initial valence band maximum is further away from the Fermi energy while the upwards shift is similar to the situation with the PBE+vdW^{TS} xc-functional.

In conclusion, we describe a mechanism for achieving effective p-type doping in ZnO thin films. The Fermi level, which is typically moved towards the valence band edge by group V dopants, is kept fixed. The position of the Fermi level is determined by the metal substrate. The valence band is moved toward the Fermi energy, because of the intrinsic field that forms over the extent of the film. The number of layers required for achieving effective p-type doping is determined by the band gap and the initial alignment of the electronic levels of ZnO and metal substrate. The mechanism might help to understand experimental reports of p-type doped ZnO and construct new devices.

In the next section we will analyze the stability of mono- and multi-layer ZnO films on metal substrates with respect to their chemical environment. We will investigate vacancies, ad-atoms and adsorbates. In Sec. 8.1.1 we will return to the topic of effective p-type doping at the surface when we compare the electronic structure of bare ZnO films, which we discussed in this section, with hydrogen terminated ZnO films.

THERMODYNAMIC STABILITY OF ZNO ON METAL SUBSTRATES

The experimental and theoretical work on the polar surfaces, (0001) and (000 $\bar{1}$), of ZnO revealed a manifold of reconstructions and terminations [73, 132, 161, 261, 267, 275, 276]. For the two surface terminations (0001)-Zn and (000 $\bar{1}$)-O different reconstructions were observed. For the ultra-thin films all of them have to be considered, effectively doubling the amount of structures, that have to be investigated. Initially the ultra-thin films have a α -BN structure (see Sec. 5), by choosing a surface preferred reconstruction (e. g. H- or OH-adsorbates) either the (0001) or (000 $\bar{1}$) side is selected. The competition of these structures as a function of the chemical potentials of H₂, O₂ and H₂O has to be investigated.

The most stable and simplest surface reconstruction of the ZnO (000 $\bar{1}$) surface is a (2 \times 1) hydrogen covered surface (50% hydrogen concentration) [161, 267]. The hydrogen saturates the surface bonds and cancels the charge accumulation at the surface. The equivalent structure on the ZnO (0001) surface is a 2 \times 1 hydroxyl (OH) reconstruction. At low oxygen chemical potentials oxygen vacancies could be stabilized. In intermediate chemical potential ranges triangular pits are predicted to form for both surface terminations, although with different stoichiometry. Experimentally they were only observed for the ZnO (0001)-Zn surface. Additionally ring structures and oxygen ad-atoms were predicted and observed [270, 267]. In this section the possible reconstructions will be discussed for 1 to 4 layers of ZnO on Ag, Cu, Pd, Pt, Rh and Ni. The focus will be on the ZnO/Ag and ZnO/Cu systems. We will begin the discussion with H-reconstructions, followed by Zn/O-vacancies and ad-atoms. Ring structures will be briefly addressed afterwards. Finally, we will address OH-reconstructions and present a full surface phase diagram for ZnO on ultra-thin films. In addition we will discuss the experimentally observed 5 \times 5 coincidence structure on Ag (111) [237] and ZnO ultra-thin films on Rh (0001) [120].

8.1 HYDROGEN ADSORPTION

We will now analyze the phase diagrams for different coverages of H on ZnO ultra-thin films on different metals as function of the number of ZnO layers with *ab initio* atomistic thermodynamics (see [226, 214] and Sec. 1.6). We consider the surface free energy γ in eq. 61 (see Sec. 7.1) as a function of the change of the H₂ chemical potential, $\Delta\mu = \mu_{\text{H}} - E_{\text{H}_2}/2$. In all structures we will discuss in this section the number of Zn and O atoms is equal and we can therefore drop the oxygen (and zinc) chemical potential from eq. 61. Reference energies for bulk ZnO and H₂ are tabulated in App. B. First, we will construct the (one-dimensional) phase diagrams by neglecting the vibrational free energy (F^{vib}) and the configurational entropy (S^{conf}). These will be included later in this section. In Fig. 42 a

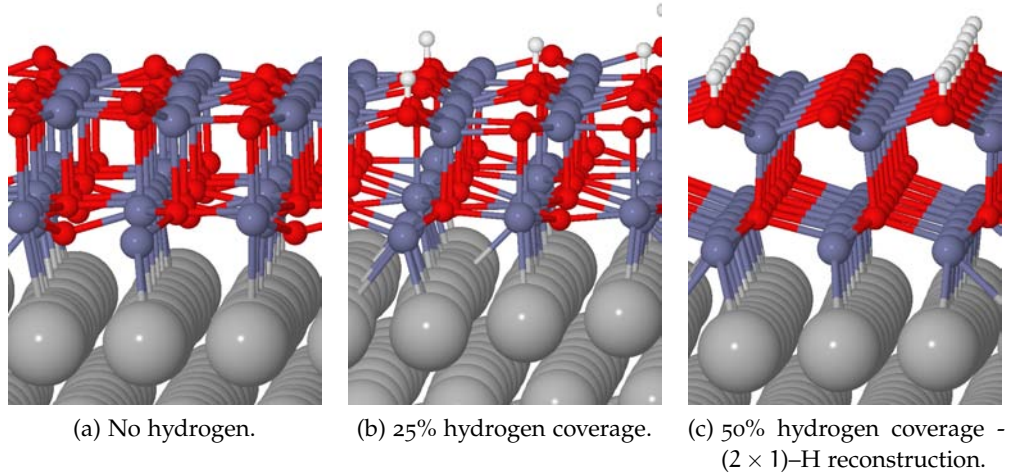


Figure 41: Atomic structure of three different amounts of hydrogen coverage for 2 layers of ZnO on Ag. Only parts of the unit cell are shown.

the result is shown for two layers of ZnO on Ag. The considered surface structures are the bare metal-supported ZnO films discussed in the previous chapters and reconstructions with different amounts of hydrogen adsorbed at the surface oxygen sites. The chemical potential is translated into partial pressures for a given, exemplary temperature at 400K with the help of the ideal gas law and thermodynamic tables [178]. In Fig. 41 a two layers of ZnO on Ag without hydrogen are shown. Fig. 41 b shows 25% of hydrogen coverage on two layers of ZnO on Ag and Fig. 41 c shows the (2×1) -H reconstruction (50% coverage of the surface oxygen sites). The different coverages result in lines with different inclination in these one-dimensional surface phase diagrams. The unreconstructed, bare ZnO on Ag is only stable (lowest line at the considered chemical potential) at low chemical potentials, that are not experimentally accessible at the chosen temperature of 400 K. The reconstruction with the lowest amount of hydrogen is stable over a wide range of low chemical potentials. This region is in the range of typical UHV conditions. The transition to the (2×1) -H reconstruction progresses quickly, lower hydrogen concentrations are only stable in a very narrow window of hydrogen chemical potentials. The (2×1) -H reconstruction is most stable for a wide range of chemical potentials, because the oxygen surface bonds are fully saturated. Higher coverages of hydrogen can only be realized at very high hydrogen chemical potentials, that are not shown in Fig. 41 a.

Now we will discuss the missing terms in the Gibbs free energy (eq. 56). Following the arguments in Sec. 1.6 the pV term can be safely neglected. The approximation of the configurational entropy follows the arguments in Sec. 1.6 and is given by eq. 70. Fig. 42 b shows the previous phase diagram now also including the configurational entropy. It is only included up to 50% coverage. For higher coverages the configurational freedom is further decreased by interaction between the adsorbed H-atoms. This might already be the case for lower coverages and highly symmetric arrangements of the H-atoms [217]. The contribution to the surface free energy of a single hydrogen atom adsorbed at the surface is smallest, but the effect in the phase diagram is the strongest. Due to the low inclination of

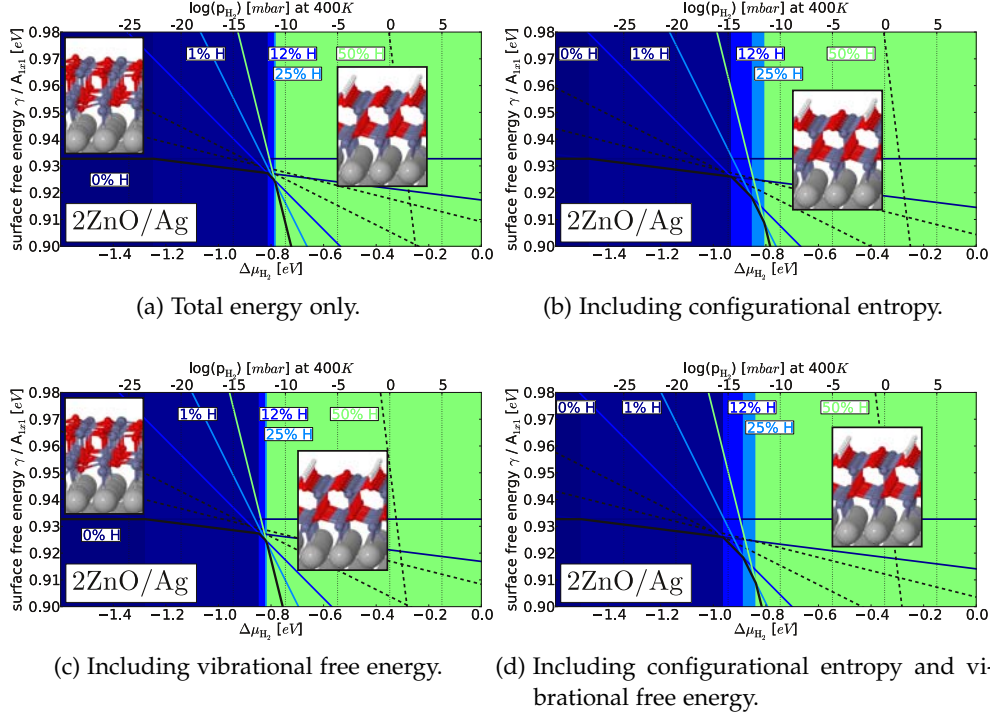


Figure 42: One dimensional surface phase diagrams for two layers of ZnO on Ag, including/excluding the different contributions to the surface free energy.

the line and the fact that the bare surface is not stabilized by the configurational entropy term, the stability range of the bare surface is significantly decreased.

The final contribution to the Gibbs free energy of our surface is the free energy of vibration F^{vib} . Only free energy differences between bulk and surface phases (G^{surf} and g^{bulk}) enter into the surface free energy $\gamma(T, p)$ (eq. 61). As a first approximation for F^{vib} at moderate temperatures ($T < 1000$) only the first term in eq. 75 is evaluated (zero point energy). The vibrational energy contribution of a hydrogen atom adsorbed at a oxygen surface site is approximated by the difference between the experimental H_2 gas phase stretching mode at $\omega_{\text{H}_2} = 4138\text{cm}^{-1}$ [207] and the the frequency obtained by a finite difference DFT calculation. The frequencies we calculated for the O-H stretching mode of hydrogen adsorbed on 1 to 3 layers of ZnO are shown in Tab. 9. The change as a function of layer numbers or metal substrate is small (only the difference to the H_2 gas phase stretching mode enters eq. 75).

The phase diagram including the vibrational contribution is shown in Fig. 42 c. The additional contributions are small. The H reconstructed structures are further stabilized but no qualitative changes are observed. The final phase diagram including all discussed contributions is shown in Fig. 42 d. They are included in the following discussions of this section.

Other H distributions than the highly ordered structures considered for the phase diagrams are close in surface free energy, but less stable. The situation is the same as discussed for ZnO (000 $\bar{1}$) by Kresse *et al.* [132]. The surface phase diagram for two layers of ZnO on Cu is shown in Fig. 43 a. The disordered H terminations (only 50% coverage) are represented by parallel black lines. The con-

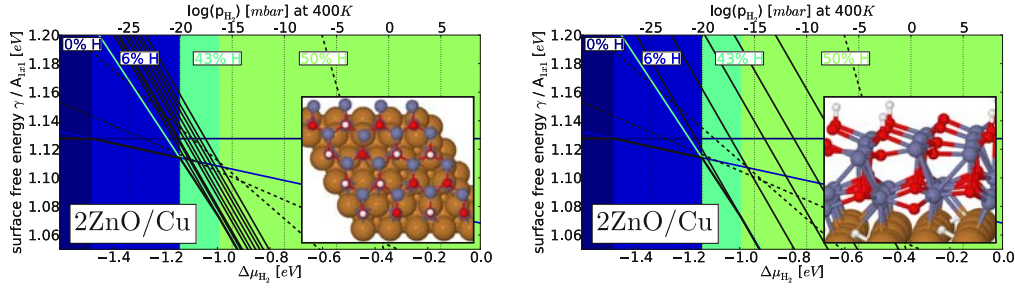
Metal	Layers	H-coverage	$\omega[\text{cm}^{-1}]$	$\frac{1}{2}\hbar\omega[\text{eV}]$
Ag	1	1.5% (1 H)	3632.974	0.2252
Ag	1	50% ((2 × 1)-H)	3643.378	0.2259
Ag	2	1.5% (1 H)	3690.411	0.2288
Ag	2	50% ((2 × 1)-H)	3693.310	0.2290
Cu	1	6.25% (1 H)	3658.597	0.2268
Cu	1	50% ((2 × 1)-H)	3657.129	0.2267
Cu	2	6.25% (1 H)	3688.506	0.2287
Cu	2	50% ((2 × 1)-H)	3701.007	0.2294
Cu	3	6.25% (1 H)	3700.087	0.2294
Pt	1	50% ((2 × 1)-H)	3673.911	0.2278
Pt	2	50% ((2 × 1)-H)	3698.991	0.2293

Table 9: Vibration frequencies for O-H stretching mode of H adsorbed on ZnO on metal substrates.

figuration lowest in energy is the "striped" (2×1) -H reconstruction. In Fig. 43 b the surface phase diagram for two layers of ZnO on Cu is shown with up to 50% of the adsorbed hydrogen at the interface between ZnO and Cu. The atomic structure is shown in the inset of Fig. 43 b. The total amount of H is the same as for the (2×1) -H reconstruction, which is the structure lowest in energy. Every H atom, that is moved from the surface to the interface increase the surface free energy by about 40 meV per 1×1 metal surface unit cell. From this we conclude that hydrogen at the metal/ZnO interface is not a stable structure. Another possible adsorption geometry for hydrogen is the adsorption at the Zn sites. Adsorbing H at the Zn forces the ZnO film into a Zn-terminated (0001) surface structure (Fig. 44 b) as compared to the O-terminated structure for H-adsorption at the O-sites. The structure in Fig. 42 b (2 layers of ZnO on Cu - (2×1) -H) is approximately 0.5 eV per 1×1 metal surface unit cell higher in energy as compared to adsorption at the O-sites.

Another considered geometry we show in Fig. 44 a is zinc-blend stacking. The ZnO mono-layer is simultaneously in the zinc-blend and wurtzite structure, because both structures can only be distinguished from two layers on. The zinc-blend stacking is analogous to the stacking of graphite. A top view for two layers of ZnO with zinc-blend stacking on Cu is shown in Fig. 44 a. This geometry is approximately 150 meV to 200 meV higher in energy than wurtzite stacking, i. e. thermodynamically not stable.

Finally we discuss the evolution of the surface phase diagram with the number of ZnO layers. The surface phase diagrams for 1 to 4 layers of ZnO on Ag are shown in Fig. 45. These results show that for Ag the clean surface as well as the (2×1) -H reconstruction is thermodynamically stable for layer numbers greater than 2 at 400K. Thus the H_2 partial pressure (chemical potential) can be used to select one of the two phases. The mono-layer is very stable in its α -BN structure. Only at intermediate to high chemical potentials first the (2×1) -H reconstructions and



(a) Surface phase diagram including disordered surface adsorption geometries, that are higher in energy than the (2×1) -H reconstruction. The inset shows one exemplary structure of randomly distributed hydrogen (50% coverage).

(b) Surface phase diagram including up-to 50% of the hydrogen present in the (2×1) -H reconstructed unit cell adsorbed at the interface between ZnO and Cu. The inset shows the atomic structure with half of the H atoms in the (2×1) -H reconstruction at the interface.

Figure 43: Surface phase diagrams for 2 layers of ZnO on Cu for different adsorption geometries.

at high hydrogen chemical potential even the full coverage will become stable. With increasing number of ZnO layers, the (2×1) -H reconstructed surface is further and further stabilized. Already for three layers the unreconstructed surface cannot be realized under typical experimental hydrogen partial pressures. This behavior is even more pronounced for the other metals.

For all calculated systems, the partial pressure region for the transition from the clean (α -BN) film to the (2×1) -H reconstruction is shown in Fig. 46. Below the colored bars (dark gray regions, lower pressures), the graphite-like films are stable, above (light gray region, higher pressures) (2×1) -H is stabilized. In the region marked by the bars H-coverages larger than 0% and smaller than 50% are stable. H coverages corresponding to one H per unit cell (determined by the coincidence structure) dominate this transition regime. For Cu and Ni the structure without H and the intermediate H-coverages are reachable only at elevated temperatures. For Pd and Rh only the (2×1) -H reconstruction is within experimentally accessible pressure ranges (also see Ref. [28]).

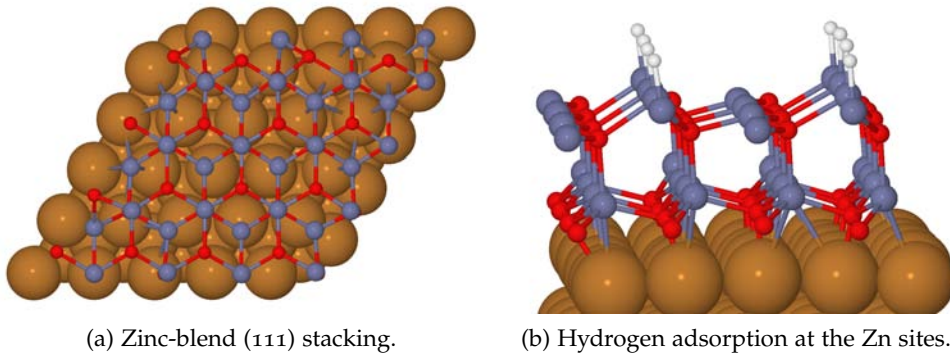


Figure 44: Atomic structure for the a) zinc-blend stacking and b) hydrogen adsorption at the Zn sites.

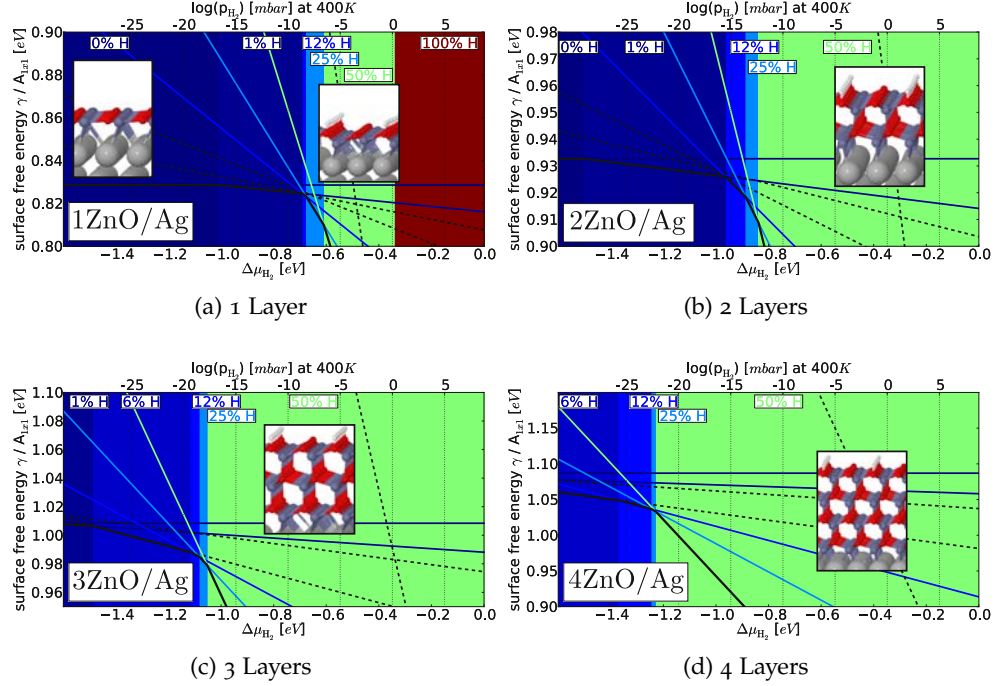


Figure 45: Evolution of the surface phase diagram for 1 to 4 layers of ZnO on Ag.

For increased H pressures, the difference in formation energies between systems with different numbers of ZnO layers is significantly reduced. For (2×1) -H reconstructed structures this difference is very small and thicker layers (3-4 layers) can exhibit a lower surface free energy than 1 or 2 layers of ZnO. The situation is shown for Ag in Fig. 47. The separation in surface free energy for the unreconstructed structure at low hydrogen chemical potentials is quite large. The (2×1) -H reconstruction is stabilized at lower chemical potentials with increasing thickness of the ZnO. Except for the mono-layer it is the most stable structure throughout most of the chemical potential range considered. The energetic separation for the (2×1) -H reconstructed ZnO films is low. The 3 and 4 layer ZnO films are lower in surface free energy than 1 and 2 layers. Under experimental conditions, some of these structures could be kinetically stabilized and further growth be hindered [159]. The formation of the (2×1) -H reconstruction, although thermodynamically most stable, could be blocked by an energy barrier for the dissociation of H_2 at the surface.

8.1.1 Electronic structure of the (2×1) -H reconstruction.

In Sec. 7.2 we discussed the pronounced upwards shift for the electronic states of each successive layer in the unreconstructed ZnO films on the metal substrates. The situation is shown for 4 layers of ZnO on Ag in Fig. 48 a and schematically in the inset of the same figure. If we now look at the projected density of states of the ZnO ultra-thin films saturated with H we can analyze their fundamentally different behavior as compared to the unreconstructed films. Figure 48 b shows the projected DOS of 4 layers of ZnO on Ag with 50% H-coverage $((2 \times 1)$ -H).

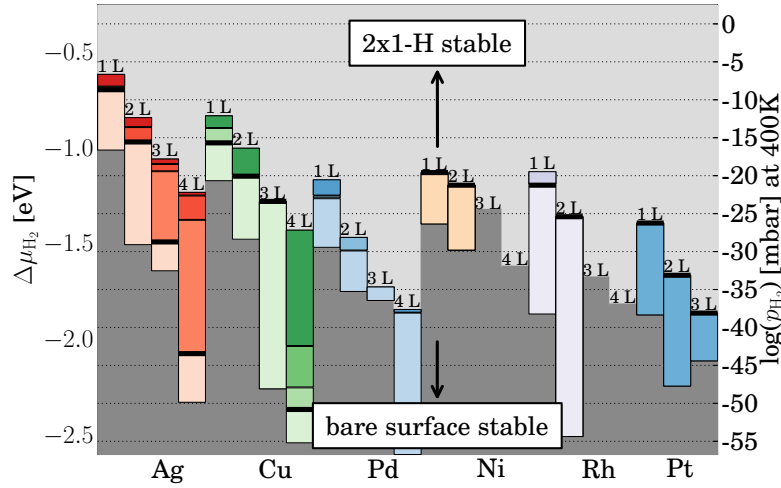


Figure 46: Surface free energy γ per (1x1) surface unit cell area as function of the change in chemical potential $\Delta\mu$ (see eq. 61) for 1 to 4 layers of ZnO (L) on Ag, Cu, Pd, Ni, Rh and Pt (111) with different coverages of H. The partial pressure, as calculated from thermodynamical tables, of H_2 at 400 K is plotted on the right axis. The colored area indicates the transition region between the ultra-thin film without H (dark gray) and the $(2 \times 1)\text{-H}$ with 50% H coverage (light gray).

The onset of the Zn d levels exhibits no shift between successive layers. The first layer being an exception due to its proximity to the metal. In the inset of Fig. 48 b the situation is shown schematically. The bonds at the surface are saturated by H, providing electrons. The intrinsic dipole moment of ZnO is quenched, no polarization of the film occurs and the position of the ZnO electronic states stays constant throughout the ultra-thin film. The position of the electronic states of the ZnO ultra-thin films with respect to the Fermi level, provided by the metal,

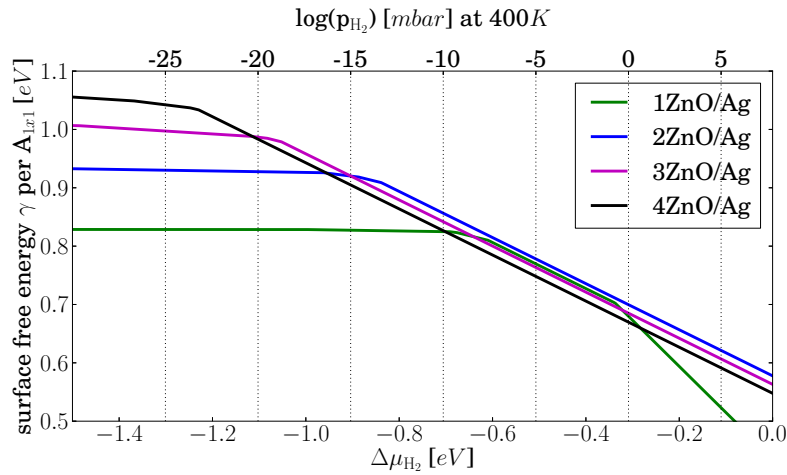


Figure 47: Comparison of the surface free energy of 1 to 4 layers of ZnO on Ag covered with different amounts of H. The colored lines correspond to the black lines in Fig. 45 a–d.

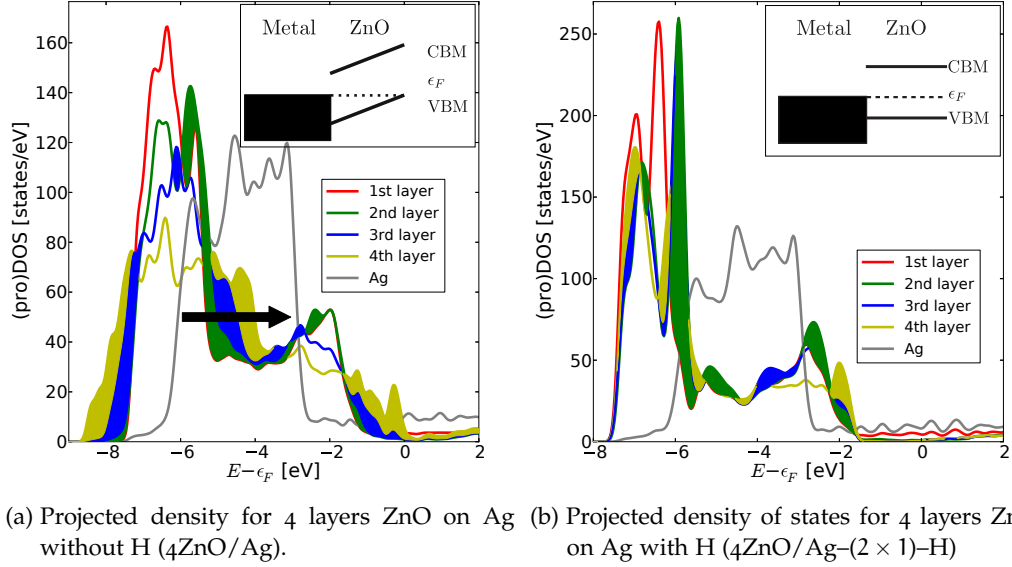


Figure 48: Projected density of states for 4 layers (8×8) ZnO on (9×9×4) Ag with and without H. The densities are projected on each successive layer of ZnO. The metal is shown in gray. The behavior of the electronic states in each layer is shown schematically in the insets.

is highly system dependent. The discussion of the mechanism governing the alignment of the electronic structure of ZnO with respect to the metal was already discussed in Sec. 7.2 and further information can be found in the literature [26, 257, 58]. The projected density of states for 2 and 4 layers of ZnO on all the previously discussed transition metals can be found in Appendix J.

In order to test the accuracy of our calculations we calculated the atomic and electronic structure for three layers of (2 × 1)-H reconstructed ZnO on Cu with the HSE06 [100] hybrid xc-functional. The ZnO film on Cu was initialized in an α -BN structure and as a first step we relaxed the geometry using the PBE xc-functional. Finally, we relaxed the geometry with the HSE06 xc-functional and calculated the projected density of states. The differences in the atomic structure are small. The projected DOS for three layers of ZnO on Cu calculated with PBE and HSE06 are compared in Fig. 49 and Fig. 50. The overall agreement between both calculations is rather good. The structure of the projected DOS for both xc-functionals shows no qualitative differences. The Zn d-band is shifted by -2 eV to lower energies for HSE06, while higher lying states are only shifted by -1 eV. We can conclude, that for our systems the accuracy of PBE+vdW^{TS} is sufficient to describe the atomic and electronic structure.

Finally, we want to compare the electronic structure of the (2 × 1)-H reconstructed ZnO to unreconstructed ZnO (see Sec. 7.1) on metal substrates and the (2 × 1)-H reconstructed ZnO surface without substrate. The comparison of the density of states for the (2 × 1)-H reconstructed ZnO (000 $\bar{1}$) surface and the ZnO films on the metals in Fig. 51 b shows that systems with 4 and more layers already resemble the (2 × 1)-H reconstructed ZnO (000 $\bar{1}$) surface very well. However, the films without H (Fig. 51 b) retain a unique character. The electronic structure differs from the ZnO (000 $\bar{1}$)-(2 × 1)-H surface and the geometry combines aspects

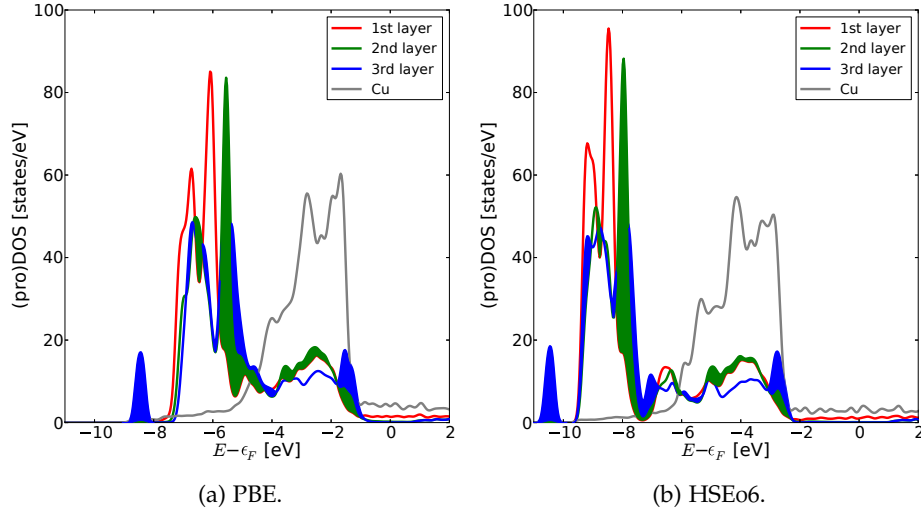


Figure 49: Projected density of states for three layers of ZnO on Cu with H, $3\text{ZnO/Cu}-(2 \times 1)\text{-H}$. The DOS is projected on the individual layers.

of wurtzite and $\alpha\text{-BN}$ (see Sec. 7.1).

We conclude that the choice of metal and the H_2 partial pressure are two additional degrees of freedom to select between unreconstructed ultra-thin ZnO films, that differ from bulk ZnO, and films $((2 \times 1)\text{-H}$ reconstructed) that resem-

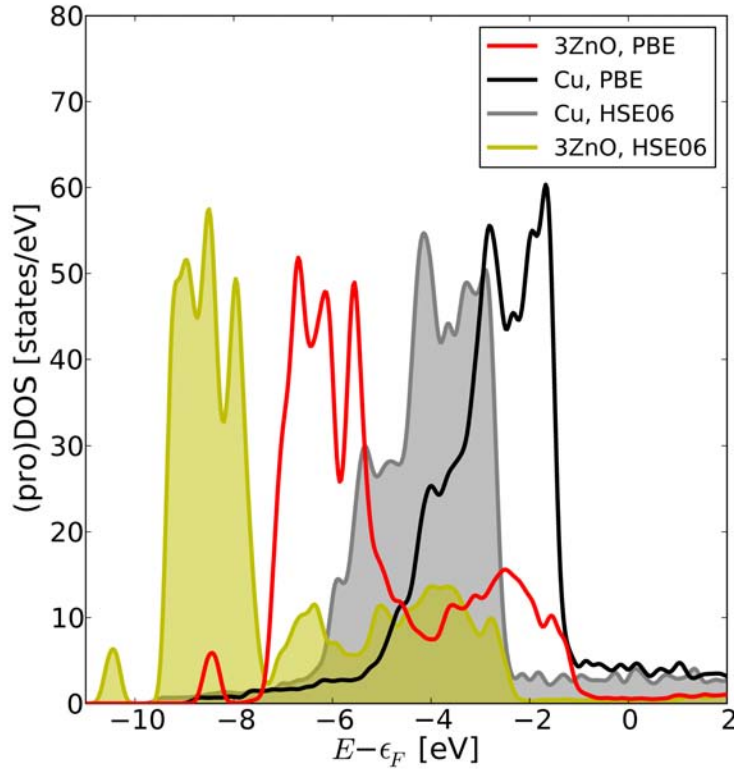


Figure 50: Projected density of states for three layers of ZnO on Cu with H, $3\text{ZnO/Cu}-(2 \times 1)\text{-H}$. Direct comparison between the PBE and HSE06 xc-functionals.

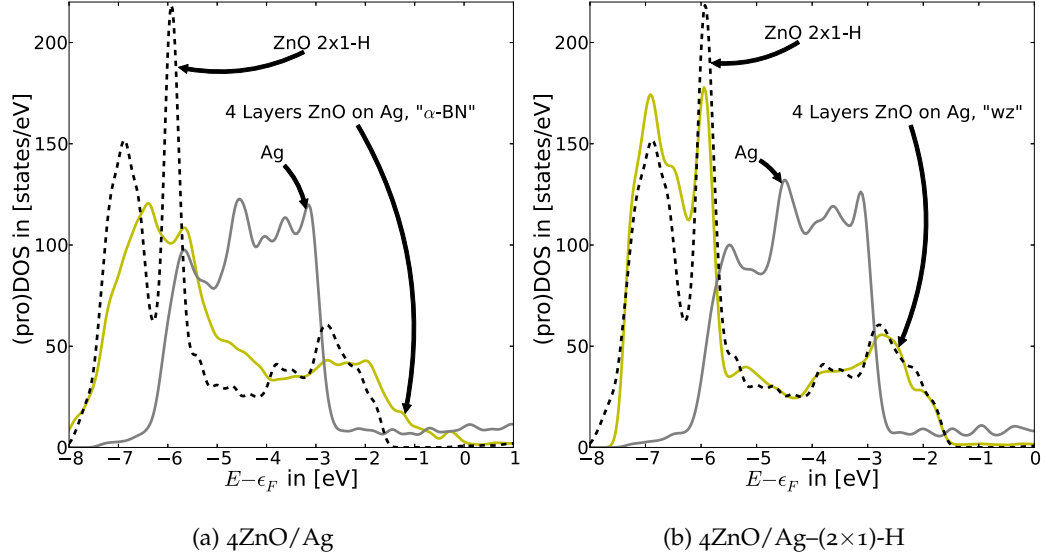


Figure 51: (a) Comparison of projected DOS of 4 Layers ZnO on Ag (4ZnO/Ag) without H and with 50% H coverage with the DOS of a ZnO (2×1) -H surface slab. The projected DOS of the ZnO (2×1) -H surface is shifted by -1eV in (a) and (b) with respect to their Fermi level.

ble wurtzite ZnO. This dual character make metal-supported thin films particularly interesting. Under certain conditions these films resemble novel materials with unique properties whereas under different conditions they could serve as important models for the study of the ZnO $(000\bar{1})$ - (2×1) -H surface.

8.2 VACANCIES AND AD-ATOMS

In Sec. 8.1 we have seen that the structure of the films is typically neither the structure of the Zn-terminated nor the O-terminated ZnO surface. It is rather a mixture of both. If we offer hydrogen to the films, the O-terminated (2×1) -H reconstructed surface forms. A similar behavior is expected for O/Zn vacancies and ad-atoms. Within the ionic model of Tasker [249] O vacancies and Zn ad-atoms would stabilize the $(000\bar{1})$ -O surface [161, 267], while O ad-atoms and Zn vacancies would achieve the same for the (0001) -Zn surface [132, 261]. We will first investigate the thermodynamic stability of O vacancies and ad-atoms before progressing to their Zn counterparts. Afterwards we will discuss more extended surface reconstructions and hydroxyl adsorption. Due to the number of surface reconstructions and their fundamentally different structures, we will neglect contributions from the vibrational free energy and entropic contributions in the following discussion, unless stated otherwise.

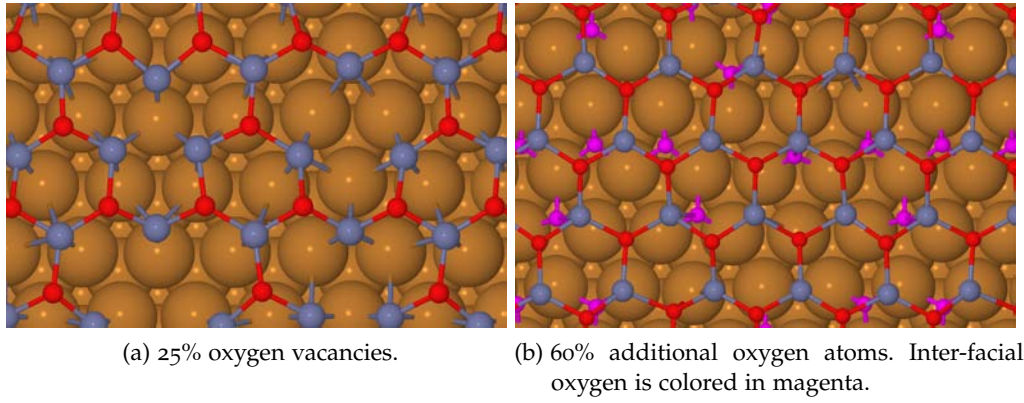


Figure 52: Atomic structure for oxygen defects in one layer of ZnO on Cu.

8.2.1 O vacancies and ad-atoms

By removing oxygen atoms from the surface, excess electrons are removed and the surface energy is reduced. For the distribution of the vacancies for a given vacancy concentration we will use the structures found by Wahl *et al.* for the ZnO (000 $\bar{1}$)-O surface [267]. Wahl *et al.* calculated the formation energy of all possible surface vacancy distributions for a 4×4 ZnO (000 $\bar{1}$)-O surface slab. The structures lowest in energy are the input for our calculations. For a detailed analysis a structure search based on a cluster expansion would be required for ZnO on the different metal substrates. This is in general possible, but not in the scope of this dissertation. We will therefore restrict the pool of investigated structures to those of Ref. [267]. The structure of mono-layer ZnO on Cu with $1/4$ of the oxygen atoms removed is shown in Fig. 52 a. When more than $1/4$ of the oxygen atoms are removed the remaining oxygen atoms start to form hexagonal ring structures, that eventually start to break up for even higher oxygen deficiencies.

The equivalent O induced mechanism for the ZnO (0001)-Zn surface are oxygen ad-atoms. One layer of ZnO with 60% additional oxygen is shown in Fig. 52 b. The oxygen ad-atoms were initially distributed randomly on top of the ZnO layer. For all systems the oxygen relaxes to the interface between metal and ZnO. For 100% of additional oxygen the film "floats" on top of these oxygen atoms. The only exception of this behavior is for the case of a gold substrate. Here the oxygen remains on top of the ZnO film. The structures discussed in this section all contain the same amount of Zn in their super cell. Structures with increased or decreased Zn- and O-concentration are discussed in Sec. 8.2.3 and 8.3.

The surface free energy is given in eq. 61 as a function of the change in chemical potential of oxygen $\Delta\mu_{\text{O}}(T, p_{\text{O}})$ and Zn $\Delta\mu_{\text{Zn}}(T, p_{\text{Zn}})$. Because all structures contain the same amount of Zn ($N_{\text{Zn}} = \text{const.}$), we can chose a value for $\Delta\mu_{\text{Zn}}(T, p_{\text{Zn}})$. We set $\Delta\mu_{\text{Zn}}(T, p_{\text{Zn}}) = -1$ eV. The formally two-dimensional equation is reduced to one dimension.

The surface phase diagram for one layer of ZnO on Cu is shown in Fig. 53 and for one layer of ZnO on Ag in Fig. 54. At low oxygen chemical potentials vacancies are the prevalent structure for both systems. They are more stable for ZnO on Cu. Oxygen vacancies in ZnO on Cu are stable until -2.4 eV of oxygen

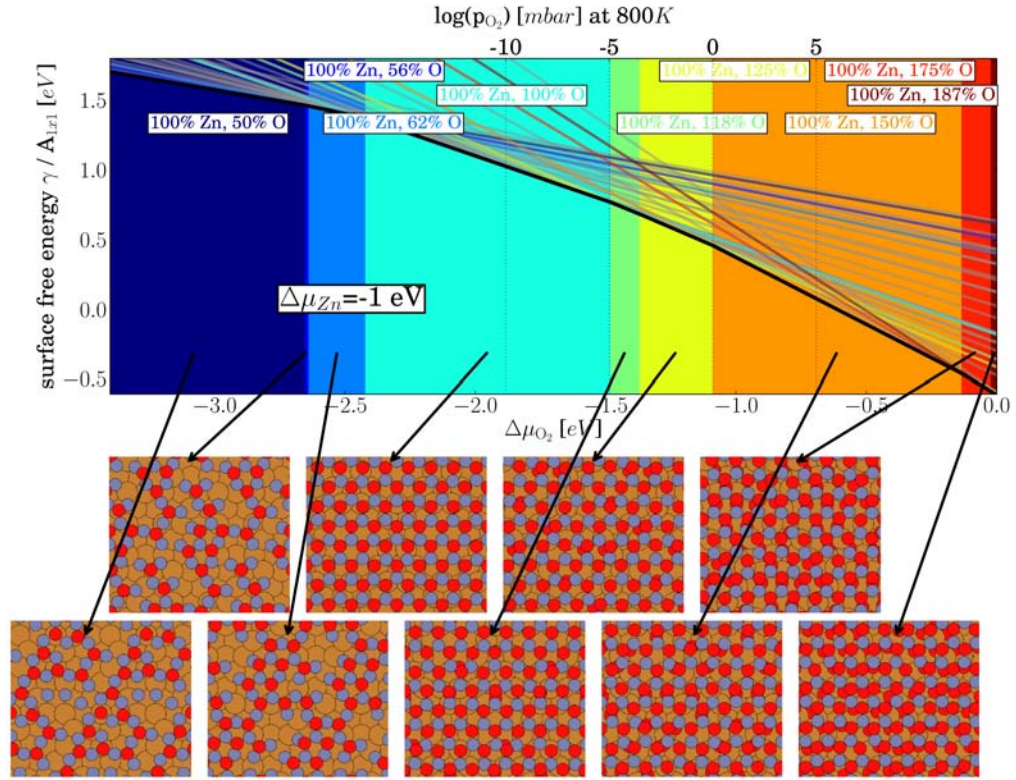


Figure 53: Surface phase diagram (eq. 61) for one layer of ZnO on Cu considering oxygen defects only. The oxygen amount in the system increases with the oxygen chemical potential. The lines of the stable structures at a certain chemical potential are colored. Thermodynamically unstable structures are represented by gray lines. The section of the line of the energetically lowest structure at a given oxygen chemical potential is colored in black. The stability region of the structures lowest in energy are marked in the same color as the line. The structures are labeled by their Zn and O content within the super cell. Below the phase diagram top views of the thermodynamically stable structures are shown, ordered by oxygen chemical potential. The chemical potential of oxygen is translated to partial pressures at the exemplary temperature of 800 K with the help of thermodynamical tables [178]. The Zn chemical potential is set to $\Delta\mu_{\text{Zn}}(T, p_{\text{Zn}}) = -1$ eV.

chemical potential when the defect free mono-layer is stabilized. On Ag the ideal mono-layer is very stable. Only below -3.0 eV oxygen defects are stabilized. A similar situation is observed for oxygen ad-atoms. Pristine ZnO films on Ag are stable up to -0.25 eV, on Cu incorporation of oxygen starts at -1.5 eV of oxygen chemical potential. The oxygen concentration at the interface is increased quickly with the chemical potential. Additional 50% of oxygen are stable for a wide range of oxygen chemical potentials for ZnO on Cu.

We conclude that the stability of oxygen defects in mono-layer ZnO depends on the oxygen affinity of the metal substrate. For Cu it is high, for Au it is very low. For the other investigated metals an intermediate situation is observed. In the next section we will extend our investigations to Zn defects and ad-atoms.

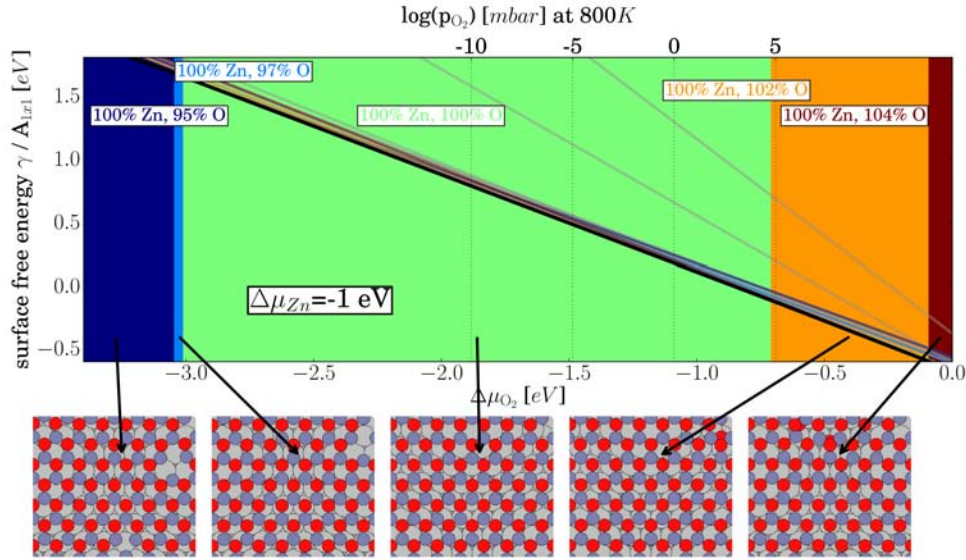


Figure 54: Surface phase diagram for one layer of ZnO on Ag considering oxygen defects only. See caption of Fig. 53 for further explanations.

8.2.2 Zinc defects and ad-atoms

Alternate reconstruction mechanisms for the ZnO (000 $\bar{1}$)-O and ZnO (000 $\bar{1}$)-Zn surface are Zn ad-atoms and Zn vacancies. For the ZnO (000 $\bar{1}$)-Zn surface the removal of 25% of the surface Zn atoms should compensate for the excess electrons in the surface state. For the ZnO (000 $\bar{1}$)-O surface the surface state can be saturated by additional Zn ad-atoms. For the determination of the surface phase diagrams we consider the surface free energy as a function of the change in Zn chemical potential $\Delta\mu_{\text{Zn}}$. The change in oxygen chemical potential is (arbitrarily) fixed to $\Delta\mu_{\text{O}_2}(T, p_{\text{O}_2}) = -1$ eV, because the amount of oxygen atoms in the super cells of all considered structures is constant. Again, the formally two-dimensional equation is reduced to one dimension. The chemical potential of Zn can be understood as a measure for the concentration of Zn at the surface. The surface phase diagram considering Zn defects for one layer of ZnO on Cu

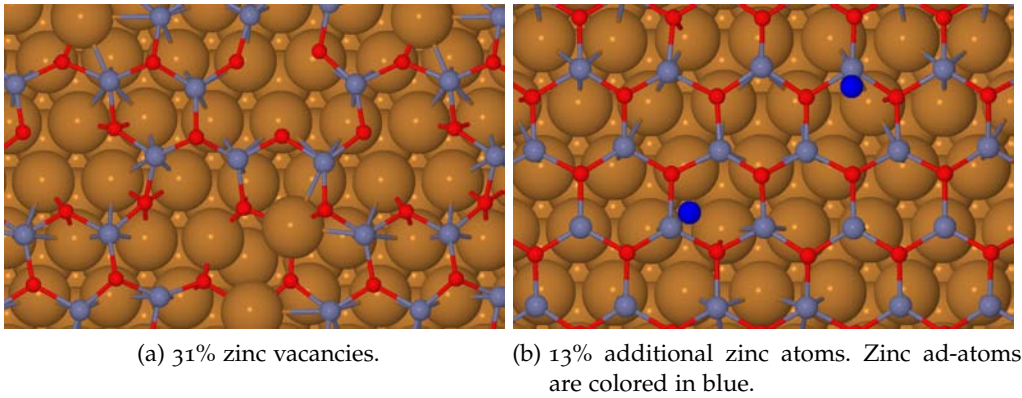


Figure 55: Atomic structure for zinc defects in one layer of ZnO on Cu.

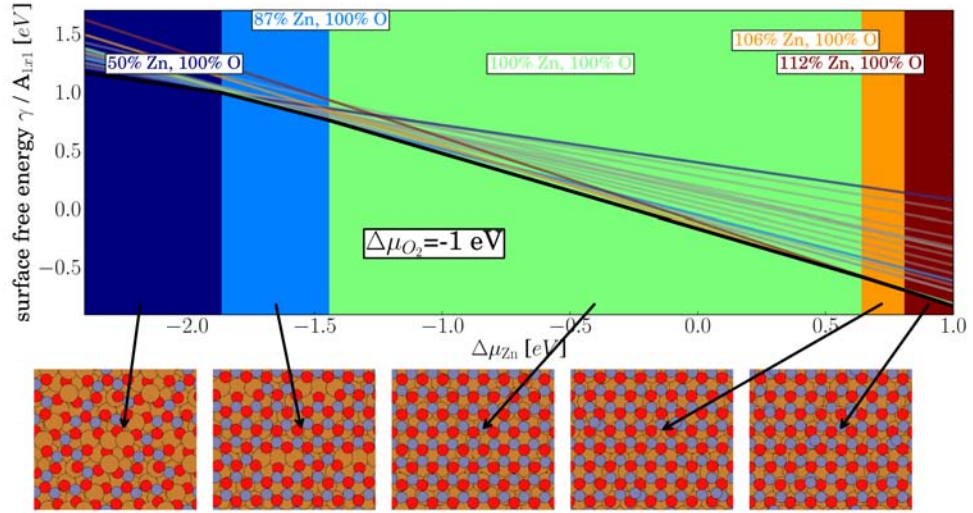


Figure 56: Surface phase diagram for one layer of ZnO on Cu considering zinc defects only. See caption of Fig. 53 for further explanations.

is shown in Fig. 56 and for ZnO on Ag in Fig. 57. It is evident, that Zn defects are less stable than O defects. For Cu, Zn vacancies are observed until -1.4 eV of Zn chemical potential. For Ag they do not show up in the selected window of chemical potentials. Analogously, Zn ad-atoms are less stable than O ad-atoms. They adsorb on top of Zn surface sites and are only observed at very high Zn chemical potentials greater than zero. At this point Zn starts to wet the surface. A very high concentration of Zn is required to form Zn ad-atoms during film growth. The observation, that Zn ad-atoms and vacancies are much higher in energy than defect free ZnO is in agreement with previous work on the (000 $\bar{1}$)-O

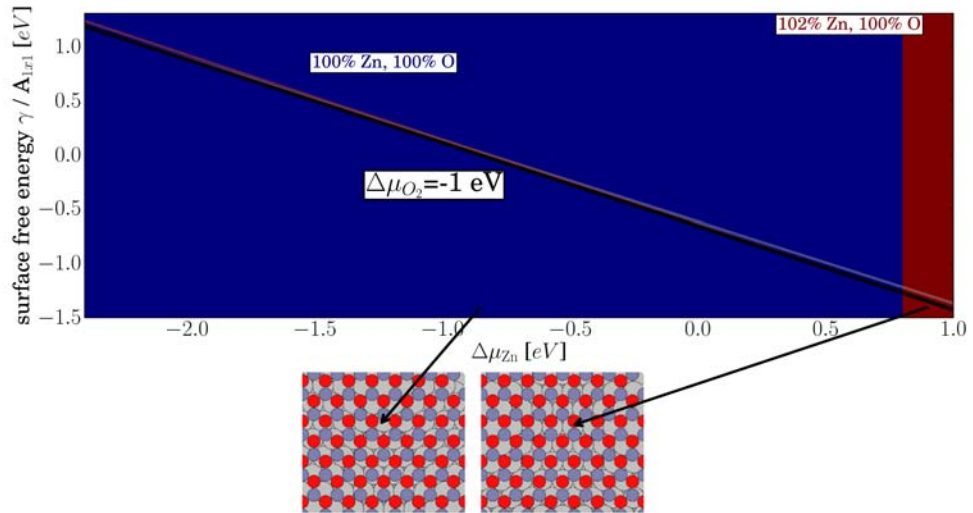


Figure 57: Surface phase diagram for one layer of ZnO on Ag considering zinc defects only. See caption of Fig. 53 for further explanations.

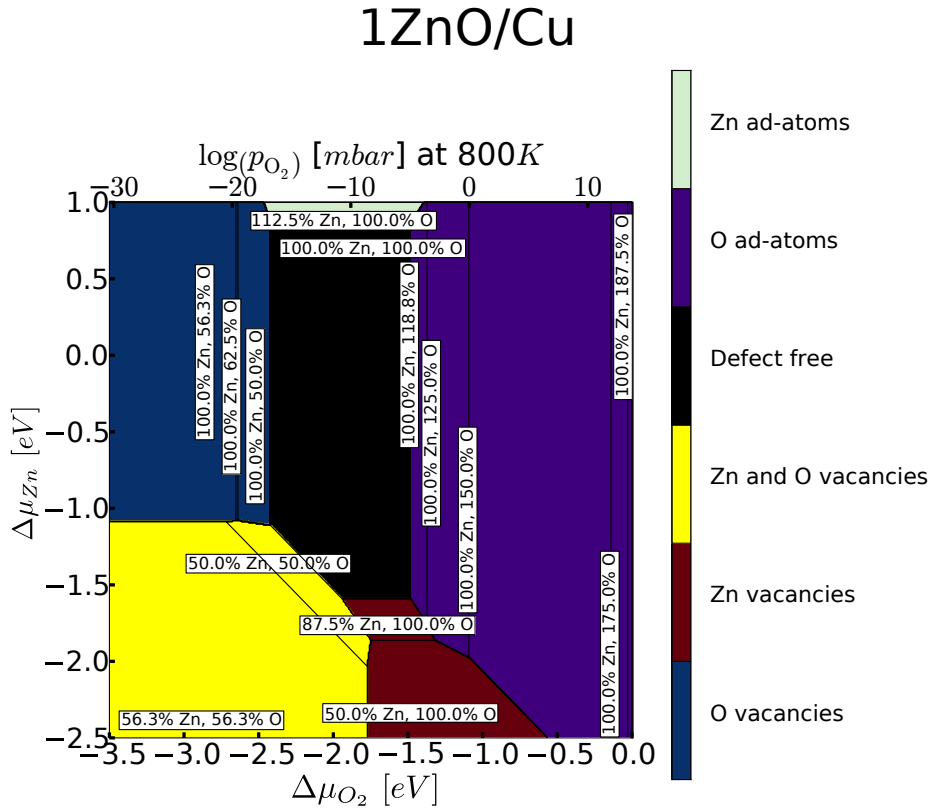


Figure 58: Two-dimensional surface phase diagram for ZnO on Cu including Zn-/O-defects, ad-atoms, and random combinations of the former. The projection of the lowest energy planes on the planes spanned by the changes in chemical potential of Zn and O are shown. The plane of the defect free mono-layer is colored black. The defect structures are indicated by a rainbow color map. The labels give the Zn and O content in percent with respect to the defect free mono-layer on the metal. The O partial pressure is determined from thermodynamical tables [178].

bulk surface [267]. We will extend our surface phase diagrams further, to analyze the stability of the simultaneous occurrence of Zn and O defects in the next section.

8.2.3 Oxygen and zinc defects

The previous sections showed, that oxygen defects in the ZnO ultra-thin films are favored considering the chemical potentials of the species. To compare the stability of the defective structures directly, we have to consider the surface free energy as a function of the change in chemical potential of Zn $\Delta\mu_{Zn}$ and O $\Delta\mu_O$. Because of the simultaneously varying amount of Zn and O atoms none of the two chemical potential can be fixed and the surface phase diagrams become two-dimensional. The oxygen chemical potential is, again, translated to partial pressures at 800 K. This is a typical temperature for the annealing step of film growth by molecular beam epitaxy [188]. The surface phase diagrams as a function of $\Delta\mu_{Zn}$ and $\Delta\mu_{O_2}$ for one layer of ZnO on Cu and Ag are shown in Fig. 58 and Fig. 59. The surface phase diagram for ZnO on Cu includes randomly distributed

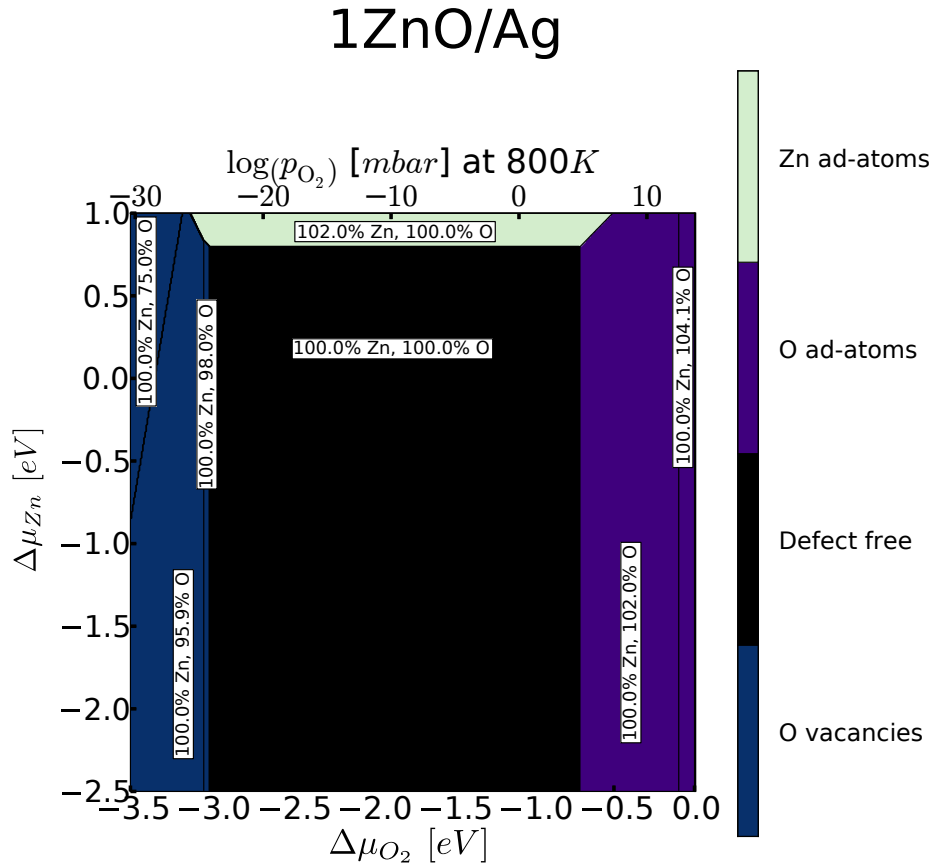


Figure 59: Two-dimensional surface phase diagram for ZnO on Ag including Zn-/O-defects and ad-atoms.

combinations of Zn and O vacancies. They are not expected to be the structures lowest in energy for a fixed vacancy concentration. For this purpose a more rigorous analysis (e. g. a cluster expansion) is required, which is not in the scope of this work. We understand our candidate structure as exemplary and expect only a small error compared to other defect arrangements. This was previously shown for defects at ZnO surfaces by Wahl et al. [267] and Kresse et al. [132].

The lines in the previous phase diagrams representing different phases are now intersecting planes. Their orientation is determined by the Zn and O content. The defect free ZnO mono-layer on the metals in Fig. 58 is colored in black. The defect structures are marked by a rainbow color map and are labeled by their Zn and O content with respect to the defect free mono-layer. By comparing the two phase diagrams for ZnO on Cu and Ag in Fig. 58 and Fig. 59 we observe an increased stability of the defect free ZnO mono-layer. On Cu, defects (Zn and O) are stabilized at lower chemical potentials. Random distributions of Zn and O vacancies are only stabilized at even lower chemical potentials. On Ag the mono-layer is more stable with respect to these reconstructions. At low chemical potentials we expect even sparser structures to be stabilized. The remaining oxygen at high oxygen vacancy concentration prefers hexagonal ring-like arrangements. We will investigate these types of structures in the next section.

For Zn and O defects, we conclude that O vacancies and O ad-atoms are in general more stable than their Zn counter parts. Similar trends were previously re-

ported for the (0001) and (000 $\bar{1}$) ZnO surface by Wahl et al. [267] and Kresse et al. [132]. The ZnO films behave similarly as the two polar ZnO surfaces with respect to the relative stability of defects, but the overall stability of the defects is system dependent. For ZnO on Ag a defect free ideal mono-layer is predicted to be stable over a wide range of Zn and O chemical potentials. In the case of a Cu substrate this stability range is reduced. In particular, O ad-atoms are stabilized, which we attribute to the higher oxygen affinity of the substrate.

8.3 RING STRUCTURES

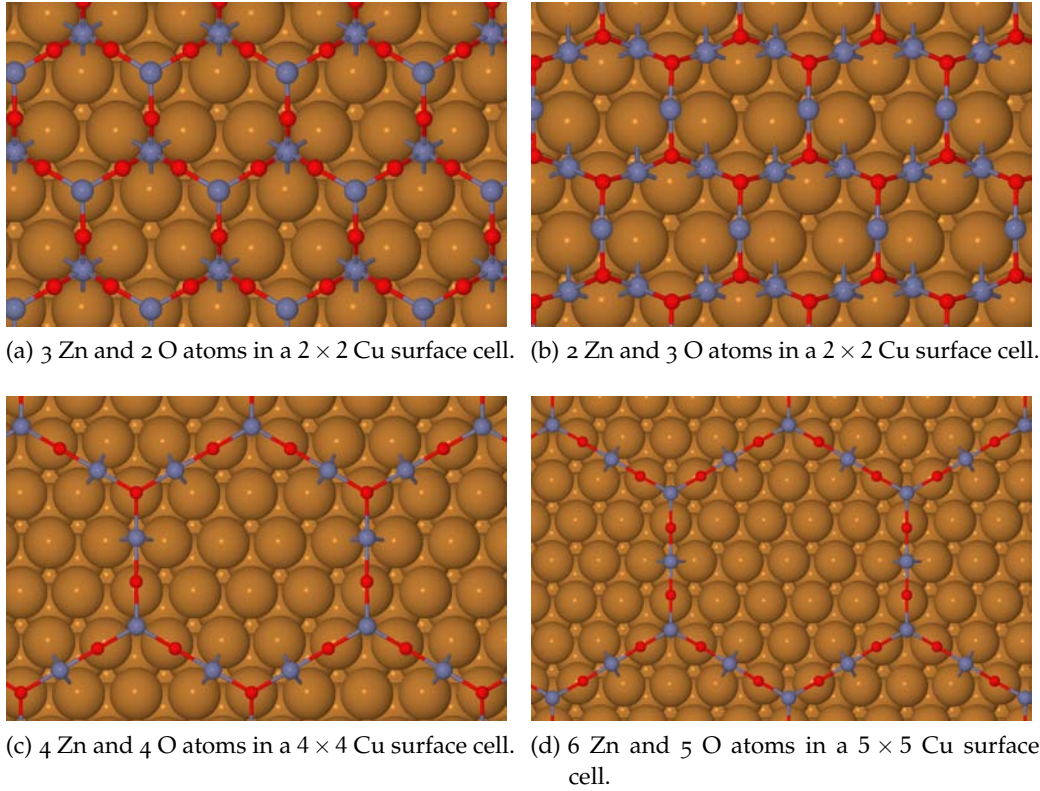


Figure 60: Atomic structure of hexagonal rings on Cu. The hexagons are constructed by putting Zn or O at the corners of the ideal α -BN ZnO mono-layer and inserting units of Zn and/or O in between. For even numbers of inserted atoms the corner atoms of the hexagons alternate. For odd numbers the Zn and O content is not equivalent. The species with the higher content is selected by the atom type placed at the corner of the hexagons.

Sparse ZnO surface reconstructions have been observed in experiment in Ref. [227, 272, 261, 45, 263, 50] and their stability was analyzed by theory in Ref. [261, 272, 267]. Weirum *et al.* observed ring structures at low coverages and specifically chosen annealing conditions [270]. Other structures include a (5×5) reconstruction and a $(\sqrt{3} \times \sqrt{3})R30^\circ$ (on ZnO) rotated ring structure.

The structures we will use in the discussion of the surface phase diagrams of ZnO on metals are shown in Fig. 60 and 61 for Cu as substrate. The structures in Fig. 60 are constructed by choosing Zn or O as the corner elements of a hexagon

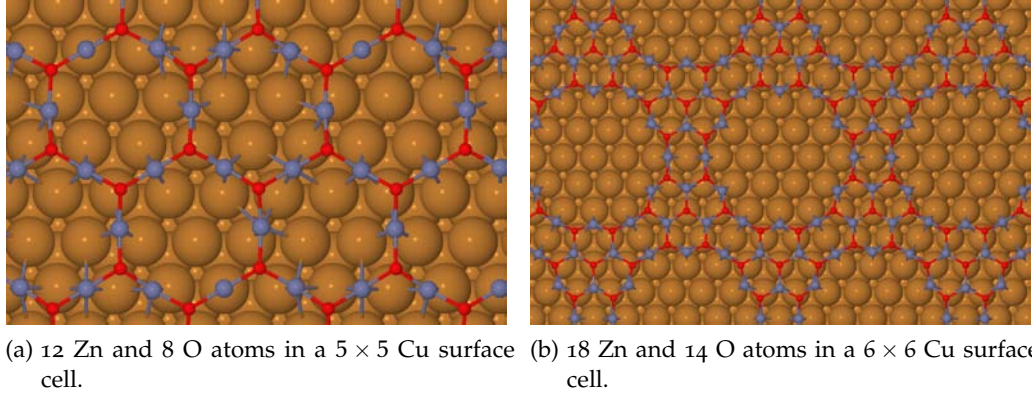


Figure 61: Atomic structure of ring structures from Valtiner *et al.* [261] and Wahl *et al.* [267].

and inserting units of Zn and O in between (1 and 3 element units in Fig. 60 a, b and d. For even numbers of inserted atoms the corner elements have to be alternated to ensure bonds only between Zn and O atoms. With increasing size of the inserted Zn-O units the sparsity of the structure is increased and greater areas of metal are exposed. For odd numbers of inserted atoms, the Zn and O content is not equivalent. The species with the higher content is selected by the atom type placed at the corner of the hexagons. In Fig. 61 a the $(\sqrt{3} \times \sqrt{3})R30^\circ$ reconstruction, investigated by Valtiner *et al.* [261], is shown. The basic structure is equivalent to the ring structure in Fig. 60 b. The coincidence is fitted to the structure proposed by Valtiner *et al.* Fig 61 b shows the (5×5) reconstruction discussed by Wahl *et al.* [267] and measured by Lauritsen *et al.* [136]. The hexagons typical for the mono-layer form larger bands creating large pores of exposed metal surface. In the theoretical studies for the ZnO surfaces in Ref. [261, 267] the $(\sqrt{3} \times \sqrt{3})R30^\circ$ and (5×5) reconstructions are predicted to be stable at low to intermediate O chemical potentials.

The surface phase diagrams for ZnO on Cu and Ag, including ring structures, are shown in Fig. 62 and Fig. 63. We have used the same form of the surface free energy as in the previous section for their construction. The defects, Zn and O ad-atoms and vacancies, are marked by the same colors as in Fig. 58 of the previous section (Sec. 8.2). The defect free, ideal coincidence structure is, again, shown in black and the different ring structures are colored in orange. The labels of the ring structures refer to the amount of Zn and O in the chosen metal surface unit cell (see Fig. 60 and 61). The ring structures are predominantly stable in regions of low Zn and O chemical potential. The lower Zn and O content of the structures is one obvious reason for this behavior. The other reason is their well ordered hexagonal structure. If ZnO cannot sustain the 3-fold bonding required for the ideal mono-layer because of the chemical environment the 3-fold bonding can be conserved for some of the constituents by forming sparser hexagonal ring structures. The Zn and O vacancies we have previously observed in Sec. 8.2 have been completely replaced by ring structures. The behavior is similar to our observation for high contents of oxygen vacancies in Sec. 8.2.1. For ZnO on Cu, oxygen vacancies are pushed from the phase diagram at low oxygen chemical

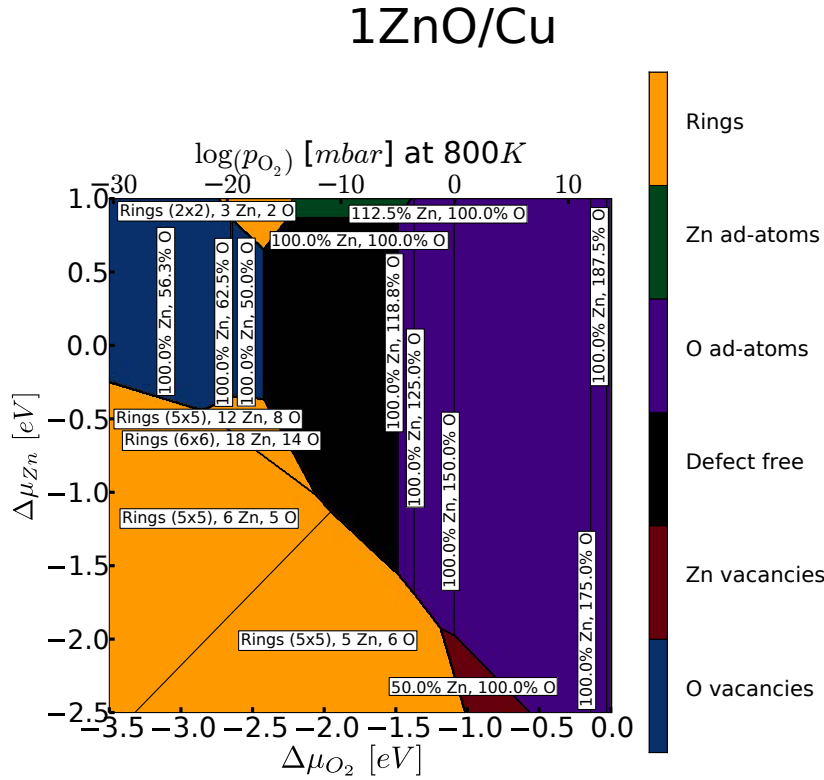


Figure 62: Surface phase diagram for Zn and O defects and ring structures on Cu. The defects are colored in green, purple, red or blue. The color of the ring structures is orange. The unreconstructed ideal mono-layer coincidence structure is shown in black. The labels for defects are as in the previous surface phase diagrams. For the ring structures the labels refer to the Zn and O content on the chosen metal surface unit cell.

potentials and high to low Zn chemical potentials. For ZnO on Ag, no oxygen vacancies remain in the surface phase diagram, only ring structures are present at low oxygen chemical potentials. At high oxygen chemical potentials O ad-atoms prevail for both metals.

We conclude, that sparse, ordered structures are more stable than disordered vacancy distributions even at intermediate chemical potential. So far we have discussed H adsorption, sparse ring structures, Zn and O defects. In the next section we will extend our surface phase diagram further by combining Zn/O defects with structures containing hydrogen.

8.4 HYDROXYL ABSORPTION

In section 8.1 we discussed the adsorption of hydrogen on ZnO ultra-thin films on different metal substrates. The phase diagrams were constructed from the one dimensional surface free energy as function of the change in hydrogen chemical potential. This was possible because the content of Zn and O remained constant for all investigated structures. In this section we will combine hydrogen adsorption with Zn and O defects. The surface free energy will, therefore, be a function of up-to 4 variables ($\Delta\mu_{H_2}$, $\Delta\mu_{O_2}$, $\Delta\mu_{Zn}$, $\Delta\mu_{H_2O}$).

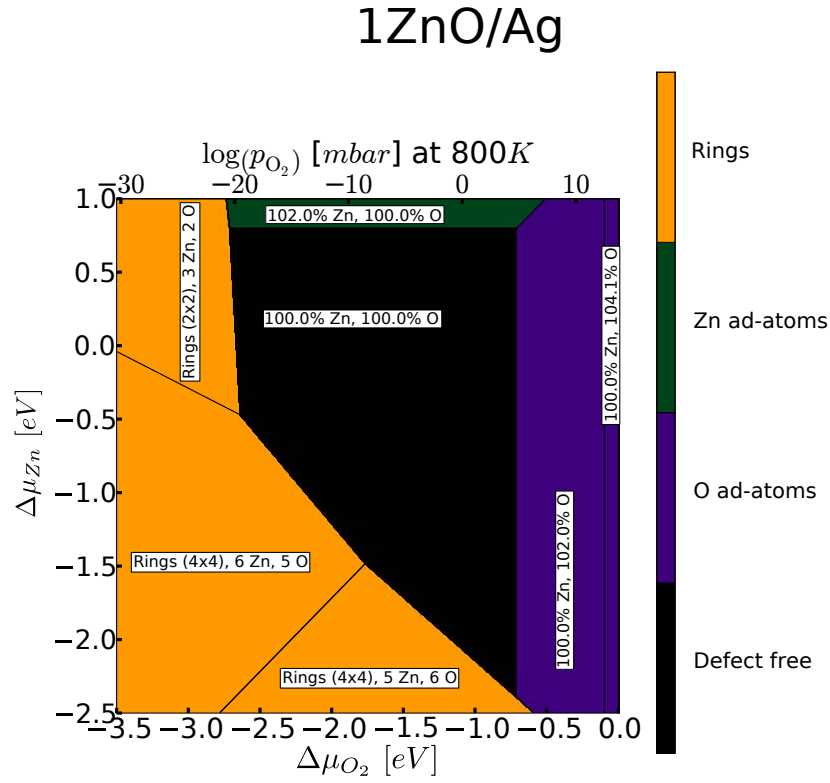


Figure 63: Surface phase diagram for Zn and O defects and ring structures on Ag. See caption of Fig. 62.

The hydrogen adsorption of Sec. 8.1 is one of the stabilization mechanisms for the O-terminated ZnO (0001) surface. The corresponding stabilization mechanism for the Zn-terminated (000 $\bar{1}$) surface is the adsorption of hydroxyl groups. The reservoir for the hydroxyl adsorbate has to be provided by at least two of the three gaseous phases of molecular oxygen, hydrogen or water. Typically, gaseous H₂O, H₂ and oxygen O₂ are considered to be in equilibrium with each other:



In the description by chemical potentials this amounts to the condition:

$$\mu_{\text{O}_2} + 2\mu_{\text{H}_2} = 2\mu_{\text{H}_2\text{O}}. \quad (103)$$

In this formalism the partial pressure of the gaseous reservoir, not included explicitly in the calculation, is ill-defined leading to unrealistic partial pressures. This problem is overcome by explicitly including all three chemical potentials in the surface free energy by the approach described by Hermann and Heimel [98] (also see Sec. 1.6). The surface free energy is a function of the four chemical potentials:

$$\begin{aligned} \gamma(T, p_{\text{H}}) = \frac{1}{A} [& E^{\text{tot}} - N_{\text{M}} E_{\text{Metal}}^{\text{bulk}} - N_{\text{Zn}} \Delta\mu_{\text{Zn}} - N_{\text{H}_2} \Delta\mu_{\text{H}_2}(T, p_{\text{H}_2}) \\ & - N_{\text{O}_2} \Delta\mu_{\text{O}_2}(T, p_{\text{O}_2}) - N_{\text{H}_2\text{O}} \Delta\mu_{\text{H}_2\text{O}}(T, p_{\text{H}_2\text{O}})]. \end{aligned} \quad (104)$$

$E_{\text{Metal}}^{\text{bulk}}$ is the bulk (fcc) reference energy of the metal (see Appendix B). The

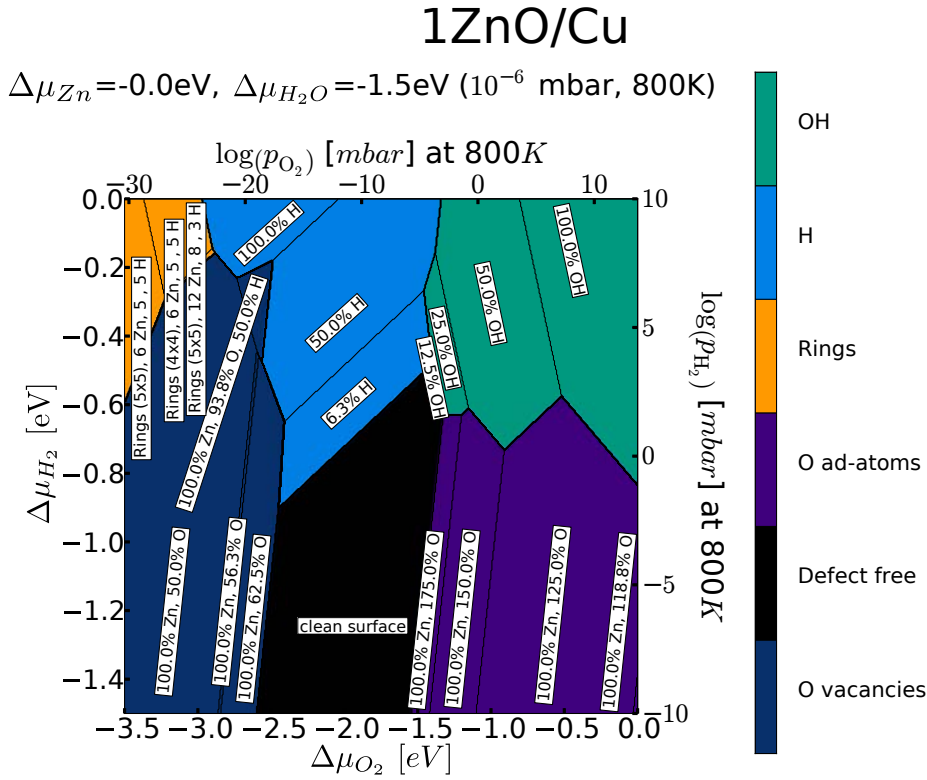


Figure 64: Surface phase diagram for one layer of ZnO on Cu. The surface free energy is plotted as a function of $\Delta\mu_{H_2}$ and $\Delta\mu_{O_2}$, for $\Delta\mu_{Zn}=0$ eV and for $\Delta\mu_{H_2O}=-1.5$ eV (see eq. 107). H-adsorption shown in light blue, hydroxyl adsorption in turquoise. Other structures are colored as in Fig. 62. The new structures are labeled by their OH-content with respect to the number of available surface sites. The chemical potential for H_2 , O_2 and H_2O are translated to partial pressures at 800 K with the help of thermodynamical tables.

change of the chemical potentials of Zn and H_2O will be treated as parameters to visualize a two-dimensional surface phase diagram. In order to correctly determine N_{Zn} , N_{H_2} , N_{O_2} and N_{H_2O} we have to consider element conservation

$$\begin{aligned}
 Z_{Zn} &= N_{Zn} \\
 Z_H &= 2N_{H_2} + 2N_{H_2O} \\
 Z_O &= 2N_{O_2} + N_{H_2O} \\
 0 &= -2N_{H_2} - N_{O_2} + 2N_{H_2O}.
 \end{aligned} \tag{105}$$

Here the Z_X are the actual numbers of atoms in the considered structures. These equations ensure, for example, that if one hydrogen atom coming from a water molecule is adsorbed, another hydrogen atom and a oxygen atom are put in to the reservoirs. The fourth equation enforces the satisfaction of the water gas-phase reaction (eq. 103). The system of equations in eq. 105 has as many equations

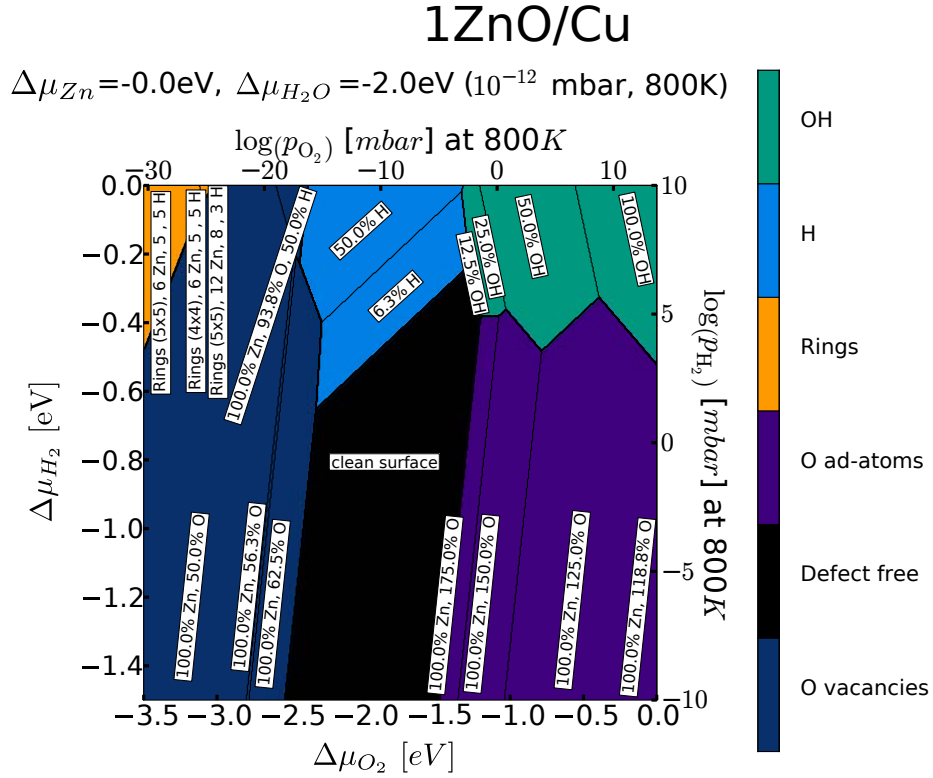


Figure 65: Surface phase diagram for one layer of ZnO on Cu. The surface free energy is plotted as a function of $\Delta\mu_{\text{H}_2}$ and $\Delta\mu_{\text{O}_2}$, for $\Delta\mu_{\text{Zn}} = 0 \text{ eV}$ and for $\Delta\mu_{\text{H}_2\text{O}} = -2.0 \text{ eV}$ (see eq. 107). See caption of Fig. 64.

as unknowns and can therefore be inverted to yield solutions for the number of gaseous species entering into the surface free energy

$$\begin{aligned}
 N_{\text{Zn}} &= Z_{\text{Zn}} \\
 N_{\text{H}_2\text{O}} &= \frac{1}{9} (Z_{\text{O}} + 2Z_{\text{H}}) \\
 N_{\text{H}_2} &= \frac{1}{9} \left(\frac{5}{2} Z_{\text{H}} - Z_{\text{O}} \right) \\
 N_{\text{O}_2} &= \frac{1}{9} (4Z_{\text{O}} - Z_{\text{H}}).
 \end{aligned} \tag{106}$$

Putting eqs. 106 into eq. 104 yields

$$\begin{aligned}
 \gamma(T, p_{\text{H}}) &= \frac{1}{A} [E^{\text{tot}} - Z_{\text{M}} E_{\text{M}}^{\text{bulk}} - Z_{\text{Zn}} \Delta\mu_{\text{Zn}} \\
 &\quad - \frac{1}{9} \left(\frac{5}{2} Z_{\text{H}} - Z_{\text{O}} \right) \Delta\mu_{\text{H}_2}(T, p_{\text{H}_2}) \\
 &\quad - \frac{1}{9} (4Z_{\text{O}} - Z_{\text{H}}) \Delta\mu_{\text{O}_2}(T, p_{\text{O}_2}) \\
 &\quad - \frac{1}{9} (Z_{\text{O}} + 2Z_{\text{H}}) \Delta\mu_{\text{H}_2\text{O}}(T, p_{\text{H}_2\text{O}})].
 \end{aligned} \tag{107}$$

This is a function of 4 independent variables. The plotting style of the previous section will be continued and the surface free energy treated as a function of $\Delta\mu_{\text{H}_2}$ and $\Delta\mu_{\text{O}_2}$. $\Delta\mu_{\text{Zn}}$ and $\Delta\mu_{\text{H}_2\text{O}}$ will be treated as parameters, that will be

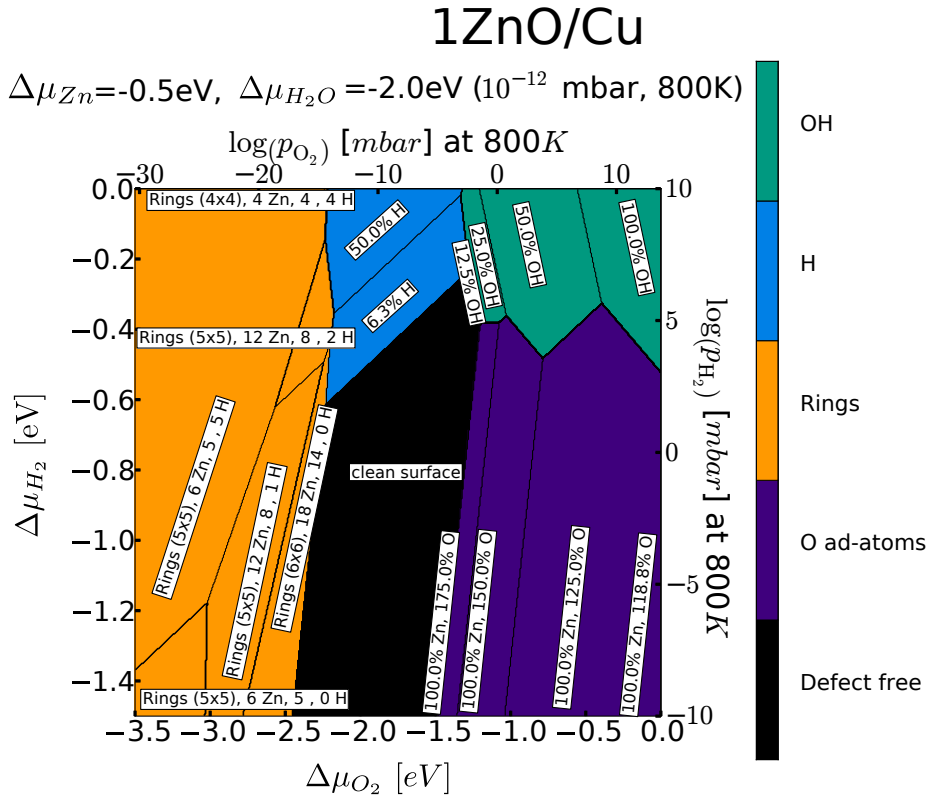


Figure 66: Surface phase diagram for one layer of ZnO on Cu. The surface free energy is plotted as a function of $\Delta\mu_{\text{H}_2}$ and $\Delta\mu_{\text{O}_2}$, for $\Delta\mu_{\text{Zn}} = -0.5$ eV and for $\Delta\mu_{\text{H}_2\text{O}} = -2.0$ eV (see eq. 107). See caption of Fig. 64.

chosen to investigate the full phase space. In Fig. 64 the surface phase diagram is shown for one layer of ZnO on Cu for $\Delta\mu_{\text{H}_2\text{O}} = -1.5$ eV and in Fig. 65 for $\Delta\mu_{\text{H}_2\text{O}} = -2.0$ eV. The general appearance of the surface phase diagram is similar to the graphs presented in the previous section. The areas representing the different most stable phases (lowest in surface free energy) for a given set of chemical potentials are slightly deformed in comparison to the example in Fig. 62. In Fig. 64 the change in chemical potential of the gaseous water reservoir ($\Delta\mu_{\text{H}_2\text{O}} = -1.5$ eV) corresponds to a partial pressure $p_{\text{H}_2\text{O}} = 1 \cdot 10^{-6}$ mbar at 800 K. By explicitly including $\Delta\mu_{\text{H}_2\text{O}}$ we can make predictions for $\Delta\mu_{\text{H}_2} + \Delta\mu_{\text{O}_2} > E_{\text{H}_2\text{O}}$. The condensation of water at the surface is predicted to occur when the critical vapor pressure of H_2O is reached. The highest impact of including $\Delta\mu_{\text{H}_2\text{O}}$ in Fig. 64 is on structures containing hydrogen. By decreasing the water chemical potential (Fig. 65) we reduce the available hydrogen in the system (cost to take H from the reservoir) and an increased hydrogen chemical potential is required to stabilize structures containing H, e. g. H- or OH-adsorbates. By adjusting the water partial pressure to typical experimental values ($< 1 \cdot 10^{-12}$ mbar) the unreconstructed ZnO monolayer is stabilized even for the previously unstable case of a Cu substrate for O_2 and H_2 partial pressure, that are of the same order as the water partial pressure (at 800 K). The affinity of the mono-layer on Cu for the formation of inter-facial oxygen (high O chemical potential) and O vacancies (low O chemical potential) prevails.

To analyze the influence of the Zn chemical potential on the composition of the

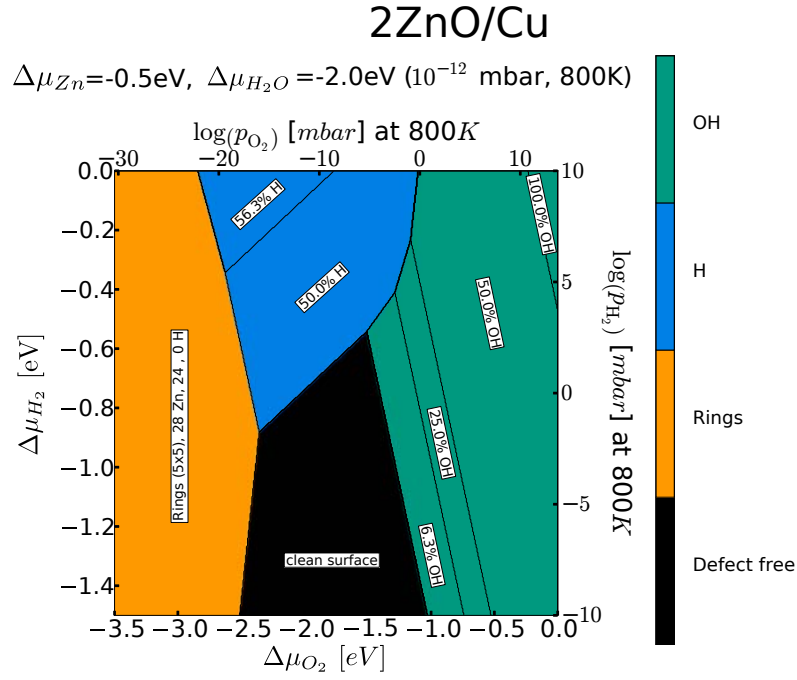


Figure 67: Surface phase diagram for 2 layers of ZnO on Cu at 800 K. The surface free energy is plotted as a function of $\Delta\mu_{\text{H}_2}$ and $\Delta\mu_{\text{O}_2}$, for $\Delta\mu_{\text{Zn}}=-0.5$ eV and for $\Delta\mu_{\text{H}_2\text{O}}=-2.0$ eV (see eq. 107). See caption of Fig. 64.

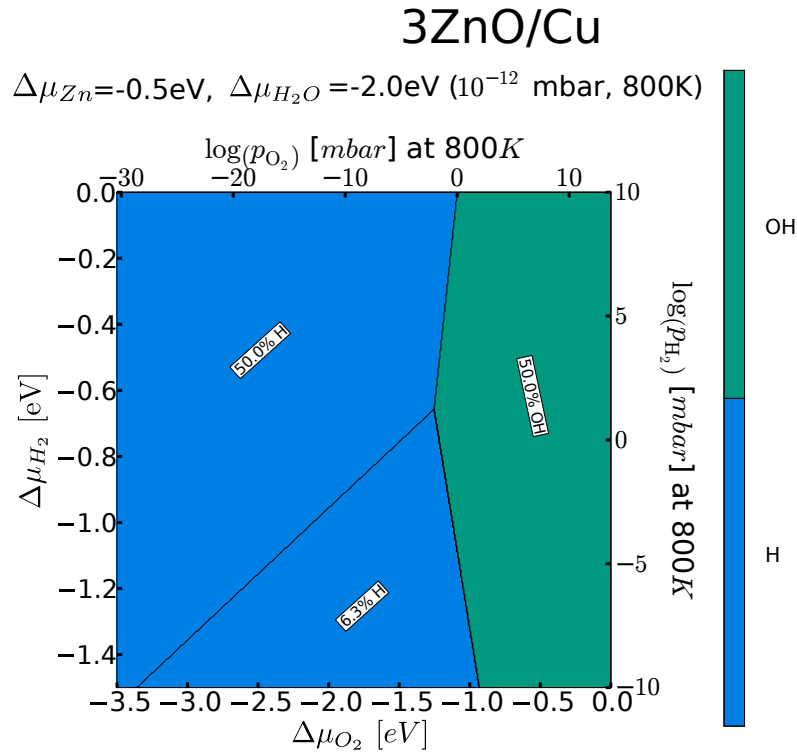


Figure 68: Surface phase diagram for 3 layers of ZnO on Cu at 800 K. The surface free energy is plotted as a function of $\Delta\mu_{\text{H}_2}$ and $\Delta\mu_{\text{O}_2}$, for $\Delta\mu_{\text{Zn}}=-0.5$ eV and for $\Delta\mu_{\text{H}_2\text{O}}=-2.0$ eV (see eq. 107). See caption of Fig. 64.

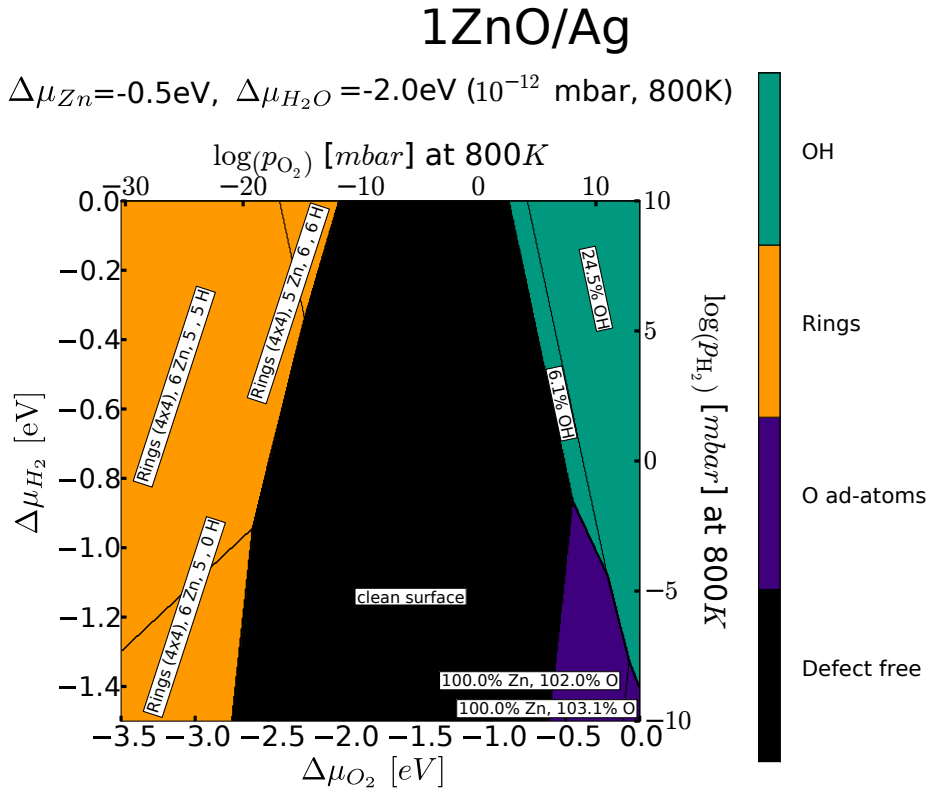


Figure 69: Surface phase diagram for 1 layer of ZnO on Ag at 800 K. The surface free energy is plotted as a function of $\Delta\mu_{\text{H}_2}$ and $\Delta\mu_{\text{O}_2}$, for $\Delta\mu_{\text{Zn}} = -0.5$ eV and for $\Delta\mu_{\text{H}_2\text{O}} = -2.0$ eV (see eq. 107). See caption of Fig. 64.

surface phase diagrams we keep the water chemical potential fixed, while $\Delta\mu_{\text{Zn}}$ is varied. In Fig. 66 the Zn chemical potential is decreased from $\Delta\mu_{\text{Zn}} = 0.0$ eV in Fig. 65 to $\Delta\mu_{\text{Zn}} = -0.5$ eV. $\Delta\mu_{\text{H}_2\text{O}}$ is in both cases -1.85 eV. For $\Delta\mu_{\text{Zn}} = -0.5$ eV sparse ring structures dominate the regime of low oxygen chemical potential. For increased hydrogen chemical potentials variants of these ring structures with hydrogen adsorbed at the O-site are energetically most favorable. For $\Delta\mu_{\text{Zn}} = 0.0$ eV in Fig. 65 the sparse ring structures have almost entirely disappeared from the surface phase diagram, only at low oxygen chemical potential and high hydrogen chemical potential they prevail against oxygen vacancies. The other structures in the surface phase diagram, H- and OH-adsorbates and O ad-atoms, are not influenced by the change in Zn chemical potential because their Zn content is constant. We will restrict the Zn chemical potential to $\Delta\mu_{\text{Zn}} = -0.5$ eV and the water chemical potential to $\Delta\mu_{\text{H}_2\text{O}} = -2.0$ eV ($p_{\text{H}_2\text{O}} = 10^{-12}$ mbar at 800 K) for the following discussion of thicker ZnO films on the metal substrates.

Fig. 66 to Fig. 68 show the surface phase diagrams for one to three layers of ZnO on Cu. The most important observation is that with increasing film thickness the unreconstructed surface is destabilized, while structures with H- and OH-adsorbates are stabilized. Already for two layers, the largest part of the surface phase diagram is occupied by structures containing H- and OH-adsorbates. At high hydrogen chemical potentials H-adsorbates, most prominently (2×1) -H reconstructed structures, dominate. For high oxygen (and hydrogen) chemical potential hydroxyl adsorbates are most stable. Only at very low chemical poten-

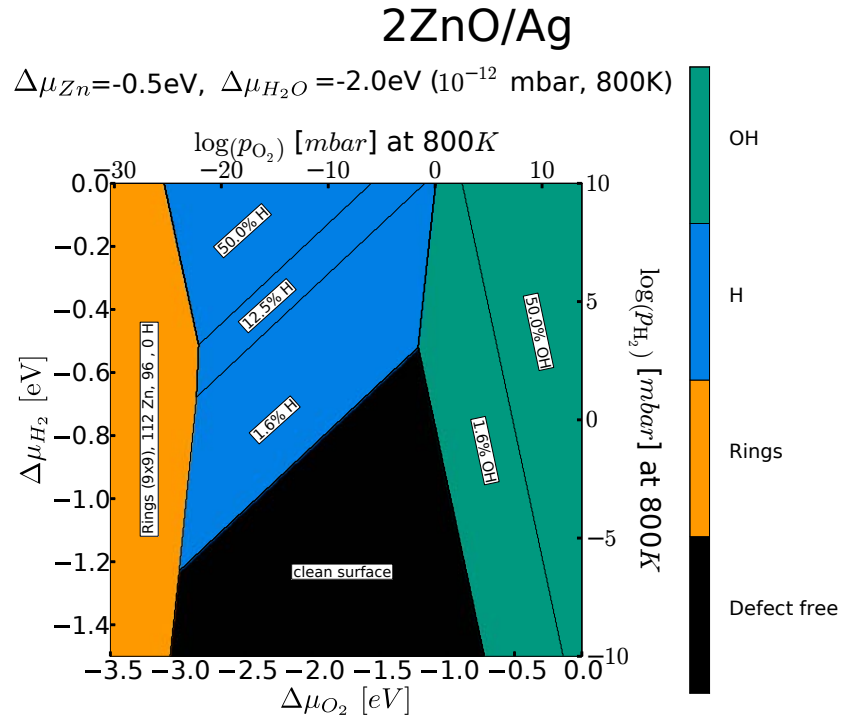


Figure 70: Surface phase diagram for 2 layers of ZnO on Ag at 800 K. The surface free energy is plotted as a function of $\Delta\mu_{\text{H}_2}$ and $\Delta\mu_{\text{O}_2}$, for $\Delta\mu_{\text{Zn}} = -0.5$ eV and for $\Delta\mu_{\text{H}_2\text{O}} = -2.0$ eV (see eq. 107). See caption of Fig. 64.

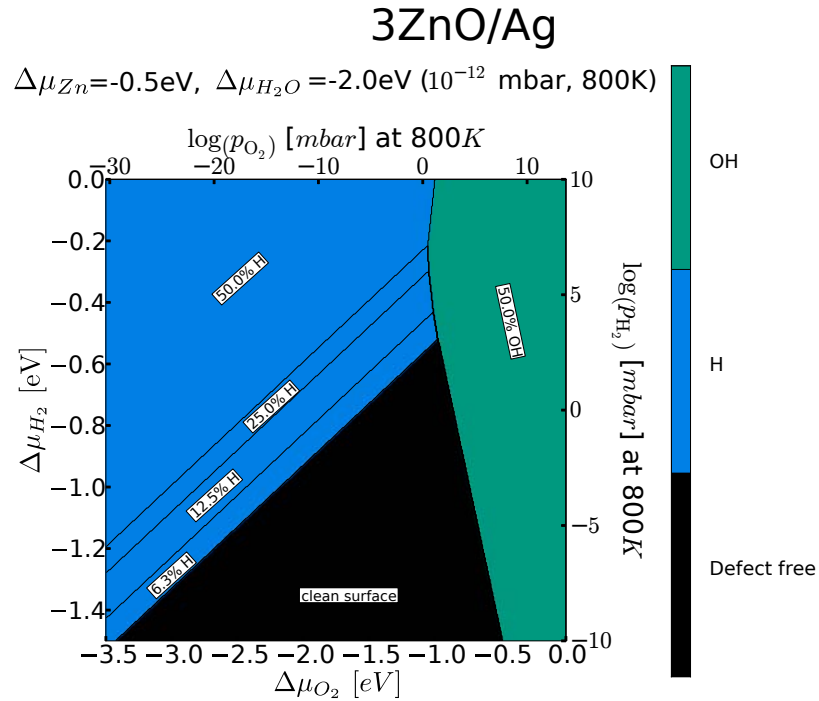


Figure 71: Surface phase diagram for 3 layers of ZnO on Ag at 800 K. The surface free energy is plotted as a function of $\Delta\mu_{\text{H}_2}$ and $\Delta\mu_{\text{O}_2}$, for $\Delta\mu_{\text{Zn}} = -0.5$ eV and for $\Delta\mu_{\text{H}_2\text{O}} = -2.0$ eV (see eq. 107). See caption of Fig. 64.

tials O-vacancies and ring structures prevail for two layers of ZnO. However, for two layers of ZnO on Cu the predicted stability range for the unreconstructed surface is within partial pressure ranges typically realized in experiments. Only for the three layers of ZnO in Fig. 68 the unreconstructed surface is pushed from the surface phase diagram by H- reconstructions. While the stability of H-reconstructed surfaces is increased with layer thickness the stability of OH- adorbates is unchanged. The portion of the surface phase diagram occupied by those reconstructions stays approximately constant with increasing film thickness (Fig. 66 to Fig. 68). This again demonstrates the previously observed high stability of H-reconstructions on Cu (see Sec. 8.1).

For Ag as substrate, we observe the unreconstructed surface in the surface phase diagrams for one to three layers in Fig. 69 to Fig. 71. The mono-layer in Fig. 69 is especially stable for a large range of O- and H- chemical potentials. For two layers of ZnO in Fig. 70 the unreconstructed system is substantially destabilized, especially with respect to H-adsorption. Hydroxyl reconstructions are stabilized for high O-chemical potentials. For three layers of ZnO on Ag in Fig. 71, the region of stability for the unreconstructed surface is hardly decreased in comparison to two layers of ZnO on Ag. Only the (2×1) -H reconstructed surface is further stabilized. Similar to the case of ZnO on Cu the portion of the phase diagram occupied by OH-reconstructions stays approximately constant for two and three layers of ZnO on Ag, while the stability of H-reconstructions increases. It is important to note that at 800 K the unreconstructed surface is stable under experimentally accessible conditions for 1, 2, and 3 layers of ZnO on Ag. For Cu this is only true for one and two layers. The stability of the unreconstructed surface is further increased by going to even lower water chemical potentials. The explicit inclusion of the water chemical potential leads to a destabilization of H- and OH-reconstructed structures at partial pressures (chemical potentials) that are relevant in experiment. The prediction of H and OH-free ultra-thin films is in agreement with previously observed experimental results [259, 237, 270, 159]. In order to systematically compare the behavior of mono- and multi-layer systems of ZnO on different metal substrates the dimensionality of the surface phase diagrams has to be reduced.

We can reduce the number of variables in our surface phase diagrams further by defining paths through the phase space represented by the previous surface phase diagrams. To analyze the stability with respect to H adsorption, $\Delta\mu_{\text{Zn}}$, $\Delta\mu_{\text{H}_2\text{O}}$ and $\Delta\mu_{\text{O}_2}$ are set to fixed values ($\Delta\mu_{\text{Zn}}=-0.5$ eV, $\Delta\mu_{\text{H}_2\text{O}}=-2.0$ eV, $\Delta\mu_{\text{O}_2}=-2.0$ eV). For the OH-adsorption the change in chemical potential of H_2 and O_2 is coupled by the relation $\Delta\mu_{\text{O}_2}=\Delta\mu_{\text{H}_2}$ and $\Delta\mu_{\text{Zn}}=-0.5$ eV, $\Delta\mu_{\text{H}_2\text{O}}=-2.0$ eV. In both cases we can now treat the surface free energy as one dimensional objects. The results are shown in Fig. 72 for H-reconstructions and in Fig. 73 for OH-reconstructions. The structures with coverages of up-to 50% of H and OH are represented by differently shaded colored bars. The color indicates the substrate, while the shading stands for the H-/OH-content. Below the bars the unreconstructed surface is stable (low H chemical potential, dark gray), above the bars the (2×1) -H reconstruction or OH-coverages equal or larger than 50% are stable. The chemical potentials of H_2 , O_2 and H_2O are translated to partial pressure at the selected temperatures. The structure of the graphs is similar to those we

presented in Sec. 8.1, but here we have explicitly included the chemical potentials of oxygen, hydrogen, zinc and water. This treatment not only allows us to describe OH-reconstructions, it also changes the predicted stability range of H-reconstructions.

As we have already observed in the discussions of the full surface phase diagrams for 1 to 3 layers of ZnO on Cu and Ag the stability of the unreconstructed surface with respect to H-reconstructions is increased for Ag, Cu, Pd, Ni, Rh and Pt by explicitly including the chemical potential of water in the surface free energy. For Ag, Cu, Ni and Rh as substrate up-to 3 layers of ZnO are predicted to be stable for partial pressure that are realized in experiment. For Pd and Pt only the first layer is predicted to be stable under such conditions. The spread with H_2 chemical potential of the H-reconstructed structures in Fig. 72 is much larger than for the OH-reconstructed structures in Fig. 73. The OH-reconstructed structures become stable in a narrow range of H_2 chemical potential around -1.0 eV, almost independent of the metal substrate and the film thickness. The stability of H-adsorbates is increased with each additional layer and becomes highly system dependent. This result is in agreement with our observations from the full surface phase diagrams for Cu and Ag, where the portion of the phase diagram occupied by OH-reconstructions hardly changes as a function of film thickness (and metal substrate). For 800 K in Fig. 73 up to three layers of unreconstructed ZnO can be stabilized with respect to OH-reconstructions on most metal substrates for experimentally accessible partial pressures. The stability of H-reconstructed structures is typically smaller than for OH-reconstructions for one and two layers. For film thicknesses greater than 2 layers of ZnO, H-reconstructions become more stable than OH-reconstructions.

The comparison to theoretical surface phase diagrams for the polar ZnO surfaces

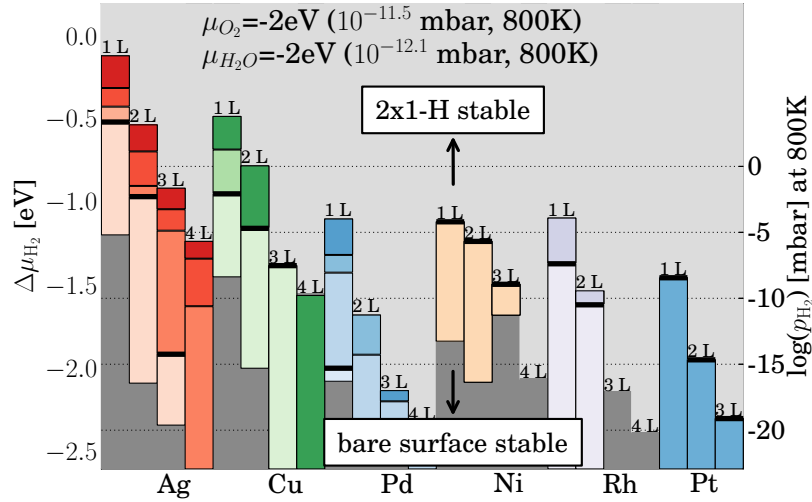


Figure 72: Stability of H-reconstruction for different metal substrates and ultra-thin films of different thicknesses at 800 K. The shade of the colored bars represents H-coverages up to 50%. The base color indicates the metal substrate. Above the bars 50% and higher coverages are stable, below the unreconstructed surface is stable. The set values for $\Delta\mu_{Zn}$, $\Delta\mu_{H_2O}$, $\Delta\mu_{O_2}$ are given in the plot.

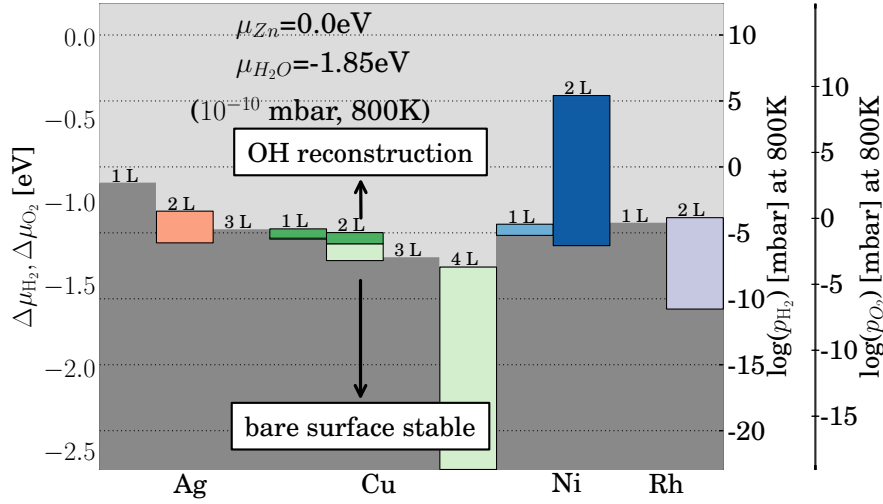


Figure 73: Stability of OH-reconstruction for different metal substrates and ultra-thin films of different thicknesses at 800 K. The shade of the colored bars represents OH-coverages up to 50%. The base color indicates the metal substrate. Above the bars 50% and higher coverages are stable, below the unreconstructed surface is stable. The set values for $\Delta\mu_{\text{Zn}}$, $\Delta\mu_{\text{H}_2\text{O}}$, $\Delta\mu_{\text{O}_2}$ are given in the plot.

by Wahl *et al.* [267] and Valtiner *et al.* [261] is difficult as we include aspects of the ZnO (0001)-Zn and (000 $\bar{1}$)-O surface in the phase diagrams for the ZnO thin films on metal substrates. Additionally, Wahl *et al.* and Valtiner *et al.* did not explicitly include the H₂O chemical potential and could couple the chemical potential of O₂ and Zn via eq. 60 (ZnO bulk reservoir). The high stability of OH- and H-reconstructions we predict for ZnO films was qualitatively also observed by Wahl *et al.* and Valtiner *et al.*. Large scale defective reconstructions, as observed/predicted for the polar ZnO surfaces, are less stable than OH- and H-reconstructions for ZnO thin films. We expect them to appear in the surface phase diagrams of thicker films, because their construction is based on the removal of atoms in the 2nd and 3rd layer below the surface.

In conclusion we find an increased stability of the unreconstructed ZnO thin films on all metal substrates by explicitly including the chemical potentials of Zn, O₂, H₂ and H₂O. H- or OH-reconstructions are the most stable reconstructions in the surface phase diagrams. Zn- and O-defects are only present at very large/small chemical potentials. Only at low O₂ chemical potentials sparse ring structure prevail, that are stabilized for increased H₂ chemical potentials by absorbing hydrogen at their oxygen sites. Up-to three unreconstructed layers of ZnO are predicted to be stable on Ag, which is in agreement with experimental results of Shiotari *et al.* [237]. These experimental findings and their comparison to our theoretical predictions are the topic of the next section.

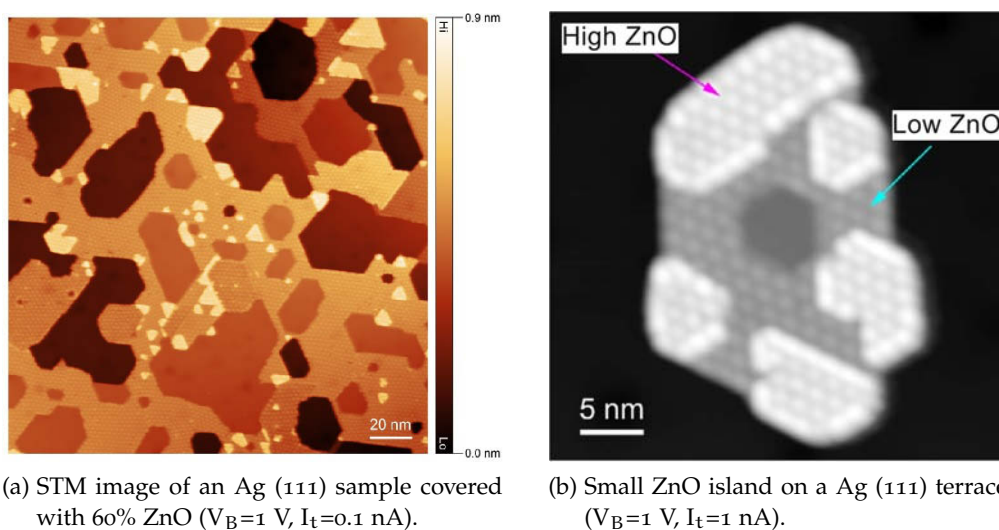
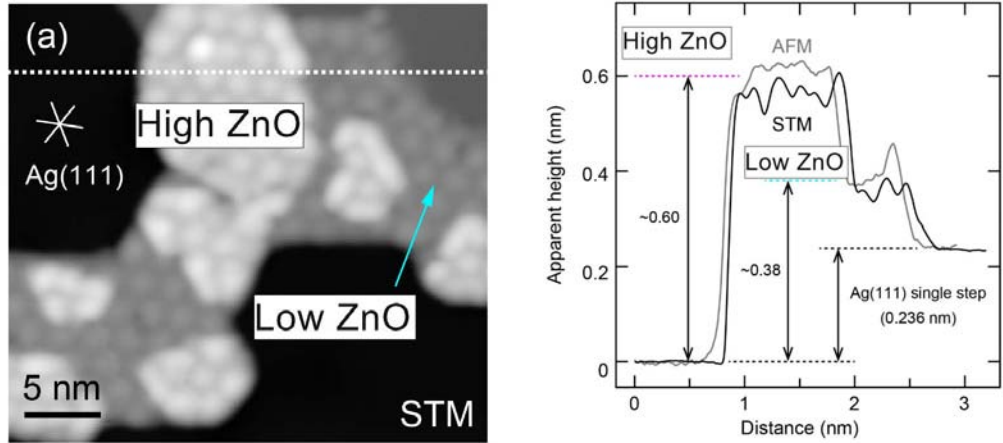


Figure 74: STM images of Ag (111) covered with 60% ZnO, measured at 5 K, courtesy of T. Kumagai [237]. The sample was annealed at 670 K after Zn deposition. The dark red area in a) and the black area and the island center in b) are the bare Ag (111) substrate. Lighter colors correspond to ZnO with different layer heights.

Apart from the question of thermodynamic stability and termination, which was addressed in the previous Chapters, the number of ZnO layers observed in experiment is a key issue. In Fig 74 a a STM graph of ZnO on Ag, annealed at 670 K, is shown. The ZnO coverage is approximately 60% and the data was measured at 5 K (courtesy of T. Kumagai) [237]. The dark red patches in Fig 74 a correspond to the Ag (111) substrate. The other areas are covered with ZnO layers of different heights. Fig 74 b shows an enlargement of a small ZnO island on an Ag (111) terrace. The black area and the central spot of the island are considered to be part of the Ag (111) substrate. Two different areas are visible in Fig 74 b. They are labeled “low ZnO” and “high ZnO”. They were initially attributed to be 1 and 2 layers or 2 and 3 layers of ZnO, respectively [237]. However, the determination of absolute heights in STM measurements is very difficult. Electronic states of the surface and the substrate typically contribute to the signal. Shiotari *et al.* [237] tried to improve their measurement by using a set-up that allows for simultaneous STM and AFM measurements. While STM, strictly speaking, does not allow for a direct measurement of atomic heights, the AFM mode records the forces between tip and surface. The AFM measurements are thus not dominated by the electronic states of the surface but by weak chemical interaction between tip and surface and are therefore more amenable to height measurements. To



(a) STM graph of Ag (111) sample covered with 60% ZnO ($V_B=1$ V, $I_t=0.1$ nA) measured at 5 K.

(b) STM and AFM apparent height line scans along the dotted line in a).

Figure 75: STM image of Ag (111) covered with 60% ZnO, measured at 5 K a) and apparent height line scans in STM and AFM mode b), courtesy of T. Kumagai [237]. The path of the line scans are indicated by the white dotted line in a). The area at the right and left ends of the scan are attributed to the Ag (111) substrate. The area to the right of the island is considered to be a single step Ag (111) higher than the left side. The high/low ZnO areas are marked in both plots.

reliably assign the number of layers, the apparent heights obtained from STM or AFM measurements have to be compared to the results of theoretical simulations.

9.1 APPARENT HEIGHTS IN EXPERIMENT

The resulting measured apparent height maps need to be calibrated by adjusting to a well known sample height. Shiotari *et al.* [237] calibrate their instrument to a single step on Ag (111). This necessary calibration is a major source of systematic errors in (any) STM/AFM measurement. As already mentioned, the STM measurements are dominated by the electronic states of the substrate, that differ significantly for a metal substrate and a semi-conductor thin film. The same is true for the chemical interactions between the tip and the surface in the AFM mode. In the AFM mode the condition of the tip has to be controlled and checked very carefully as contaminations such as adsorbed molecules can change the interaction between tip and surface significantly.

Figure 75 a shows the STM image of an Ag (111) sample covered with 60% ZnO (courtesy of T. Kumagai) [237]. The Moiré pattern of the (8x8) Ag (7x7) ZnO coincidence structure is visible. This is absent in the AFM image (not shown, see Shiotari *et al.* [237]), indicating the electronic structure as source of the Moiré pattern.

In Fig. 75 b the results of line scans along the white dashed line in Fig. 75 a in AFM and STM mode are shown [237]. Both measurement modes were calibrated to the Ag (111) single step height (2.36 Å). The right and left end of the line scans

are attributed to the Ag substrate. The right side is one Ag single step higher. The results of both measurements are shown in Tab. 10. AFM results are listed first, STM results are in brackets. The height of “low ZnO” is 4.0 ± 0.3 Å. This is high compared to results obtained for Pd (111) (2.0 Å [271]) and Pt (111) (1.8 Å [159]). In combination with the high oxygen partial pressure during deposition, which lead to ZnO double layers on Pd (111) [271], Shiotari *et al.* [237] concluded that “low ZnO” is two layers thick and “high ZnO” three layers thick. The height difference between low and high ZnO agrees well with step height measurements obtained by SXRD of 2.1 Å [259]. Further evidence has to be collected and the error due to the calibration procedure requires quantification to solidify this conclusion.

System	Apparent height AFM (STM) [Å]
Low ZnO	3.8 (4.0) ± 0.3
High ZnO	5.8 (6.1) ± 0.3
Ag(111) step	2.36

Table 10: Experimental heights obtained from the measurement in Fig. 75 a. The AFM results are given first, STM results are in brackets.

9.2 RESULTS FROM DFT SIMULATIONS

Experimental results do not give a clear picture of the thickness of ultra-thin ZnO films on Ag. Simulations based on DFT provide absolute values for all atomic positions, that can be compared to experimental results. In Tab. 11 the thickness of ZnO ultra-thin films on Ag (111) is presented, more details are shown in Fig. 126 in Appendix K. The heights presented in Tab. 11 are the difference in the mean value of the z-components of the atoms in the top Ag layer and the top ZnO layer in the super cell. The atomic structure of these films was already discussed in detail in Sec. 7.1. Here we will focus on the film heights and the comparison of theory and experiment.

The values for the layer heights of unreconstructed ZnO on Ag (111) obtained from the calculation do not fit the measured values. One layer of ZnO is not thick enough to compare to the “low ZnO” and two layers are too thick. Experiment and theory apparently do not match. In the previous sections we have learned that the ZnO on Ag (111) reconstructs by absorbing hydrogen on 50% of the available surface sites. This (2×1) -H reconstruction is predicted to be stable under thermodynamic conditions (partial pressure of the residual gases in the measurement chamber) that are met during the experimental data acquisition. The layer heights obtained from DFT simulations employing the PBE+vdW^{TS} xc-functional for the (2×1) -H reconstructed ZnO on Ag (111) are presented in Tab. 11. Further details can be found in Fig. 127 in Appendix K and Sec. 7.1. The film thickness for the (2×1) -H reconstructed ZnO on Ag (111) agree well with the values reported from experiments. The mono-layer film is 4.02 Å in theory and “low ZnO” 3.8 ± 0.3 Å in experiment. The double layer is 6.48 Å in theory

System	h DFT [\AA]	σ DFT [\AA]	App. h DFT [\AA]
1 layer ZnO	2.61	0.095	1.74
2 layers ZnO	6.48	0.317	4.16
3 layers ZnO	9.16	0.315	6.82
1 layer ZnO-(2×1)-H	4.02	0.354	2.01
2 layers ZnO-(2×1)-H	6.48	0.317	4.62
3 layers ZnO-(2×1)-H	9.16	0.315	7.33
Ag(111) step	2.36		

Table 11: Height of ZnO layers on Ag (111) obtained by DFT calculations employing the PBE+vdW^{TS} xc-functional [196, 254]. The heights are measured as difference between the mean value of the lateral position of the atoms in the top Ag layers and the mean value of the lateral position of the atoms in the top ZnO layers. The deviation from the calculated mean height, due to corrugation, is quantified by the standard deviation σ . See text for a description of the procedure to calculate apparent heights from DFT calculations.

whereas “high ZnO” is $5.8 \pm 0.3 \text{ \AA}$ in experiment. This indicates that the surface could be covered with hydrogen, but a careful analysis of the surface vibrations by infrared spectroscopy (courtesy of Bo-Hong Liu and Shamil Shaikhutdinov, FHI, Berlin) did not reveal any characteristic O-H vibration modes. The experimental conclusion is that no hydrogen is adsorbed at the surface. Indeed the analysis of the thermodynamic stability of the (2×1)-H reconstruction in Sec. 8.1 revealed, that the unreconstructed surface is stable under annealing conditions (800 K) for up to three layers. Additionally, the formation of the (2×1)-H overlayer could be blocked under measurement conditions (5 K) by a barrier for the dissociation and/or diffusion of hydrogen.

Further theoretical evidence for a hydrogen free surface can be gained by a comparison of formation energies for a clean Ag (111) surface and the unreconstructed and reconstructed ZnO mono- and double-layer films. By adding the total energy from the DFT simulation of a clean Ag (111) surface and 2 layers of ZnO on Ag (111) and subtracting twice the total energy of a mono-layer film on Ag (111) we obtain:

$$\overline{\overline{\text{Ag(111)}}} + \overline{\overline{\text{ZnO(2x1)-H}}} - 2 \times \overline{\overline{\text{ZnO}}} = 0.063 \text{ eV}$$

The energy balance is positive. Thus the system prefers to form ZnO double layers and leave patches of Ag (111) surface uncovered rather than to form a closed mono-layer. This is in agreement with experimental observations for ZnO on Ag (111) [237, 192] and Pt(111) [159] of island formation after catalytic experiments. For the (2×1)-H reconstructed films adding two layers of (2×1)-H reconstructed ZnO, a layer of hydrogen and the clean Ag (111) surface and subtracting twice the (2×1)-H reconstructed ZnO mono-layer yield a negative value:

$$\begin{array}{c} \bullet \bullet \bullet \bullet \bullet \\ \hline \blacksquare \end{array} + \bullet \bullet \bullet \bullet \bullet + \blacksquare - 2 \times \begin{array}{c} \bullet \bullet \bullet \bullet \bullet \\ \hline \blacksquare \end{array} = -0.058 \text{ eV}$$

This implies that a closed (2×1) -H reconstructed ZnO mono-layer should be more stable than two layers and patches of Ag. This is in disagreement with experimental observations. To further investigate the difference between experimental apparent heights and the atomic structure obtained from DFT calculations theoretical STM graphs were calculated within the Tersoff-Hamann approach (Ref. [250] and Sec. 1.9). The density was summed up from the Fermi level to the bias voltage at Cartesian grid points. This yields a theoretical current map for different (constant) heights. To compare to experimental constant current STM measurements, the maps are sorted by their current values at each grid point. For these (constant) current values the corresponding heights are plotted. These simulated constant current STM graphs for one and two layers of ZnO and ZnO-

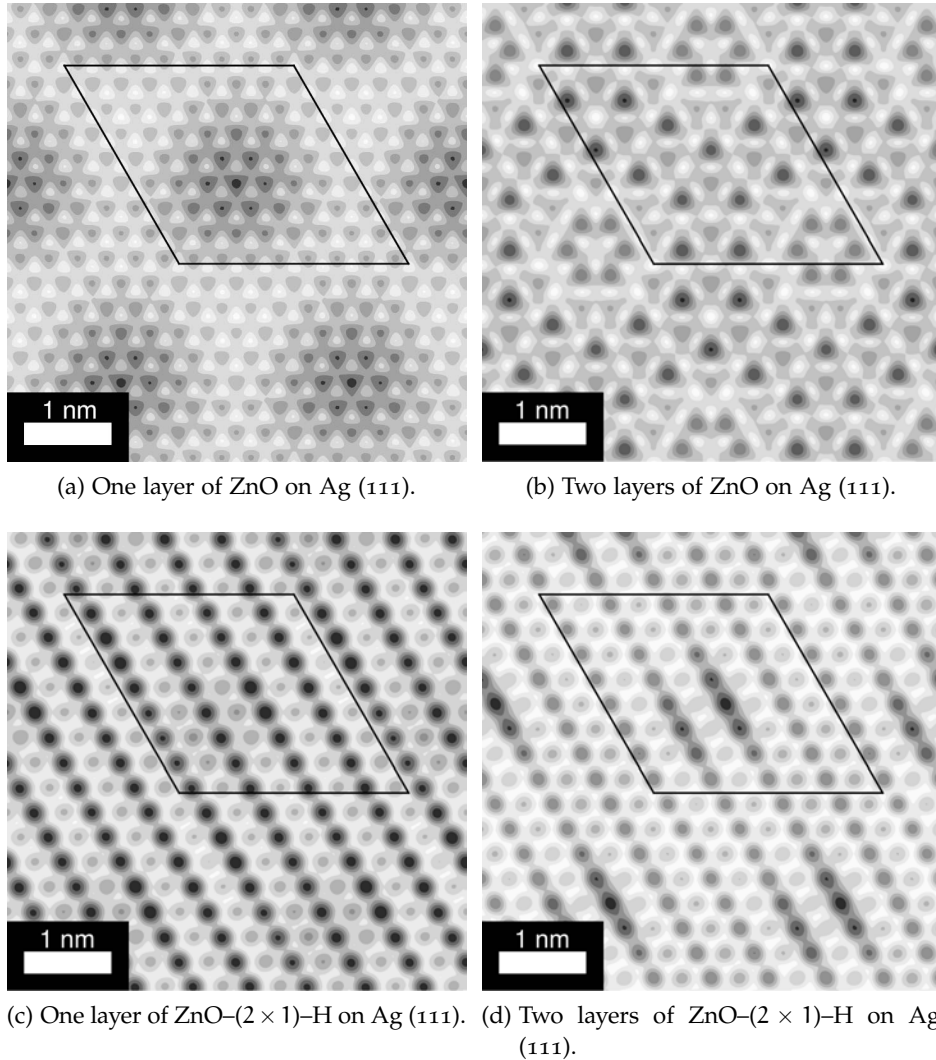


Figure 76: Simulated constant current STM graphs of 1 and 2 layers of ZnO and ZnO- (2×1) -H on Ag (111). The super cell used in the DFT calculation is indicated in the graphs.

(2×1) -H on Ag (111) are shown in Fig. 76 for a constant current of $1 \cdot 10^{-4}$ eV/Å. The (2×1) -H reconstructed films show stripes, that correspond to the rows of adsorbed hydrogen. In experiment no stripes were observed (see Fig. 75 and Ref. [237]), indicating the lack of hydrogen.

From the simulated constant current maps the film height cannot be obtained directly. In analogy to experiment, where the instrument is calibrated at Ag single steps, the film thickness has to be calculated as height difference between a simulated Ag (111) STM graph and ZnO on Ag (111). The required values are calculated by averaging the absolute heights at the same constant current for the bare Ag and ZnO on Ag over the super cell. A further discussion concerning the choice of the current for the image creation of the constant current STM graphs can be found in Appendix L. The calculated apparent heights are listed in Tab. 11. With 1.74 Å the height of the mono-layer is too small if compared to experimental results. The apparent height of the double layer (4.16 Å) and of three ZnO layers (6.82 Å) are in good agreement with the experimental results. The same procedure can be carried out for (2×1) -H reconstructed ZnO on Ag (111). The calculated apparent heights are listed in Tab. 11. The obtained values are too high compared to experiment. We can confirm the assessment of Shiotari *et al.* [237] that their experimentally observed films are indeed two and three layers of hydrogen free ZnO. The agreement between theory and experiment can be explained by the improved theoretical description of the measurement process.

9.3 CONCLUSION

In conclusion, the combination of experiment and theory gives further evidence for the proposition that the ZnO ultra-thin films observed by Shiotari *et al.* are indeed at least two layers in thickness. The *low* ZnO is two layers of unreconstructed ZnO on Ag and the *high* ZnO is three layers of unreconstructed ZnO on Ag (111). Thermodynamic and total energy results lead to this conclusion. The disagreement between experimental apparent height and the atomic structure can be remedied by calculating the apparent height from simulated constant current STM graphs based on DFT calculations.

In this chapter we will focus on coincidence structures and reconstructions of ultra-thin ZnO films on Ag (111) and Rh (100). For Ag we will discuss a (5×5) coincidence structure of ZnO on Ag that was experimentally observed by Shiotari *et al.* [237] as minority phase together with the more abundant (8×8) coincidence structure. We will analyze the stability of the (5×5) reconstruction and include it in the surface phase diagrams of Sec. 8.4. For Rh experimental results are available for the (100) surface. This substrate provides a completely different symmetry than the previously discussed (111) surface. We will analyze and compare the stability of ZnO on both surfaces of Rh. This will lead us to a broader understanding of strain in the ZnO films and how it influences their stability with respect to H-reconstructions.

10.1 ZnO (0001)- (5×5) /Ag (111)- $(3\sqrt{3} \times 3\sqrt{3})R30^\circ$

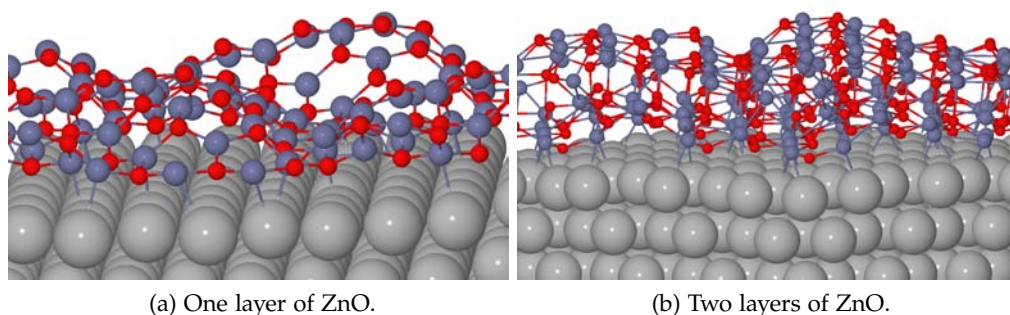
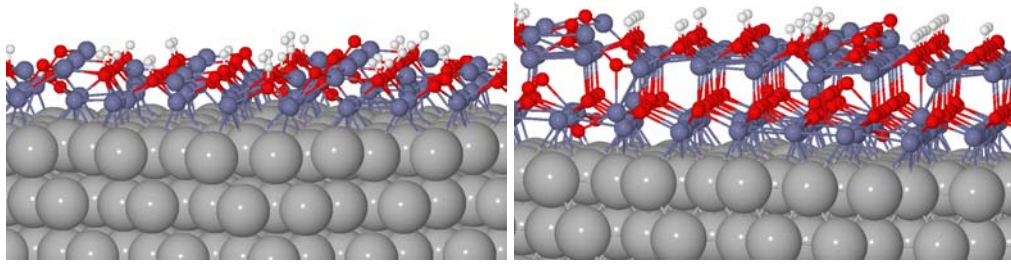


Figure 77: Side view of one a) and two b) layers of ZnO on Ag in the ZnO (0001)- (5×5) /Ag (111)- $(3\sqrt{3} \times 3\sqrt{3})R30^\circ$ reconstruction proposed by Shiotari *et al.* [237]. A highly corrugated, domed structure is formed for one and two layers.

Several authors reported coincidence structures from direct (STM) or indirect observation (LEED) that differ from the structure deduced in Sec. 6 [237, 159]. The focus in this section will be on the ZnO (0001)- (5×5) /Ag (111)- $(3\sqrt{3} \times 3\sqrt{3})R30^\circ$ reconstruction observed and described by Shiotari *et al.* [237]. In their work ZnO was grown on an Ag (111) substrate, that was cleaned by Ar ion sputtering and annealing prior to Zn deposition. The deposition chamber ($p < 5 \times 10^{-10}$ mbar) was separated from the measurement chamber. The Zn was deposited on the substrate at room temperature by heating a Zn-rod in a Knudsen cell [188] to 490 K. During growth a high partial pressure of O_2 was set (5×10^{-5} mbar). This procedure followed an annealing step under UHV conditions ($p < 5 \times 10^{-10}$ mbar) at 670 K. In the following, we will consider a temperature of 600 K.

Shiotari *et al.* [237] showed that the ZnO islands and films become well-ordered



(a) One layer of (2×1) -H reconstructed ZnO. (b) Two layers of (2×1) -H reconstructed ZnO.

Figure 78: Side view of one a) and two b) layers of ZnO on Ag in the ZnO (0001)- (5×5) /Ag (111)- $(3\sqrt{3} \times 3\sqrt{3})R30^\circ$ reconstruction proposed by Shiotari *et al.* [237]. The ZnO is (2×1) -H reconstructed. The corrugated and domed structure is regularized by H-adsorption and a nearly regular wurtzite structure in the ZnO is observed.

only for annealing temperatures above 600 K. Significantly higher temperatures lead to the sublimation of ZnO. The edges of the observed islands at low coverages act as aggregation point for subsequent layers during annealing. The films grow in preferential directions following the crystallographic plains of the Ag (111) substrate. The predominantly observed structure is the ZnO (0001)- (7×7) /Ag (111)- (8×8) reconstruction, also reported by other authors [259, 192]. LEED patterns revealed streaky ZnO refraction spots, indicating different azimuthal orientations of the films with respect to the Ag substrate [237] (for ZnO on Pt see Ref. [159]). Apart from the ZnO (0001)- (7×7) /Ag (111)- (8×8) reconstruction Shiotari *et al.* [237] could image another Moiré structure that is less abundant. The structure has a periodicity of about 16\AA and an azimuthal orientation of 30° relative to the Ag (111) high symmetry directions. Shiotari *et al.* [237] proposed a ZnO (0001)- (5×5) /Ag (111)- $(3\sqrt{3} \times 3\sqrt{3})R30^\circ$ reconstruction as a possible model for this structure. We will assess the stability of this model structure with the *ab initio* thermodynamics framework presented in the previous sections (see [214] and Sec. 1.6).

In Fig. 77 the structure of one layer of ZnO (0001)- (5×5) /Ag (111)- $(3\sqrt{3} \times 3\sqrt{3})R30^\circ$ is shown. The structure was initialized in the ideal α -BN structure with an in-plane lattice parameter of $a=3.05\text{\AA}$ which results in 7% strain with respect to the ideal freestanding ZnO mono-layer. The strain for the theoretically predicted ZnO (8×8) /Ag (9×9) reconstruction is only $\sim 1\%$. The lattice parameter of the substrate was kept at the equilibrium value obtained with the PBE xc-functional [196]. The strain in the ZnO (0001)- (5×5) /Ag (111)- $(3\sqrt{3} \times 3\sqrt{3})R30^\circ$ reconstruction leads to a highly corrugated structure for one and two layers of ZnO (see Fig. 77). The complete film is partially lifted from the substrate and a "domed" structure is formed. The regular but highly strained wurtzite structure of ZnO can be retained by absorbing H at the surface. In Fig. 78 the ZnO (0001)- (5×5) /Ag (111)- $(3\sqrt{3} \times 3\sqrt{3})R30^\circ$ reconstruction is shown with an additional (2×1) -H reconstruction of the ZnO for one and two layers of ZnO. The ZnO (0001)-O structure is not recovered as perfectly as for the regular coincidence

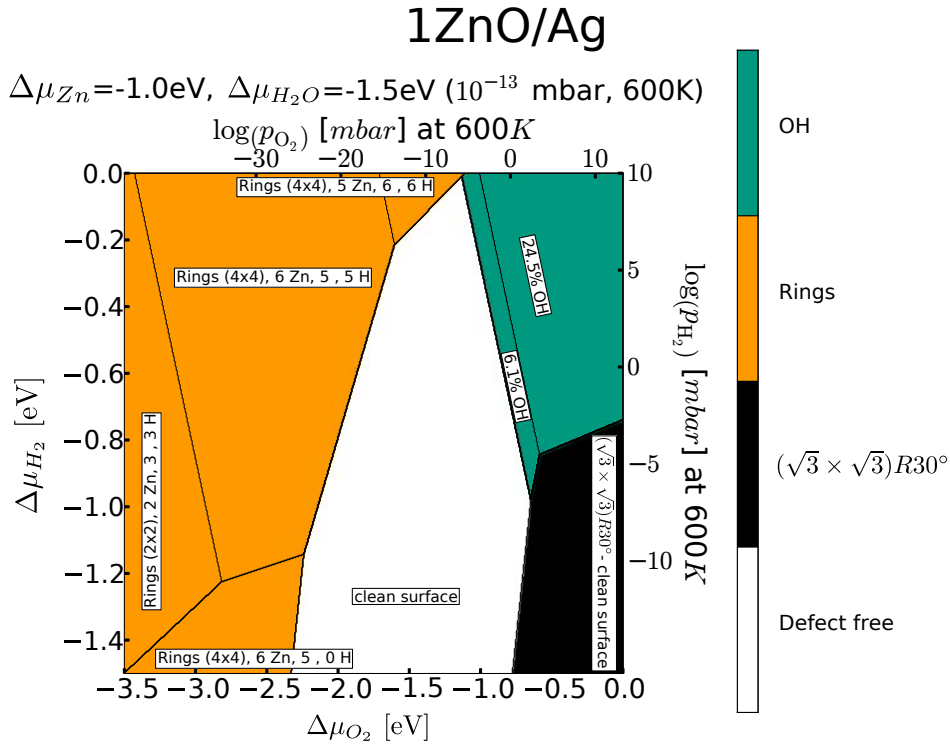


Figure 79: Surface phase diagram for one layer of ZnO on Ag including the ZnO (0001)-(5 × 5)/Ag (111)-(3√3 × 3√3)R30° reconstruction [237] for $\mu_{\text{Zn}} = -1.0$ eV.

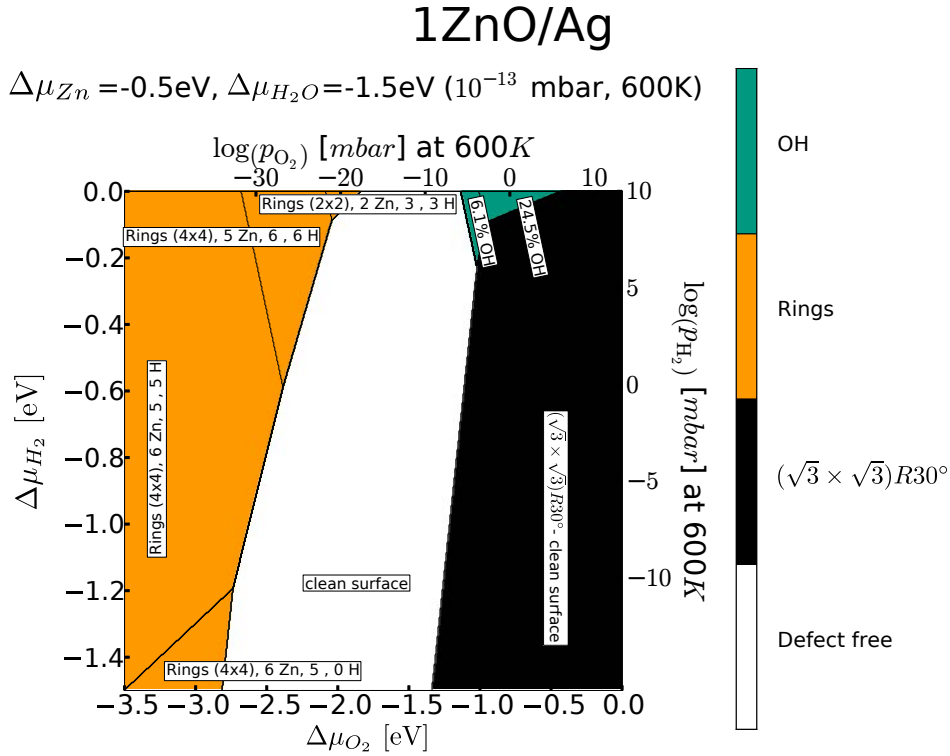


Figure 80: Surface phase diagram for one layer of ZnO on Ag including the ZnO (0001)-(5 × 5)/Ag (111)-(3√3 × 3√3)R30° reconstruction [237] for $\mu_{\text{Zn}} = -0.5$ eV.

structure. A few O and Zn atoms still deviate from the wurtzite structure, but no large scale corrugation or partial lifting of the film from the substrate was found. The ZnO (0001)-(5 × 5)/Ag (111)-(3√3 × 3√3)R30° reconstruction has a much denser structure as compared to the ZnO (8×8)/Ag (9×9) coincidence. We expect the Zn and O chemical potentials to influence the stability of those two types of structures and we therefore will investigate this dependence next.

In Fig. 79 and Fig. 80 the surface phase diagram for one layer of ZnO on Ag is shown for two different values of μ_{ZnO} . The pool of structures includes the ZnO (0001)-(5 × 5)/Ag (111)-(3√3 × 3√3)R30° reconstruction with and without hydrogen. The water chemical potential is kept constant at -1.5 eV for both surface phase diagrams. The temperature is set to 600 K to be comparable to experimental results. The previously discussed behavior of sparse ring structures being stabilized at low Zn chemical potentials is observed for low O chemical potentials (see sec. 8.3). For low Zn chemical potentials (Fig. 79) the ZnO (0001)-(5 × 5)/Ag (111)-(3√3 × 3√3)R30° reconstruction is only stabilized at high O chemical potentials and no H-reconstruction is present for this reconstruction. At low O₂ chemical potential sparse ring structures prevail. Upon increasing the Zn chemical potential the ring structures start to retreat from the surface phase diagram. The stability region of the ZnO (0001)-(5 × 5)/Ag (111)-(3√3 × 3√3)R30° reconstruction on the other hand is increased to O partial pressures at 600 K that are encountered in experiment. Both coincidence structures (reconstructions) lie in the region of experimental conditions. Further increase of the Zn chemical potential results in a further stabilization of the ZnO (0001)-(5 × 5)/Ag (111)-(3√3 × 3√3)R30° reconstruction, which then dominates the surface phase dia-

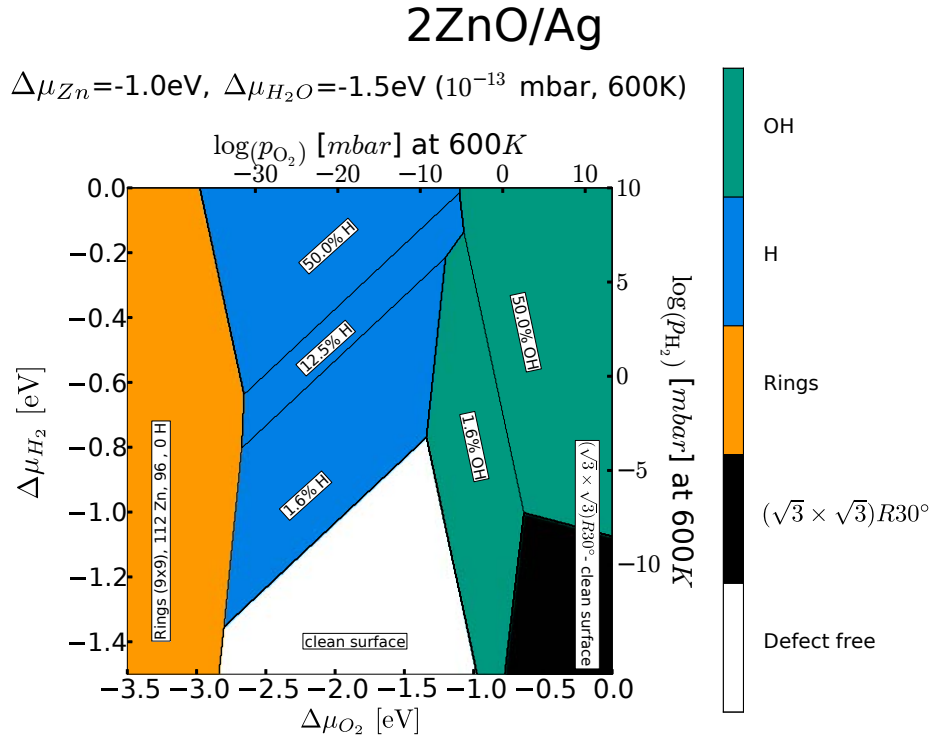


Figure 81: Surface phase diagram for two layers of ZnO on Ag including the ZnO (0001)-(5 × 5)/Ag (111)-(3√3 × 3√3)R30° reconstruction [237] for $\mu_{\text{Zn}} = -1.0$ eV.

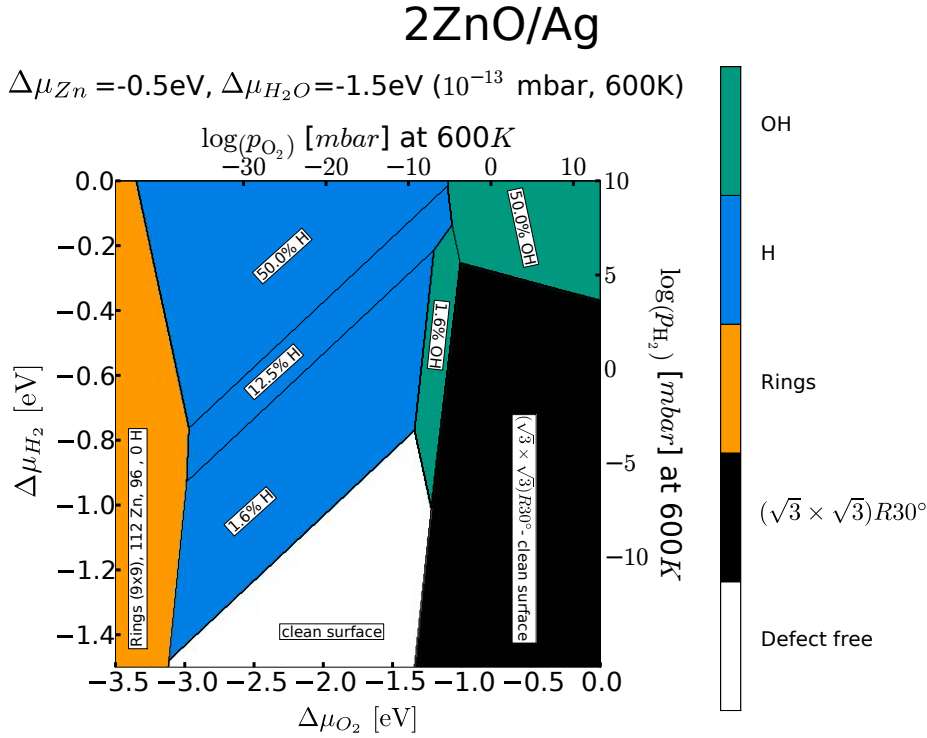


Figure 82: Surface phase diagram for two layers of ZnO on Ag including the ZnO (0001)-(5 × 5)/Ag (111)-(3√3 × 3√3)R30° reconstruction [237] for $\mu_{\text{Zn}} = -0.5$ eV.

gram. This would contradict experimental results, which report the ZnO (0001)-(5 × 5)/Ag (111)-(3√3 × 3√3)R30° reconstruction to be less abundant than the ZnO (0001)-(7×7)/Ag (111)-(8×8) reconstruction.

Shiotari *et al.* [237] suggested that their films have a thickness of two layers, although some uncertainty remains. In Fig. 81 and Fig. 82 the surface phase diagrams for two layers of ZnO on Ag for two different Zn chemical potentials are shown including the ZnO (0001)-(5 × 5)/Ag (111)-(3√3 × 3√3)R30° reconstruction. The behavior is similar to the one layer case. With increasing Zn chemical potential the ZnO (0001)-(5 × 5)/Ag (111)-(3√3 × 3√3)R30° reconstruction is stabilized. We expect that the observation of the ZnO (0001)-(5 × 5)/Ag (111)-(3√3 × 3√3)R30° reconstruction is highly dependent on the conditions during film growth. The initial high surface concentration of Zn during film growth by MBE is subsequently reduced during the annealing step, when ZnO forms by oxidation. ZnO (0001)-(5 × 5)/Ag (111)-(3√3 × 3√3)R30° will initially form, but is expected to transform to ZnO (0001)-(7×7)/Ag (111)-(8×8). This (full) transformation could be kinetically hindered e. g. by a reduced diffusion length due to the low temperature (5 K) during the measurement process.

In conclusion, we find the experimentally observed ZnO (0001)-(5 × 5)/Ag (111)-(3√3 × 3√3)R30° reconstruction of Ref. [237] to be stable under experimental conditions for high Zn chemical potentials. During growth/annealing the Zn chemical potential is expected to decrease due to the formation of ZnO and possible sublimation of Zn. The ZnO (0001)-(5 × 5)/Ag (111)-(3√3 × 3√3)R30° structure is than expected to transform to the regular coincidence structure, that is predicted to be the most stable structure at low Zn chemical potentials (also

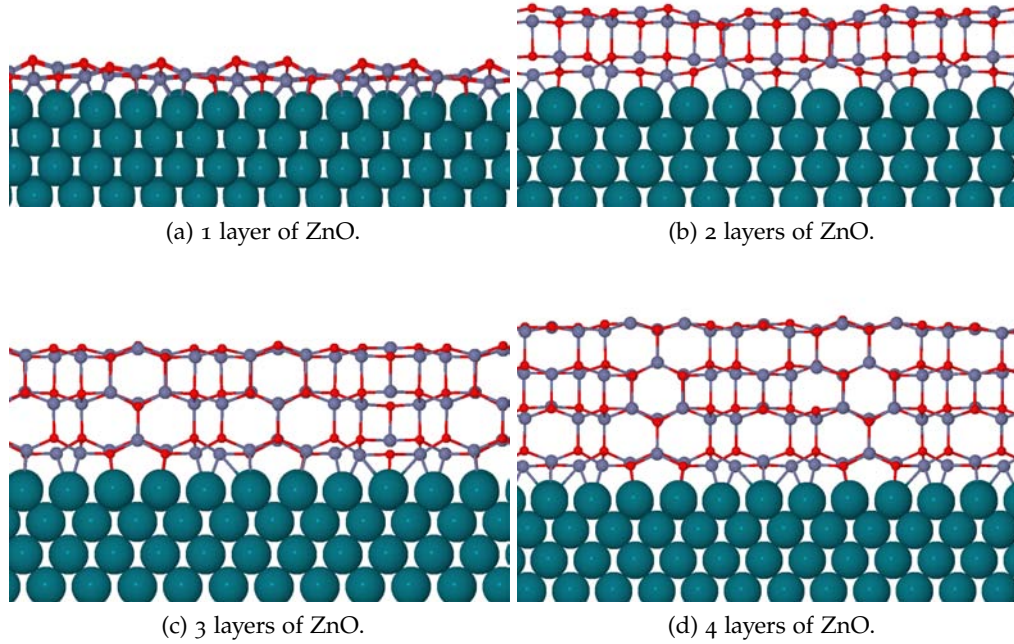


Figure 83: Atomic structure of 1 to 4 layers (a - c) of ZnO deposited on Rh (100). The calculation was initialized in the α -BN structure and the forces on the atoms relaxed by a DFT calculation employing the semi-local functional PBE [196]. The coincidence structure between ZnO and Rh is based on the data measured by Kato et al.[120] and the model proposed by the same authors.

see discussion in Sec. 8.4). The transformation of the ZnO (0001)- (5×5) /Ag (111)- $(3\sqrt{3} \times 3\sqrt{3})R30^\circ$ reconstruction could be hindered due to kinetic effects, such as small diffusion lengths due to the very low temperatures during measurements (5 K).

10.2 RH (100)

In the previous sections we discussed the structure of ZnO (0001) on different transition metals. The focus was entirely on the (111) surfaces of these metals. The choice of this crystallographic surface is obvious. The three-fold symmetry of ZnO is matched with the same symmetry on the (111) metal surface (see Sec. 6). The ZnO films align with the substrate and the mismatch in lattice parameter is compensated by a coincidence structure. To investigate the influence of non-uniaxial strain, other substrates without three-fold symmetry can be used. Experimentally the same technique to deposit ZnO on the (111) surface (MBE, see Ref. [188]) can be applied for other crystallographic surfaces. In this section, we will investigate the atomic structure, stability and electronic structure of ZnO on the (100) surface of Rh. This combination of transition metal surface and ZnO thin films has been experimentally prepared and investigated by Kato *et al.* [120]. The analysis will make use of the surface/interface model developed by those

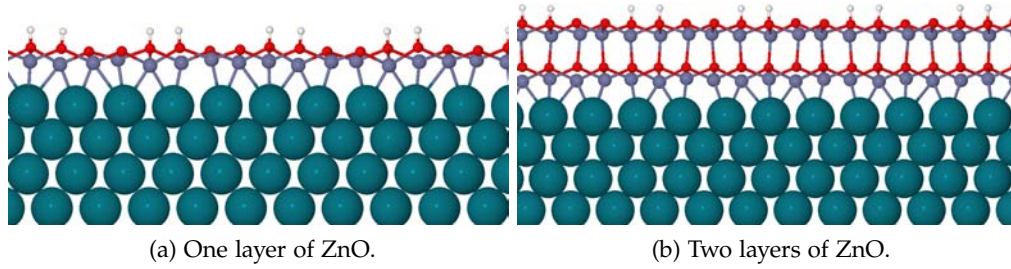


Figure 84: Atomic structure of one a) and two b) layers of (2×1) -H reconstructed ZnO on Rh (100). The geometries were initialized in α -BN structure and relaxed employing the semi-local xc-functional PBE [196].

authors.

Kato *et al.* [120] deposited a Zn film on a Rh (100) crystal surface, that was cleaned by Ar sputtering and annealing. Zn was deposited by a degassed quartz crucible evaporator at room temperature. The sample was subsequently annealed up to 600 K at oxygen partial pressures ranging from 1×10^{-9} mbar to 2×10^{-7} mbar. The base pressure of the vacuum system consisting of a preparation and measurement chamber was 5×10^{-10} mbar (4×10^{-11} mbar in measurement chamber). The long range order of the sample was determined by LEED and local high resolution data was acquired by STM at room temperature. Based on their high resolution STM measurements Kato *et al.* [120] proposed a ZnO $(13 \times 2)/\text{Rh}(100)$ (16×2) coincidence structure. In their model the ZnO film is compressed by 5% in the $[1000]$ direction and, 2% stretched in the $[0\bar{1}00]$ direction. Kato *et al.* [120] measured the corrugation to be 0.04 nm.

We will use this model structure of Kato *et al.* [120] as input for a DFT investigation based on the semi-local PBE xc-functional [196]. For our calculations we employed the equilibrium lattice parameter for Rh, obtained with the PBE xc-functional, to minimize strain in the substrate. The lattice parameter of ZnO we adjusted to produce the experimentally observed ZnO- $(13 \times 2)/\text{Rh}(100)$ - (16×2) coincidence structure. In this structure, based on the theoretical lattice parameter, ZnO is strained by -3.8% in the $[1000]$ direction and +1.6% in the $[0\bar{1}00]$ direction. The compression/stretching is slightly less than in experiment. We initialized the ZnO film in the α -BN structure and allowed it to relax until the forces on the atoms in the film and the two top most Rh layers were below $0.05 \text{ eV}/\text{\AA}$. The results for one to four layers of ZnO in the ZnO $(13 \times 2)/\text{Rh}(100)$ (16×2) reconstruction are shown in Fig. 83.

In our calculations, the strain leads to the formation of a d-BCT structure proposed for ZnO thin films by Morgan *et al.* [171, 169, 170] and Demiroglu *et al.* [65]. The actual realization of this structure depends strongly on the strain because of the lattice mismatch between the Rh substrate and the ZnO ultra-thin film. The inhomogeneous strain (extension/compression) seems to facilitate the formation of the d-BCT for ZnO on Rh (100). For ZnO on the (111) surface of different transition metal substrates no such pronounced d-BCT structure could be observed

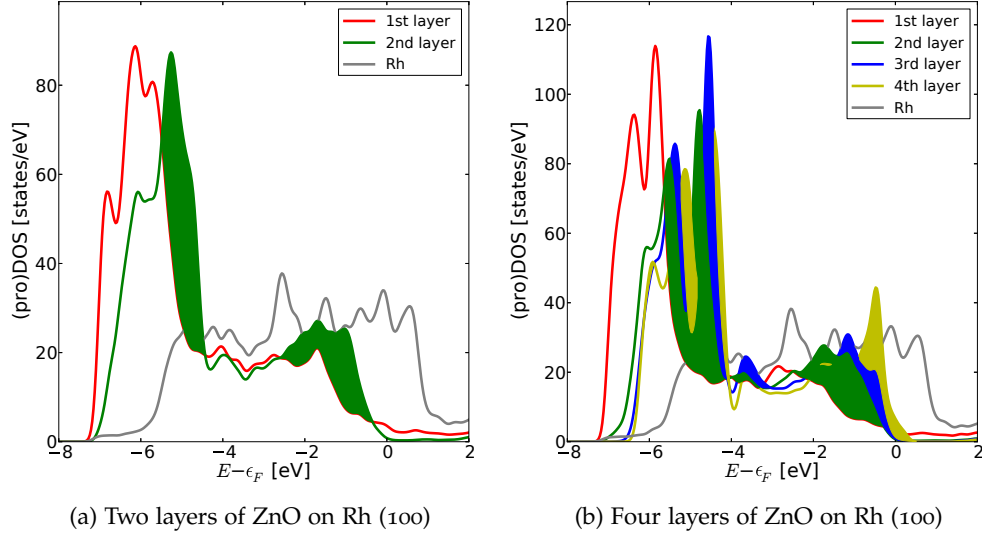


Figure 85: Projected density of states for two layers and four layers of ZnO on Rh (100). The density is projected on Rh and each ZnO layer. The area underneath the curves for layer numbers greater than one, which have shifted up in energy is filled with the color of the curve of this layer.

(see Sec. 7.1). Only for 3 and 4 layers of ZnO on Ni and 4 layers on Rh (111) the d-BCT ZnO was observed. For ZnO on Rh (100) already the mono-layer shows the regular corrugation leading to the full d-BCT structure for thicker films.

To assess the stability of the ZnO films on Rh (100) we will investigate the effect of hydrogen adsorption by considering the unreconstructed surface and the (2×1) -H reconstruction. The focus lies on the point in the surface phase diagram, at which the (2×1) -H reconstructed ZnO thin film becomes stable with respect to the unreconstructed film. The atomic structures of (2×1) -H reconstructed one and two layer thick ZnO films on Rh (100) are shown in Fig. 84. The ZnO films have adopted the wurtzite structure. The alignment of the Zn and O atoms is not as perfect as in the case of the (111) metal surface substrate. Some residual disorder remains. With the help of the modified *ab initio* thermodynamics approach proposed by Hermann and Heimel [98] (also see sec. 1.6) we can determine the transition point from the clean to the (2×1) -H reconstructed surface as a function of H_2 chemical potential. For fixed Zn ($\Delta\mu_{Zn}=0.0$ eV), O_2 ($\Delta\mu_{O_2}=-0.9$ eV) and H_2O ($\Delta\mu_{H_2O}=-0.9$ eV) chemical potential the transition occurs at a H_2 chemical potential of $\Delta\mu_{H_2}=-0.1$ eV for one layer of ZnO and at even higher H_2 chemical potential for two layers. For ZnO on Rh (111) the transition is predicted to occur already at -1.0 eV for one layer and at -1.5 eV for two layers (see Fig. 72). Expressed in partial pressure at 400 K this would amount to 1×10^{-20} mbar and 1×10^{-25} mbar for one and two layers of ZnO on Rh (111). We therefore predict the unreconstructed ZnO films on Rh (100) for the coincidence structure by Kato et al.[120] to be more stable than the films on Rh (111) with respect to hydrogen absorption.

Finally, we will discuss the electronic structure of ZnO on Rh (100). The projected density of states for one and two layers of ZnO on Rh (100) with and without hydrogen are shown in Fig. 85 and Fig. 86. The density is projected on the single

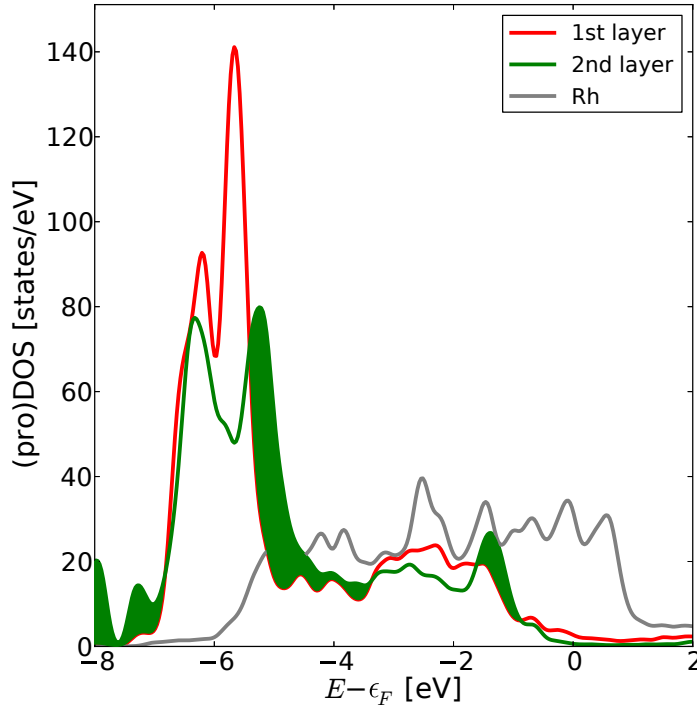


Figure 86: Projected density of states for two layers of (2×1) -H reconstructed ZnO on Rh (100). The density is projected on the metal and each ZnO layer. The area underneath the curves for layer numbers greater than one, which have shifted up in energy is filled with the color of the curve of this layer.

layers of ZnO. A shift towards the Fermi level provided by the metal is observed for both cases. For the hydrogen free case the effect is larger. For four layers of ZnO on Rh (100) the behavior is similar to the situation for ZnO on metal (111) substrates. Due to the intrinsic field inside the ZnO films the electronic states of each successive layer are pushed higher in energy, closer to the Fermi level, where they are eventually pinned. The electronic states of four layers of ZnO on Rh (100) are shifted slightly less up in energy than for ZnO on Rh (111) and the states close to the Fermi energy show a smaller density. For the (2×1) -H reconstructed surface in Fig. 86 the intrinsic field is quenched and the position of the electronic states stays fixed throughout the extend of the film.

In conclusion we find that the uniaxial strain imposed on the ZnO films by depositing on the Rh (100) surface promotes the formation of a d-BCT structure. The regular wurtzite structure can be retained by absorbing hydrogen at the surface, leading to a (2×1) -H surface reconstruction. With the help of *ab initio* thermodynamics we predict the (2×1) -H reconstruction to be much less stable than in the case of a (111) metal substrate. The surface without hydrogen is predicted to be stable for a wide range of chemical potentials and therefore different from the polar ZnO surfaces (0001)-Zn and (000 $\bar{1}$)-O. We find the evolution of the electronic structure with film thickness to be governed by the same effects as for a (111) metal substrate described in Sec. 7.2.

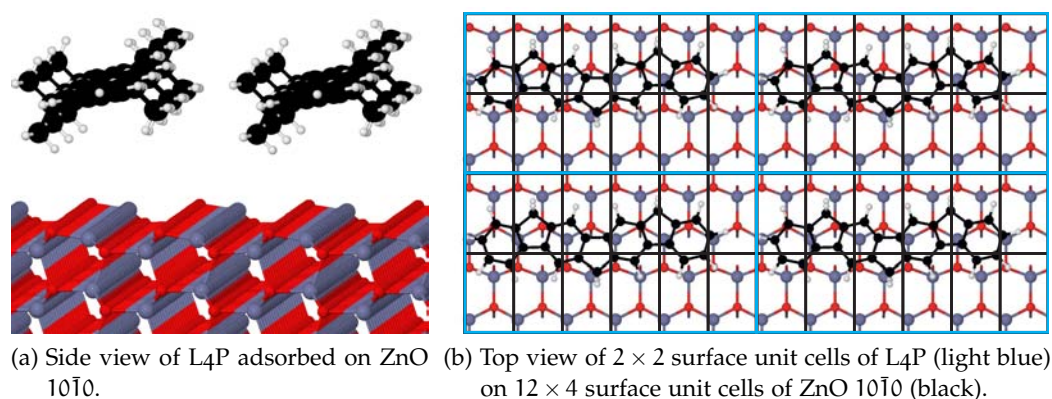


Figure 87: Ladder-type oligomers (L4P) [127] adsorbed on ZnO $10\bar{1}0$.

In the previous Chapters the focus of the theoretical work was on the description of the atomic and electronic structure of ZnO ultra-thin films on transition metals. These systems are the first step to quantitatively characterize hybrid systems composed of an inorganic semiconductor and an organic light harvesting molecule [21, 176, 3, 142], which opens the path to new device functionality. Recently, experimental evidence for non-radiative energy transfer processes between ZnO and organic molecule has been found [108, 46, 34]. However, the exact excitation transfer mechanism is difficult to determine experimentally. A proper description of those processes could open the path for tailoring new devices for opto-electronics. While it is crucial to understand the inorganic substrate (ZnO) fully (by modeling via ultra-thin films) a significant effort is required to accurately describe the interaction processes between organic molecule and the ZnO surface. As a first step towards this description, we investigated the optical absorption in such a hybrid system in collaboration with E. Verdenhalven, A. Knorr and M. Richter from the Technical University of Berlin (TU Berlin) as part of this work [265]. Within a Heisenberg equation of motion technique, Bloch equations for such hybrid systems were derived by E. Verdenhalven, A. Knorr and M. Richter. We then parameterized the model with the atomic and electronic structure obtained from DFT calculations (this work) employing the hybrid xc-functional HSE06 [100]. A more detailed description and derivation of the "hybrid Bloch equations" can be found in the next section and in Ref. [265].

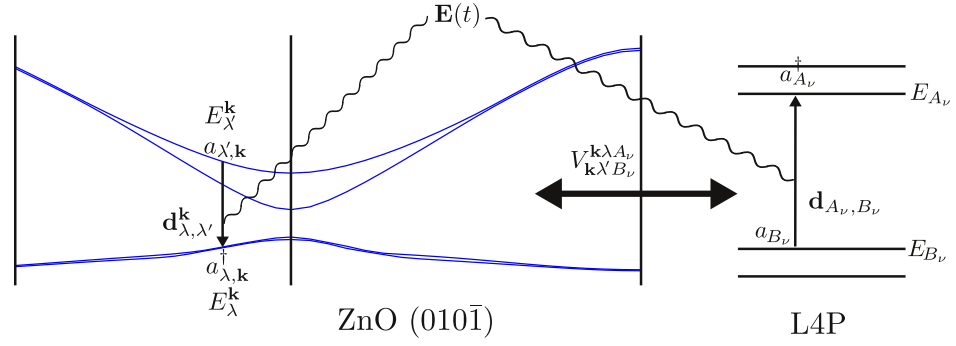


Figure 88: Illustration of the operators and values entering the Hamiltonian (eq.110).

11.1 LINKING TO DENSITY-MATRIX THEORY

Density functional theory can be used to investigate equilibrium properties of surfaces. To gain inside into the dynamical properties of inorganic/organic hybrid systems a density matrix formalism based on a Heisenberg equation of motion technique [143, 218] is applied [265]. Of special interest are excitonic processes between the organic and inorganic component of our system without electronic wave-function overlap (Förster processes [82]). We here consider energy transfer from molecular excitations to semiconductor continuum states. The semiconductor offers many states for coupling to the molecule. If the coupling proves to be strong enough this would provide an efficient way for exciting the molecule by external electrical pumping. The equations presented below are based on a canonically quantized description (second quantization). We will focus on ladder-type oligomers (L4P) [127] adsorbed on a semiconducting surface (ZnO (10\bar{1}0)). An example of such a model systems is shown in Fig. 87. The description of excitonic processes can in principle be achieved on the level of a first principle calculation e.g. by Greens function based perturbation theory (GW) [97, 106, 10] extended by the Bethe-Salpeter equation (BSE) [224, 216]. These methods provide a powerful tool set for investigating excited states, but are not (yet) feasible for the system of interest in this work. The reader is referred to recent reviews from the literature for further information [10, 186]. Here we follow the approach developed by E. Verdenhalven, A. Knorr and M. Richter based on a density matrix formalism [265].

The Hamiltonian for the systems described above can be defined as:

$$H = H_M + H_{SC} + H_{e-l} + H_{int} \quad (108)$$

which is divided into four parts. The Hamiltonian for the isolated molecule

$$H_M = \sum_{A,\nu} E_{A_\nu} a_{A_\nu}^\dagger a_{A_\nu}. \quad (109)$$

and for the isolated semiconductor

$$H_{SC} = \sum_{k,\lambda} E_\lambda^k a_{\lambda,k}^\dagger a_{\lambda,k}. \quad (110)$$

The electron-light interaction, described as interaction between the quantized electrons and an external classical field [108], is treated semi-classically within the dipole approximation [123]

$$H_{e-l} = \sum_{\mathbf{k}, \lambda \neq \lambda'} \mathbf{d}_{\lambda, \lambda'}^{\mathbf{k}} \cdot \mathbf{E}(t) a_{\lambda, \mathbf{k}}^{\dagger} a_{\lambda', \mathbf{k}} + \sum_{\nu, A \neq B} \mathbf{d}_{A_{\nu}, B_{\nu}} \cdot \mathbf{E}(t) a_{A_{\nu}}^{\dagger} a_{B_{\nu}} \quad (111)$$

and the Coulomb interaction between the electrons in the semiconductor and the molecule

$$H_{\text{int}} = \sum_{\mathbf{k}, \mathbf{k}', \nu} \left(V_{\mathbf{k}'cH_{\nu}}^{\mathbf{k}\nu L_{\nu}} a_{\mathbf{k}\nu}^{\dagger} a_{L_{\nu}}^{\dagger} a_{H_{\nu}} a_{\mathbf{k}'c} + V_{\mathbf{k}'\nu L_{\nu}}^{\mathbf{k}c H_{\nu}} a_{\mathbf{k}c}^{\dagger} a_{H_{\nu}}^{\dagger} a_{L_{\nu}} a_{\mathbf{k}'\nu} \right). \quad (112)$$

All contributions are illustrated in Fig. 88. The indexes A_{ν} number the states of the ν -th molecule in the model. Here we only take the highest occupied molecular orbital (HOMO) and lowest unoccupied molecular orbital into account. They are indexed with H_{ν} and L_{ν} for the ν -th molecule. \mathbf{k} is the wave vector in the semiconductor. For a surface it is a two-dimensional vector, corresponding to the in-plane directions. The bands are indexed by λ . The conduction band is labeled c and the valence band is labeled v . $E_{A_{\nu}}$ is the quasi electron/hole energy of the molecule and $E_{\lambda}^{\mathbf{k}}$ the quasi-electron/hole energy of the semiconductor. They will be approximated by the Kohn-Shan eigenenergies obtained from DFT calculations.

We have described the molecule in a localized, non-lattice periodic basis. In order to describe semiconductor and molecules in the same Bloch momentum representation [240] we assume a periodic arrangement of equal molecules. This is achieved by introducing two dimensional wave-vectors \mathbf{l} for the molecular operators in eq. 110-112

$$a_{A_{\nu}} = \sum_{\mathbf{l}} \frac{1}{\sqrt{N_M}} e^{-i\mathbf{l} \cdot \mathbf{R}_{\nu}} a_{A, \mathbf{l}}. \quad (113)$$

N_M is the total number of molecules in our model. By definition the area of the super cell containing the molecules $A = N_M A_M$ must be equal to the area of the surface unit cell containing the semiconductor unit cells $A = N_{SC} A_{SC}$ to not violate periodic boundary conditions. With eq. 110-112 and the properties of the periodically arranged molecules the Hamiltonian can be transformed to the Bloch basis representation

$$H_M = \sum_A E_A \sum_{\mathbf{l}} a_{A, \mathbf{l}}^{\dagger} a_{A, \mathbf{l}}, \quad (114)$$

$$H_{e-l} = \sum_{\mathbf{k}, \lambda \neq \lambda'} \mathbf{d}_{\lambda, \lambda'}^{\mathbf{k}} \cdot \mathbf{E}(t) a_{\lambda, \mathbf{k}}^{\dagger} a_{\lambda', \mathbf{k}} + \sum_{A, B} \mathbf{d}_{AB} \cdot \mathbf{E}(t) \sum_{\mathbf{l}} a_{A, \mathbf{l}}^{\dagger} a_{B, \mathbf{l}}, \quad (115)$$

$$H_{\text{int}} = \frac{1}{A_{SC} N_{SC}} \sum_{\mathbf{k}, \mathbf{k}', \mathbf{l}, \mathbf{l}'} \sum_{\mathbf{G}} \delta_{\mathbf{l}-\mathbf{l}', \mathbf{k}-\mathbf{k}'+\mathbf{G}} \left(V_{\mathbf{k}'cH}^{\mathbf{k}\nu L} a_{\nu, \mathbf{k}}^{\dagger} a_{L, \mathbf{l}}^{\dagger} a_{H, \mathbf{l}'} a_{c, \mathbf{k}'} \right. \\ \left. + V_{\mathbf{k}'\nu L}^{\mathbf{k}c H} a_{c, \mathbf{k}}^{\dagger} a_{H, \mathbf{l}}^{\dagger} a_{L, \mathbf{l}'} a_{\nu, \mathbf{k}'} \right). \quad (116)$$

The Coulomb matrix element $V_{\mathbf{k}'\lambda'\Lambda}^{\mathbf{k}\lambda\Lambda}$ is now defined without the molecular positions \mathbf{R}_ν

$$V_{\mathbf{k}'\lambda'\Lambda}^{\mathbf{k}\lambda\Lambda} = A_{SC} N_{SC} \sum_{\nu} e^{-i(\mathbf{k}-\mathbf{k}')\cdot\mathbf{R}_\nu} V_{\mathbf{k}'\lambda'\Lambda_\nu}^{\mathbf{k}\lambda\Lambda_\nu}. \quad (117)$$

The combination of the two periodic lattices of molecule and semiconductor surface give the Kronecker-symbol in eq. 114-116, which yields a selection rule for the momentum transfer.

The goal is to calculate the (macroscopic) absorption of the semiconductor $\mathbf{P}_{SC}(t)$ and the molecule $\mathbf{P}_M(t)$. They are linked to the microscopic expectation values of the electronic transition amplitudes $\sigma_{vc}^{\mathbf{k}\mathbf{k}'}$ and $\sigma_{HL}^{\mathbf{l}\mathbf{l}'}$ via

$$\mathbf{P}_{SC}(t) = \frac{2}{V} \sum_{\mathbf{k}} \text{Re} \left[\mathbf{d}_{\mathbf{k}}^{vc} \sigma_{vc}^{\mathbf{k}\mathbf{k}'} \right] \quad (118)$$

$$\mathbf{P}_M(t) = \frac{2}{V} \sum_{\mathbf{l}} \text{Re} \left[\mathbf{d}_{HL} \sigma_{HL}^{\mathbf{l}\mathbf{l}'} \right] \quad (119)$$

where V is the volume of the full system. The microscopic inter-band polarization in the semiconductor $\sigma_{vc}^{\mathbf{k}\mathbf{k}'} = \langle a_{\mathbf{k},v}^\dagger a_{\mathbf{k}',c} \rangle$ and the microscopic molecular polarization $\sigma_{HL}^{\mathbf{l}\mathbf{l}'} = \langle a_{\mathbf{l},H}^\dagger a_{\mathbf{l}',L} \rangle$ can be calculated by the Heisenberg equation of motion

$$\frac{d}{dt} \sigma(t) = \frac{i}{\hbar} [H, \sigma(t)] + \frac{\partial \sigma}{\partial t}. \quad (120)$$

Here the hierarchy problem resulting from the correlation expansion of the Coulomb interaction is truncated at the level of Hartree-Fock [143, 123, 15, 89]. The resulting closed set of equations can be solved in frequency space by Fourier transformation. Here we only reproduce the closed solution

$$\sigma_{HL}^{\mathbf{l}\mathbf{l}'} \equiv \sigma_{HL}^{\mathbf{l}}(\omega) = X_{LH}(\omega) \hat{\mathbf{E}}(\omega) \cdot \mathbf{d}_{LH} (\rho_H - \rho_L) \left[1 - X_{LH}(\omega) \frac{N_m}{A^2} \times \sum_{\mathbf{k}_l} \sum_{\mathbf{G}} \left| V_{\mathbf{k}_l+\mathbf{G}cH}^{\mathbf{k}_l vL} \right|^2 Y_{\mathbf{k}_l, \mathbf{k}_l+\mathbf{G}}(\omega) \left(\rho_v^{\mathbf{k}_l} - \rho_c^{\mathbf{k}_l+\mathbf{G}} \right) (\rho_H - \rho_L) \right]^{-1}, \quad (121)$$

with the single energy particle poles

$$X_{LH}(\omega) = [\hbar\omega - (E_L - E_H) + i\gamma_M]^{-1} \quad (122)$$

and

$$Y_{\mathbf{k}, \mathbf{k}'}(\omega) = [\hbar\omega - (E_c^{\mathbf{k}'} - E_v^{\mathbf{k}}) + i\gamma_{SC}]^{-1}. \quad (123)$$

We introduced the phenomenological line-widths γ_M and γ_{SC} for transitions in the molecular layer and semiconductor surface. The missing ingredients are the dipole-matrix-elements \mathbf{d}_{LH} and the Coulomb matrix elements $V_{\mathbf{k}_l+\mathbf{G}cH}^{\mathbf{k}_l vL}$ in eq. 121. The input geometry and energy (band structure) have to be obtained as well. We will approximate those with the band structure of ZnO and the eigen-energies

of L4P obtained from DFT calculations carried out with the hybrid-xc-functional HSE06 [100]. The dipole-matrix-elements are taken from the same DFT calculation. For the Coulomb-matrix elements (Förster Transfer elements), facilitating the interaction between L4P and ZnO appropriate approximations have to be found. We will see in the next section, that this can be achieved by a parameterization derived from DFT calculations.

11.1.1.1 Dipole Approximation

The parameterization of the density matrix formalism has previously been developed for purely crystalline semiconductor surfaces [41]. The optical excitations and electron relaxation dynamics of Silicon surfaces were calculated by a DFT parameterization based on the band structure, momentum-matrix elements and phonon band structure obtained with a (semi)-local xc-functional. The first order approximation for the Coulomb-matrix elements appearing in eq. 121 is equivalent to the dipole-matrix elements between the semiconductor and the molecular system. The Coulomb matrix element is given by

$$V_{H_\nu k' \nu}^{L_\nu k c} = \int d^3 r \int d^3 r' \Psi_{L_\nu}^*(\mathbf{r}) \Psi_{k' \nu}^*(\mathbf{r}') V(\mathbf{r} - \mathbf{r}') \Psi_{H_\nu}(\mathbf{r}) \Psi_{k' c}(\mathbf{r}') \quad (124)$$

with the Coulomb potential

$$V(\mathbf{r} - \mathbf{r}') = \frac{1}{|\mathbf{r} - \mathbf{r}'|}. \quad (125)$$

Ψ_{A_ν} are the wave-functions of the ν th molecule. Next we Taylor expand [59] eq. 125. This leads to a factorization of the nested integrals in eq. 124. The integrals over the molecules and the semiconductor are evaluated independently. By taking into account the two-dimensionality of our surface we obtain a closed analytical form of the Förster transfer element:

$$V_{H_\nu k + q c}^{L_\nu k \nu} = \frac{1}{A} \frac{e^2}{2\epsilon_0} e^{i\mathbf{q} \cdot \mathbf{R}^\parallel} \frac{e^{-|\mathbf{q}| \Delta z}}{|\mathbf{q}|} \left[\begin{pmatrix} q_x \\ q_y \\ -i|\mathbf{q}| \end{pmatrix} \cdot \mathbf{d}_{LH} \right] \times \quad (126)$$

$$\left[\begin{pmatrix} q_x \\ q_y \\ -i|\mathbf{q}| \end{pmatrix} \cdot \mathbf{d}_{k, k+q}^{vc} \right]$$

Here we have defined $\mathbf{q} = \mathbf{k} - \mathbf{k}'$, \mathbf{R}^\parallel is the in-plane component of the center of mass of the semiconductor/molecule unit cell and Δz the distance between surface and molecule.

The dipole-matrix elements entering into eq. 126 and subsequently into eq. 121 can be calculated as a post-processing step in the same DFT-calculation. The option to calculate these matrix elements was implemented into FHI-aims as part of this dissertation. The implementation consists of three steps. First the integral over the unit cell is evaluated in real-space:

$$\langle \phi_{iM} | \mathbf{r} | \phi_{iN} \rangle = \int_{\text{unit cell}} d^3 r \phi_{iM}(\mathbf{r}) \mathbf{r} \phi_{iN}(\mathbf{r}) \quad (127)$$

with the numerical atom base functions $\phi_i(\vec{r})$ centered at unit cells shifted by $\vec{T}(\vec{N})$, $\vec{N} = (N_1, N_2, N_3)$. Further information about the basis set used in FHI-aims can be found in Sec. 1.7 and Ref. [33]. From these translation vectors the phase of the matrix elements is calculated. In the last step the matrix elements are transformed into the Kohn-Sham basis by matrix multiplication with the Kohn-Sham orbitals $c_{i\lambda}^k$.

$$d_{k',k}^{\lambda'\lambda} = \langle \psi_{\lambda'k} | r | \psi_{\lambda k} \rangle = \sum_{ij} c_{i\lambda'}^{*k} c_{j\lambda}^k \sum_{N,M} e^{ik[T(N)-T(M)]} \langle \phi_{iM} | r | \phi_{jN} \rangle \quad (128)$$

11.1.2 Partial charge approximation

The dipole approximation for the Coulomb matrix elements is quite drastic. To improve on the description, a well known method from the force field community is adapted to our problem. A similar approach was used for the description of strongly coupled pigments in light-harvesting complexes [150].

Here we will present a simplified derivation of the Coulomb matrix element from electro-static potential (ESP) partial charges. The starting point is again the Coulomb matrix element

$$V_{B_v k' \lambda'}^{A_v k \lambda} = \int d^3 r \int d^3 r' \Psi_{A_v}^*(\mathbf{r}) \Psi_{k\lambda}^*(\mathbf{r}') V(\mathbf{r} - \mathbf{r}') \Psi_{B_v}(\mathbf{r}) \Psi_{k' \lambda'}(\mathbf{r}'). \quad (129)$$

One-particle transition densities are defined as:

$$\rho_{A_v}^{B_v}(\mathbf{r}) = \Psi_{A_v}^*(\mathbf{r}) \Psi_{B_v}(\mathbf{r}). \quad (130)$$

With the help of this definition we can rewrite the Coulomb matrix as:

$$V_{B_v k' \lambda'}^{A_v k \lambda} = \int d^3 r \int d^3 r' \frac{\rho_{A_v}^{B_v}(\mathbf{r}) \rho_{k\lambda}^{k' \lambda'}(\mathbf{r}')}{|\mathbf{r} - \mathbf{r}'|}. \quad (131)$$

We can define the potential of the molecular part as

$$\phi_{A_v}^{B_v}(\mathbf{r}) = - \int d^3 r' \frac{\rho_{A_v}^{B_v}(\mathbf{r}')}{|\mathbf{r} - \mathbf{r}'|} \approx \sum_I \frac{q_{I, A_v}^{B_v}}{|\mathbf{r} - \mathbf{R}_{I_v}|} \quad (132)$$

and approximate it by atomic partial charges $q_{I, A_v}^{B_v}$, summed up over the atomic positions \mathbf{R}_{I_v} within the v -th molecule: $\mathbf{R}_{I_v} = \mathbf{R}_v + \mathbf{r}_I$. The Coulomb matrix element then reduces to

$$V_{B_v k' \lambda'}^{A_v k \lambda} \approx - \sum_I q_{I, A_v}^{B_v} \int d^3 r' \frac{\rho_{k\lambda}^{k' \lambda'}(\mathbf{r}')}{|\mathbf{R}_{I_v} - \mathbf{r}'|}. \quad (133)$$

We introduced the potential for the semiconductor $\phi_{k\lambda}^{k' \lambda'}$ in a similar fashion as for the molecular part of the system in eq. 132. The final expression for the Coulomb matrix approximated by sums over the partial charges from the molec-

ular part $q_{I,\Lambda_v}^{B_v}$ at the atomic positions \mathbf{R}_I and the semiconductor part $q_{J,k\lambda}^{k'\lambda'}$ at the atomic positions \mathbf{R}_J is

$$\begin{aligned} V_{B_v k' \lambda'}^{A_v k \lambda} &\approx \sum_I q_{I,\Lambda_v}^{B_v} \sum_{i=1}^{N_{\text{unitcell}}} \int_{\text{unitcell}} d\mathbf{r}_i \frac{\rho_{k\lambda}^{k'\lambda'}(\mathbf{r}_i)}{|\mathbf{r}_i - \mathbf{R}_{I_v}|} \\ &= \sum_{i=1}^{N_{\text{unitcell}}} e^{i(\mathbf{k}-\mathbf{k}') \cdot \mathbf{R}_{i\parallel}} \sum_{I,J} \frac{q_{Ik\lambda}^{k'\lambda'} q_{I,\Lambda_v}^{B_v}}{|\mathbf{R}_v + \mathbf{r}_J - \mathbf{R}_i - \mathbf{r}_I|}. \end{aligned} \quad (134)$$

The challenge is to find reliable partial charges for molecule and semiconductor. Such charges are widely used in the context of force fields ([168, 56, 239, 27], CHELP [48], CHELPG [39], RESP-charges [22], CHELP-BOW/CHELMO [238] or ESP-charge from multi-pole-moments [104]). As part of this dissertation a simple method for cluster calculations (molecules) as well as two methods for solids (periodic boundary conditions) [44, 47] were implemented in the FHI-aims code. The starting point for these methods is the calculation of the electrostatic potential at a sufficiently high number of grid points outside the vdW radius of the atoms. To define a spatial region for the grid, two parameters are necessary: a minimal and a maximal radius around the atoms. These radii are defined as multiples of the vdW-radius of the atoms, see Fig. 89 for details. The values for the vdW radii of most atoms in the periodic table have been taken from Ref. [35, 219, 155]. For the generation of the points, the atom-centered radial grids are used. All points lie on N spheres with radii between the minimal and maximal multiples of the vdW radius. The spacing between the radii of the N spheres is equidistant (default) or logarithmic (optional). Alternatively, cubic (Cartesian) grids are available. For cluster calculations, points within a cube encapsulating the spheres with the maximal radius (multiple of the vdW radius) around all atoms are generated. For periodic boundary conditions the provided unit cell is used. The points within the superposition of the spheres with the minimal radius (minimal multiple of the vdW radius) are again excluded.

For molecules and clusters (no periodic boundary conditions) the electrostatic

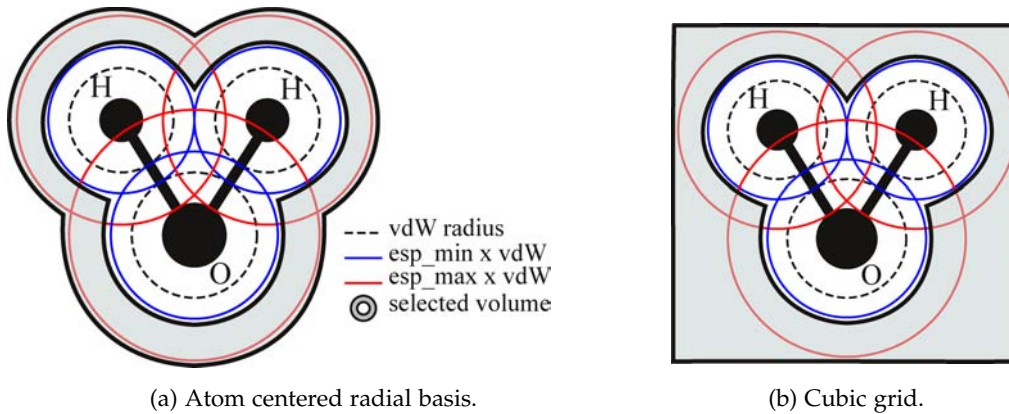


Figure 89: Definition of the volume used for the selection of grid points at which the potential is evaluated.

potential can be expressed by a sum of Coulomb potentials with charges q_i , the ESP-charges, at the atomic position \mathbf{R}_i :

$$V_{\text{ESP}}(\mathbf{r}) = \sum_{i=1}^{N_{\text{at}}} \frac{q_i}{|\mathbf{r} - \mathbf{R}_i|} \quad (135)$$

The q_i are calculated by a least squares fit with the additional constraint of constant total charge $q_{\text{tot}} = \sum_{i=1}^{N_{\text{at}}} q_i$. We use the method of Lagrange multipliers to minimize the function

$$F = \sum_{k=1}^{N_{\text{grid}}} (V_{\text{DFT}}(\mathbf{r}_k) - V_{\text{ESP}}(\mathbf{r}_k))^2 - \lambda \left(q_{\text{tot}} - \sum_{i=1}^{N_{\text{at}}} q_i \right)^2. \quad (136)$$

This can be translated into a system of linear equations

$$\hat{\mathbf{A}}\mathbf{q} = \mathbf{B}. \quad (137)$$

with the $N_{\text{at}+1} \times N_{\text{at}+1}$ matrix $\hat{\mathbf{A}}$

$$A_{ij} = \sum_{k=1}^{N_{\text{grid}}} \frac{1}{|\mathbf{r}_k - \mathbf{R}_i|} \frac{1}{|\mathbf{r}_k - \mathbf{R}_j|} \quad \text{with } i, j \leq N_{\text{at}} \quad (138)$$

$$A_{i=N_{\text{at}}+1, j} = A_{i, j=N_{\text{at}}+1} = 1; \quad A_{i=N_{\text{at}}+1, j=N_{\text{at}}+1} = 0$$

and the $N_{\text{at}} + 1$ vector \mathbf{B}

$$B_i = \sum_{k=1}^{N_{\text{grid}}} \frac{V_{\text{DFT}}(\mathbf{r}_k)}{|\mathbf{r}_k - \mathbf{R}_i|} \quad \text{with } i \leq N_{\text{at}} \quad (139)$$

$$B_{i=N_{\text{at}}+1} = q_{\text{tot}}. \quad (140)$$

\mathbf{q} are the N_{at} charges.

For solids (periodic boundary conditions) the situation is more complicated because all charges are repeated infinitely and the potential is only defined up-to an arbitrary offset. The methods implemented as part of this work solve this problem by Ewald summation [77]. They were developed by Campana et.al. [44] and later further improved by Chen et al. [47]. The electrostatic potential is split into a real space and reciprocal space part by an error function (Ewald summation [77]). The function for the potential generated by the ESP charges centered at the atoms of the unit cell then reads

$$V_{\text{ESP}}(\mathbf{r}) = \sum_{i=1, \mathbf{T}}^{N_{\text{at}}} q_i \frac{\text{erfc}(\alpha|\mathbf{r} - \mathbf{R}_{i, \mathbf{T}}|)}{|\mathbf{r} - \mathbf{R}_{i, \mathbf{T}}|} \quad (141)$$

$$+ \frac{4\pi}{V_{\text{cell}}} \sum_{i=1, \mathbf{k}}^{N_{\text{at}}} q_i \cos(\mathbf{k}(\mathbf{r} - \mathbf{R}_i)) \frac{e^{-\frac{k^2}{4\alpha^2}}}{k^2}$$

with $\mathbf{T} = n_1 \mathbf{a}_1 + n_2 \mathbf{a}_2 + n_3 \mathbf{a}_3$ the real space (periodic) translation vector and \mathbf{a}_i being the lattice vectors with $n_i \in \mathbf{Z}$. $\mathbf{k} = m_1 \mathbf{b}_1 + m_2 \mathbf{b}_2 + m_3 \mathbf{b}_3$ is the reciprocal space translation vector and the \mathbf{b}_i are the reciprocal lattice vectors with $m_i \in \mathbf{Z}$.

V_{cell} is the volume of the unit cell. The parameter α is defined as $\alpha = \frac{\sqrt{\pi}}{R_c}$ with R_c the cutoff radius of the Ewald summation [77]. Apart from Ewald summation, the electrostatic potential can be calculated by Wolf summation [274, 47] (also implemented in the FHI-aims code as part of this work):

$$V_{\text{ESP}}(\mathbf{r}) = \sum_{i=1}^{N_{\text{at}}} q_i \left[\frac{\text{erfc}(\sqrt{\alpha}|\mathbf{r} - \mathbf{R}_i|)}{|\mathbf{r} - \mathbf{R}_i|} - \frac{\text{erfc}(\sqrt{\alpha}R_c)}{R_c} + \left(\frac{\text{erfc}(\sqrt{\alpha}R_c)}{R_c^2} + \frac{2\sqrt{\alpha} \exp(\alpha R_c^2)}{\sqrt{\pi} R_c} \right) \right] \times (|\mathbf{r} - \mathbf{R}_i| - R_c) \quad (142)$$

The function to minimize, derived by Campana *et al.* [44], then is:

$$F_1^{\text{PBC}} = \sum_{k=1}^{N_{\text{grid}}} \left(V_{\text{DFT}}(\mathbf{r}_k) - V_{\text{ESP}}(\mathbf{r}_k) - \frac{1}{N_{\text{grid}}} \sum_{j=1}^{N_{\text{grid}}} (V_{\text{DFT}}(\mathbf{r}_j) - V_{\text{ESP}}(\mathbf{r}_j)) \right)^2 - \lambda \left(q_{\text{tot}} - \sum_{i=1}^{N_{\text{at}}} q_i \right) + \sum_{i=1}^{N_{\text{at}}} w_i \left(E_i^0 + \chi_i q_i + \frac{1}{2} J_i^{00} q_i^2 \right).$$

The χ_i is the electro-negativity and J_i^{00} the self-Coulomb interaction of the respective elements, which can be used to constrain the desired charges. w_i are weighting factors for the constraints. The fit produces the elements of $\hat{\mathbf{A}}$ and \mathbf{B}

$$A_{ij} = \sum_{k=1}^{N_{\text{grid}}} \left(\frac{\partial V_{\text{ESP}}(\mathbf{r}_k)}{\partial q_i} - \frac{1}{N_{\text{grid}}} \sum_{j=1}^{N_{\text{grid}}} \frac{\partial V_{\text{ESP}}(\mathbf{r}_j)}{\partial q_i} \right) \times \left(\frac{\partial V_{\text{ESP}}(\mathbf{r}_k)}{\partial q_j} - \frac{1}{N_{\text{grid}}} \sum_{m=1}^{N_{\text{grid}}} \frac{\partial V_{\text{ESP}}(\mathbf{r}_m)}{\partial q_j} \right) + \frac{w_i}{2} J_i^{00} \delta_{ij} \quad ; \quad i, j \leq N_{\text{at}} \quad (143)$$

$$A_{i=N_{\text{at}}+1, j} = A_{i, j=N_{\text{at}}+1} = 1; \quad A_{i=N_{\text{at}}+1, j=N_{\text{at}}+1} = 0$$

$$B_i = \sum_{k=1}^{N_{\text{grid}}} \left(V_{\text{DFT}}(\mathbf{r}_k) - \frac{1}{N_{\text{grid}}} \sum_{j=1}^{N_{\text{grid}}} V_{\text{DFT}}(\mathbf{r}_j) \right) \times \left(\frac{\partial V_{\text{ESP}}(\mathbf{r}_k)}{\partial q_i} - \frac{1}{N_{\text{grid}}} \sum_{m=1}^{N_{\text{grid}}} \frac{\partial V_{\text{ESP}}(\mathbf{r}_m)}{\partial q_i} \right) - w_m \frac{\chi_m}{2} \quad ; \quad i \leq N_{\text{at}}$$

$$B_{i=N_{\text{at}}+1} = q_{\text{tot}}$$

The function to minimize, derived by Chen *et al.* [47] is:

$$F_2^{\text{PBC}} = \sum_{k=1}^{N_{\text{grid}}} (V_{\text{DFT}}(\mathbf{r}_k) - (V_{\text{ESP}}(\mathbf{r}_k) + V_{\text{DFT}}^{\text{offset}}))^2 \quad (144)$$

$$- \lambda \left(q_{\text{tot}} - \sum_{i=1}^{N_{\text{at}}} q_i \right) + \beta \sum_{i=1}^{N_{\text{at}}} (q_i - q_{i0})^2.$$

The constraint charges q_{i0} can be determined with other methods (e. g. Mulliken charge analysis [173]). β is the weighting factor. This gives $\hat{\mathbf{A}}$ and \mathbf{B}

$$A_{ij} = \sum_{k=1}^{N_{\text{grid}}} \left(\frac{\partial V_{\text{ESP}}(\mathbf{r}_k)}{\partial q_i} \frac{\partial V_{\text{ESP}}(\mathbf{r}_k)}{\partial q_j} \right) + \beta \delta_{ij} \quad ; \quad i, j \leq N_{\text{at}} \quad (145)$$

$$A_{i=N_{\text{at}}+1,j} = A_{i,j=N_{\text{at}}+1} = \sum_{k=1}^{N_{\text{grid}}} \frac{\partial V_{\text{ESP}}(\mathbf{r}_k)}{\partial q_j} \quad j \leq N_{\text{at}}$$

$$A_{i=N_{\text{at}}+2,j} = A_{i,j=N_{\text{at}}+2} = 1$$

$$A_{i=N_{\text{at}}+2,j=N_{\text{at}}+2} = A_{i=N_{\text{at}}+1,j=N_{\text{at}}+2} = 0$$

$$A_{i=N_{\text{at}}+2,j=N_{\text{at}}+1} = 0$$

$$B_i = \sum_{k=1}^{N_{\text{grid}}} \left(V_{\text{DFT}}(\mathbf{r}_k) \frac{\partial V_{\text{ESP}}(\mathbf{r}_k)}{\partial q_i} \right) - \beta q_{0i} \quad ; \quad i \leq N_{\text{at}} \quad (146)$$

$$B_{i=N_{\text{at}}+1} = \sum_{j=1}^{N_{\text{grid}}} V_{\text{DFT}}(\mathbf{r}_j) \quad (147)$$

$$B_{i=N_{\text{at}}+2} = q_{\text{tot}}$$

Here the arbitrary offset of the potential V_{offset} is an additional fitting parameter. The matrix $\hat{\mathbf{A}}$ is of dimension $N_{\text{at}+2} \times N_{\text{at}+2}$ and \mathbf{B} of dimension $N_{\text{at}+2}$. The arbitrary offset of the electrostatic potential is calculated for the method derived by Campana *et al.* [44] by

$$V_{\text{offset}} = \frac{1}{N_{\text{grid}}} \sum_{k=1}^{N_{\text{grid}}} (V_{\text{DFT}}(\mathbf{r}_k) - V_{\text{ESP}}(\mathbf{r}_k)) \quad (148)$$

from the fitted charges q_i . As a measure for the quality of the fit the root-mean-square (RRMS) is defined as

$$\text{RRMS} = \left\{ \frac{\sum_{k=1}^{N_{\text{grid}}} ((V_{\text{ESP}}(\mathbf{r}_k) + V_{\text{offset}}) - V_{\text{DFT}}(\mathbf{r}_k))^2}{\sum_{k=1}^{N_{\text{grid}}} (V_{\text{DFT}}(\mathbf{r}_k))^2} \right\}^2. \quad (149)$$

The partial charges obtained by fitting to the electrostatic potential from a DFT calculation give direct excess to the dipole-moment, calculated directly as described in Sec. 11.1.1 by summing over the charges at the atomic positions

$$\mathbf{d} = \sum_i q_i \mathbf{R}_i. \quad (150)$$

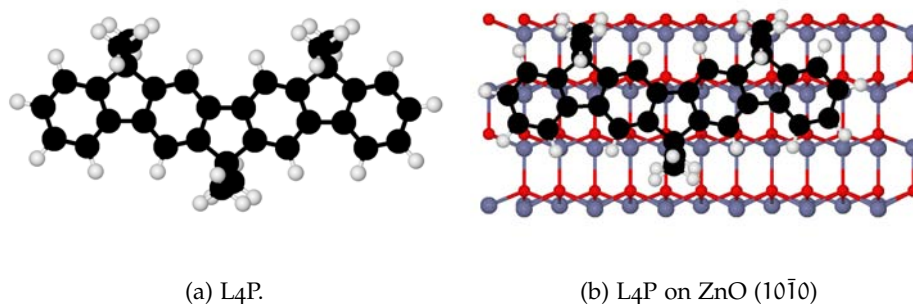


Figure 90: Atomic structure of the ladder type quarterphenyl molecule L4P on ZnO (10 $\bar{1}$ 0). The structure was determined by employing the semi-local xc-functional PBE+vdw^{TS} [196, 254]

The goal of this work is to approximate the Coulomb matrix element (eq. 124). To accomplish this task we need to calculate the partial charges for the electronic states (orbitals) or rather products of states. The charges for those states can be calculated analogous to the charges calculated for the full potential, once the transition potential has been obtained. The full electrostatic potential is typically calculated by solving the Poisson equation for the full density. In FHI-aims a very efficient algorithm is used, that employs the multi-pole moments of the density [63, 64]. Instead of using the full density as input for this algorithm we implemented the option to calculate a transition density. The ESP-charges can be fitted to the electrostatic potential calculated on different grids, based on these transition densities.

11.2 RESULTS

As a model structure for demonstrating the combination of the density matrix formalism and *ab initio* calculations, we selected a ladder type quarterphenyl (L4P) molecule adsorbed on ZnO (10 $\bar{1}$ 0). This class of molecules provides an electronic structure, which is well suited for opto-electronics and can be easily processed and tailored to fit the electronic structure of quantum wells that are used in devices and experiment [127]. In Fig. 90 a the atomic structure of L4P relaxed with the hybrid functional HSE06 [100] is shown. In Fig. 90 b the adsorption geometry of L4P on ZnO (10 $\bar{1}$ 0) calculated employing the semi-local xc-functional PBE+vdW is shown. We only considered adsorption geometries of flat lying molecules, these are best suited for Förster type exciton transfer [82]. The alignment between the flat lying molecule follows the description brought forward by F. Della Sala *et al.* [62]. The interaction is governed by the electrostatic coupling of the molecule to the periodic dipolar electric field originating from the Zn-O surface dimers. The molecules either align along the field created by the surface dimers or perpendicular to it. In Fig. 91 and Fig. 92 the situation is depicted for the equilibrium adsorption geometry of L2P (fluorene) on ZnO (10 $\bar{1}$ 0) obtained with the semi-local xc-functional PBE+vdW^{TS} [196, 254]. Along the axis of the dimers a periodically oscillating field is formed by Zn-O rows

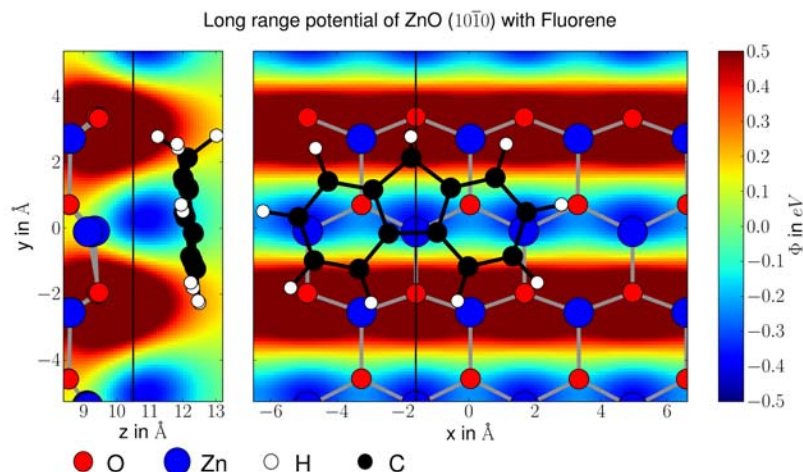


Figure 91: Alignment of L2P (Fluorene) perpendicular to the Zn-O dimers within the long range potential of the ZnO ($10\bar{1}0$) surface. The relaxed adsorption geometry is shown. The potential was taken from the unperturbed ZnO ($10\bar{1}0$) surface. The long range potential is calculated by Ewald summation in reciprocal space [77].

of opposite charge. Perpendicular to the dimers the change of the potential is small. The molecules align in such a way, that the hydrogen atoms at the ends of the long axis of the molecule are in the vicinity of the positive potential. The largest overlap between the positive potential region and the hydrogen atoms of the molecule is achieved by alignment of the long molecular axis perpendicular to the dimers. The alignment along the axis of the dimers is achieved by bridging one or more positive/negative potential regions while the ends of the molecule are in the vicinity of positive potential regions.

The adsorption geometry for L4P on ZnO ($10\bar{1}0$) is shown in Fig. 90 b. The atomic structure of L4P and ZnO ($10\bar{1}0$) are the first inputs for parameterizing

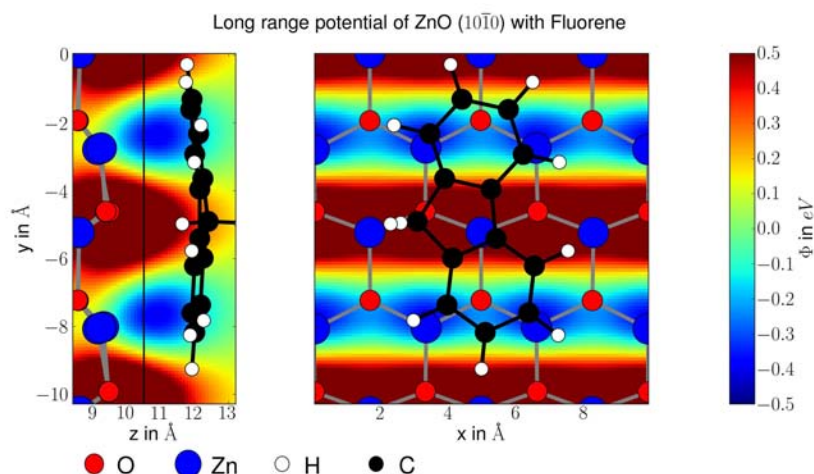


Figure 92: Alignment of L2P (Fluorene) parallel to the Zn-O dimers within the long range potential of the ZnO ($10\bar{1}0$) surface. See caption of Fig. 91.

Atom	ESP charge in e_0
Zn	1.02344470
O	-1.02344470
Zn	1.02344470
O	-1.02344470
RRMS	0.34405930

Table 12: ESP charges fitted to the electrostatic potential of bulk wurtzite ZnO

the model based on a density matrix formalism developed by E. Verdenhalven, A. Knorr and M. Richter [265]. The parametrization of the electronic structure obtained by *ab initio* calculations for the isolated molecule and ZnO (10 $\bar{1}$ 0) surface is achieved within the dipole approximation (see Sec. 11.1.1 and Ref. [265]). The transition dipole moment matrix elements $\langle \varphi_i | \mathbf{r} | \varphi_j \rangle$ are calculated on the real space grid of the FHI-aims code and transformed to the KS-basis (see sec. 11.1.1). The transition dipole matrix element for the HOMO-LUMO transition of the molecule and the CBM-VBM transition of the ZnO (10 $\bar{1}$ 0) surface are:

$$|\mathbf{d}_{\text{HL}}| = 0.35e_0\text{nm} \quad |\mathbf{d}_{\text{CV}}| = 0.012e_0\text{nm} \quad (151)$$

The direction of the substrate dipole \mathbf{d}_{HL} is chosen and fixed to point out of the surface plane, while the direction of the molecule transition dipole is tuned via the angle α between both transition dipole moments.

Putting together the theoretical framework derived by E. Verdenhalven, A. Knorr and M. Richter [265] and the DFT parametrization we investigated the interaction between molecule and substrate. At low coverages of molecules the interaction is stronger than at high coverages because the oscillator strength of the semiconductor substrate is distributed between fewer molecules. From varying the orientation of the molecule on the surface and thus the angle α between

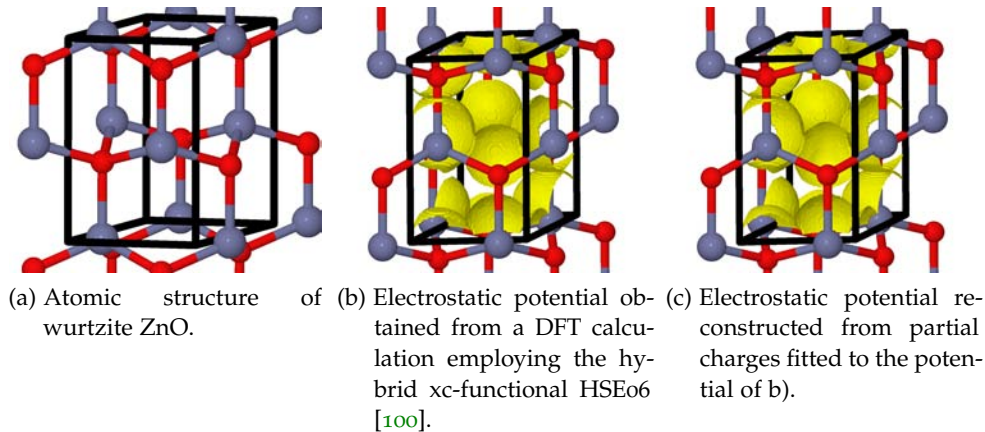


Figure 93: Electrostatic potential of ZnO in wurtzite structure. The unit cell is shown in black.

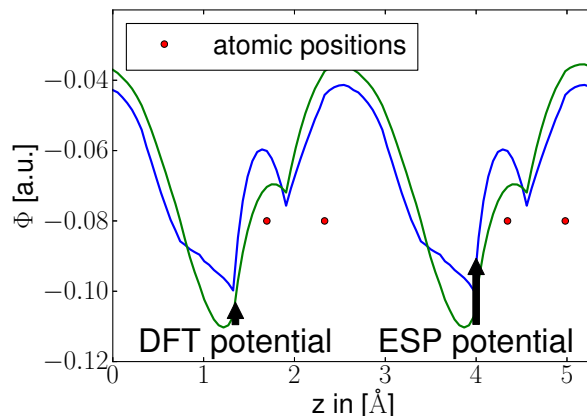
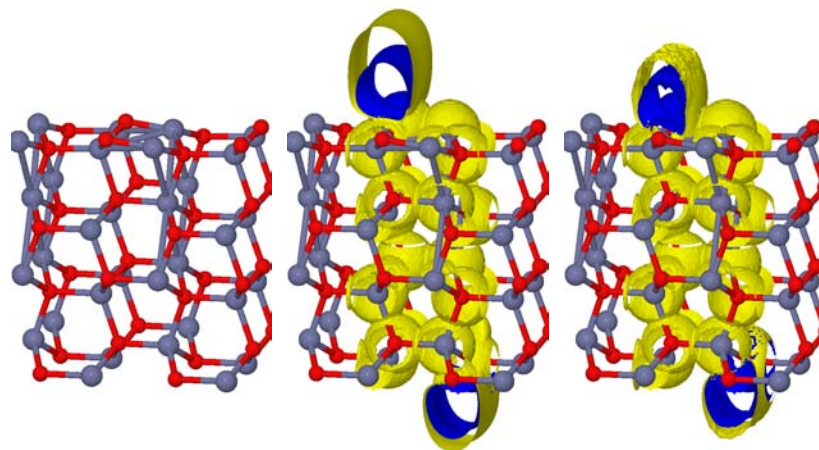


Figure 94: Electrostatic potential of the ZnO ($10\bar{1}0$) surface from a DFT calculation (HSE06) (green) and reconstructed from ESP-charges (blue) in Tab. 12 summed up perpendicular to the c -axis of the crystal. The atomic positions (z) of Zn and O are marked by red dots.

surface and molecular transition dipole we found that the interaction is strongest for a parallel alignment of the dipoles. The decrease follows a cosine behavior and is lowest for perpendicular moments. With increasing interaction strength the HOMO-LUMO transition line is shifted toward lower energies. By optimizing the coverage and the alignment of surface and molecular dipole moments the performance of hybrid inorganic/organic devices can be tuned or adjusted to possible applications in photo voltaics and opto-electronics.

The dipole and momentum transition matrix elements implemented into the



(a) Atomic structure of the ZnO ($10\bar{1}0$) surface. (b) Electrostatic potential obtained from a DFT calculation employing the hybrid xc-functional HSE06 [100]. (c) Electrostatic potential reconstructed from partial charges fitted to the potential of b).

Figure 95: Electrostatic potential of the ZnO ($10\bar{1}0$) surface. The unit cell is periodically extended perpendicular to the surface.

Atom	ESP charge in e_0
O (top)	-1.24697845
Zn (top)	1.09027791
Zn	1.29658012
O	-1.07867024
O	-1.24578893
Zn	1.15653704
O	-1.15471412
Zn	1.19946914
O	-1.14578008
Zn	1.14171604
O	-1.17959763
Zn	1.13330173
O	-0.97913785
Zn	1.20932943
O (bottom)	-1.20174231
Zn (bottom)	1.00519817

Table 13: ESP charges fitted to the electrostatic potential of the ZnO (10 $\bar{1}$ 0) surface.

FHI-aims DFT code as part of this work have many further applications. They are utilized in different theoretical approaches based on first order perturbation theory (Fermi's Golden rule). They can be used to calculate the macroscopic dielectric function and absorption spectra [6], which were used to test the implementation. Other applications are the calculation of thermo-electric constants such as the Seebeck coefficient [151, 6], the simulation of NEXAFS data [69] and the parameterization of Förster interaction/energy transfer for functionalized graphene [152, 153]. Additionally we added the versatile HDF5 container file format [251] to the FHI-aims code in this work. It allows for a flexible input/output structure to distribute data between different working groups. All data is collected within one container file, that hosts different data structures and allows for a straight forward annotation of all contents. A key advantage for the application in highly parallelized scientific codes such as FHI-aims is the capability of synchronous output from many computing processes. The data does not have to be collected on one processor, which is typically limited by the available memory, but can be written directly to the container file.

The modeling was so far based on a parametrization, that essentially reduces the information contained in the electronic structure obtained by the DFT calculation to two transition dipole matrix elements. This approximation is quite severe considering the spatial extent of the molecule and the surface that clearly will contribute differently to the interaction between the constituents. The next step for a better modeling of the materials at hand is the partial charge technique

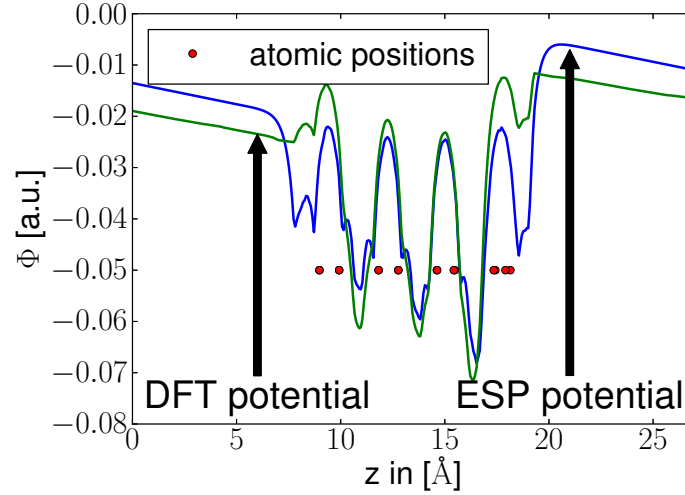


Figure 96: Electrostatic potential from a DFT calculation (HSE06) (green) and reconstructed from ESP-charges of the ZnO (10 $\bar{1}$ 0) surface, summed up perpendicular to the surface normal. Atomic positions (z) are marked by red dots.

[150], described in Sec 11.1.2.

In Fig. 93 b the electrostatic potential for ZnO in wurtzite structure is shown. To the four atoms in the unit cell (black in Fig. 93, two Zn and two O) partial charges are assigned by fitting with the method of Chen *et al.* [47] to the potential in Fig. 93 b. The partial charges are listed in Tab. 12. ZnO is a strongly ionic crystal. The partial charges slightly deviate from the values of +1 and -1 for Zn and O, respectively, predicted by the simple ionic model of Tasker [249]. From the partial charges the electrostatic potential is reconstructed and shown in Fig. 93 b as an iso-surface. In Fig. 94 the electrostatic potential obtained directly from the DFT calculation and the reconstruction are summed up along the c -axis of the crystal. The agreement between the DFT potential and the reconstructed potential is good. The quality of the fit crucially depends on the real space region selected for fitting. If the atomic structure is dense, less space is available for fitting points. For bulk wurtzite ZnO the partial charge approach yields a good approximation for the electrostatic potential.

As a next step the electrostatic potential for a ZnO (10 $\bar{1}$ 0) is approximated by partial charges in Fig. 95. The electrostatic potential directly obtained from the DFT calculation shows two different regions because of the broken symmetry at the surface. Inside the slab, used for modeling the surface, the potential nearly behaves as for bulk wurtzite ZnO in Fig. 93. At the surface a strong potential is formed perpendicular to the Zn-O dimers of the surface. The fitted partial charges are listed in Tab. 13 and the reconstructed potential is shown in Fig. 95 c. The partial charges inside the slab are close to the partial charges of bulk wurtzite ZnO. In Fig. 96 we show the electrostatic potential obtained from the DFT calculation and the reconstruction summed up along the surface normal. At the surface the deviation of the reconstructed potential from the potential obtained from the DFT calculation is the strongest. The few partial charges placed at the surface atoms are not capable of fully describing the behavior of the poten-

tial, but the overall agreement is good and might be sufficient for approximating the Coulomb matrix elements required as input for the density matrix formalism. The accuracy of the fit could be improved in the future by introducing additional charges at the surface.

Part IV

CONCLUSION

We have performed a first principles investigation of ultra-thin ZnO films on metal supports. These films are of interest as model systems in e. g. optoelectronics and heterogeneous catalysis. Despite the multitude of applications the actual structure of ZnO surfaces and interfaces, which are essential for devices and chemical reactions, is still under debate [132, 161, 276, 262, 136, 267]. Starting from bulk ZnO in Chap. 3, we employed the tool set of surface science to develop well defined model systems for the notoriously difficult to characterize polar ZnO surfaces, ZnO (0001)-Zn and (000 $\bar{1}$)-O. By going from the ZnO surface to ultra-thin films on conducting substrates experimental techniques that rely on the conductivity of the sample can be applied. The rapid progress in thin film growth makes it possible to prepare these films with very high precision regarding orientation and termination. The most evident question, which arises by switching from surfaces to ultra thin films, is how well these films resemble the surface they are supposed to model. Ultra-thin films are known to sometimes have unique properties of their own, that yield new applications [88, 189, 234, 181].

In Chap. 5 we found, that the hypothetical ideal ZnO mono-layer has a very stable α -BN structure, which can be derived from the ZnO bulk wurtzite structure by bringing the Zn and O atoms into the same plains. By minimizing the strain in the ZnO mono-layer we deduced coincidence structures between the (111) surfaces of Ag, Cu, Pd, Pt, Ni, and Rh, which are in good agreement with experiment (Chap. 6). The mono-layer retains its α -BN structure on the metal substrates, however, the corrugation is highly system dependent. After assessing the stability and atomic structure of the coincidences we progressed to thicker films in Sec. 7.1. With increasing thickness the corrugation of the films grows substantially and eventually the wurtzite structure is formed. The number of layers required for the formation of a full wurtzite structure depends on the metal substrates. For Cu 6 layers are necessary, while for Ni already 4 layers are sufficient.

In addition to the atomic structure, the electronic structure gives insight into the mechanisms governing the transition from mono- to multi-layer systems. Due to the intrinsic polar nature of the ZnO films a dipolar electric field forms across the film (Sec. 7.2). This field shifts the electronic structure of each successive layer up in energy. This upwards shift is only stopped when the Fermi level, which is provided by the metal substrate, is reached. This mechanism results in an effectively p-type doped sample. Our model presents a fundamentally different approach than doping with shallow acceptors and might even lead to new applications within the rapidly developing field of epitaxial film growth.

Next, we investigated the stability of ultra-thin metal supported ZnO films in Sec. 8.1 to Sec. 8.4 by developing an extensive surface phase diagram for 1 to 4 layers of ZnO on the different metal substrates. We found that the stability of the well known (2 \times 1)-H reconstruction is increased with growing film thickness, but the affinity for H-adsorption is highly system dependent. While ZnO on Cu is very susceptible to hydrogen adsorption, ZnO on Ag is very stable in its clean, unreconstructed form. By analyzing the atomic and electronic structure of (2 \times 1)-H reconstructed ZnO on metal substrates we found that it resembles the wurtzite structure of bulk ZnO very well. Both the atomic and electronic struc-

ture of four layer thick ZnO films are comparable to (2×1) -H reconstructed ZnO surfaces without metal substrates. In conclusion, the (2×1) -H reconstructed films are good models for the polar ZnO surfaces.

We also investigated Zn and O defects in Sec. 8.2 and 8.2.1 and confirmed the validity of results for the ZnO surfaces [132, 161, 276, 262, 136, 267] for our ultra thin films. Oxygen defects (vacancies and ad-atoms) are more stable than their Zn counterparts. The stability of the O defects depends on the oxygen affinity of the metal substrate. For Cu it is strong, while it is weaker for Ag. The other metals form an intermediate situation between those extremes. At low chemical potentials sparse ring structures (Sec. 8.3) with or without hydrogen are stabilized, which allow the Zn/O atoms to retain a three-fold bonding environment. The ring structures are more stable than normal defects and dominate the phase diagram at low oxygen chemical potentials.

Another reconstruction, known from the (0001) -Zn terminated ZnO surface, we found to be dominant in the surface phase diagrams at high oxygen chemical potentials is OH adsorption. It is the equivalent reconstruction to H adsorption on the $(000\bar{1})$ -O terminated ZnO surface. In contrast to H adsorption we did not find a strong dependence of the stability of OH reconstructions on the film thickness or the metal substrates.

The explicit inclusion of the chemical potentials of hydrogen, oxygen, zinc and gaseous water lead us to complete surface phase diagrams [98]. Reconstructions containing hydrogen are destabilized with respect to the unreconstructed surface, which are predicted to be stable up-to 3 layers of thickness.

We compared our *ab initio* results to experimental measurements of ZnO on Ag by Shiotari *et al.* [237]. The combination of experiment and theory allows for a conclusive determination of film thickness and surface termination. Additionally, we were able to explain the appearance of the (5×5) minority coincidence structure reported by Shiotari *et al.* in Chap. 9. The reduction of the Zn concentration during annealing is predicted to lead to a transformation of the (5×5) coincidence, which is only stable at high Zn chemical potentials, to the regular coincidence structure. The complete transformation could be hindered by kinetic effects such as reduced diffusion length because of low temperatures during the measurement process.

In the final chapter 11 of this work we made a first effort to bridge the gap between our *ab initio* calculations of model structures and more realistic hybrid inorganic organic systems for opto-electronics. In close collaboration with Verdenhalven, Richter and Knorr from the TU Berlin we parameterized their "hybrid Bloch equations". This model based on a density matrix formalism allowed us to investigate excitonic effects in hybrid systems of organic molecules and inorganic semi-conductors. We chose the ladder-type oligomer L4P and the ZnO $(10\bar{1}0)$ surface to test our formalism. As part of this work we implemented the calculation of dipole matrix elements into the FHI-aims [33] code. The further development of the model let to a more detailed parametrization based on partial charges, which are fitted to the electrostatic potential obtained from DFT calculations. We implemented the calculation of the full and the transition potential into FHI-aims, as well as the fitting procedure for periodic and non-periodic systems. The transition potentials are calculated from the density matrix, constructed from

two different eigenstates.

We have established that under certain conditions ultra-thin ZnO on metal substrates can be used to model the polar ZnO surfaces. The H_2 partial pressure and the choice of the metal allow to select between unreconstructed ultra-thin ZnO films, that differ from the polar ZnO surfaces, and films $((2\times 1)\text{-H}$ reconstructed) that resemble these surfaces. The unreconstructed ultra-thin ZnO films thereby have a unique atomic and electronic structure, that may lead to interesting new applications in e. g. opto-electronics. The extensive results of this work regarding atomic and electronic structure and stability of ZnO ultra thin films will be a valuable guideline for experimentalists in their efforts to prepare well defined samples.

As an outlook, the further refinement of our models developed together with the TU Berlin is expected to result in intriguing insights in the mechanisms governing excitonic effects in HIOS systems. This will eventually lead to a better understanding of charge separation in realistic devices. The next step in the investigation of ZnO ultra-thin films on metal substrates will be the inclusion of organic molecules into the calculations. In close collaboration with experimentalists the effect of the unique electronic structure of ZnO on metal substrates and the Fermi level provided by the metal on the molecules will be investigated (effective p-type doping). This has the potential to be the basis for further work that will eventually lead to better devices and catalysts. To further improve the quality of our theoretical results, image charge effects could be included in the description of the ultra-thin ZnO on metal substrates.

Part V

APPENDIX

CONSTANTS

In this section the physical constants used throughout this dissertation are listed [166].

Quantity	Symbol	Value
Atomic mass unit	$\text{amu} \equiv u$	$1.660\,538\,921\,(73) \cdot 10^{-27} \text{ kg}$
Avogadro constant	N_A	$6.022\,141\,29\,(27) \cdot 10^{23} \frac{1}{\text{mol}}$
Bohr magneton	$\mu_B = \frac{e \hbar}{2 m_e}$	$9.274\,009\,68\,(20) \cdot 10^{-24} \frac{\text{J}}{\text{T}}$
Bohr radius	$a_0 = \frac{4 \pi \epsilon_0 \hbar^2}{e^2 m_e}$	$5.291\,772\,109\,2\,(17) \cdot 10^{-11} \text{ m}$
Boltzmann constant	k_B	$1.380\,648\,8\,(13) \cdot 10^{-23} \frac{\text{J}}{\text{K}}$
Electric constant	ϵ_0	$(\mu_0 c^2)^{-1}$
	$\frac{1}{4 \pi \epsilon_0}$	$299\,792\,458^2 \cdot 10^{-7} \frac{\text{Vm}}{\text{As}}$
Electron charge	e	$1.602\,176\,565\,(35) \cdot 10^{-19} \text{ C}$
Electron mass	m_e	$9.109\,382\,91\,(40) \cdot 10^{-31} \text{ kg}$
Fine struc. constant	$\alpha = \frac{\mu_0 e^2 c_0}{2 \hbar}$	$7.297\,352\,569\,8\,(24) \cdot 10^{-3}$
Hartree energy	E_h	$4.359\,744\,34\,(19) \cdot 10^{-18} \text{ J}$
Magnetic constant	μ_0	$4 \times 10^{-7} \text{ N A}^{-2}$
Planck constant	h	$6.626\,069\,57\,(29) \cdot 10^{-34} \text{ Js}$
	$\hbar = \frac{h}{2 \pi}$	$1.054\,571\,726\,(47) \cdot 10^{-34} \text{ Js}$
Rydberg energy	$R_\infty c \hbar$	$13.605\,692\,53\,(30) \text{ eV}$
Rydberg constant	$R_\infty c$	$3.289841960364(17) \cdot 10^{15} \text{ Hz}$
Speed of light	c, c_0	$299\,792\,458 \text{ m s}^{-1}$
Universal gas const.	$R_o = N_A k_B$	$8.314\,462\,1\,(75) \frac{\text{J}}{\text{K} \cdot \text{mol}}$

Table 14: Physical constants in SI units [166].

REFERENCE ENERGIES

In this section the total energies calculated with FHI-aims [33] are listed for atoms and bulk structures used to calculate cohesive and surface free energies.

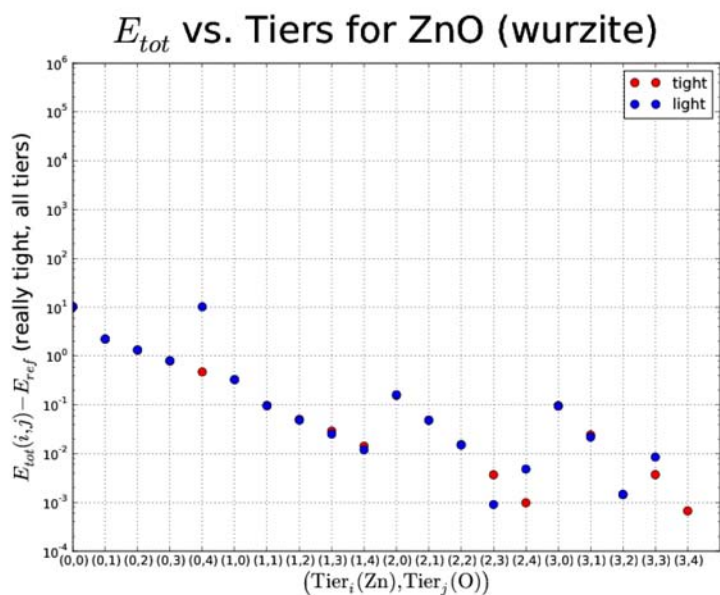
System	Basis[33]	xc-functional	Total energy [eV]
Zn	tight	PBE	-49117.0526
Zn	tight	HSE06	-49117.1589
O	tight	PBE	-2043.2223
H	tight	PBE	-12.4875
Ag	tight	PBE	-146385.2978
Cu	tight	PBE	-45242.3900
Cu	tight	HSE06	-45241.8872
Pd	tight	PBE	-138878.7157
Pt	tight	PBE	-518285.9446
Au	tight	PBE	-535650.8830
Rh	tight	PBE	-131611.9493
C	tight	PBE	-1027.8640
O ₂	tight	PBE	-4093.4322
H ₂	tight	PBE	-31.7461
H ₂	tight	PBE+vdW	-31.7480
H ₂ O	tight	PBE	-2080.9643

Table 15: Reference energy for different xc-functionals. For the bulk values equilibrium lattice constants obtained by a fit to the Birch-Murnaghan equation of states [174] were used.

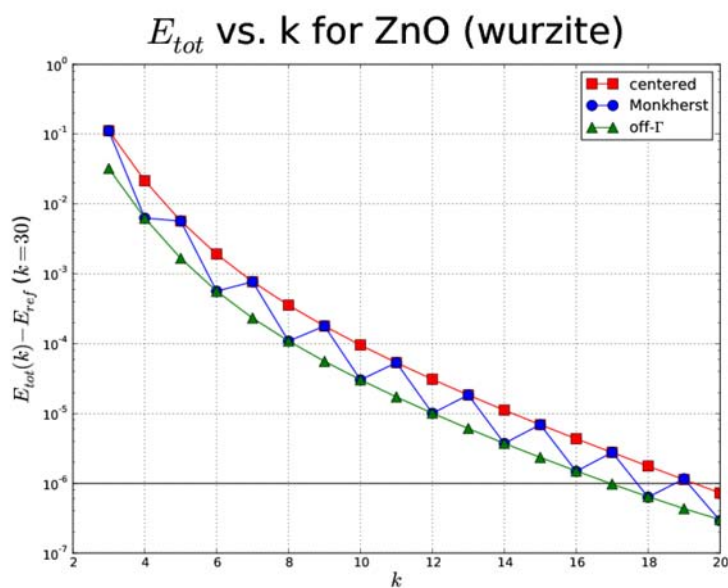
System	Basis[33]	xc-functional	Total energy [eV]
Ag bulk (fcc) (exp)	tight	PBE	-146388.0076
Ag bulk (fcc)	tight	PBE	-146388.0192
Cu bulk (fcc)	tight	PBE	-45246.1515
Pd bulk (fcc)	tight	PBE	-138882.4397
Pt bulk (fcc)	tight	PBE	-518291.9131
Au bulk (fcc)	tight	PBE	-535654.1015
Rh bulk (fcc)	tight	PBE	-131618.3056
Ni bulk (fcc)	tight	PBE	-41565.3733
Zn bulk (bcc)	tight	PBE	-98235.8869
ZnO bulk wrz	tight	PBE	-102335.4173
ZnO bulk wrz	tight	PBE+vdW	-102335.8198
ZnO bulk zb	tight	PBE	-51167.6922
ZnO bulk rs	tight	PBE	-204669.5881

Table 16: Reference energy for different xc-functionals. For the bulk values equilibrium lattice constants obtained by a fit to the Birch-Murnaghan equation of states [174] were used.

CONVERGENCE TESTS



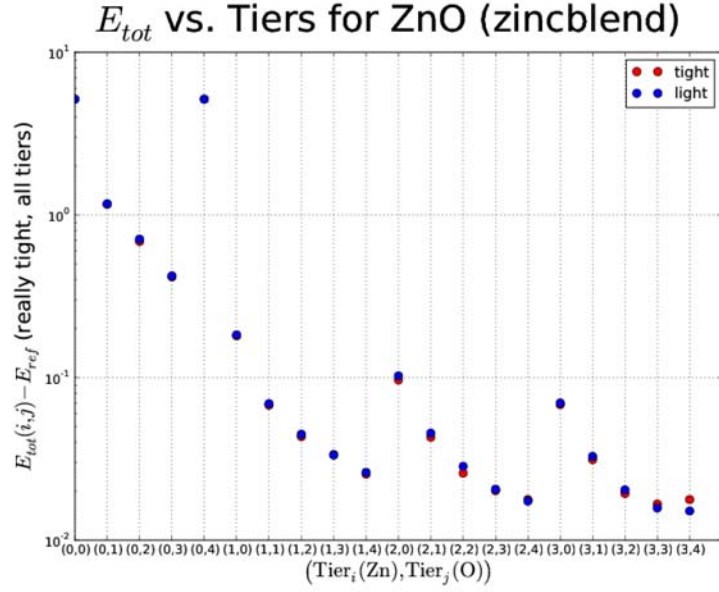
(a) Total energy vs. tiers



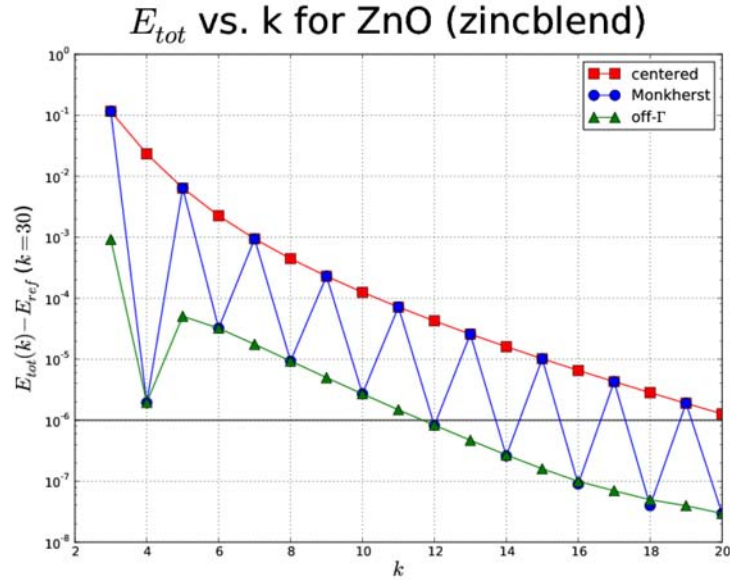
(b) Total energy vs. k-points

Figure 97: Convergence tests for bulk wurtzite ZnO

In this section the convergence tests for determining the settings of the basis set and the k-point sampling for bulk ZnO are presented. Based on these settings the parameters for larger super cells and surface calculations are selected. The



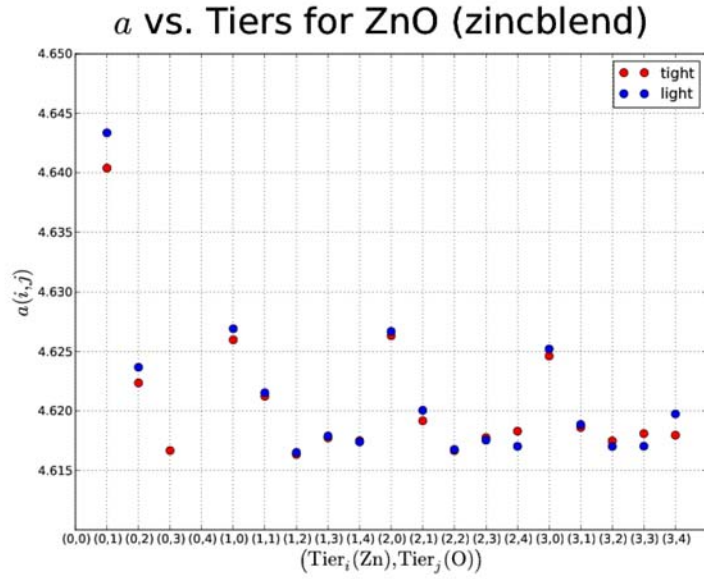
(a) Total energy vs. tiers



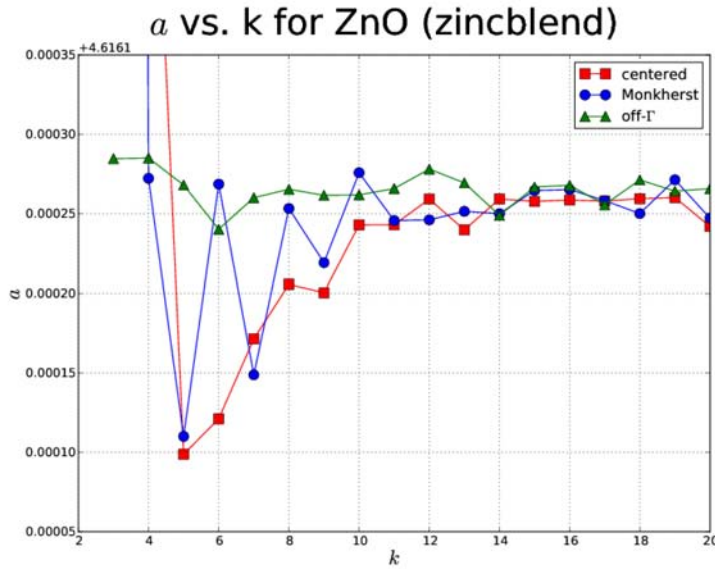
(b) Total energy vs. k-points

Figure 98: Convergence tests for bulk zinc-blend ZnO

number of k-points in each reciprocal space direction is reduced by the same factor the real space lattice vectors have increased. The basis sets are the numerically tabulated atomic orbitals provided by the FHI-aims package [33]. The default settings allow a successive increase of the basis set size by hydrogen-like spherical orbitals. The grid size can be adjusted accordingly, but typically is selected in steps, that also increase the basis set size (*light*, *tight*, *really tight*). In Fig. 97 the change of the total energy of bulk wurtzite ZnO as a function of basis set size and k-point sampling is shown. For the ZnO bulk wurtzite structure $18 \times 18 \times 18$ k-points with off- Γ k-point grid and the standard light/tight basis are sufficiently



(a) Lattice parameter vs. tiers



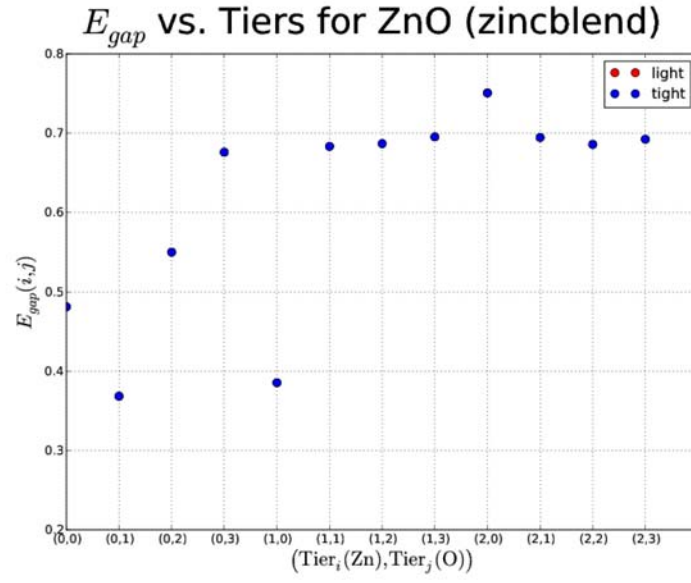
(b) Lattice parameter vs. k-points

Figure 99: Additional convergence tests for bulk zinc-blend ZnO

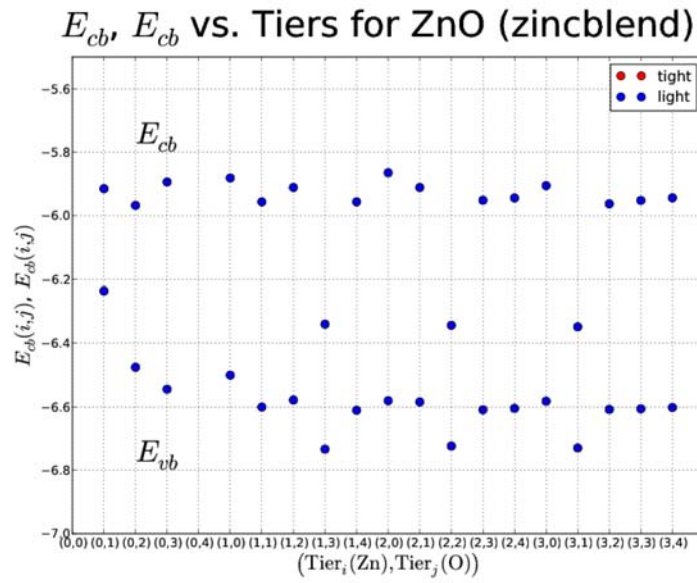
converged. All surface slab calculations are scaled to these values. The lattice parameters have been taken from a fit to the Murnaghan equation of states [174] and the PBE xc-functional was used.

In Fig. 98 the change of the total energy of bulk zinc-blend ZnO as a function of basis set size and k-point sampling is shown. For the ZnO bulk zinc-blend structure $12 \times 12 \times 12$ k-points with off- Γ k-point grid and the standard light/tight basis are sufficiently converged. All surface slab calculations are scaled to these values. The lattice parameters have been taken from a fit to the Murnaghan equation of states [174] and the PBE xc-functional was used. Additional convergence

test are shown in Fig. 99.



(a) Band gap vs. tiers



(b) Valence/Conduction band vs. tiers

Figure 100: Additional convergence tests for bulk zinc-blend ZnO

COINCIDENCE STRUCTURES

The most likely coincidence structure can be estimated by minimizing the strain on the in-plane lattice parameter a of the ZnO mono layer.

$$\min_m \left(a_{\text{ZnO}} - \frac{m}{m-1} \frac{a_M}{\sqrt{2}} \right) \quad (152)$$

The lattice parameters of ZnO as well as for the metal depend on the xc-functional. Small difference in their ratio can lead to different coincidence structures if large structures ($m > 6$) are favored. In the tables below the lattice parameters obtained by a Birch-Murnigan-fit [174] for different metals and the ZnO mono-layer are listed. The coincidence structure leading to an in-plane lattice parameter of the ZnO, which is closest to the free-standing case is given for various xc-functionals (PBE [196], PW-LDA [198], PZ-LDA [195], VWN [266], AM05 [9], BLYP [23, 138], PBEint [78], PBEsol [200], rPBE [94] and revPBE [288]). The 2nd and 3rd likeliest coincidence structures are reported, too.

xc / Ag	a	$a/\sqrt{2}$	da_{\min}	coincidences		
pbe	4.15	2.934	0.017	10 / 9	9 / 8	11 / 10
pw-lda	4.003	2.831	0.014	9 / 8	8 / 7	10 / 9
pz-lda	4.004	2.831	0.015	9 / 8	8 / 7	10 / 9
vwn	4.005	2.832	0.006	9 / 8	8 / 7	10 / 9
am05	4.055	2.867	0.015	9 / 8	8 / 7	10 / 9
blyp	4.262	3.014	0.008	11 / 10	12 / 11	10 / 9
pbeint	4.077	2.883	0.009	9 / 8	8 / 7	10 / 9
pbesol	4.054	2.867	0.01	9 / 8	8 / 7	10 / 9
rpbe	4.215	2.98	0.002	10 / 9	11 / 10	9 / 8
revpbe	4.196	2.967	0.005	10 / 9	9 / 8	11 / 10

Table 17: Lattice parameter of **Ag**, 1st, 2nd and 3rd likeliest coincidence structure leading to an in-plane lattice parameter of the ZnO, which is closest to the free-standing case for various xc-functionals.

xc / Pt	a	$a/\sqrt{2}$	da_{\min}	coincidences		
pbe	3.97	2.807	0.002	7 / 6	8 / 7	6 / 5
pw-lda	3.894	2.754	0.014	7 / 6	8 / 7	9 / 8
pz-lda	3.895	2.754	0.014	7 / 6	8 / 7	9 / 8
vwn	3.889	2.75	0.016	7 / 6	8 / 7	9 / 8
amo5	3.908	2.764	0.016	7 / 6	6 / 5	8 / 7
blyp	4.054	2.867	0.031	8 / 7	7 / 6	9 / 8
pbeint	3.924	2.775	0.015	7 / 6	6 / 5	8 / 7
pbesol	3.918	2.77	0.004	7 / 6	8 / 7	6 / 5
rpbe	3.993	2.823	0.015	7 / 6	6 / 5	8 / 7
revpbe	3.986	2.819	0.012	7 / 6	8 / 7	6 / 5

Table 18: Lattice parameter of **Pt**, 1st, 2nd and 3rd likeliest coincidence structure leading to an in-plane lattice parameter of the ZnO, which is closest to the free-standing case for various xc-functionals.

xc / Pd	a	$a/\sqrt{2}$	da_{\min}	coincidences		
pbe	3.942	2.787	0.025	7 / 6	6 / 5	8 / 7
pw-lda	3.839	2.715	0.031	7 / 6	6 / 5	8 / 7
pz-lda	3.84	2.715	0.031	7 / 6	6 / 5	8 / 7
vwn	3.844	2.718	0.021	7 / 6	6 / 5	8 / 7
amo5	3.869	2.736	0.042	6 / 5	7 / 6	8 / 7
blyp	4.03	2.85	0.017	7 / 6	8 / 7	9 / 8
pbeint	3.887	2.749	0.045	7 / 6	6 / 5	8 / 7
pbesol	3.874	2.74	0.039	7 / 6	6 / 5	8 / 7
rpbe	3.98	2.814	0.026	7 / 6	6 / 5	8 / 7
revpbe	3.969	2.807	0.027	7 / 6	6 / 5	8 / 7

Table 19: Lattice parameter of **Pd**, 1st, 2nd and 3rd likeliest coincidence structure leading to an in-plane lattice parameter of the ZnO, which is closest to the free-standing case for various xc-functionals.

xc / Au	a	$a/\sqrt{2}$	d_{\min}	coincidences		
pbe	4.158	2.94	0.01	10 / 9	9 / 8	11 / 10
pw-lda	4.049	2.863	0.017	10 / 9	9 / 8	11 / 10
pz-lda	4.05	2.864	0.017	10 / 9	9 / 8	11 / 10
vwn	4.043	2.859	0.016	10 / 9	9 / 8	11 / 10
amo5	4.077	2.883	0.003	9 / 8	10 / 9	8 / 7
blyp	4.271	3.02	0.013	12 / 11	11 / 10	13 / 12
pbeint	4.095	2.895	0.005	9 / 8	10 / 9	8 / 7
pbesol	4.083	2.887	0.012	9 / 8	10 / 9	11 / 10
rpbe	4.199	2.969	0.011	10 / 9	9 / 8	11 / 10
revpbe	4.187	2.961	0.011	10 / 9	9 / 8	11 / 10

Table 20: Lattice parameter of **Au**, 1st, 2nd and 3rd likeliest coincidence structure leading to an in-plane lattice parameter of the ZnO, which is closest to the free-standing case for various xc-functionals.

xc / Cu	a	$a/\sqrt{2}$	d_{\min}	coincidences		
pbe	3.632	2.568	0.067	5 / 4	4 / 3	6 / 5
pw-lda	3.518	2.488	0.089	5 / 4	4 / 3	6 / 5
pz-lda	3.519	2.488	0.089	5 / 4	4 / 3	6 / 5
vwn	3.521	2.489	0.08	5 / 4	4 / 3	6 / 5
amo5	3.56	2.517	0.093	5 / 4	4 / 3	6 / 5
blyp	3.708	2.622	0.03	5 / 4	6 / 5	4 / 3
pbeint	3.582	2.533	0.086	5 / 4	4 / 3	6 / 5
pbesol	3.564	2.52	0.085	5 / 4	4 / 3	6 / 5
rpbe	3.676	2.599	0.061	5 / 4	4 / 3	6 / 5
revpbe	3.663	2.59	0.063	5 / 4	4 / 3	6 / 5

Table 21: Lattice parameter of **Cu**, 1st, 2nd and 3rd likeliest coincidence structure leading to an in-plane lattice parameter of the ZnO, which is closest to the free-standing case for various xc-functionals.

xc / Ni	a	$a/\sqrt{2}$	da_{\min}	coincidences		
pbe	3.51	2.482	0.033	4 / 3	5 / 4	6 / 5
pw-lda	3.416	2.416	0.022	4 / 3	5 / 4	6 / 5
pz-lda	3.417	2.416	0.022	4 / 3	5 / 4	6 / 5
vwn	3.416	2.416	0.029	4 / 3	5 / 4	6 / 5
amo5	3.45	2.439	0.012	4 / 3	5 / 4	6 / 5
blyp	3.57	2.524	0.058	4 / 3	5 / 4	6 / 5
pbeint	3.469	2.453	0.019	4 / 3	5 / 4	6 / 5
pbesol	3.455	2.443	0.022	4 / 3	5 / 4	6 / 5
rpbe	3.544	2.506	0.032	4 / 3	5 / 4	6 / 5
revpbe	3.535	2.499	0.032	4 / 3	5 / 4	6 / 5

Table 22: Lattice parameter of **Ni**, 1st, 2nd and 3rd likeliest coincidence structure leading to an in-plane lattice parameter of the ZnO, which is closest to the free-standing case for various xc-functionals.

CONVERGENCE WITH NUMBER OF METAL LAYERS

For the found coincidence the convergence of the surface energy is tested with respect to the number of metal layers. The following form of the surface energy is used for the tests:

$$\gamma = \frac{1}{A} (E_{\text{slab}}(n_{\text{Zn}}, n_{\text{O}}) - n_{\text{metal}} \frac{1}{2} E_{\text{metal}}^{\text{bulk}} - n_{\text{O}} \frac{1}{2} E_{\text{O}_2} - n_{\text{Zn}} \frac{1}{2} E_{\text{Zn}}^{\text{bulk}}) \cdot A_0, \quad (153)$$

with n_{Zn} , n_{O} , n_{metal} the number of atoms of the species in the slab and A_0 the Area of a 1×1 unit-cell of metal surface. As reference energies the values presented in Appendix B are used. The evolution of the surface free energy γ of a mono-layer of ZnO with the number of metal substrate layers is shown in Fig. 101 for Ag, and in Fig. 102 for Cu. The defect free structure is plotted in red, the behavior with one additional oxygen atom is shown in blue. By taking into account the scale of both plots it can be summarized, that four layers of metal substrate are sufficient. The change of the surface free energy for the substrate thicknesses shown in Fig. 101 and Fig. 102 does not exceed 5 meV.

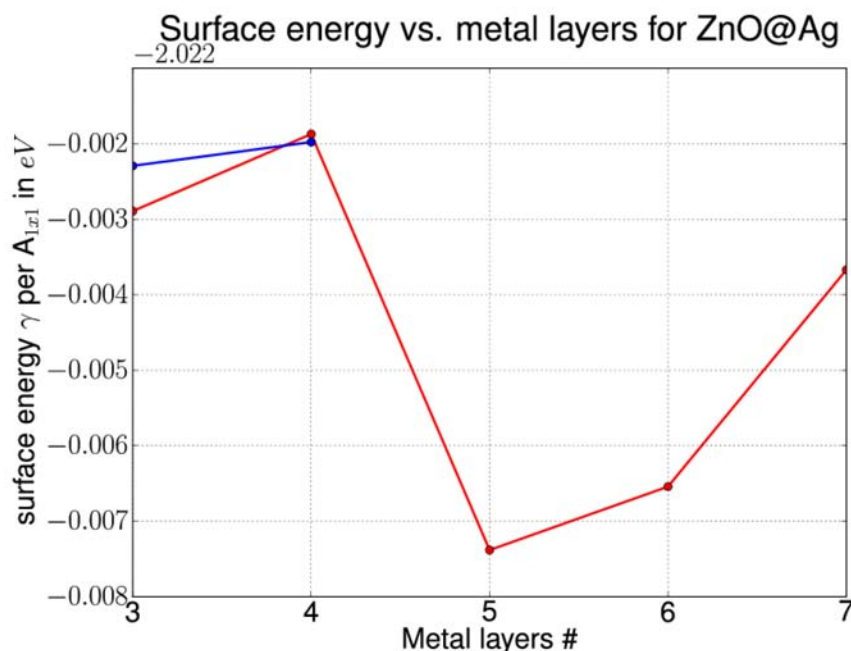


Figure 101: Convergence of the surface energy with the thickness of the metal substrate for one layer of ZnO on Ag. The ideal mono layer is plotted in red, with an additional oxygen atom in blue.

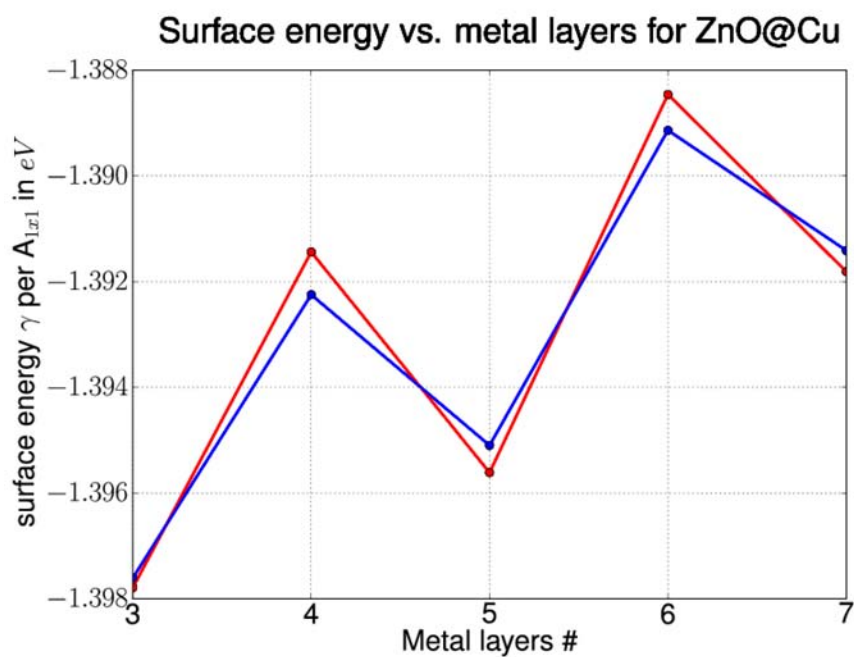


Figure 102: Convergence of the surface energy with the thickness of the metal substrate for one layer of ZnO on Cu. The ideal mono layer is plotted in red, with an additional oxygen atom in blue.

CORRUGATION MAPS

In this section the corrugations maps of mono-layer ZnO on the (111) surface of Ni, Rh, Pd, and Pt are reproduced. The corrugation maps for Cu and Ag can be found in chapter 6.3 together with the discussion of these results.

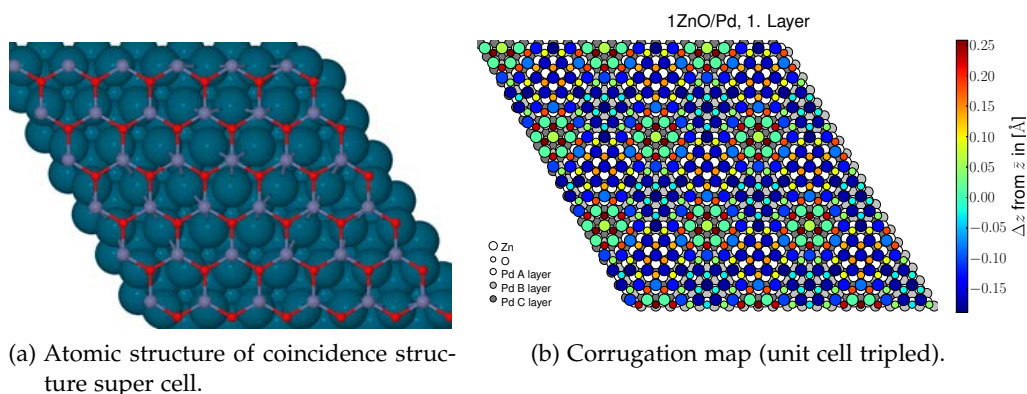


Figure 103: Atomic structure and corrugation of ZnO on Pd. Each Zn and O atom is assigned a color according to their lateral position.

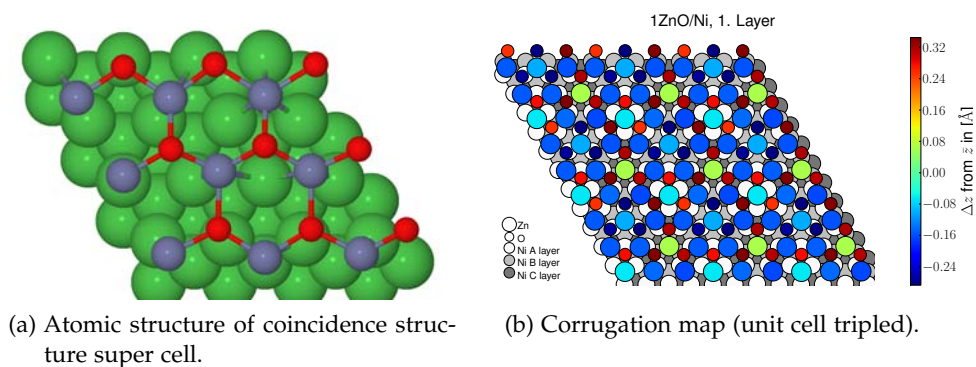


Figure 104: Atomic structure and corrugation of ZnO on Ni. Each Zn and O atom is assigned a color according to their lateral position.

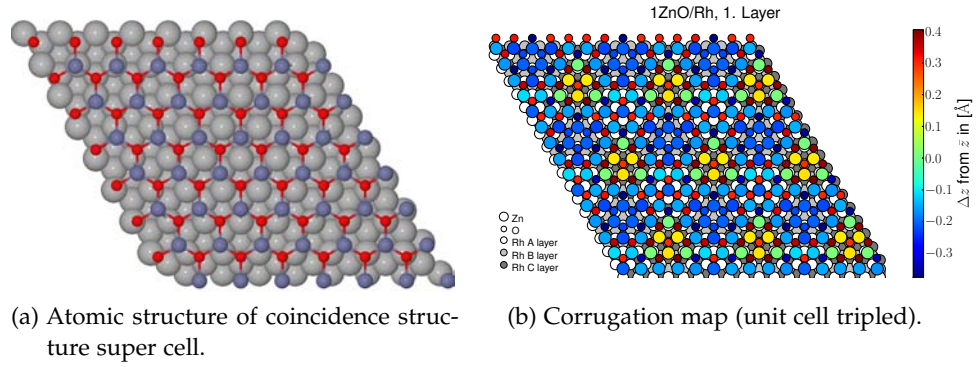


Figure 105: Atomic structure and corrugation of ZnO on Rh. Each Zn and O atom is assigned a color according to their lateral position.

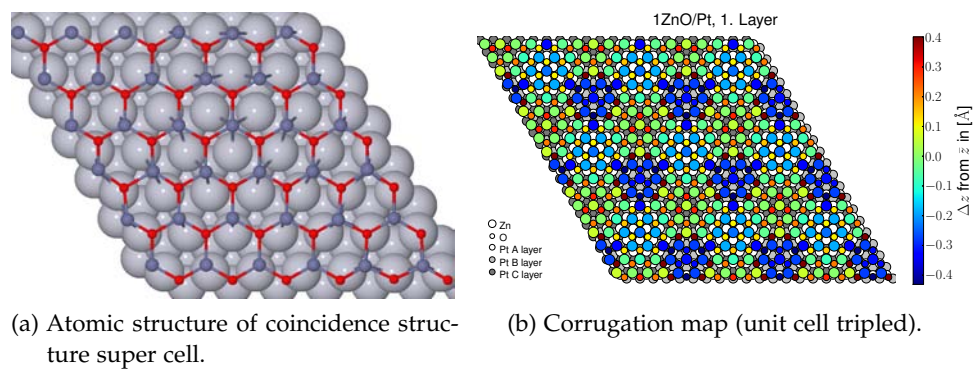


Figure 106: Atomic structure and corrugation of ZnO on Pt. Each Zn and O atom is assigned a color according to their lateral position.

STRUCTURE OF MULTIPLE ZNO LAYERS

The atomic structure of 1 to 4 layers of ZnO on Pd, Pt, Rh and Ni is presented in this section. With growing number of ZnO layers on the metal substrates the corrugation of the ZnO ultra-thin films increases. The films gradually progress from an α -BN to the wurtzite structure. They exhibit patches of α -BN and simultaneously patches of wurtzite structure. The disorder can be understood by a competition between different phases that are stable in a very narrow energy range as previously demonstrated for unsupported ZnO films [65]. The strain in the films plays a key role for the occurrence of the observed structures. Only for the 3 layers of ZnO on Ni the structure of the ZnO resembles the phases proposed by Demiroglu *et al.* [65].

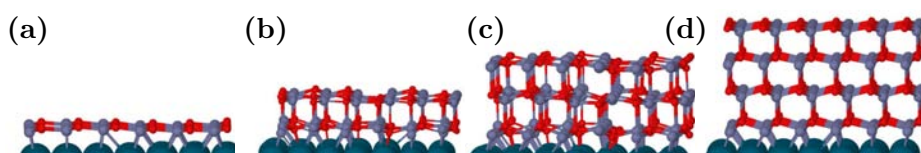


Figure 107: The relaxed structures for the hydrogen free ZnO on **Pd**. a) Mono-layer, b) Bilayer, c) 3 Layers, d) 4 Layers of ZnO.

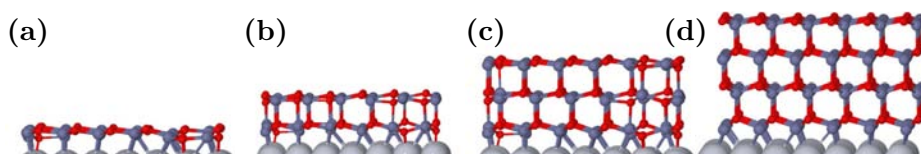


Figure 108: The relaxed structures for the hydrogen free ZnO on **Pt**. a) Mono-layer, b) Bilayer, c) 3 Layers, d) 4 Layers of ZnO.

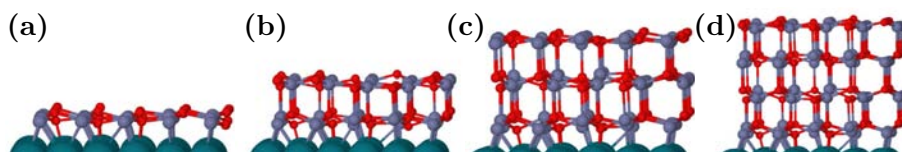


Figure 109: The relaxed structures for the hydrogen free ZnO on **Rh**. a) Mono-layer, b) Bilayer, c) 3 Layers, d) 4 Layers of ZnO.

LAYER RESOLVED CORRUGATION MAPS

In this section the evolution of the surface corrugation of up to 6 layers of ZnO on the different transition metals is shown. The results reflect the fact, that with increasing thickness the behavior of the ZnO becomes more bulk like. The structure transforms from the flat α -BN structure to the wurtzite structure with an intrinsic lateral distance between Zn and O atoms of 0.63 \AA . This ideal value is not reached due to the effect known from bulk ZnO surfaces, that the top surface layers contract inwards [162].

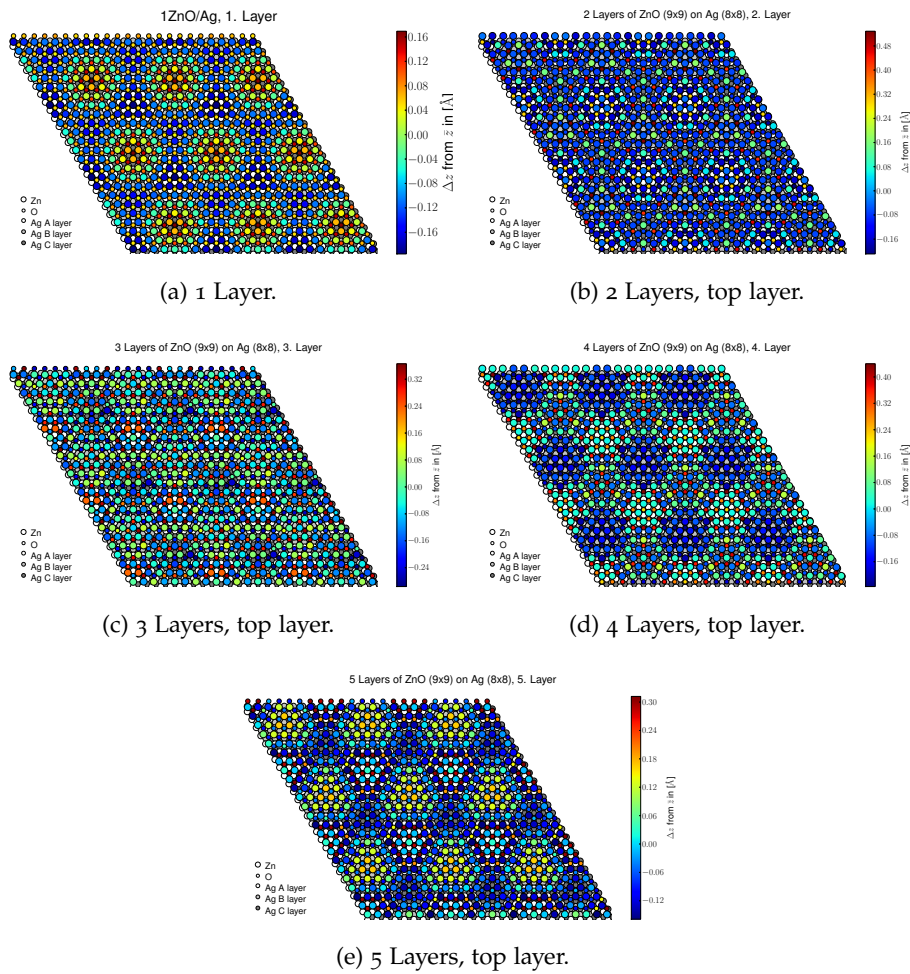


Figure 110: Layer resolved corrugation maps (unit cell tripled) for 1 to 5 layers of ZnO on Ag.

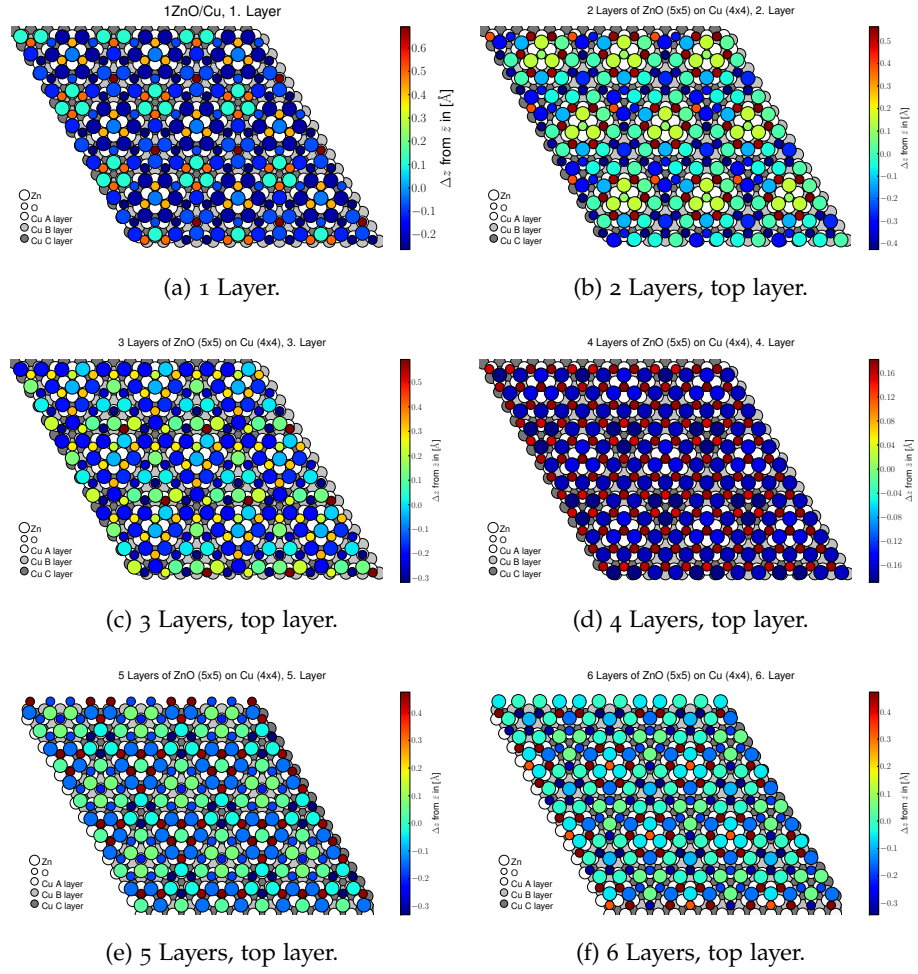


Figure 111: Layer resolved corrugation maps (unit cell tripled) for 1 to 6 layers of ZnO on Cu.

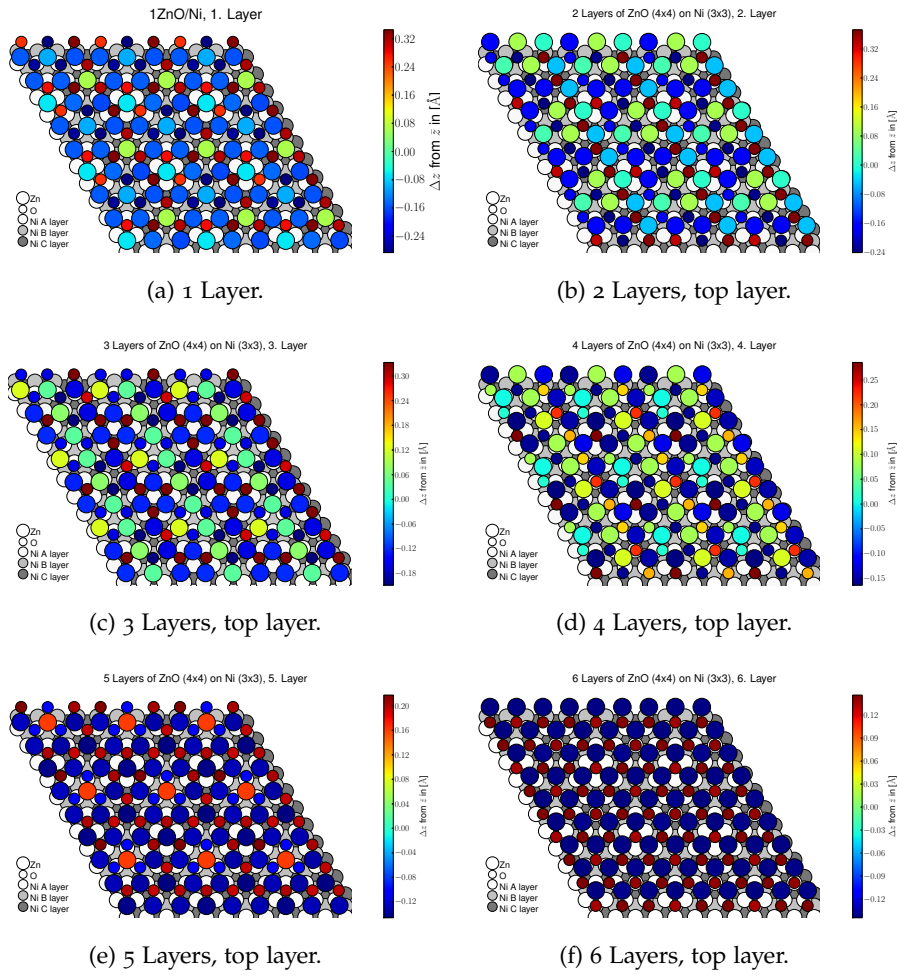


Figure 112: Layer resolved corrugation maps (unit cell tripled) for 1 to 6 layers of ZnO on Ni.

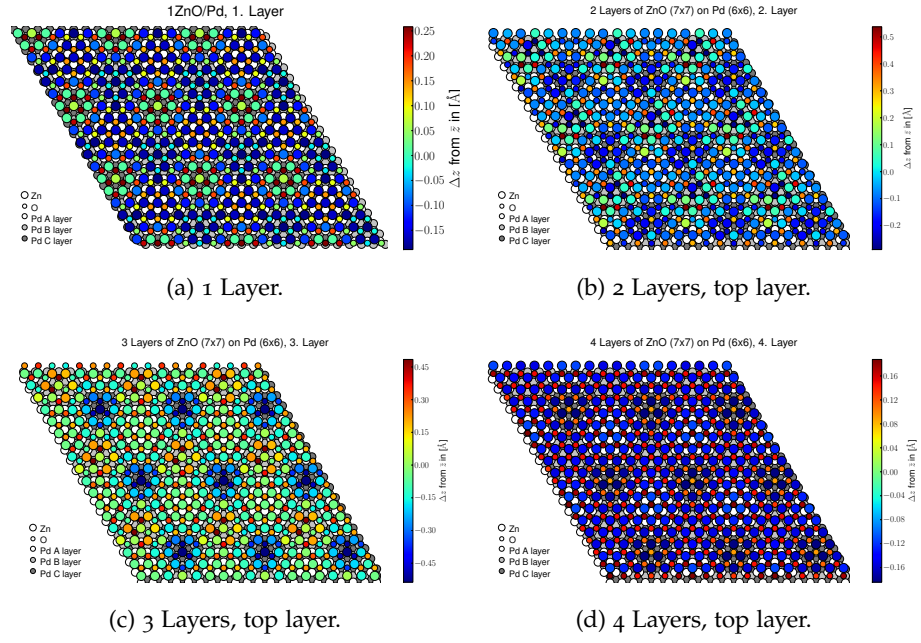


Figure 113: Layer resolved corrugation maps (unit cell tripled) for 1 to 4 layers of ZnO on Pd.

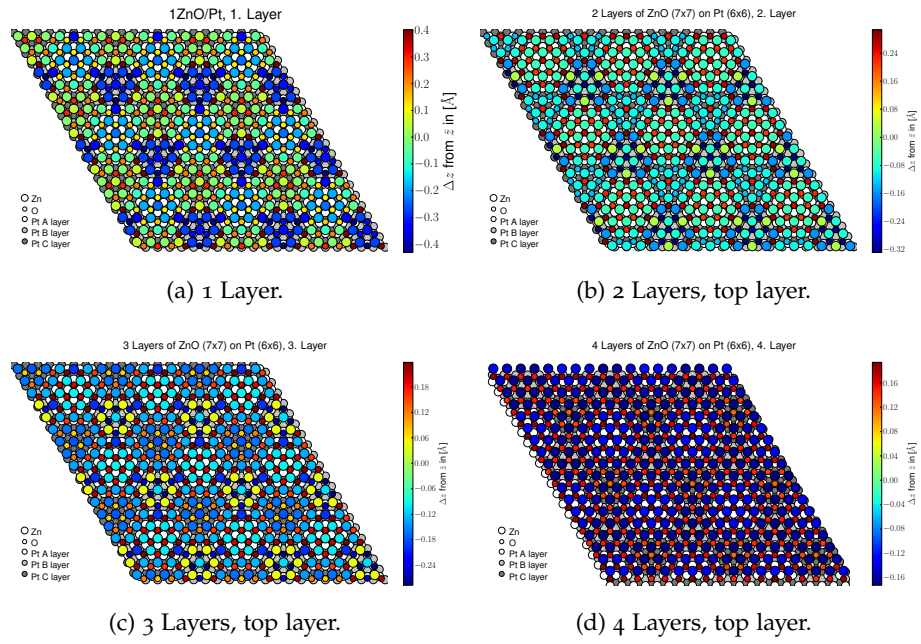


Figure 114: Layer resolved corrugation maps (unit cell tripled) for 1 to 4 layers of ZnO on Pt.

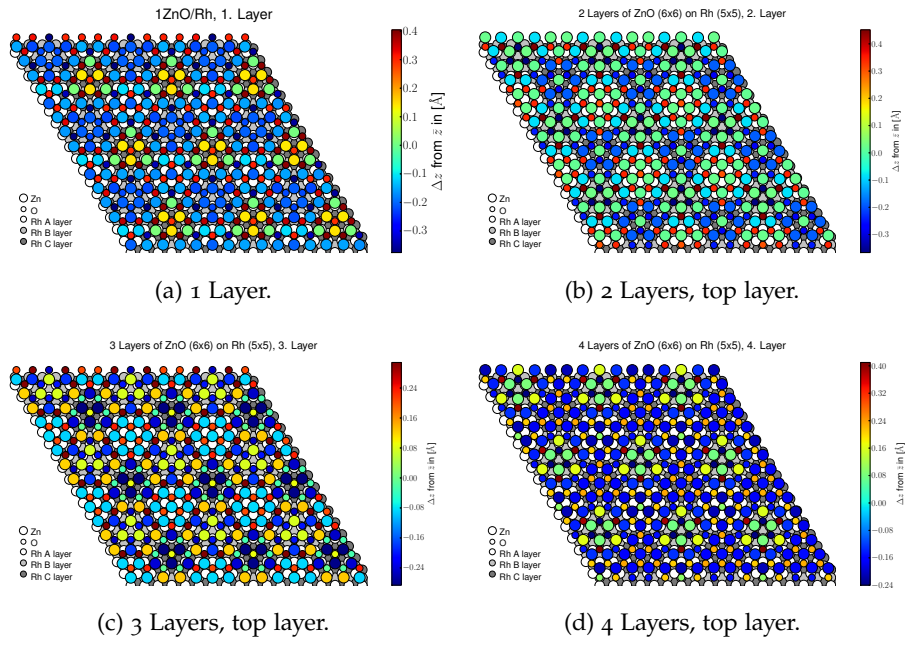


Figure 115: Layer resolved corrugation maps (unit cell tripled) for 1 to 4 layers of ZnO on Rh.

ELECTRONIC STRUCTURE OF MULTI-LAYER SYSTEMS

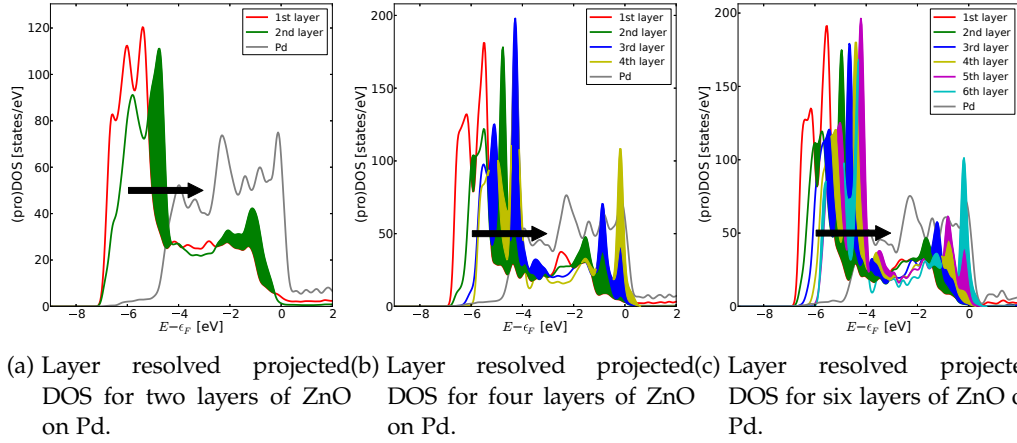


Figure 116: Projected density of states for a) two layers of ZnO on Pd, b) four layers of ZnO on Pd, and c) six layers of ZnO on Pd. The DOS is projected on the individual layers. The area that corresponds to higher density than the projected DOS of the previous layer is filled with the color of the layer. The direction of the shift of the Zn 3d bands is indicated by a black arrow.

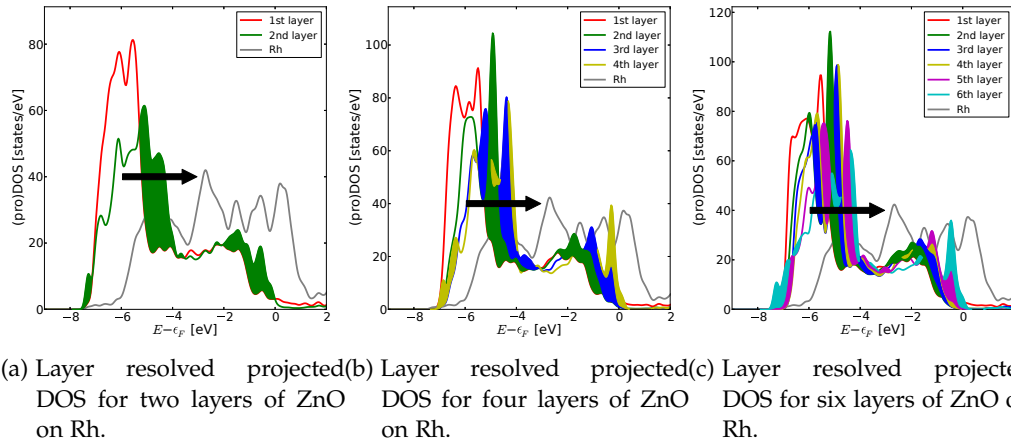
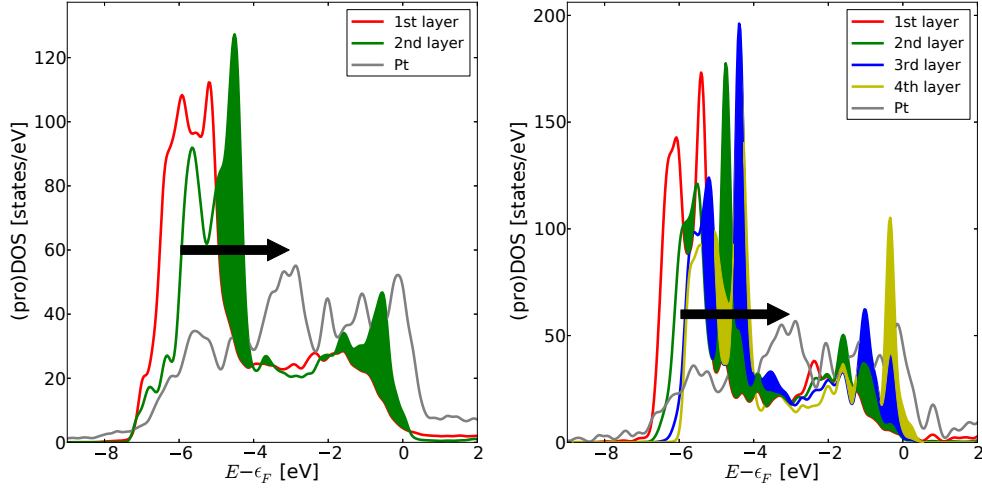


Figure 117: Projected density of states for a) two layers of ZnO on Rh, b) four layers of ZnO on Rh, and c) six layers of ZnO on Rh. The DOS is projected on the individual layers. The area that corresponds to higher density than the projected DOS of the previous layer is filled with the color of the layer. The direction of the shift of the Zn 3d bands is indicated by a black arrow.

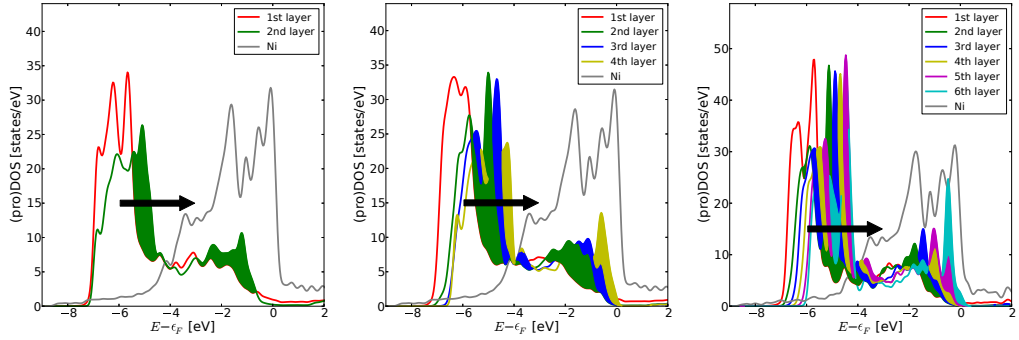
In this section the layer resolved projected DOS for Pd, Pt, Rh and Ni are presented. The DOS is projected separately on the metal and the single ZnO layers in the systems. In the plots their evolution is marked by filling the area

underneath the curves that have shifted higher in energy, closer to the Fermi level, as compared to the previous layer. The direction of the evolution is indicated by an arrow. The behavior is discussed in Sec. 7.2.



(a) Layer resolved projected DOS for two layers of ZnO on Pt. (b) Layer resolved projected DOS for four layers of ZnO on Pt.

Figure 118: Projected density of states for a) two layers of ZnO on Pt and b) four layers of ZnO on Pt. The DOS is projected on the individual layers. The area that corresponds to higher density than the projected DOS of the previous layer is filled with the color of the layer. The direction of the shift of the Zn 3d bands is indicated by a black arrow.

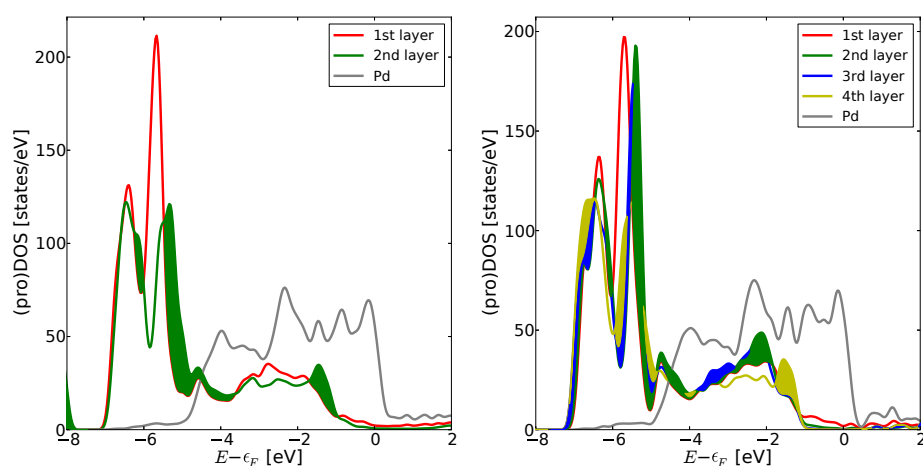


(a) Layer resolved projected DOS for two layers of ZnO on Ni. (b) Layer resolved projected DOS for four layers of ZnO on Ni. (c) Layer resolved projected DOS for six layers of ZnO on Ni.

Figure 119: Projected density of states for a) two layers of ZnO on Ni, b) four layers of ZnO on Ni, and c) six layers of ZnO on Ni. The DOS is projected on the individual layers. The area that corresponds to higher density than the projected DOS of the previous layer is filled with the color of the layer. The direction of the shift of the Zn 3d bands is indicated by a black arrow.

ELECTRONIC STRUCTURE OF (2×1) -H SYSTEMS

In this section the layer projected DOS for (2×1) -H reconstructed ZnO on the various transition metals is shown. The DOS is projected separately on the metal and the single ZnO layers in the systems. In the plots their evolution is marked by filling the area underneath the curves that have shifted higher in energy, closer to the Fermi level, as compared to the previous layer. Typically the change is very small and no direction is indicated as in the previous section. The behavior of the electronic states is discussed in Sec. 8.1.1 and compared to the results of Sec. 7.2.



(a) Layer resolved projected DOS for two layers of ZnO on Pd, (2×1) -H. (b) Layer resolved projected DOS for four layers of ZnO on Pd, (2×1) -H.

Figure 120: Projected density of states for a) two layers of ZnO on Pd, (2×1) -H, b) four layers of ZnO on Pd, (2×1) -H. The DOS is projected on the individual layers. The area that corresponds to higher density than the projected DOS of the previous layer is filled with the color of the layer.

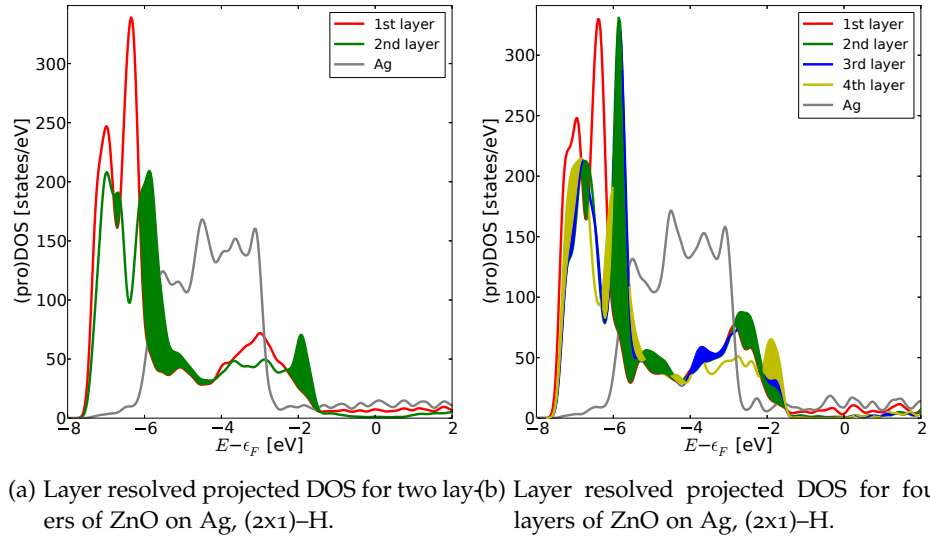


Figure 121: Projected density of states for a) two layers of ZnO on Ag, (2x1)-H, b) four layers of ZnO on Ag, (2x1)-H. The DOS is projected on the individual layers. The area that corresponds to higher density than the projected DOS of the previous layer is filled with the color of the layer.

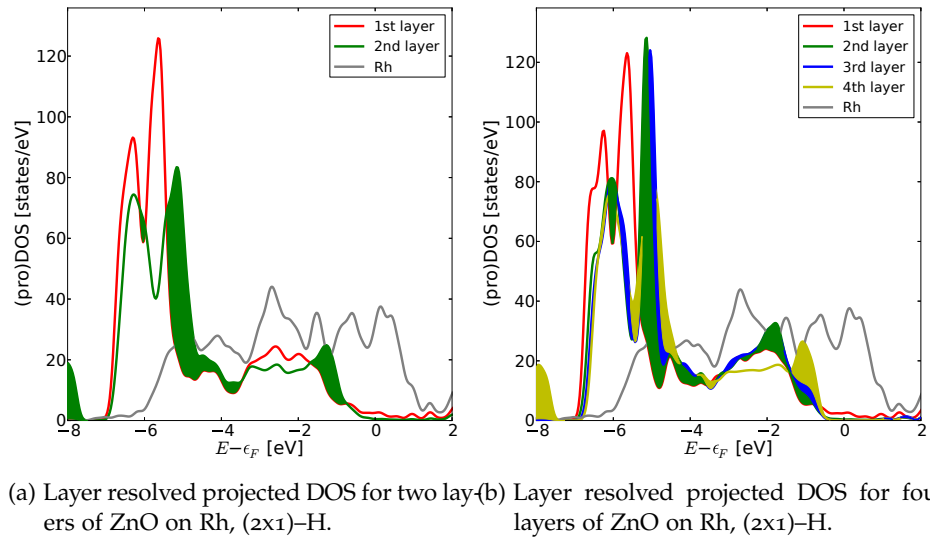
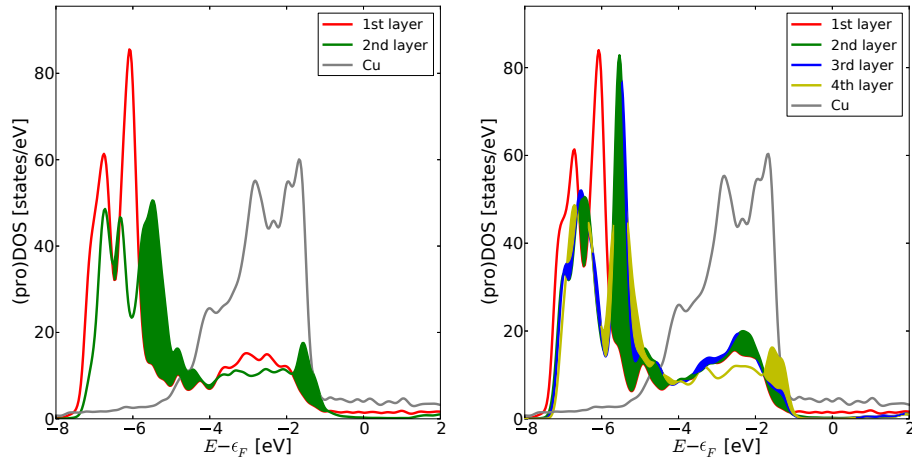


Figure 122: Projected density of states for a) two layers of ZnO on Rh, (2x1)-H, b) four layers of ZnO on Rh, (2x1)-H. The DOS is projected on the individual layers. The area that corresponds to higher density than the projected DOS of the previous layer is filled with the color of the layer.



(a) Layer resolved projected DOS for two layers of ZnO on Cu, (2x1)-H. (b) Layer resolved projected DOS for four layers of ZnO on Cu, (2x1)-H.

Figure 123: Projected density of states for a) two layers of ZnO on Cu, (2x1)-H, b) four layers of ZnO on Cu, (2x1)-H. The DOS is projected on the individual layers. The area that corresponds to higher density than the projected DOS of the previous layer is filled with the color of the layer.

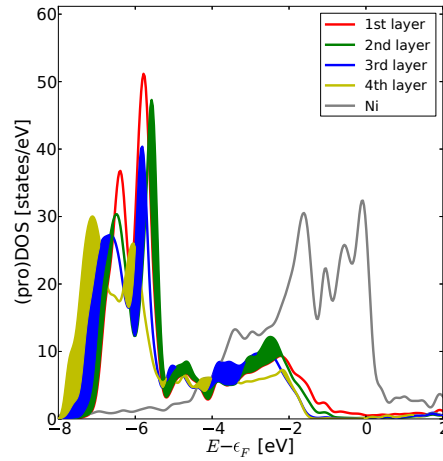


Figure 124: Projected density of states for four layers of ZnO on Ni, (2x1)-H. The DOS is projected on the individual layers. The area that corresponds to higher density than the projected DOS of the previous layer is filled with the color of the layer.

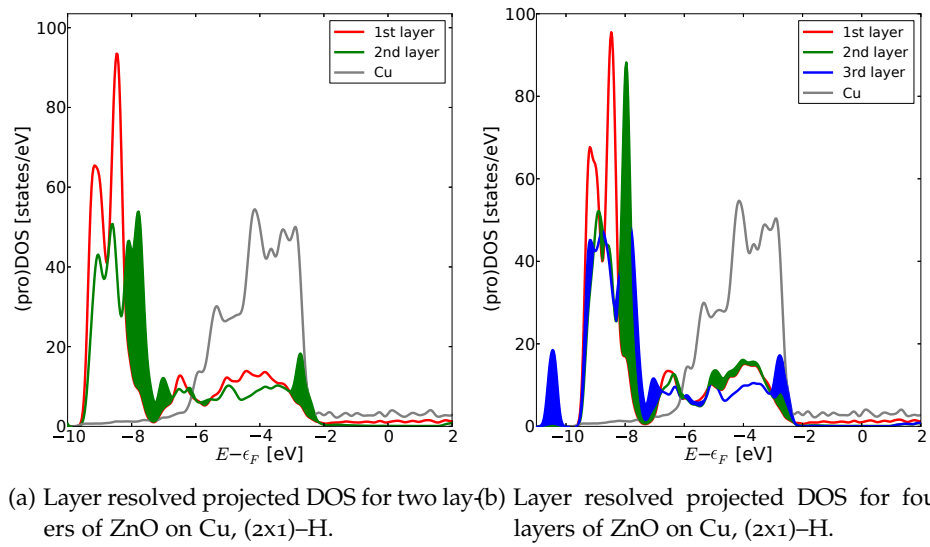


Figure 125: Projected density of states for a) two layers of ZnO on Cu, $(2 \times 1)\text{-H}$, b) three layers of ZnO on Cu, $(2 \times 1)\text{-H}$ calculated with **HSE06**. The DOS is projected on the individual layers. The area that corresponds to higher density than the projected DOS of the previous layer is filled with the color of the layer.

LAYER HEIGHTS FOR ZNO ON AG (111)

The film thicknesses and interlayer spacing including their standard deviation for one to four layers of ZnO (unreconstructed and (2x1)-H reconstructed) are presented in this section. A discussion and further explanations can be found in Sec. 9.

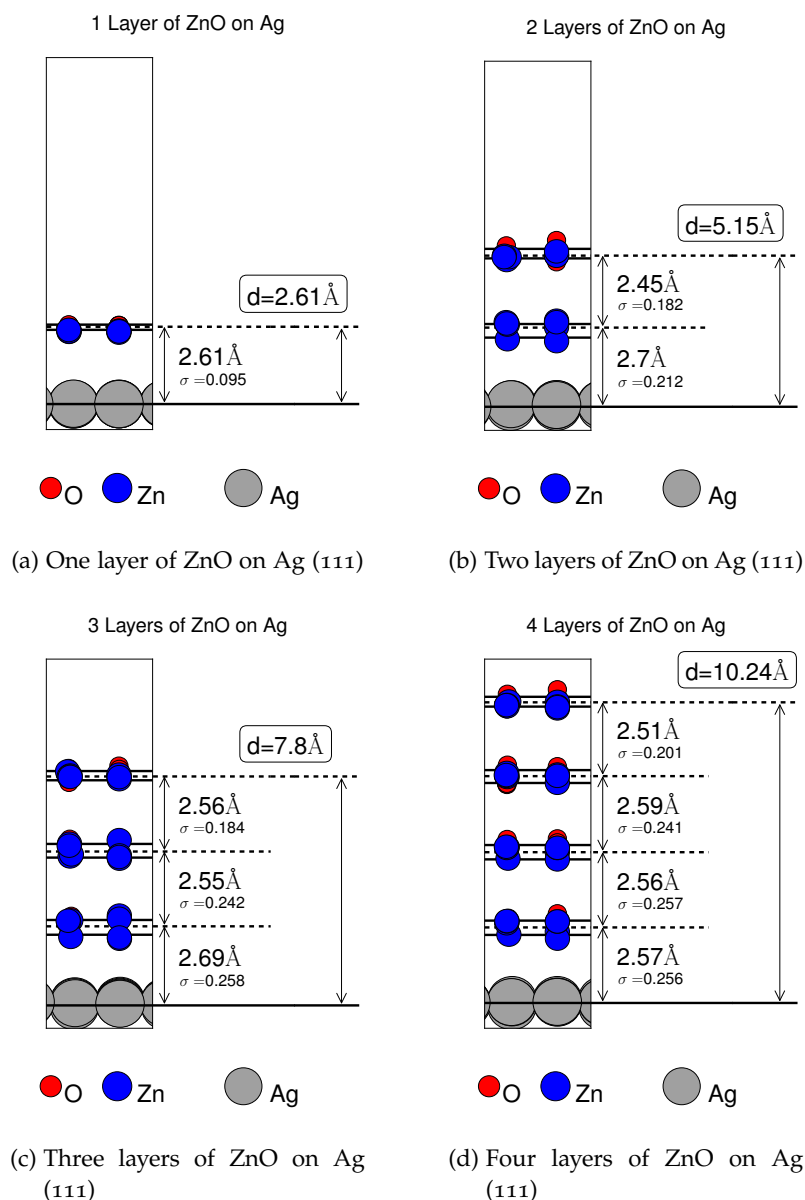


Figure 126: Film thickness and interlayer thicknesses for 1 to 4 layers of ZnO on Ag (111). The distances are the differences between the mean value of the atoms z-positions of the layer in question and the atom z-positions one layer below. From the data for the mean values the standard deviation σ is calculated.

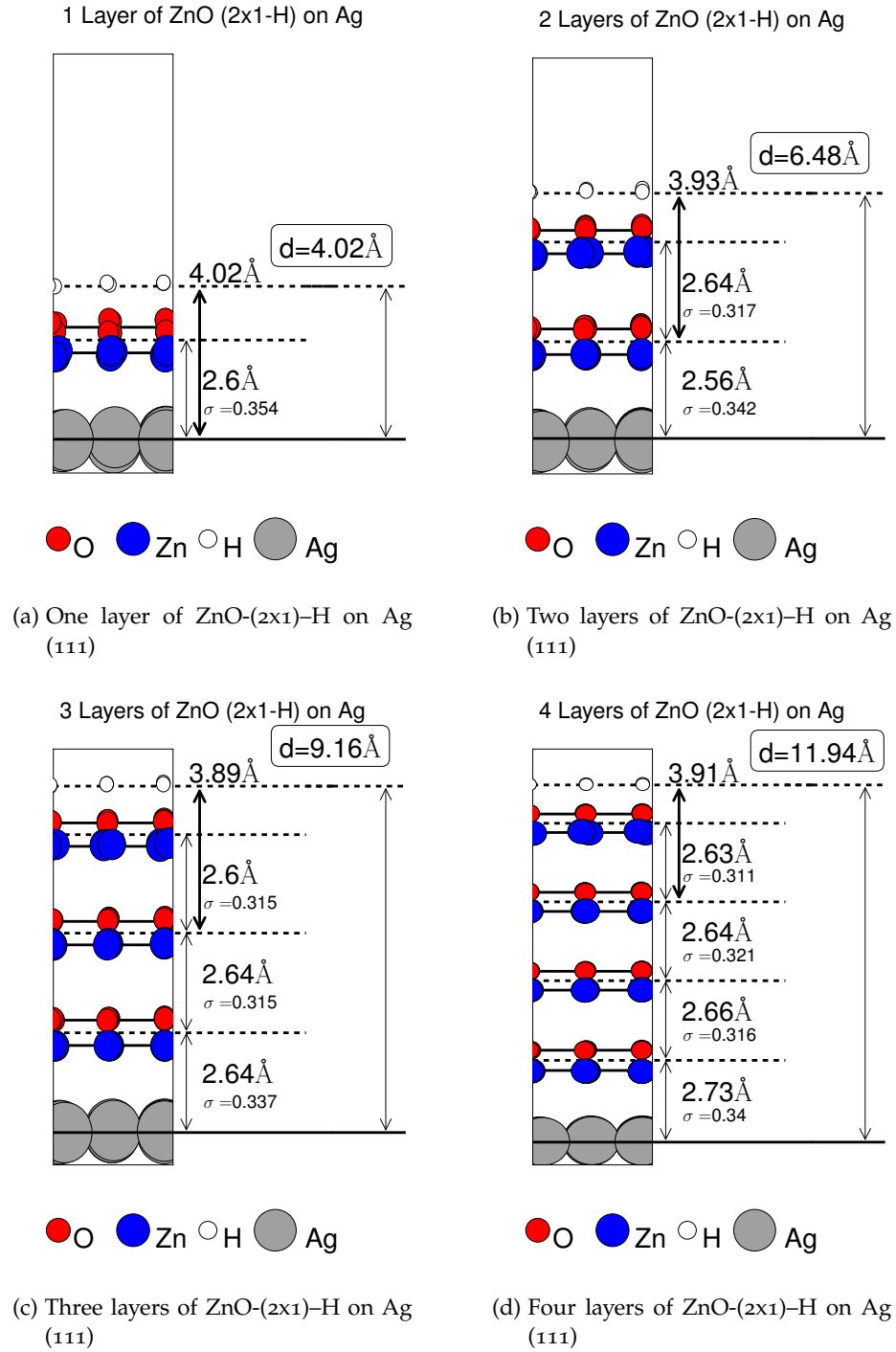


Figure 127: Film thickness and interlayer thicknesses for 1 to 4 layers of (2x1)-H reconstructed ZnO on Ag (111). The distances are the differences between the mean value of the atoms z-positions of the layer in question and the atom z-position one layer below. From the data for the mean values the standard deviation σ is calculated.

CURRENT DEPENDENCY OF APPARENT HEIGHTS

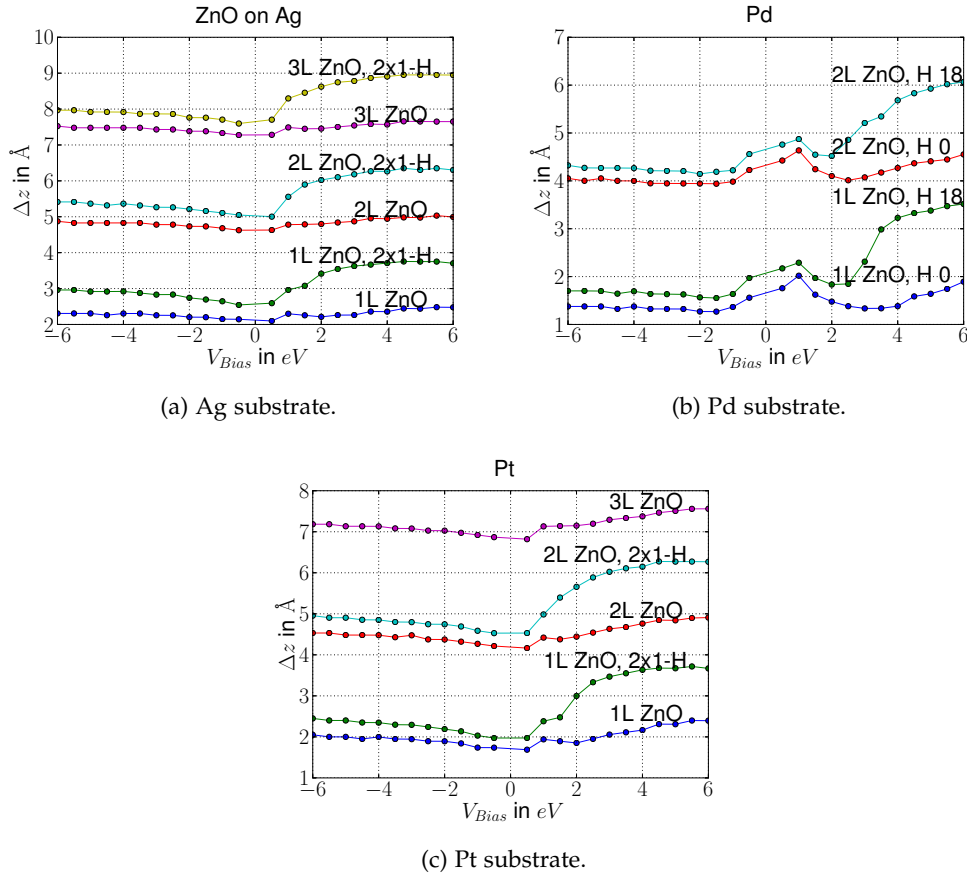


Figure 128: Bias voltage dependence of simulated STM graphs for (2x1)-H reconstructed and unreconstructed ZnO on Ag (111), Pd (111) and Pt (111) for one to three layers of ZnO. The underlying STM graphs were calculated within the Tersoff-Hamann approach as constant height STM graphs. The constant heights were sorted by current to yield constant current graphs, that were averaged to yield absolute height values. The apparent heights are the difference between the absolute height of the ZnO on the metal and the metal at the same constant current of $1 \cdot 10^{-5}$.

In this chapter the constant current dependency of the calculated apparent heights is presented. The apparent heights are calculated as averages over simulated constant current STM graphs. The constant height STM graphs are calculated from the local density by summing from the Fermi energy to the Fermi energy plus the selected bias voltage (V_{Bias}). The apparent heights thus yield a bias dependence, that depends on the electronic structure of the system. In Fig. 128 the bias dependence of reconstructed and unreconstructed ZnO on Ag, Pd and Pt is shown. For bias voltages below 0 eV only a slight decline on the

calculated height is observed. For Pd a small dip exists around the Fermi level. With increasing positive bias the calculated apparent height grows almost linearly until a saturation is reached. The large distance from the surface yields a low electron density and therefore a low tunneling current. The increase for positive bias voltages is stronger for the (2x1)-H reconstructed ZnO films.

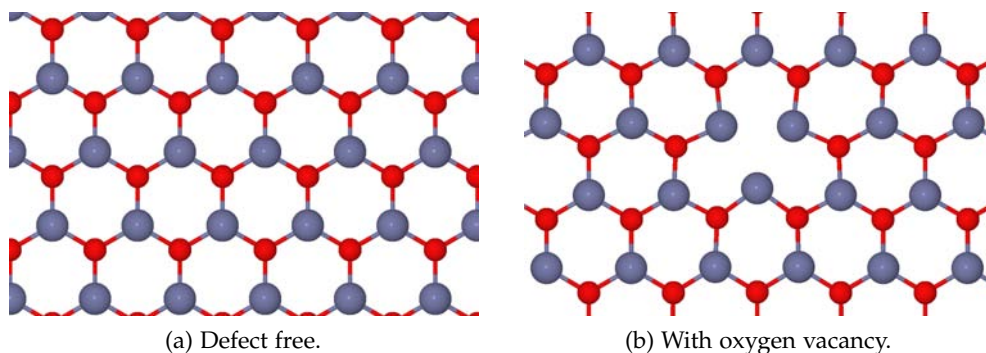
DEFECTS IN IDEAL α -BN ZNO MONO LAYER

Figure 129: Atomic structure of 4×4 unit-cells of an ideal α -BN ZnO mono layer without a) and with a oxygen vacancy b). The unit-cell is periodically continued.

To assess the error resulting from employing the semi-local xc-functional PBE [196], the formation energies of a oxygen vacancy in an ideal α -BN ZnO mono-layer is discussed and compared to results from calculations with the higher level hybrid xc-functional HSE06 [100] (includes 25% exact exchange). Calculations for bulk defects of ZnO and other materials have shown substantial differences in the formation energies obtained by PBE and HSE06 [211]. In Fig. 129 the atomic structure of a sheet of ZnO in α -BN structure is shown with and without a oxygen vacancy. From these two structures, relaxed with the PBE and HSE06 xc-functional the energy for removing one oxygen atom from the lattice can be calculated. The Formation energies are calculated as the difference between the ideal structure and the mono-layer with one oxygen vacancy and an isolated oxygen atom. All

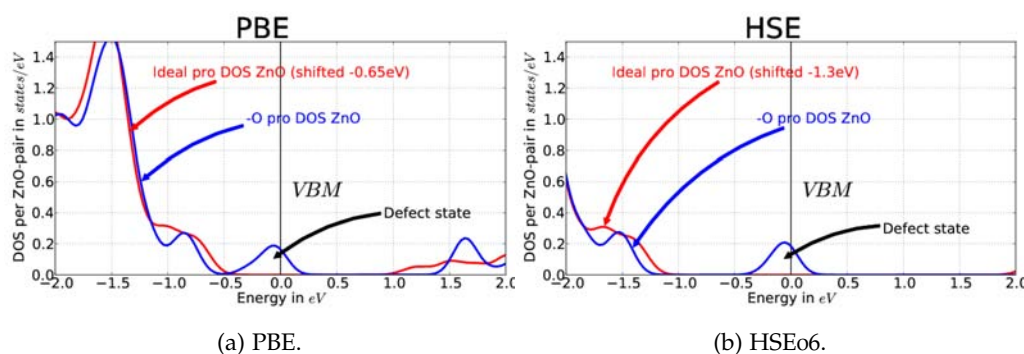


Figure 130: Density of states of a 4×4 ZnO mono-layer with one ZnO vacancy calculated with the PBE and HSE06 xc-functional. Both structures were relaxed with the underlying xc-functional.

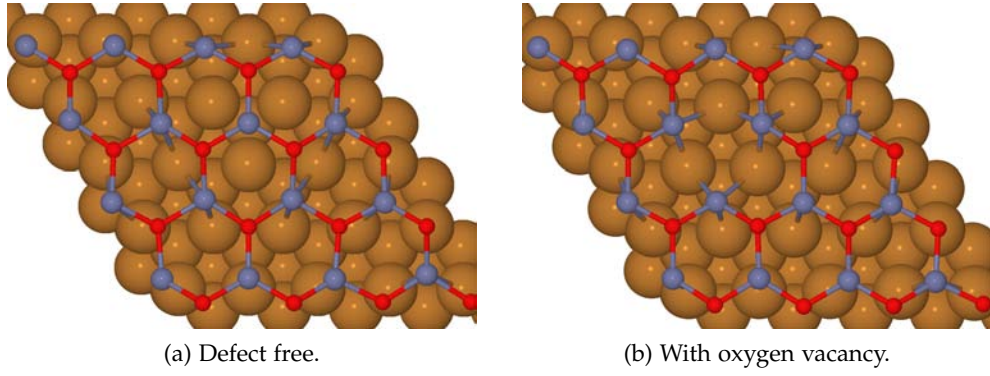


Figure 131: Atomic structure of one layer of ZnO on Cu (111) without a) and with a oxygen vacancy b). The unit-cell is periodically continued.

structures were relaxed with the xc-functional used to calculate the energies. The reference energies are taken from Tab. 15

$$E_{\text{Form}} = (E_{\text{ZnO-O}} + \frac{1}{2}E_{\text{O}}) - E_{\text{ZnO}}. \quad (154)$$

The formation energies defined in such a way are 6.54 eV for HSE06 and 6.48 eV for PBE for a 4x4 sheet of ZnO and one oxygen vacancy (1/16 of defect concentration). The difference per ZnO unit cell is 4 meV. The error encountered in the calculation is therefore considered small.

A further qualitative error estimation is achieved by comparing the electronic structures of the structure with oxygen vacancy calculated by HSE06 and PBE. In Fig. 130 density of states for PBE and HSE06 are shown. The qualitative agreement between both graphs is very good. For both calculations a defect state is observed around the Fermi energy. For HSE06 the rest of the electronic states are further shifted up or downwards in energy as compared to the PBE calculation resulting in an increased band gap.

The errors introduced by using PBE are expected to be negligible for the ZnO

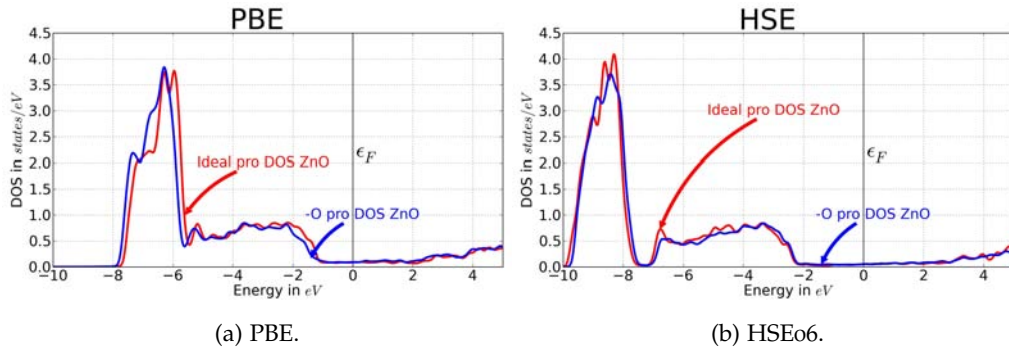


Figure 132: Density of states of a ZnO mono-layer on Cu (111) with one ZnO vacancy calculated with the PBE and HSE06 xc-functional. Both structures were relaxed with the underlying xc-functional.

mono-layer.

In this work ZnO on metal substrates is investigated. To quantify the errors for those systems a similar analysis as for the mono-layer is conducted. In Fig. 131 the atomic structure of one layer of ZnO on Cu (111) is shown with and without an oxygen vacancy. The full super cell is shown, being the coincidence structure previously determined (see Sec. 6). The structures were relaxed with HSE06 and PBE. The defect formation energies as calculated before, are 2.56 eV for the PBE xc-functional and 2.52 eV for HSE06. This results in a difference of 3 meV per 1×1 ZnO surface unit cell. The error can be considered negligible for the investigation of the surface free energies. The DOS for the calculation with PBE and HSE06 are shown in Fig 132. The qualitative differences in the DOS have further reduced as compared to the free-standing mono-layer. The most prominent difference is due to the stronger localization of the Zn d-states because of the use of exact exchange in HSE06. Also in this case we can conclude, that the semi-local xc-functional PBE is sufficient for the calculation of surface phase diagrams (total energy) and the description of the electronic structure.

CHARGE DENSITY DIFFERENCES

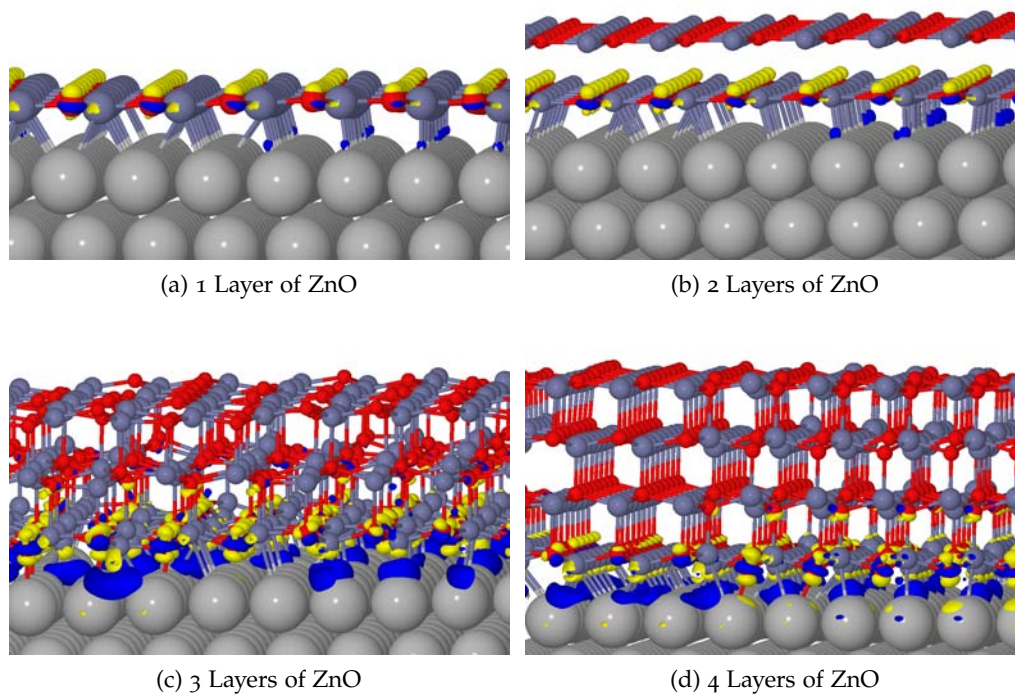


Figure 133: Charge density differences for 1 to 4 layers of ZnO on Ag (111). The differences are calculated between the full coincidence structures and the Ag substrate and ZnO ad-layer with frozen geometries. The cutoff for all graphs is $0.02 \text{ electrons}/a_B^3$. Yellow refers to electron density decrease and blue to electron density increase.

PUBLICATIONS

Some ideas and figures have appeared previously in the following publications:

Bjoern Bieniek, Oliver T. Hofmann, and Patrick Rinke. Influence of hydrogen on the structure and stability of ultra-thin zno on metal substrates. *Applied Physics Letters*, 106(13):-, 2015

Eike Verdenhalven, Andreas Knorr, Marten Richter, Bjoern Bieniek, and Patrick Rinke. Theory of optical excitations in dipole-coupled hybrid molecule-semiconductor layers: Coupling of a molecular resonance to semiconductor continuum states. *Phys. Rev. B*, 89:235314, Jun 2014

COLOPHON

This document was typeset using the typographical look-and-feel `classicthesis` developed by André Miede. The style was inspired by Robert Bringhurst's seminal book on typography "*The Elements of Typographic Style*". `classicthesis` is available for both \LaTeX and \LyX :

<http://code.google.com/p/classicthesis/>

Postprocessing of data obtained by DFT calculations was done by scientific libraries `numpy` and `scipy` for python:

<http://www.scipy.org> <http://www.numpy.org>

Plots of density of states, phase diagrams, band structure, etc. were prepared with the 2D plotting library `matplotlib` for python:

<http://matplotlib.org>

Illustrations of atomic structures were created by `Jmol`:

<http://www.jmol.org>

and rendered with `povray`:

www.povray.org

BIBLIOGRAPHY

- [1] Sadao Adachi. Zinc oxide (zno). In *Handbook on Physical Properties of Semiconductors*, pages 65–97. Springer US, 2004.
- [2] C. Adamo and V. Barone. *J. Chem. Phys.*, 110:6158, 1999.
- [3] V. M. Agranovich, Yu. N. Gartstein, and M. Litinskaya. Hybrid resonant organic-inorganic nanostructures for optoelectronic applications. *Chemical Reviews*, 111(9):5179–5214, 2011.
- [4] Audrius Alkauskas, Peter Broqvist, and Alfredo Pasquarello. Defect levels through hybrid density functionals: Insights and applications. *physica status solidi (b)*, 248(4):775–789, 2011.
- [5] C. G. Allen, D. J. Baker, T. M. Brenner, C. C. Weigand, J. M. Albin, K. X. Steirer, D. C. Olson, C. Ladam, D. S. Ginley, R. T. Collins, and T. E. Furtak. Alkyl surface treatments of planar zinc oxide in hybrid organic/inorganic solar cells. *The Journal of Physical Chemistry C*, 116(16):8872–8880, 2012.
- [6] C. Ambrosch-Draxl and J. O. Sofo. Linear optical properties of solids within the full-potential linearized augmented planewave method. *Computer Physics Communications*, (175):1–14, 2006.
- [7] E. Anderson, Z. Bai, C. Bischof, S. Blackford, J. Demmel, J. Dongarra, J. Du Croz, A. Greenbaum, S. Hammarling, A. McKenney, and D. Sorensen. *LAPACK Users' Guide*. Society for Industrial and Applied Mathematics, Philadelphia, PA, third edition, 1999.
- [8] George B. Arfken, Hans J. Weber, and Frank E. Harris. *Mathematical Methods for Physicists, Sixth Edition: A Comprehensive Guide*. Academic Press, 6 edition, July 2005.
- [9] R. Armiento and Ann E. Mattsson. *Phys. Rev. B*, 72:085108, 2005.
- [10] F Aryasetiawan and O Gunnarsson. The gw method. *Reports on Progress in Physics*, 61(3):237, 1998.
- [11] N.W. Ashcroft and N.D. Mermin. *Solid State Physics*. Saunders College, Philadelphia, 1976.
- [12] A. Ashrafi and C. Jagadish. Review of zincblende zno: Stability of metastable zno phases. *Journal of Applied Physics*, 102(7):–, 2007.
- [13] A. B. M. Almamun Ashrafi, Akio Ueta, Adrian Avramescu, Hidekazu Kumanomoto, Ikuo Suemune, Young-Woo Ok, and Tae-Yeon Seong. Growth and characterization of hypothetical zinc-blende zno films on gaas(001) substrates with zns buffer layers. *Applied Physics Letters*, 76(5):550–552, 2000.

- [14] Viktor Atalla, Mina Yoon, Fabio Caruso, Patrick Rinke, and Matthias Scheffler. Hybrid density functional theory meets quasiparticle calculations: A consistent electronic structure approach. *Phys. Rev. B*, 88:165122, Oct 2013.
- [15] V.M. Axt and A. Stahl. A dynamics-controlled truncation scheme for the hierarchy of density matrices in semiconductor optics. *Zeitschrift für Physik B Condensed Matter*, 93(2):195–204, 1994.
- [16] George A. Baker and Peter Graves-Morris. *Padé Approximants (Encyclopedia of Mathematics and its Applications)*. Encyclopedia of mathematics and its applications, v. 59. Cambridge University Press, 2 edition, January 1996.
- [17] J. Baker, J. Andzelm, A. Scheiner, and B. Delley. *J. Chem. Phys.*, 101:8894, 1994.
- [18] A. Bakin, A. El-Shaer, A. C. Mofor, M. Al-Suleiman, E. Schlenker, and A. Waag. Znmggo-zno quantum wells embedded in zno nanopillars: Towards realisation of nano-leds. *physica status solidi (c)*, 4(1):158–161, 2007.
- [19] C. Baltes, S. Vukojević, and F. Schüth. Correlations between synthesis, precursor, and catalyst structure and activity of a large set of cuo/zno/al₂o₃ catalysts for methanol synthesis. *Journal of Catalysis*, 258(2):334 – 344, 2008.
- [20] J. Bardeen. Tunnelling from a many-particle point of view. *Phys. Rev. Lett.*, 6:57–59, Jan 1961.
- [21] Basko, D., La Rocca, G. C., Bassani, F., and Agranovich, V. M. Förster energy transfer from a semiconductor quantum well to an organic material overlay. *Eur. Phys. J. B*, 8(3):353–362, 1999.
- [22] C. I. Bayly, P. Cieplak, W. D. Cornell, and P. A. Kollman. A well-behaved electrostatic potential based method using charge restraints for deriving atomic charges: The resp model. *J. Phys. Chem.*, 97:10269–10280, 1993.
- [23] A.D. Becke. *J. Chem. Phys.*, 88:1053, 1988.
- [24] Axel D. Becke. A new mixing of hartree-fock and local density-functional theories. *The Journal of Chemical Physics*, 98(2):1372–1377, 1993.
- [25] Malte Behrens, Felix Studt, Igor Kasatkin, Stefanie Kühn, Michael Hävecker, Frank Abild-Pedersen, Stefan Zander, Frank Girgsdies, Patrick Kurr, Benjamin-Louis Kniep, Michael Tovar, Richard W. Fischer, Jens K. Nørskov, and Robert Schlögl. The active site of methanol synthesis over cu/zno/al₂o₃ industrial catalysts. *Science*, 336(6083):893–897, 2012.
- [26] C. Berthod, N. Binggeli, and A. Baldereschi. Schottky barrier heights at polar metal/semiconductor interfaces. *Phys. Rev. B*, 68:085323, Aug 2003.
- [27] B. H. Besler, K. M. Merz, and P. A. Kollman. Atomic charges derived from semiempirical methods. *J. Comput. Chem.*, 11:431–439, 1990.
- [28] Bjoern Bieniek, Oliver T. Hofmann, and Patrick Rinke. Influence of hydrogen on the structure and stability of ultra-thin zno on metal substrates. *Applied Physics Letters*, 106(13):–, 2015.

- [29] K. Binder. Recent trends in the development and application of the monte carlo method. In Kurt Binder, editor, *Monte Carlo Methods in Statistical Physics*, volume 7 of *Topics in Current Physics*, pages 357–392. Springer Berlin Heidelberg, 1986.
- [30] L. S. Blackford, J. Choi, A. Cleary, E. D’Azevedo, J. Demmel, I. Dhillon, J. Dongarra, S. Hammarling, G. Henry, A. Petitet, K. Stanley, D. Walker, and R. C. Whaley. *ScaLAPACK Users’ Guide*.
- [31] P. Blaha, H. Hofstätter, O. Koch, R. Laskowski, and K. Schwarz. Iterative diagonalization in augmented plane wave based methods in electronic structure calculations. *Journal of Computational Physics*, 229(2):453 – 460, 2010.
- [32] P. E. Blöchl. Projector augmented-wave method. *Phys. Rev. B*, 50:17953–17979, Dec 1994.
- [33] Volker Blum, Ralf Gehrke, Felix Hanke, Paula Havu, Ville Havu, Xinguo Ren, Karsten Reuter, and Matthias Scheffler. Ab initio molecular simulations with numeric atom-centered orbitals. *Comput. Phys. Commun.*, 180(11):2175–2196, 2009.
- [34] S Blumstengel, S Sadofev, and F Henneberger. Electronic coupling of optical excitations in organic/inorganic semiconductor hybrid structures. *New Journal of Physics*, 10(6):065010, 2008.
- [35] A. Bondi. van der waals volumes and radii. *J. Phys. Chem.*, 68:441–451, 1964.
- [36] M. Born and R. Oppenheimer. Zur quantentheorie der molekeln. *Annalen der Physik*, 389(20):457–484, 1927.
- [37] Christoph J. Brabec, Sean E. Shaheen, Christoph Winder, N. Serdar Sariciftci, and Patrick Denk. Effect of lif/metal electrodes on the performance of plastic solar cells. *Applied Physics Letters*, 80(7):1288–1290, 2002.
- [38] J. L. Bredas, J. P. Calbert, D. A. da Silva Filho, and J. Cornil. Organic semiconductors: A theoretical characterization of the basic parameters governing charge transport. *Proceedings of the National Academy of Sciences*, 99(9):5804–5809, 2002.
- [39] C. M. Breneman and K. B. Wiberg. Determining atom-centered monopoles from molecular electrostatic potentials. the need for high sampling density in formamide conformational analysis. *J. Comput. Chem.*, 11:361–373, 1990.
- [40] Alejandro L. Briseno, Thomas W. Holcombe, Akram I. Boukai, Erik C. Garnett, Steve W. Shelton, Jean J. M. Fréchet, and Peidong Yang. Oligo- and polythiophene/zno hybrid nanowire solar cells. *Nano Letters*, 10(1):334–340, 2010. PMID: 20000808.
- [41] N. Buecking, P. Kratzer, M. Scheffler, and A. Knorr. Linking density functional and density-matrix theory: Picosecond electron relaxation at the si(100) surface. *Phys. Rev. B*, 77:233305, Jun 2008.

- [42] Kieron Burke et al. The abc of dft. *Department of Chemistry, University of California*, 2007.
- [43] Burroughes J. H., Bradley D. D. C., Brown A. R., Marks R. N., Mackay K., Friend R. H., Burns P. L., and Holmes A. B. Light-emitting diodes based on conjugated polymers. *Nature*, 347(6293):539–541, oct 1990. 10.1038/347539a0.
- [44] C. Campana, B. Mussard, and T. K. Woo. Electrostatic potential derived atomic charges for periodic systems using a modified error functional. *J. Chem. Theory Comput.*, 5:2866–2878, 2009.
- [45] Shih-Chia Chang and Peter Mark. The crystallography of the polar (0001) zn and (000-1)o surfaces of zinc oxide. *Surface Science*, 46(1):293 – 300, 1974.
- [46] S. Chanyawadee, P. G. Lagoudakis, R. T. Harley, D. G. Lidzey, and M. Henini. Nonradiative exciton energy transfer in hybrid organic-inorganic heterostructures. *Phys. Rev. B*, 77:193402, May 2008.
- [47] D.-J. Chen, A. C. Stern, B. Space, and J. K. Johnson. Atomic charges derived from electrostatic potential for molecular and periodic systems. *J. Phys. Chem. A*, 114:10225–10233, 2010.
- [48] L. E. Chirlian and M. M. Francl. Atomic charges derived from electrostatic potentials: A detailed study. *J. Comput. Chem.*, 8:894–905, 1987.
- [49] S. Chu, J. H. Lim, L. J. Mandalapu, Z. Yang, L. Li, and J. L. Liu. Sb-doped p-zno–Ga-doped n-zno homojunction ultraviolet light emitting diodes. *Applied Physics Letters*, 92(15):–, 2008.
- [50] M.F. Chung and H.E. Farnsworth. Investigations of surface stability of ZnS wurtzite compounds by {LEED}. *Surface Science*, 22(1):93 – 110, 1970.
- [51] Frederik Claeysens, Colin L. Freeman, Neil L. Allan, Ye Sun, Michael N. R. Ashfold, and John H. Harding. Growth of zno thin films-experiment and theory. *J. Mater. Chem.*, 15:139–148, 2005.
- [52] R. Clausius. Ueber die art der bewegung, welche wir wärme nennen. *Annalen der Physik*, 176(3):353–380, 1857.
- [53] R. Clausius. *Die mechanische Wärmetheorie*, volume 2. F. Vieweg und Sohn, 1879.
- [54] J. Clerk-Maxwell. Xxii.-on the dynamical evidence of the molecular constitution of bodies. *J. Chem. Soc.*, 28:493–508, 1875.
- [55] Aron J. Cohen, Paula Mori-Sánchez, and Weitao Yang. Challenges for density functional theory. *Chemical Reviews*, 112(1):289–320, 2012.
- [56] S. R. Cox and D. E. Williams. Representation of the molecular electrostatic potential by a net atomic charge model. *J. Comput. Chem.*, 2:304–323, 1981.

- [57] Gábor I. Csonka, John P. Perdew, Adrienn Ruzsinszky, Pier H. T. Philipsen, Sébastien Lebègue, Joachim Paier, Oleg A. Vydrov, and János G. Ángyán. Assessing the performance of recent density functionals for bulk solids. *Phys. Rev. B*, 79:155107, Apr 2009.
- [58] N R D’Amico, G Cantele, C A Perroni, and D Ninno. Electronic properties and schottky barriers at zno-metal interfaces from first principles. *Journal of Physics: Condensed Matter*, 27(1):015006, 2015.
- [59] J. Danckwerts, K. J. Ahn, J. Förstner, and A. Knorr. Theory of ultrafast nonlinear optics of coulomb-coupled semiconductor quantum dots: Rabi oscillations and pump-probe spectra. *Phys. Rev. B*, 73:165318, Apr 2006.
- [60] R. de L. Kronig. On the theory of dispersion of x-rays. *J. Opt. Soc. Am.*, 12(6):547–556, Jun 1926.
- [61] F. Decremps, F. Datchi, A. M. Saitta, A. Polian, S. Pascarelli, A. Di Cicco, J. P. Itié, and F. Baudalet. Local structure of condensed zinc oxide. *Phys. Rev. B*, 68:104101, Sep 2003.
- [62] F. Della Sala, S. Blumstengel, and F. Henneberger. Electrostatic-field-driven alignment of organic oligomers on zno surfaces. *Phys. Rev. Lett.*, 107:146401, Sep 2011.
- [63] B. Delley. *J. Chem. Phys.*, 92:508, 1990.
- [64] B. Delley. *J. Comp Chem.*, 17:1152, 1995.
- [65] Ilker Demiroglu and Stefan T. Bromley. Nanofilm versus Bulk Polymorphism in Wurtzite Materials. *Phys. Rev. Lett.*, 110(24):245501, 2013.
- [66] Ilker Demiroglu, Daniele Stradi, Francesc Illas, and Stefan T. Bromley. A theoretical study of a ZnO graphene analogue: adsorption on Ag(111) and hydrogen transport. *J. Phys.: Condens. Matter*, 23(33):334215, 2011.
- [67] Xingyi Deng, Kun Yao, Keju Sun, Wei-Xue Li, Junseok Lee, and Christopher Matranga. Growth of single- and bilayer zno on au(111) and interaction with copper. *J. Phys. Chem. C*, 117(21):11211–11218, MAY 30 2013.
- [68] Serge Desgreniers. High-density phases of zno: structural and compressive parameters. *Phys. Rev. B*, 58:14102–14105, Dec 1998.
- [69] Katharina Diller, Florian Klappenberger, Francesco Allegretti, Anthoula C. Papageorgiou, Sybille Fischer, David A. Duncan, Reinhard J. Maurer, Julian A. Lloyd, Seung Cheol Oh, Karsten Reuter, and Johannes V. Barth. Temperature-dependent templated growth of porphine thin films on the (111) facets of copper and silver. *The Journal of Chemical Physics*, 141(14):–, 2014.
- [70] M. Dion, H. Rydberg, E. Schröder, D. C. Langreth, and B. I. Lundqvist. Van der waals density functional for general geometries. *Phys. Rev. Lett.*, 92:246401, Jun 2004.

- [71] John F Dobson and Tim Gould. Calculation of dispersion energies. *Journal of Physics: Condensed Matter*, 24(7):073201, 2012.
- [72] Olga Dulub, Lynn A Boatner, and Ulrike Diebold. {STM} study of the geometric and electronic structure of $\text{ZnO}(0001)\text{-Zn}$, $(000\bar{1})\text{-O}$, $(10\bar{1}0)$ and $(11\bar{2}0)$ surfaces. *Surface Science*, 519(3):201 – 217, 2002.
- [73] Olga Dulub, Ulrike Diebold, and G. Kresse. Novel stabilization mechanism on polar surfaces: $\text{ZnO}(0001)\text{-Zn}$. *Phys. Rev. Lett.*, 90:016102, Jan 2003.
- [74] A. Einstein. Die plancksche theorie der strahlung und die theorie der spezifischen wärme. *Annalen der Physik*, 327(1):180–190, 1906.
- [75] R. Eisenschitz and F. London. Über das verhältnis der van der waalsschen kräfte zu den homöopolaren bindungskräften. *Zeitschrift für Physik*, 60(7-8):491–527, 1930.
- [76] Helmut Eschrig. *The fundamentals of density functional theory*, volume 32. Springer.
- [77] P. P. Ewald. Die berechnung optischer und elektrostatischer gitterpotentiale. *Annalen der Physik*, 369(3):253–287, 1921.
- [78] E. Fabiano, L. A. Constantin, and F. Della Sala. Generalized gradient approximation bridging the rapidly and slowly varying density regimes: A pbe-like functional for hybrid interfaces. *Phys. Rev. B*, 82:113104, 2010.
- [79] E. Fermi. Eine statistische methode zur bestimmung einiger eigenschaften des atoms und ihre anwendung auf die theorie des periodischen systems der elemente. *Zeitschrift für Physik*, 48(1-2):73–79, 1928.
- [80] Denis Fichou. Structural order in conjugated oligothiophenes and its implications on opto-electronic devices. *J. Mater. Chem.*, 10:571–588, 2000.
- [81] T. Fließbach. *Quantenmechanik*. Lehrbuch zur Theoretischen Physik. BI-Wiss.-Verlag, 1991.
- [82] Th. Förster. Zwischenmolekulare energiewanderung und fluoreszenz. *Annalen der Physik*, 437(1-2):55–75, 1948.
- [83] Colin L. Freeman, Frederik Claeysens, Neil L. Allan, and John H. Harding. Graphitic nanofilms as precursors to wurtzite films: Theory. *Phys. Rev. Lett.*, 96:066102, Feb 2006.
- [84] Roger H. French, V. Adrian Parsegian, Rudolf Podgornik, Rick F. Rajter, Anand Jagota, Jian Luo, Dilip Asthagiri, Manoj K. Chaudhury, Yet-ming Chiang, Steve Granick, Sergei Kalinin, Mehran Kardar, Roland Kjellander, David C. Langreth, Jennifer Lewis, Steve Lustig, David Wesolowski, John S. Wettlaufer, Wai-Yim Ching, Mike Finnis, Frank Houlihan, O. Anatole von Lilienfeld, Carel Jan van Oss, and Thomas Zemb. Long range interactions in nanoscale science. *Rev. Mod. Phys.*, 82:1887–1944, Jun 2010.

- [85] Daan Frenkel and Berend Smit. *Understanding Molecular Simulation, Second Edition: From Algorithms to Applications (Computational Science)*. Academic Press, 2 edition, November 2001.
- [86] Hans-Joachim Freund, Markus Heyde, Niklas Nilius, Svetlana Schauer-mann, Shamil Shaikhutdinov, and Martin Sterrer. Model studies on hetero-geneous catalysts at the atomic scale: From supported metal particles to two-dimensional zeolites. *Journal of Catalysis*, 308(0):154 – 167, 2013. 50th Anniversary Special Issue.
- [87] Hans-Joachim Freund and Gianfranco Pacchioni. Oxide ultra-thin films on metals: new materials for the design of supported metal catalysts. *Chem. Soc. Rev.*, 37:2224–2242, 2008.
- [88] Christoph Freysoldt, Patrick Rinke, and Matthias Scheffler. Ultrathin ox-ides: Bulk-oxide-like model surfaces or unique films? *Phys. Rev. Lett.*, 99:086101, Aug 2007.
- [89] Jens Fricke. Transport equations including many-particle correlations for an arbitrary quantum system: A general formalism. *Annals of Physics*, 252(2):479 – 498, 1996.
- [90] Friend R. H., Gymer R. W., Holmes A. B., Burroughes J. H., Marks R. N., Taliani C., Bradley D. D. C., Santos D. A. Dos, Bredas J. L., Logdlund M., and Salaneck W. R. Electroluminescence in conjugated polymers. *Nature*, 397(6715):121–128, jan 1999. 10.1038/16393.
- [91] Martin Fuchs and Matthias Scheffler. Ab initio pseudopotentials for electronic structure calculations of poly-atomic systems using density-functional theory. *Computer Physics Communications*, 119(1):67–98, 1999.
- [92] Gene H. Golub and Henk A. van der Vorst. Eigenvalue computation in the 20th century. *Journal of Computational and Applied Mathematics*, 123(1&2):35 – 65, 2000. Numerical Analysis 2000. Vol. III: Linear Algebra.
- [93] Jan Götzen and Gregor Witte. Rapid preparation of highly ordered ultraflat zno surfaces. *Applied Surface Science*, 258(24):10144 – 10147, 2012.
- [94] B. Hammer, L.B. Hansen, and J.K. Nørskov. *Phys. Rev. B*, 59:7413, 1999.
- [95] J. B. Hansen and P. E. Højlund Nielsen. *Methanol Synthesis*. Wiley-VCH, 2008.
- [96] V. Havu, V. Blum, P. Havu, and M. Scheffler. Efficient integration for all-electron electronic structure calculation using numeric basis functions. *Journal of Computational Physics*, 228(22):8367 – 8379, 2009.
- [97] Lars Hedin. New method for calculating the one-particle green’s function with application to the electron-gas problem. *Phys. Rev.*, 139:A796–A823, Aug 1965.

- [98] Philipp Herrmann and Georg Heimel. Structure and stoichiometry prediction of surfaces reacting with multicomponent gases. *Advanced Materials*, 27(2):255–260, 2015.
- [99] Jochen Heyd, Gustavo E. Scuseria, and Matthias Ernzerhof. *J. Chem. Phys.*, 118:8207, 2003.
- [100] Jochen Heyd, Gustavo E. Scuseria, and Matthias Ernzerhof. Hybrid functionals based on a screened coulomb potential. *The Journal of Chemical Physics*, 118(18):8207–8215, 2003.
- [101] F.L. Hirshfeld. *Theor. Chim. Acta (Berl.)*, 44:129, 1977.
- [102] P. Hohenberg and W. Kohn. Inhomogeneous electron gas. *Phys. Rev.*, 136:B864–B871, Nov 1964.
- [103] Harald Hoppe and Niyazi Serdar Sariciftci. Organic solar cells: An overview. *Journal of Materials Research*, 19:1924–1945, 2004.
- [104] H. Hu, Z. Lu, and W. yang yang yang yang. Fitting molecular electrostatic potentials from quantum mechanical calculations. *J. Chem. Theory Comput.*, 3:1004–1013, 2007.
- [105] G Hughes and N R McLean. Zinc oxide tape: a useful dressing for the recalcitrant finger-tip and soft-tissue injury. *Archives of Emergency Medicine*, 5(4):223–227, 1988.
- [106] Mark S. Hybertsen and Steven G. Louie. Electron correlation in semiconductors and insulators: Band gaps and quasiparticle energies. *Phys. Rev. B*, 34:5390–5413, Oct 1986.
- [107] Hisao Ishii, Kiyoshi Sugiyama, Eisuke Ito, and Kazuhiko Seki. Energy level alignment and interfacial electronic structures at organic/metal and organic/organic interfaces. *Advanced Materials*, 11(8):605–625, 1999.
- [108] G. Itskos, G. Heliotis, P. G. Lagoudakis, J. Lupton, N. P. Barradas, E. Alves, S. Pereira, I. M. Watson, M. D. Dawson, J. Feldmann, R. Murray, and D. D. C. Bradley. Efficient dipole-dipole coupling of mott-wannier and frenkel excitons in (ga,in)n quantum well/polyfluorene semiconductor heterostructures. *Phys. Rev. B*, 76:035344, Jul 2007.
- [109] John E. Jaffe, James A. Snyder, Zijing Lin, and Anthony C. Hess. Lda and gga calculations for high-pressure phase transitions in zno and mgo. *Phys. Rev. B*, 62:1660–1665, Jul 2000.
- [110] Anderson Janotti and Chris G. Van de Walle. New insights into the role of native point defects in zno. *Journal of Crystal Growth*, 287(1):58 – 65, 2006. Proceedings of the International Conference on Materials for Advanced Technologies (ICMAT 2005) Symposium N ZnO and Related Materials Proceedings of the International Conference on Materials for Advanced Technologies (ICMAT 2005) Symposium N.

- [111] Anderson Janotti and Chris G Van de Walle. Fundamentals of zinc oxide as a semiconductor. *Reports on Progress in Physics*, 72(12):126501, 2009.
- [112] Anderson Janotti and Chris G. Van de Walle. Oxygen vacancies in zno. *Applied Physics Letters*, 87(12):–, 2005.
- [113] Anderson Janotti and Chris G. Van de Walle. Native point defects in zno. *Phys. Rev. B*, 76:165202, Oct 2007.
- [114] Frank Jensen. *Introduction to Computational Chemistry*. Wiley, 2 edition, November 2006.
- [115] Mikkel Jørgensen, Kion Norrman, and Frederik C. Krebs. Stability/degradation of polymer solar cells. *Solar Energy Materials and Solar Cells*, 92(7):686 – 714, 2008. Degradation and Stability of Polymer and Organic Solar Cells.
- [116] Robert A DiStasio Jr, Vivekanand V Gobre, and Alexandre Tkatchenko. Many-body van der waals interactions in molecules and condensed matter. *Journal of Physics: Condensed Matter*, 26(21):213202, 2014.
- [117] Petr Jurecka, Jiri Sponer, Jiri Cerny, and Pavel Hobza. Benchmark database of accurate (mp2 and ccsd(t) complete basis set limit) interaction energies of small model complexes, dna base pairs, and amino acid pairs. *Phys. Chem. Chem. Phys.*, 8:1985–1993, 2006.
- [118] M. Kalay, H.H. Kart, S. Oezdemir Kart, and T. Cagin. Elastic properties and pressure induced transitions of zno polymorphs from first-principle calculations. *Journal of Alloys and Compounds*, 484(1&2):431 – 438, 2009.
- [119] H. Karzel, W. Potzel, M. Köfferlein, W. Schiessl, M. Steiner, U. Hiller, G. M. Kalvius, D. W. Mitchell, T. P. Das, P. Blaha, K. Schwarz, and M. P. Pasternak. Lattice dynamics and hyperfine interactions in zno and znse at high external pressures. *Phys. Rev. B*, 53:11425–11438, May 1996.
- [120] D. Kato, T. Matsui, and J. Yuhara. Oxidation of ultra-thin zinc films on rh(100) surface. *Surface Science*, 604(15&16):1283 – 1286, 2010.
- [121] G.P. Kerker. *Phys. Rev. B*, 23:3082, 1981.
- [122] Kyoung-Kook Kim, Hyun-Sik Kim, Dae-Kue Hwang, Jae-Hong Lim, and Seong-Ju Park. Realization of p-type zno thin films via phosphorus doping and thermal activation of the dopant. *Applied Physics Letters*, 83(1):63–65, 2003.
- [123] M. Kira and S.W. Koch. Many-body correlations and excitonic effects in semiconductor spectroscopy. *Progress in Quantum Electronics*, 30(5):155 – 296, 2006.
- [124] Charles Kittel. *Introduction to Solid State Physics*. Wiley, NY, 8 edition, November 2005.
- [125] C. Klingshirn. Zno: From basics towards applications. *physica status solidi (b)*, 244(9):3027–3073, 2007.

- [126] Claus Klingshirn, J. Fallert, H. Zhou, J. Sartor, C. Thiele, F. Maier-Flaig, D. Schneider, and H. Kalt. 65 years of zno research – old and very recent results. *physica status solidi (b)*, 247(6):1424–1447, 2010.
- [127] Bjorn Kobin, Lutz Grubert, Sylke Blumstengel, Fritz Henneberger, and Stefan Hecht. Vacuum-processable ladder-type oligophenylenes for organic-inorganic hybrid structures: synthesis, optical and electrochemical properties upon increasing planarization as well as thin film growth. *J. Mater. Chem.*, 22:4383–4390, 2012.
- [128] Klaus Koepernik and Helmut Eschrig. Full-potential nonorthogonal local-orbital minimum-basis band-structure scheme. *Phys. Rev. B*, 59:1743–1757, Jan 1999.
- [129] W. Kohn and L. J. Sham. Self-consistent equations including exchange and correlation effects. *Phys. Rev.*, 140:A1133–A1138, Nov 1965.
- [130] H.A. Kramers. La diffusion de la lumiere par les atome. *Atti Cong. Intern. Fisici, (Transactions of Volta Centenary Congress)*, 2:545–557, 1927.
- [131] G. Kresse and J. Furthmüller. Efficiency of ab-initio total energy calculations for metals and semiconductors using a plane-wave basis set. *Comp. Mat. Sci.*, 6:15–50, 1996.
- [132] Georg Kresse, Olga Dulub, and Ulrike Diebold. Competing stabilization mechanism for the polar zno(0001)-zn surface. *Phys. Rev. B*, 68:245409, Dec 2003.
- [133] A. Krönig. Grundzüge einer theorie der gase. *Annalen der Physik*, 175(10):315–322, 1856.
- [134] Aliaksandr V. Krukau, Oleg A. Vydrov, Artur F. Izmaylov, and Gustavo E. Scuseria. *J. Chem. Phys.*, 125:224106, 2006.
- [135] Joyce G. Laquindanum, Howard E. Katz, Andrew J. Lovinger, and Ananth Dodabalapur. Morphological origin of high mobility in pentacene thin-film transistors. *Chemistry of Materials*, 8(11):2542–2544, 1996.
- [136] Jeppe V. Lauritsen, Soeren Porsgaard, Morten K. Rasmussen, Mona C. R. Jensen, Ralf Bechstein, Kristoffer Meinander, Bjerne S. Clausen, Stig Helveg, Roman Wahl, Georg Kresse, and Flemming Besenbacher. Stabilization principles for polar surfaces of zno. *ACS Nano*, 5(7):5987–5994, 2011. PMID: 21671628.
- [137] Matt Law, Lori E. Greene, Justin C. Johnson, Richard Saykally, and Peidong Yang. Nanowire dye-sensitized solar cells. *Nat. Mater.*, 4(6):455–459, 2005.
- [138] C.L. Lee, W. Yang, and R.G. Parr. *Phys. Rev. B*, 37:785, 1988.
- [139] J. W. Levell, M. E. Giardini, and I. D. W. Samuel. A hybrid organic semiconductor/silicon photodiode for efficient ultraviolet photodetection. *Opt. Express*, 18(4):3219–3225, Feb 2010.

- [140] Mel Levy. Universal variational functionals of electron densities, first-order density matrices, and natural spin-orbitals and solution of the v-representability problem. *Proceedings of the National Academy of Sciences*, 76(12):6062–6065, 1979.
- [141] Liang Li, Tianyou Zhai, Yoshio Bando, and Dmitri Golberg. Recent progress of one-dimensional zno nanostructured solar cells. *Nano Energy*, 1(1):91 – 106, 2012.
- [142] Ting Liang, Yuanjing Cui, Jiancan Yu, Wenxin Lin, Yu Yang, and Guodong Qian. Large nonlinear optical activity from hybrid inorganic–organic films with fluorinated benzene as isolation group. *Thin Solid Films*, 544(0):407 – 411, 2013. The 6th International Conference on Technological Advances of Thin Films and Surface Coatings.
- [143] M. Lindberg and S. W. Koch. Effective bloch equations for semiconductors. *Phys. Rev. B*, 38:3342–3350, Aug 1988.
- [144] Carlos Lizandara Pueyo, Stephan Siroky, Steve Landsmann, Maurits W. E. van den Berg, Markus R. Wagner, Juan S. Reparaz, Axel Hoffmann, and Sebastian Polarz. Molecular precursor route to a metastable form of zinc oxide. *Chemistry of Materials*, 22(14):4263–4270, 2010.
- [145] F. London. Zur theorie und systematik der molekularkräfte. *Zeitschrift für Physik*, 63(3-4):245–279, 1930.
- [146] F. London. The general theory of molecular forces. *Trans. Faraday Soc.*, 33:8b–26, 1937.
- [147] D. C. Look, D. C. Reynolds, C. W. Litton, R. L. Jones, D. B. Eason, and G. Cantwell. Characterization of homoepitaxial p-type zno grown by molecular beam epitaxy. *Applied Physics Letters*, 81(10):1830–1832, 2002.
- [148] D.C. Look. Recent advances in zno materials and devices. *Materials Science and Engineering: B*, 80(1–3):383 – 387, 2001.
- [149] J. L. Lyons, A. Janotti, and C. G. Van de Walle. Why nitrogen cannot lead to p-type conductivity in zno. *Applied Physics Letters*, 95(25):–, 2009.
- [150] M. E. Madjet, A. Abdurahman, and T. Renger. Intermolecular coulomb couplings from ab initio electrostatic potentials: application to optical transitions of strongly coupled pigments in photosynthetic antennae and reaction centers. *The Journal of Physical Chemistry B*, 110(34):17268–17281, 2006.
- [151] Georg K.H. Madsen and David J. Singh. Boltztrap. a code for calculating band-structure dependent quantities. *Computer Physics Communications*, 175(1):67 – 71, 2006.
- [152] Ermin Malic, Heiko Appel, Oliver T. Hofmann, and Angel Rubio. Energy-transfer in porphyrin- functionalized graphene. *physica status solidi (b)*, 251(12):2495–2498, 2014.

- [153] Ermin Malic, Heiko Appel, Oliver T. Hofmann, and Angel Rubio. Förster-induced energy transfer in functionalized graphene. *The Journal of Physical Chemistry C*, 118(17):9283–9289, 2014.
- [154] M. Manninen, R. Nieminen, and P. Hautojärvi. *Phys. Rev. B*, 12:4012, 1975.
- [155] M. Mantina, A. C. Chamberlin, R. Valero, C. J. Cramer, and D. G. Truhlar. Consistent van der waals radii for the whole main group. *J. Phys. Chem. A*, 113:5806–5812, 2009.
- [156] A Marek, V Blum, R Johanni, V Havu, B Lang, T Auckenthaler, A Heinecke, H-J Bungartz, and H Lederer. The elpa library: scalable parallel eigenvalue solutions for electronic structure theory and computational science. *Journal of Physics: Condensed Matter*, 26(21):213201, 2014.
- [157] M. A. L. Marques and E. K. U. Gross. Time-Dependent Density Functional Theory. *Annual Review of Physical Chemistry*, 55(1):427–455, January 2004.
- [158] Miguel A. L. Marques, Julien Vidal, Micael J. T. Oliveira, Lucia Reining, and Silvana Botti. Density-based mixing parameter for hybrid functionals. *Phys. Rev. B*, 83:035119, Jan 2011.
- [159] Y. Martynova, B.-H. Liu, M.E. McBriarty, I.M.N. Groot, M.J. Bedzyk, S. Shaikhutdinov, and H.-J. Freund. Co oxidation over zno films on pt(111) at near-atmospheric pressures. *Journal of Catalysis*, 301(0):227 – 232, 2013.
- [160] W.F. McDonough and S. s. Sun. The composition of the earth. *Chemical Geology*, 120(3&4):223 – 253, 1995. Chemical Evolution of the Mantle.
- [161] B. Meyer. First-principles study of the polar o-terminated zno surface in thermodynamic equilibrium with oxygen and hydrogen. *Phys. Rev. B*, 69:045416, Jan 2004.
- [162] B. Meyer and Dominik Marx. Density-functional study of the structure and stability of zno surfaces. *Phys. Rev. B*, 67:035403, Jan 2003.
- [163] Kazunori Minegishi, Yasushi Koiwai, Yukinobu Kikuchi, Koji Yano, Masanobu Kasuga, and Azuma Shimizu. Growth of p-type zinc oxide films by chemical vapor deposition. *Japanese Journal of Applied Physics*, 36(11A):L1453, 1997.
- [164] Mark A. Mitchnick, David Fairhurst, and Sheldon R. Pinnell. Microfine zinc oxide (z-cote) as a photostable uva/uvb sunblock agent. *Journal of the American Academy of Dermatology*, 40(1):85 – 90, 1999.
- [165] Amir Moezzi, Andrew M. McDonagh, and Michael B. Cortie. Zinc oxide particles: Synthesis, properties and applications. *Chemical Engineering Journal*, 185&186(0):1 – 22, 2012.
- [166] Peter J. Mohr, Barry N. Taylor, and David B. Newell. Codata recommended values of the fundamental physical constants: 2010*. *Rev. Mod. Phys.*, 84:1527–1605, Nov 2012.

- [167] Nikolaj Moll, Yong Xu, Oliver T Hofmann, and Patrick Rinke. Stabilization of semiconductor surfaces through bulk dopants. *New Journal of Physics*, 15(8):083009, 2013.
- [168] F. A. Momany. Determination of partial atomic charges from ab initio molecular electrostatic potentials. application to formamide, methanol, and formic acid. *J. Chem. Phys.*, 82:592–601, 1978.
- [169] Benjamin J. Morgan. Preferential stability of the d-bct phase in zno thin films. *Phys. Rev. B*, 80:174105, Nov 2009.
- [170] Benjamin J. Morgan. First-principles study of epitaxial strain as a method of stabilization in zno, zns, and cds. *Phys. Rev. B*, 82:153408, Oct 2010.
- [171] Benjamin J. Morgan and Paul A. Madden. A molecular dynamics study of structural relaxation in tetrahedrally coordinated nanocrystals. *Phys. Chem. Chem. Phys.*, 9:2355–2361, 2007.
- [172] O. F. Mossotti. *Mem. di mathem. e fisica in Modena*, 24(11):49, 1850.
- [173] R.S. Mulliken. *J. Chem. Phys.*, 23:1833, 1955.
- [174] F. D. Murnaghan. The compressibility of media under extreme pressures. *Proceedings of the National Academy of Sciences*, 30(9):244–247, 1944.
- [175] R. Naumann d’Alnoncourt, X. Xia, J. Strunk, E. Löffler, O. Hinrichsen, and M. Muhler. The influence of strongly reducing conditions on strong metal-support interactions in cu/zno catalysts used for methanol synthesis. *Phys. Chem. Chem. Phys.*, 8:1525–1538, 2006.
- [176] Antonio Alvaro Ranha Neves, Andrea Camposeo, Roberto Cingolani, and Dario Pisignano. Interaction scheme and temperature behavior of energy transfer in a light-emitting inorganic-organic composite system. *Advanced Functional Materials*, 18(5):751–757, 2008.
- [177] R. Nieminen. *J. Phys. F*, 7:375, 1977.
- [178] NIST. <http://kinetics.nist.gov/janaf>.
- [179] Jorge Nocedal and Stephen J. Wright. *Numerical optimization*. Springer, 2. edition, 2006.
- [180] Fernando Nogueira, Alberto Castro, and Miguel Marques. A Tutorial on Density Functional Theory A Primer in Density Functional Theory. In Carlos Fiolhais, Fernando Nogueira, and Miguel A. L. Marques, editors, *A Primer in Density Functional Theory*, volume 620 of *Lecture Notes in Physics*, chapter 6, pages 218–256. Springer Berlin / Heidelberg, Berlin, Heidelberg, June 2003.
- [181] Claudine Noguera and Jacek Goniakowski. Polarity in oxide nano-objects. *Chemical Reviews*, 113(6):4073–4105, 2013. PMID: 23206162.
- [182] Wolfgang Nolting. *Grundkurs Theoretische Physik. 5/1, Quantenmechanik - Grundlagen*. Springer, 2009.

- [183] Fumiyasu Oba, Atsushi Togo, Isao Tanaka, Joachim Paier, and Georg Kresse. Defect energetics in zno: A hybrid hartree-fock density functional study. *Phys. Rev. B*, 77:245202, Jun 2008.
- [184] George A. Olah, Alain Goepfert, and G. K. Surya Prakash. *Introduction*, pages 1–10. Wiley-VCH Verlag GmbH & Co. KGaA, 2009.
- [185] Inchem (International Programme on Chemical Safety). Health and safety guides (hsg).
- [186] Giovanni Onida, Lucia Reining, and Angel Rubio. Electronic excitations: density-functional versus many-body green's-function approaches. *Rev. Mod. Phys.*, 74:601–659, Jun 2002.
- [187] Ü. Özgür, Ya. I. Alivov, C. Liu, A. Teke, M. A. Reshchikov, S. Dogan, V. Avrutin, S.-J. Cho, and H. Morkoc. A comprehensive review of zno materials and devices. *Journal of Applied Physics*, 98(4):–, 2005.
- [188] Ü. Özgür, V. Avrutin, and H. Morkoc. Chapter 16 - zinc oxide materials and devices grown by mbe. In Mohamed Henini, editor, *Molecular Beam Epitaxy*, pages 369 – 416. Elsevier, Oxford, 2013.
- [189] Gianfranco Pacchioni. Two-dimensional oxides: Multifunctional materials for advanced technologies. *Chemistry â€š A European Journal*, 18(33):10144–10158, 2012.
- [190] Nagarajan Padmavathy and Rajagopalan Vijayaraghavan. Enhanced bioactivity of zno nanoparticlesâ€šAn antimicrobial study. *Science and Technology of Advanced Materials*, 9(3):035004, 2008.
- [191] Joachim Paier, Martijn Marsman, and Georg Kresse. Dielectric properties and excitons for extended systems from hybrid functionals. *Phys. Rev. B*, 78:121201, Sep 2008.
- [192] Q. Pan, B.H. Liu, M.E. McBriarty, Y. Martynova, I.M.N. Groot, S. Wang, M.J. Bedzyk, S. Shaikhutdinov, and H.-J. Freund. Reactivity of ultra-thin zno films supported by ag(111) and cu(111): A comparison to zno/pt(111). *Catalysis Letters*, 144(4):648–655, 2014.
- [193] C. H. Park, S. B. Zhang, and Su-Huai Wei. Origin of p -type doping difficulty in zno: The impurity perspective. *Phys. Rev. B*, 66:073202, Aug 2002.
- [194] Qing Peng, AmirR. Zamiri, Wei Ji, and Suvranu De. Elastic properties of hybrid graphene/boron nitride monolayer. *Acta Mechanica*, 223(12):2591–2596, 2012.
- [195] J. P. Perdew and A. Zunger. Self-interaction correction to density-functional approximations for many-electron systems. *Phys. Rev. B*, 23:5048–5079, 1981.
- [196] John P. Perdew, Kieron Burke, and Matthias Ernzerhof. Generalized gradient approximation made simple. *Phys. Rev. Lett.*, 77:3865–3868, Oct 1996.

- [197] John P. Perdew, J. A. Chevary, S. H. Vosko, Koblar A. Jackson, Mark R. Pederson, D. J. Singh, and Carlos Fiolhais. Atoms, molecules, solids, and surfaces: Applications of the generalized gradient approximation for exchange and correlation. *Phys. Rev. B*, 46:6671–6687, Sep 1992.
- [198] John P. Perdew, J. A. Chevary, S. H. Vosko, Koblar A. Jackson, Mark R. Pederson, D. J. Singh, and Carlos Fiolhais. Atoms, molecules, solids, and surfaces: Applications of the generalized gradient approximation for exchange and correlation. *Phys. Rev. B*, 46:6671–6687, Sep 1992.
- [199] John P. Perdew and Yue Wang. Accurate and simple analytic representation of the electron-gas correlation energy. *Phys. Rev. B*, 45:13244–13249, Jun 1992.
- [200] J.P. Perdew, A. Ruzsinszky, G.I. Csonka, O.A. Vydrov, G.E. Scuseria, L.A. Constantin, X. Zhou, and K. Burke. *Phys. Rev. Lett.*, 100:136406, 2008.
- [201] Roberto Peverati and Donald G. Truhlar. Quest for a universal density functional: the accuracy of density functionals across a broad spectrum of databases in chemistry and physics. *Philosophical Transactions of the Royal Society of London A: Mathematical, Physical and Engineering Sciences*, 372(2011), 2014.
- [202] Alain J. Phares. The occupation statistics for indistinguishable dumbbells on a rectangular lattice space. i. *Journal of Mathematical Physics*, 25(6):1756–1770, 1984.
- [203] Alain J. Phares and Francis J. Wunderlich. Monomer adsorption on a square lattice with first- and second-neighbor interactions. *Phys. Rev. E*, 55:2403–2408, Mar 1997.
- [204] J. Philip, A. Punnoose, B. I. Kim, K. M. Reddy, S. Layne, J. O. Holmes, B. Satpati, P. R. LeClair, T. S. Santos, and J. S. Moodera. Carrier-controlled ferromagnetism in transparent oxide semiconductors. *Nat Mater*, 5(4):298–304, 2006.
- [205] M. Pope, H. P. Kallmann, and P. Magnante. Electroluminescence in organic crystals. *The Journal of Chemical Physics*, 38(8):2042–2043, 1963.
- [206] William H. Press, Saul A. Teukolsky, William T. Vetterling, and Brian P. Flannery. *Numerical Recipes 3rd Edition: The Art of Scientific Computing*. Cambridge University Press, New York, NY, USA, 3 edition, 2007.
- [207] Frank T. Prochaska and Lester Andrews. Vibration-rotation and pure rotational laser Raman spectra of h₂, d₂, and hd in matrices at 12 k. *The Journal of Chemical Physics*, 67(3):1139–1143, 1977.
- [208] L. Pugazhenth. *Zinc Handbook: Properties, Processing, and Use In Design*. MECHANICAL ENGINEERING. Taylor & Francis, 1991.
- [209] P. Pulay. Convergence acceleration of iterative sequences. the case of scf iteration. *Chem. Phys. Lett.*, 73:393–398, 1980.

- [210] Bipul Rakshit and Priya Mahadevan. Stability of the bulk phase of layered zno. *Phys. Rev. Lett.*, 107:085508, Aug 2011.
- [211] R. Ramprasad, H. Zhu, Patrick Rinke, and Matthias Scheffler. New perspective on formation energies and energy levels of point defects in nonmetals. *Phys. Rev. Lett.*, 108:066404, Feb 2012.
- [212] Ian D. Rees, Kay L. Robinson, Andrew B. Holmes, Carl R. Towns, and Richard O'Dell. Recent developments in light-emitting polymers. *MRS Bulletin*, 27:451–455, 6 2002.
- [213] Sivan Refaely-Abramson, Roi Baer, and Leeor Kronik. Fundamental and excitation gaps in molecules of relevance for organic photovoltaics from an optimally tuned range-separated hybrid functional. *Phys. Rev. B*, 84:075144, Aug 2011.
- [214] K. Reuter, C. Stampfl, and M. Scheffler. *Ab initio atomistic thermodynamics and statistical mechanics of surface properties and functions*. Springer Berlin Heidelberg, 2005.
- [215] J. Robertson and S. J. Clark. Limits to doping in oxides. *Phys. Rev. B*, 83:075205, Feb 2011.
- [216] Michael Rohlfing and Steven G. Louie. Electron-hole excitations and optical spectra from first principles. *Phys. Rev. B*, 62:4927–4944, Aug 2000.
- [217] F. Romá and A.J. Ramirez-Pastor. Configurational entropy of adsorbed particles on two-dimensional heterogeneous surfaces. *Physica A: Statistical Mechanics and its Applications*, 328(3–4):513 – 524, 2003.
- [218] Fausto Rossi and Tilmann Kuhn. Theory of ultrafast phenomena in photoexcited semiconductors. *Rev. Mod. Phys.*, 74:895–950, Aug 2002.
- [219] R. S. Rowland and R. Taylor. Intermolecular nonbonded contact distances in organic crystal structures: Comparison with distances expected from van der waals radii. *J. Phys. Chem.*, 100:7384–7391, 1996.
- [220] Victor G. Ruiz, Wei Liu, Egbert Zojer, Matthias Scheffler, and Alexandre Tkatchenko. Density-Functional Theory with Screened van der Waals Interactions for the Modeling of Hybrid Inorganic-Organic Systems. *Phys. Rev. Lett.*, 108(14):146103, 2012.
- [221] Pierre Van Rysselberghe. Remarks concerning the clausius-mossotti law. *The Journal of Physical Chemistry*, 36(4):1152–1155, 1931.
- [222] Y.R Ryu, S Zhu, D.C Look, J.M Wrobel, H.M Jeong, and H.W White. Synthesis of p-type zno films. *Journal of Crystal Growth*, 216(1–4):330 – 334, 2000.
- [223] J. J. Sakurai. *Modern Quantum Mechanics (Revised Edition)*. Addison Wesley, 1 edition, September 1993.

- [224] E. E. Salpeter and H. A. Bethe. A relativistic equation for bound-state problems. *Phys. Rev.*, 84:1232–1242, Dec 1951.
- [225] A. Savin, F. Colonna, and R. Pollet. Adiabatic connection approach to density functional theory of electronic systems. *International Journal of Quantum Chemistry*, 93(3):166–190, 2003.
- [226] M. Scheffler and J. Dabrowski. *Philos. Mag. A*, 58, 1988.
- [227] R. Schennach, F. Weber, M. Piffl, G. Weirum, and S. Surnev. Growth and reactivity of Zn and ZnO on Pd(111). *Surface Engineering*, 28(2):87–90, MAR 2012.
- [228] A. Schleife, F. Fuchs, J. Furthmüller, and F. Bechstedt. First-principles study of ground- and excited-state properties of MgO, ZnO, and CdO polymorphs. *Phys. Rev. B*, 73:245212, Jun 2006.
- [229] Vadim Schott, Harald Oberhofer, Alexander Birkner, Mingchun Xu, Yuemin Wang, Martin Muhler, Karsten Reuter, and Christof Wöll. Chemical activity of thin oxide layers: Strong interactions with the support yield a new thin-film phase of zno. *Angewandte Chemie International Edition*, 52(45):11925–11929, 2013.
- [230] E. Schrödinger. An undulatory theory of the mechanics of atoms and molecules. *Phys. Rev.*, 28:1049–1070, Dec 1926.
- [231] Franz Schwabl. *Advanced Quantum Mechanics*. Springer, August 2005.
- [232] G.E. Scuseria and V.N. Staroverov. Progress in the development of exchange-correlation functionals. In C.E. Dykstra, G. Frenking, K.S. Kim, and G.E. Scuseria, editors, *Theory and Applications of Computational Chemistry: The First 40 Years*, chapter 24. Elsevier, Amsterdam, 2005. The parameters for "VWN"-LDA as implemented in the Gaussian code are given in Table 1.
- [233] Michele Sessolo and Henk J. Bolink. Hybrid organic–inorganic light-emitting diodes. *Advanced Materials*, 23(16):1829–1845, 2011.
- [234] S. Shaikhutdinov and H. J. Freund. Ultrathin Oxide Films on Metal Supports: Structure-Reactivity Relations. 63:619–633, 2012.
- [235] James R. Sheats, Homer Antoniadis, Mark Hueschen, William Leonard, Jeff Miller, Ron Moon, Daniel Roitman, and Andrew Stocking. Organic electroluminescent devices. *Science*, 273(5277):884–888, 1996.
- [236] Joseph Shinar and Vadim Savvateev. Introduction to organic light-emitting devices. In Joseph Shinar, editor, *Organic Light-Emitting Devices*, pages 1–41. Springer New York, 2004.
- [237] Akitoshi Shiotari, Bo Hong Liu, Simon Jaekel, Leonhard Grill, Shamil Shaikhutdinov, Hans-Joachim Freund, Martin Wolf, and Takashi Kumagai.

Local characterization of ultrathin zno layers on ag(111) by scanning tunneling microscopy and atomic force microscopy. *The Journal of Physical Chemistry C*, 118(47):27428–27435, 2014.

- [238] E. Sigfridsson and U. Ryde. Atomic charges from the electrostatic potential and moments. *J. Comput. Chem.*, 19(4), 1998.
- [239] U. C. Singh and P. A. Kollman. An approach to computing electrostatic charges for molecules. *J. Comput. Chem.*, 5:129–145, 1984.
- [240] J. C. Slater. The electronic structure of metals. *Rev. Mod. Phys.*, 6:209–280, Oct 1934.
- [241] Sérgio Filipe Sousa, Pedro Alexandrino Fernandes, and Maria Joao Ramos. General performance of density functionals. *The Journal of Physical Chemistry A*, 111(42):10439–10452, 2007.
- [242] Michelle J.S. Spencer, Kester W.J. Wong, and Irene Yarovsky. Density functional theory modelling of and surfaces: Structure, properties and adsorption of {N₂O}. *Materials Chemistry and Physics*, 119(3):505 – 514, 2010.
- [243] Tamar Stein, Helen Eisenberg, Leeor Kronik, and Roi Baer. Fundamental gaps in finite systems from eigenvalues of a generalized kohn-sham method. *Phys. Rev. Lett.*, 105:266802, Dec 2010.
- [244] P. J. Stephens, F. J. Devlin, C. F. Chabalowski, and M. J. Frisch. Ab initio calculation of vibrational absorption and circular dichroism spectra using density functional force fields. *The Journal of Physical Chemistry*, 98(45):11623–11627, 1994.
- [245] Anthony Stone. *The Theory of Intermolecular Forces*. Oxford University Press, 2013.
- [246] R.E. Stratmann, G.E. Scuseria, and M.J. Frisch. *Chem. Phys. Lett.*, 257:213, 1996.
- [247] Attila Szabo and Neil S. Ostlund. *Modern quantum chemistry : introduction to advanced electronic structure theory*. Dover Publications, Mineola (N.Y.), 1996. Premi re  dition Macmillan 1982. Edition revue chez McGraw-Hill 1989.
- [248] James D. Talman. Numerical methods for multicenter integrals for numerically defined basis functions applied in molecular calculations. *International Journal of Quantum Chemistry*, 93(2):72–90, 2003.
- [249] P W Tasker. The stability of ionic crystal surfaces. *Journal of Physics C: Solid State Physics*, 12(22):4977, 1979.
- [250] J. Tersoff and D. R. Hamann. Theory of the scanning tunneling microscope. *Phys. Rev. B*, 31:805–813, Jan 1985.
- [251] The HDF Group. Hierarchical Data Format, version 5, 1997-NNNN. <http://www.hdfgroup.org/HDF5/>.

- [252] L. H. Thomas. The calculation of atomic fields. *Mathematical Proceedings of the Cambridge Philosophical Society*, 23:542–548, 1 1927.
- [253] Alexandre Tkatchenko, Lorenz Romaner, Oliver T. Hofmann, Egbert Zojer, Claudia Ambrosch-Draxl, and Matthias Scheffler. Van der waals interactions between organic adsorbates and at organic/inorganic interfaces. *MRS Bulletin*, 35:435–442, 6 2010.
- [254] Alexandre Tkatchenko and Matthias Scheffler. Accurate Molecular Van Der Waals Interactions from Ground-State Electron Density and Free-Atom Reference Data. *Phys. Rev. Lett.*, 102(7):073005, 2009.
- [255] M. Topsakal, S. Cahangirov, E. Bekaroglu, and S. Ciraci. First-principles study of zinc oxide honeycomb structures. *Phys. Rev. B*, 80:235119, Dec 2009.
- [256] Alessandro Troisi. Charge transport in high mobility molecular semiconductors: classical models and new theories. *Chem. Soc. Rev.*, 40:2347–2358, 2011.
- [257] K. Y. Tse, D. Liu, and J. Robertson. Electronic and atomic structure of metal-hfo₂ interfaces. *Phys. Rev. B*, 81:035325, Jan 2010.
- [258] Z. C. Tu and X. Hu. Elasticity and piezoelectricity of zinc oxide crystals, single layers, and possible single-walled nanotubes. *Phys. Rev. B*, 74:035434, Jul 2006.
- [259] C. Tusche, H. L. Meyerheim, and J. Kirschner. Observation of depolarized zno(0001) monolayers: Formation of unreconstructed planar sheets. *Phys. Rev. Lett.*, 99:026102, Jul 2007.
- [260] E. K. U. Gross und E. Runge. *Vielteilchentheorie*. B. G. Teubner, Stuttgart, 1986.
- [261] Markus Valtiner, Mira Todorova, Guido Grundmeier, and Jörg Neugebauer. Temperature stabilized surface reconstructions at polar zno(0001). *Phys. Rev. Lett.*, 103:065502, Aug 2009.
- [262] Markus Valtiner, Mira Todorova, and Jörg Neugebauer. Hydrogen adsorption on polar zno(0001)-zn: Extending equilibrium surface phase diagrams to kinetically stabilized structures. *Phys. Rev. B*, 82:165418, Oct 2010.
- [263] H. van Hove and R. Leysen. Leed study on the polar surfaces of zno. *physica status solidi (a)*, 9(1):361–367, 1972.
- [264] Daniel Vanmaekelbergh and Lambert K. van Vugt. Zno nanowire lasers. *Nanoscale*, 3:2783–2800, 2011.
- [265] Eike Verdenhalven, Andreas Knorr, Marten Richter, Bjoern Bieniek, and Patrick Rinke. Theory of optical excitations in dipole-coupled hybrid molecule-semiconductor layers: Coupling of a molecular resonance to semiconductor continuum states. *Phys. Rev. B*, 89:235314, Jun 2014.

- [266] S.H. Vosko, L. Wilk, and M. Nusair. *Can. J. Phys.*, 58:1200, 1980.
- [267] Roman Wahl, Jeppe V. Lauritsen, Flemming Besenbacher, and Georg Kresse. Stabilization mechanism for the polar $\text{ZnO}(000\bar{1})$ -o surface. *Phys. Rev. B*, 87:085313, Feb 2013.
- [268] Vei Wang, Deming Ma, Wanli Jia, and Weili Ji. Structural and electronic properties of hexagonal ZnO : A hybrid functional study. *Solid State Communications*, 152(22):2045 – 2048, 2012.
- [269] Kenji Watanabe, Takashi Taniguchi, and Hisao Kanda. Direct-bandgap properties and evidence for ultraviolet lasing of hexagonal boron nitride single crystal. *Nat Mater*, 3(6):404–409, Jun 2004.
- [270] G. Weirum, G. Barcaro, A. Fortunelli, F. Weber, R. Schennach, S. Surnev, and F. P. Netzer. Growth and surface structure of zinc oxide layers on a $\text{Pd}(111)$ surface. *The Journal of Physical Chemistry C*, 114(36):15432–15439, 2010.
- [271] G. Weirum, M. Kratzer, H. P. Koch, A. Tamtögl, J. Killmann, I. Bako, A. Winkler, S. Surnev, F. P. Netzer, and R. Schennach. Growth and desorption kinetics of ultrathin Zn layers on $\text{Pd}(111)$. *The Journal of Physical Chemistry C*, 113(22):9788–9796, 2009.
- [272] Gunther Weirum. *Structural investigation of zinc-palladium and zinc oxide-palladium model catalyst surfaces*. PhD thesis.
- [273] E. Wigner. On the interaction of electrons in metals. *Phys. Rev.*, 46:1002–1011, Dec 1934.
- [274] D. Wolf, P. Keblinski, S. R. Phillpot, and J. Eggebrecht. Exact method for the simulation of coulombic systems by spherically truncated, pairwise r^{-1} summation. *The Journal of Chemical Physics*, 110(17):8254–8282, 1999.
- [275] Ch Wöll. Hydrogen adsorption on metal oxide surfaces: a reinvestigation using he-atom scattering. *Journal of Physics: Condensed Matter*, 16(29):S2981, 2004.
- [276] Christof Wöll. The chemistry and physics of zinc oxide surfaces. *Progress in Surface Science*, 82(2–3):55 – 120, 2007.
- [277] D M Wood and A Zunger. A new method for diagonalising large matrices. *Journal of Physics A: Mathematical and General*, 18(9):1343, 1985.
- [278] Dangxin Wu, M. G. Lagally, and Feng Liu. Stabilizing Graphitic Thin Films of Wurtzite Materials by Epitaxial Strain. *Phys. Rev. Lett.*, 107(23):236101, 2011.
- [279] F. X. Xiu, Z. Yang, L. J. Mandalapu, D. T. Zhao, J. L. Liu, and W. P. Beyersmann. High-mobility Sb -doped p -type ZnO by molecular-beam epitaxy. *Applied Physics Letters*, 87(15):–, 2005.

- [280] Qimin Yan, Patrick Rinke, M Winkelnkemper, A Qteish, D Bimberg, Matthias Scheffler, and Chris G Van de Walle. Band parameters and strain effects in zno and group-iii nitrides. *Semiconductor Science and Technology*, 26(1):014037, 2011.
- [281] Y. Yang, G. A. Turnbull, and I. D. W. Samuel. Hybrid optoelectronics: A polymer laser pumped by a nitride light-emitting diode. *Applied Physics Letters*, 92(16):–, 2008.
- [282] D. Zagorac, J. C. Schön, J. Zagorac, and M. Jansen. Prediction of structure candidates for zinc oxide as a function of pressure and investigation of their electronic properties. *Phys. Rev. B*, 89:075201, Feb 2014.
- [283] Stefan Zander, Edward L. Kunkes, Manfred E. Schuster, Julia Schumann, Gisela Weinberg, Detre Teschner, Nikolas Jacobsen, Robert Schlögl, and Malte Behrens. The role of the oxide component in the development of copper composite catalysts for methanol synthesis. *Angewandte Chemie International Edition*, 52(25):6536–6540, 2013.
- [284] A. Zangwill. University Press, Cambridge, 1988.
- [285] E. Zaremba and W. Kohn. Van der waals interaction between an atom and a solid surface. *Phys. Rev. B*, 13:2270–2285, Mar 1976.
- [286] Guo-Xu Zhang, A. Tkatchenko, J. Paier, H. Appel, and M. Scheffler. van der Waals Interactions in Ionic and Semiconductor Solids. *Phys. Rev. Lett.*, 107:245501, 2011.
- [287] Qifeng Zhang, Christopher S. Dandeneau, Xiaoyuan Zhou, and Guozhong Cao. Zno nanostructures for dye-sensitized solar cells. *Advanced Materials*, 21(41):4087–4108, 2009.
- [288] Y. Zhang and W. Yang. *Phys. Rev. Lett.*, 80:890, 1998.
- [289] Huaxing Zhou, Liqiang Yang, and Wei You. Rational design of high performance conjugated polymers for organic solar cells. *Macromolecules*, 45(2):607–632, 2012.